# Effects of Triaxial Stress and Strain on Multiphase Flow in 3D-Printed Fractured Reservoir Rock Analogues

by

Angel de Jesus Sanchez Barra

A thesis submitted in partial fulfillment of the requirements for the degree of

Doctor of Philosophy

in

Geotechnical Engineering

Department of Civil and Environmental Engineering
University of Alberta

## Abstract

The oil and gas industry, fundamental to the global energy economy, faces an ever-increasing quest for new reserves to meet growing demand. Hydrocarbon reservoirs, dynamic systems by nature, undergo significant changes throughout their lifecycle, particularly due to deformation from effective stress variations during production and stimulation operations. This thesis introduces an integrated approach to characterizing the impact of geomechanical processes on multiphase-flow mechanisms within naturally fractured reservoirs. It examines the effects of stress dependency (both normal and shear stresses) on porosity, absolute permeability, drainage relative permeability, drainage capillary pressure, and matrix-to-fracture flow contributions using 3D-printed fractured reservoir rock analogues, which include intact and fractured components to mimic actual reservoir conditions.

This research systematically investigates the Akal KL reservoir, analyzing its geological attributes and stress-strain behavior over its exploitation cycle. A key innovation is the use of binder-jet additive manufacturing (3D printing technology) to create sandstone models that closely replicate the reservoir rock's porosity, permeability, and other critical properties. These 3D-printed analogues provide a new method to study reservoir rock behaviors under various stress scenarios, overcoming challenges posed by the heterogeneity and scarcity of natural samples.

A specialized multiphase triaxial experimental setup was instrumental in assessing the stress-dependent flow properties of these analogues, providing crucial insights into the geomechanical behaviors that influence multiphase flow in fractured porous media. Experimental findings, such as the observed stress-dependent drainage relative permeability in 3D-printed analogues, were

incorporated into dynamic flow simulations of Akal KL to estimate the uncertainty in oil recovery due to changes in relative permeability. These insights highlight the significant influence of stress alterations on reservoir flow and recovery processes, providing valuable strategies for enhancing hydrocarbon extraction in fractured reservoirs.

The study's experimental outcomes contribute to understanding the practical aspects of hydrocarbon recovery, considering the stress sensitivity of naturally fractured reservoirs during depletion, with Akal KL serving as a key case study. The stress-path sensitivity of multiphase flow in fractured porous media significantly affects hydrocarbon recovery, geothermal processes, radioactive waste repositories, and carbon capture and storage operations, highlighting the broad applicability and importance of this research.

## Preface

This thesis is an original work by Angel Sanchez, conducted under the supervision of Dr. Rick Chalaturnyk and Dr. Gonzalo Zambrano. The research design, experimental work, engineering analysis, simulations, and writing were conducted by me. Sections of this thesis have been published through journal articles and conference papers.

Chapter 4 was presented as a conference paper at the 56th US Rock Mechanics/Geomechanics Symposium in Santa Fe, New Mexico, USA, from June 26-29, 2022. I extend my gratitude to Dr. Nathan Deisman and the GeoREF team for their crucial contributions to the design and manufacturing of the Multiphase Triaxial System, which was highlighted in the following conference paper:

Sanchez-Barra, A., Deisman, N., Guerrero, F., Brandl, J., & Chalaturnyk, R. (2022). Experimental Facility for Testing Unconventional Reservoirs: Effect of Geomechanics on Multiphase Flow Properties. *American Rock Mechanics Association*. https://doi.org/https://doi.org/10.56952/ARMA-2022-0543

Chapter 5 is based on research findings published in two journal articles. I was responsible for designing and executing geomechanical experiments, conducting 3D printing, and preparing the manuscripts. I extend my gratitude to Dr. Kevin Hodder for his expertise in scanning electron microscopy imaging, and to Dr. Sergey Ishutov for assisting with porosity measurements. I also thank Dr. Rick Chalaturnyk and Dr. Gonzalo Zambrano for their contributions through supervision, conceptualization, review, editing, and securing funding.

Sanchez-Barra, A., Zambrano-Narvaez, G., & Chalaturnyk, R. (2023). An In-Depth Analysis of Strength and Stiffness Variability in 3D-Printed Sandstones: Implications for Geomechanics. *Energies*, *16*(14). https://doi.org/10.3390/en16145406

Hodder, K. J., Sanchez-Barra, A. J., Ishutov, S., Zambrano-Narvaez, G., & Chalaturnyk, R. J. (2022). Increasing Density of 3D-Printed Sandstone through Compaction. *Energies*. https://doi.org/10.3390/en15051813

Additionally, I have contributed to several other publications mentioned in Chapter 1, the results of which are not included in this thesis.

*Dedicated to my wife Felisa*

*and our soon-to-be-born daughter Anna Lucia*

*"Lo mejor está por venir"*

## Acknowledgments

First, I would like to thank God for guiding me over the years in His unique and perfect way. I also want to thank my beloved wife, Felisa, for her unconditional love and support. She has been the main driver and motivation for becoming a better version of myself. Thank you for being there in the most difficult times and always pushing me to the other side. Special thanks to my parents, Victor and Tere, and my little sister, Abril, who have always been there for me with love and support and who have taught me the most valuable lessons in life.

I want to express my sincere gratitude to my supervisor, Dr. Rick Chalaturnyk, for his guidance, support, and trust. Thank you for your valuable lessons, patience, and for helping me understand the real value of research. You have been a great mentor in my professional life.

I would also like to thank my co-supervisor, Dr. Gonzalo Zambrano, for your guidance and support. Thank you for always ensuring that I was on the right track. Thanks to Dr. Nathan Deisman for your mentorship and friendship; I will always be grateful for your help and support. The guidance of the supervisory committee, Dr. Renato Macciotta and Dr. Albert Liu, is greatly appreciated.

Many thanks to Cecilia Guzman and Hope Walls for their administrative support and insightful conversations. I am also thankful to all my friends in the Reservoir Geomechanics Research Group (present and alumni), from whom I have been fortunate to work with smart and talented people: Stephen Talman, Bhavesh Morker, Francy Guerrero, Jakob Brandl, Noga Vaisblat, Gilbert Wong, Juan Arias, Kevin Hodder, Sergey Ishutov, Daniel Cartagena, Dmytro Pantov, Bo Zhang, Chao Liu, and everyone at $RG^2$.

Thanks to Dr. Erick Luna, Dr. Manuel Coronado, and everyone involved in the IMP-Ualberta Geomechanics Research Network. I gratefully acknowledge the financial support from Consejo Nacional de Ciencia y Tecnología (CoNaCyT), the Natural Sciences and Engineering Research Council of Canada (NSERC), and the Energi Simulation Industrial Research Consortium on Reservoir Geomechanics for Unconventional Resources.

## Table of Contents

## List of Tables

## List of Figures

# 1. Introduction

## 1.1. Background and Motivation

Naturally Fractured Reservoirs (NFRs) are geological formations characterized by a highly heterogeneous distribution of porosity and permeability. Porosity is the fraction of void space in the total volume of the rock, while absolute permeability reflects the total flow capacity of the rock. Commonly, these rock structures comprise low porosity and low permeability matrix blocks surrounded by a highly permeable fracture network. Consequently, the overall fluid flow within the reservoir is predominantly determined by the flow properties of these fractures, with isolated matrix blocks serving as hydrocarbon storage (Fernø, 2016; Khanal and Weijermars, 2019).

Fractures are formed through various mechanisms, typically induced by tensile, shear, or thermal stresses. Additionally, chemical processes such as dissolution, precipitation, or rock alteration contribute to fracture generation (Adler and Thovert, 1999). In naturally fractured reservoirs, fluid flow is influenced by a combination of viscous, gravitational, and capillary forces. Fractures are primarily controlled by viscous-dominated fluid flow, whereas fluid migration from the matrix to fractures is dominated by capillary forces. The progression of multiphase fluids through fractures is controlled by fracture aperture, flow rate, and wettability, which consequently dictate the shape of relative permeability functions (Rangel-German and Kovscek, 2005).

Relative permeability is defined as the ratio of the mobility of a continuous phase (effective permeability) to the absolute permeability of the rock. Furthermore, capillary forces can either assist or impede the progression of multiphase fluid flow, depending on whether the process is conducted as spontaneous imbibition of the wetting phase or drainage. In the drainage process, the non-wetting phase displaces the wetting phase. Capillary pressure and relative permeability curves are crucial hydraulic properties for describing multiphase flow in fractured porous media as they control the interaction between the matrix and fractures. These multiphase flow properties are subject to continual changes due to their dependency on multiple factors such as stress, wettability, interfacial tension (IFT), and saturation history (Jahanbakhsh et al., 2016; Hamoud et al., 2020).

During the exploitation of naturally fractured reservoirs, primary hydrocarbon production induces reservoir depletion, thereby altering the *in-situ* stress state. This process increases the effective stress and deforms the reservoir rock mass. Effective stress is defined as the difference between the overburden or total stress and pore pressure, a theory initially proposed by Terzaghi (Terzaghi, 1943). The deformation of the rock mass alters the single and multiphase flow properties of the intact rock matrix and fractures (e.g., porosity, absolute permeability, and relative permeability) and modifies the pore throat geometry, affecting the capillary entry pressure. These mechanisms modify the balance between the viscous and capillary forces that control the exchange of fluids between the matrix and fractures (Smart et al., 2001; Rangel-German and Kovscek, 2005).

The influence of stress on multiphase flow during reservoir depletion can be separated into normal and shear stresses. These two components of the total state of stress induce different hydro-mechanical behaviors. In most materials, the hydrostatic or normal stress alters the volume of the material, while the deviatoric or shear stress causes distortional changes. The stress-dependent multiphase flow in fractured porous media significantly impacts the performance of hydrocarbon recovery, geothermal processes, radioactive waste repositories, and carbon capture and storage operations (Yin et al., 2017; Yang et al., 2017; Agheshlui and Matthai, 2018; Haghi et al., 2020; Phillips et al., 2021).

## 1.2. Statement of Problem

Reservoir rock deformation often occurs in response to changes in the effective stress during production and stimulation operations (Buchsteiner et al., 1993; Sanchez-Barra et al., 2022). The state of stress at any given point within the reservoir is defined by three mutually orthogonal normal total stresses. When the equilibrium of these stresses is disrupted by alterations in effective stress, shear and normal stresses come into play, impacting the multiphase flow properties of fractured porous media.

Shear stress induces contraction and dilation, which promote dilatant microcracking, fracture dilation, and displacement. This initially contracts the fractured porous media and is followed by the formation of high-permeability conduits as shearing progresses and gouge is produced. If the engagement of the fracture surface is too extensive, the asperities may progressively fill the aperture space, thereby acting as a permeability barrier (Smart et al., 2001). Conversely, normal stress contracts the fractured porous media, reducing permeability, and typically does not interact with the asperities. The evolution of shear and normal stresses dictates the total stress dependency of multiphase flow during reservoir depletion.

The stress dependency of multiphase flow in fractured porous media is evidenced by alterations in relative permeability and capillary pressure. If the fracture aperture decreases under a constant flow rate, viscous pressure gradients increase and enhance drainage processes. Under such circumstances, pressure gradients become significant and the non-wetting phase flow path broadens, invading peripheral regions with smaller apertures. Previous studies have suggested that during oil displacements by immiscible gas (non-wetting phase), the increased pressure differential between the matrix and the fracture fluids provides the necessary force to drive gas from the fracture to the matrix, producing additional oil (McDonald et al., 1991; Longeron et al., 1994). However, if the fracture dilates, the viscous-dominated non-wetting phase flow will be confined to the largest apertures. This restriction can lead to an early breakthrough of the non-wetting phase, while the wetting phase predominantly follows the critical path (Pyrak-Nolte et al., 1991).

In the matrix, an increase in effective stress causes deformation, which reduces the pore system and increases capillary pressure. Depending on whether the process is carried out as spontaneous imbibition or drainage, capillary forces can either assist or impede fluid transfer between the matrix and the fracture. For reservoirs with oil wettability, like the case study of Akal KL, the increased effective stress may promote capillary entrapments, raising the residual oil saturation. These mechanisms could potentially impair the reservoir flow characteristics, thereby affecting hydrocarbon recovery.

### 1.3. Research Objectives

The primary objective of this thesis is to develop an integrated approach for characterizing the impact of geomechanical processes on flow mechanisms within naturally fractured reservoirs. This research primarily focuses on how the evolution of shear and normal stresses, collectively termed the “stress path”, affects drainage relative permeability, drainage capillary pressure, and the dynamics of fluid transfer between the matrix and fractures.

A key research objective includes a comprehensive characterization of the field case reservoir Akal KL. This encompasses determining its reservoir rock properties and analyzing the stress-strain conditions throughout its lifecycle. Central to this study is the use of binder-jet additive manufacturing techniques (3D-printing) to fabricate physical sandstone models that statistically represent the reservoir rock. Essential steps involve analyzing the variability and repeatability of

3D-printed sandstones and developing a densification approach to achieve desired sandstone properties such as modified porosity and permeability, thus assisting in the creation of an accurate 3D-printed reservoir rock analogue. Moreover, the research involves characterizing the hydraulic and geomechanical properties of these 3D-printed reservoir rock analogues. This includes measuring parameters such as porosity, permeability, uniaxial compressive strength (UCS), Young's modulus, bulk modulus, Poisson's ratio, friction angle, and cohesive strength.

An integral part of the study is the design and implementation of an experimental system custom-made for multiphase triaxial experiments. This includes conducting laboratory tests to assess stress-dependent multiphase flow properties in 3D-printed reservoir rock analogues, both intact and with a single fracture, and deriving stress-dependent functions for drainage relative permeability, drainage capillary pressure, and hydraulic aperture.

The final goal of this research is to evaluate the impact of geomechanical processes on recovery mechanisms in naturally fractured reservoirs, using the Akal KL case study as a key reference. This understanding is vital due to the significant influence of stress-dependent multiphase flow in fractured porous media, particularly in the contexts of hydrocarbon recovery, geothermal processes, radioactive waste repositories, and carbon capture and storage operations.

### 1.4. Methodology

This research employed a structured, three-stage methodology to investigate the effects of the effective stress path on multiphase flow properties in naturally fractured reservoirs, utilizing 3D-printed fractured reservoir rock analogues.

*Stage One* involves a detailed characterization of the Akal KL reservoir, the chosen case study. This initial step encompasses assessing key reservoir properties and integrating the fundamentals of reservoir flow physics into the experimental design. This comprehensive understanding of the reservoir's intrinsic characteristics ensures that the subsequent experimental stages are grounded in realistic and relevant conditions.

*Stage Two* focuses on the binder-jet additive manufacturing process used to create the 3D-printed reservoir rock analogues. This stage details the specific post-processing techniques implemented to replicate the hydraulic and geomechanical properties of natural reservoir rocks as closely as possible. These meticulously fabricated 3D-printed samples serve as the core elements in subsequent core flooding experiments, enabling a controlled and accurate investigation of reservoir behaviors under varying conditions.

*Stage Three* encompasses the laboratory determination of stress-dependent properties, namely the drainage relative permeability and capillary pressure curves under both shear and normal stress conditions. This crucial phase involves conducting meticulous laboratory tests with the 3D-printed samples to derive these key parameters. The results from these experiments are instrumental in assessing the extent to which stress dependency influences recovery mechanisms within naturally fractured reservoirs.

The comprehensive methodology of this study is summarized in a detailed workflow, presented in Figure 1. This visual representation provides a clear, step-by-step overview of the research process, illustrating the interconnected nature of each stage and emphasizing the methodological rigor applied throughout the study.

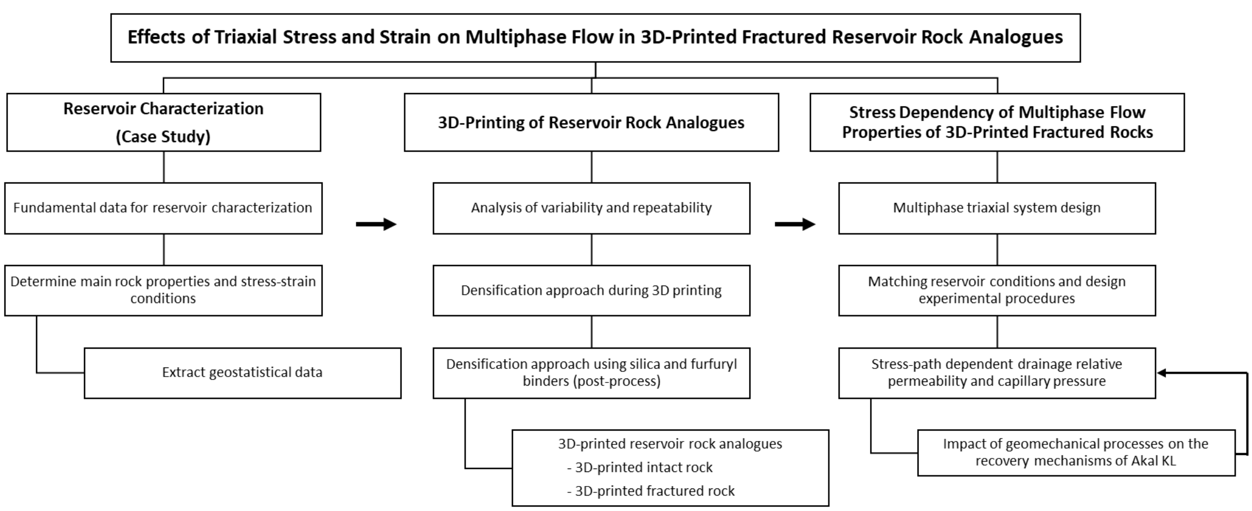


Figure 1.1. Schematic representation of the research methodology. The figure visually depicts the three primary stages of the research: (1) the characterization of the Akal KL field case, (2) the binder-jet additive manufacturing process and post-processing to create 3D-printed reservoir rock analogues, and (3) the laboratory determination of stress-dependent drainage relative permeability and capillary pressure curves.

### 1.5. Organization of Thesis

This thesis is composed of nine chapters, each focusing on distinct aspects of the research conducted to achieve the specified objectives and discussing the derived results. Following the introductory chapter, the organization of the thesis is as follows:

Chapter 2 – Theoretical Framework in Naturally Fractured Reservoirs:

This chapter examines the key processes governing naturally fractured reservoirs and explores the impact of geomechanics on their flow properties. It addresses the complex dynamics of multiphase fluid flow, influenced by stress-dependent factors such as nonlinear characteristics of permeability and porosity in the rock fractures.

Chapter 3 – Akal Field Case Study: Geomechanical and Flow Properties in a Naturally Fractured Reservoir:

This chapter presents a comprehensive case study of the Akal field, a naturally fractured reservoir. It focuses on an in-depth analysis of the reservoir's main properties and the key mechanisms essential for oil recovery. A significant aspect of this study is understanding the impact of pore pressure depletion on the primary flow properties of the rock throughout its lifecycle. Additionally, the fundamental geomechanical and flow physics have been integrated into the experimental design to replicate realistic reservoir conditions during testing.

Chapter 4 – Design and Execution of Multiphase Triaxial Testing:

This chapter outlines the design and functionality of the Multiphase Triaxial System, covering its primary hydraulic and electrical components and operation within an oven to ensure isothermal conditions. The chapter shows the system's capabilities through tests on sandpack and Berea sandstone specimens and highlights its applicability in various disciplines that require an understanding of two-phase flow under variable effective stress conditions. It emphasizes the importance of triaxial stress in influencing multiphase fluid flow mechanisms, providing insights into theoretical and practical aspects of geomechanics and fluid dynamics.

Chapter 5 – Advancements in 3D-Printed Sandstone Analysis: Exploring Strength, Stiffness, and Densification in Geomechanical Applications:

This chapter introduces a methodology to assess mechanical property variability in binder-jet additive manufacturing and focuses on how the location of samples within the print bed influences the strength of 3D-printed sandstones. It also proposes a densification approach for compacted sandstone analogues, analyzing bimodal sand grain size distributions and incorporating different compacting rollers to examine their effects on porosity and material properties.

Chapter 6 – Geomechanical and Flow Characterization of 3D-Printed Reservoir Rock Analogues:

A comprehensive investigation into the geomechanical and flow properties of 3D-printed reservoir rock analogues is presented in this chapter. A methodology is developed for customizing these properties to mirror those of natural reservoir rocks, including techniques like sodium silicate-carbon dioxide treatment to modify porosity and permeability.

Chapter 7 – Effects of Triaxial Stress and Strain on Multiphase Flow Properties Using 3D-Printed Fractured Reservoir Rock Analogues:

This chapter focuses on examining the complex relationship between triaxial stress and strain, and its subsequent effects on multiphase flow properties in both intact and artificially fractured 3D-printed reservoir rock analogues. It presents the experimental findings on stress-dependent multiphase flow properties, conducted under isothermal conditions and varying effective confining stresses, using 3D-printed samples in a gas-oil system. Essential aspects such as porosity, absolute permeability, drainage relative permeability, and capillary pressure in fractured porous media are thoroughly analyzed. The results from these rigorous experiments provide valuable insights into the geomechanical effects influencing flow properties under different stress regimes.

Chapter 8 – Applications: Impact of Stress-Dependent Relative Permeability on Oil Recovery in the Akal KL Field:

This chapter analyzes the influence of stress-dependent relative permeability on recovery processes within the Akal KL reservoir, highlighting the role of geomechanical changes on oil recovery through the use of 3D-printed rock analogues.

Chapter 9 – Conclusions and Recommendations:

The final chapter synthesizes the main findings and conclusions of the thesis, providing a summary of significant discoveries and offering recommendations for future research directions.

### 1.6. List of Publications

**Sanchez-Barra, A.**, Zambrano-Narvaez, G., & Chalaturnyk, R. (2023). An In-Depth Analysis of Strength and Stiffness Variability in 3D-Printed Sandstones: Implications for Geomechanics. *Energies*, *16*(14). https://doi.org/10.3390/en16145406

**Sanchez-Barra, A.**, Deisman, N., Guerrero, F., Brandl, J., & Chalaturnyk, R. (2022). Experimental Facility for Testing Unconventional Reservoirs: Effect of Geomechanics on Multiphase Flow Properties. *American Rock Mechanics Association*. https://doi.org/https://doi.org/10.56952/ARMA-2022-0543

Hodder, K. J., **Sanchez-Barra, A. J.**, Ishutov, S., Zambrano-Narvaez, G., & Chalaturnyk, R. J. (2022). Increasing Density of 3D-Printed Sandstone through Compaction. *Energies*. https://doi.org/10.3390/en15051813

Vanessa Santiago, Francy Guerrero Zabala, **Angel J. Sanchez-Barra**, Nathan Deisman, Richard J. Chalaturnyk, Ruizhi Zhong, S. H. (2022). Experimental investigation of the flow properties of layered coal-rock analogues. *Chemical Engineering Research and Design*, *186*, 685–700. https://doi.org/10.1016/j.cherd.2022.08.046

Johnson, R. L., Ramanandraibe, H. M., Di Vaira, N., Leonardi, C., You, Z., Santiago, V., Ribeiro, A., Badalyan, A., Bedrikovetsky, P., Zeinijahromi, A., Carageorgos, T., **Sanchez-Barra, A.**, Chalaturnyk, R., & Deisman, N. (2022). Implications of Recent Research into the Application of Graded Particles or Micro-Proppants for Coal Seam Gas and Shale Hydraulic Fracturing. *Society of Petroleum Engineers - SPE Asia Pacific Oil and Gas Conference and Exhibition 2022, APOG 2022*. https://doi.org/10.2118/210628-MS

Hodder, K., Ishutov, S., **Sanchez, A**., Zambrano, G., & Chalaturnyk, R. (2020). 3D printing of rock analogues in sand: A tool for design and repeatable testing of geomechanical and transport properties. *E3S Web of Conferences*, *205*. https://doi.org/10.1051/e3sconf/202020504014

# 2. Theoretical Framework in Naturally Fractured Reservoirs

## 2.1. Introduction

Naturally fractured reservoirs (NFRs) play an essential role in the global energy landscape, accounting for a significant portion of the world's hydrocarbon resources, with recent estimates suggesting that about 40% of known reserves are found in these reservoirs (Zimmerman, 2018). NFRs are often characterized by short production periods with high initial flow rates, but they also face challenges like rapid production declines, early gas or water breakthroughs, and low ultimate recovery factors (Nelson, 1985). The development and recovery techniques for these reservoirs are associated with increased costs and risks due to their complex nature.

These reservoirs are typically classified based on the roles of fractures and matrix in storage capacity and permeability (Nelson, 2001; Sun and Pollitt, 2020). Type I reservoirs, where fractures provide both essential storage and permeability, often experience rapid production decline and early water encroachment. Type II reservoirs use the rock matrix for storage and fractures for permeability, showing poor recovery when matrix permeability is low. However, with higher matrix permeability, they can be highly productive. Type III reservoirs gain additional permeability from fractures and are often treated as conventional reservoirs. Type IV reservoirs, where fractures mainly create permeability anisotropy, are highly compartmentalized and may exhibit discrepancies between predicted and actual reservoir performance due to cemented fractures acting as flow barriers.

Prominent examples of NFRs include the Akal Carbonates in the Gulf of Mexico, the Monterey Shales in California, the West Texas Carbonates, the North Sea Chalks, and the Asmari Limestones in Iran (Rangel-German, 2002). Figure 2.1 illustrates the geographical locations of these well-known reservoirs, along with additional reservoirs that are frequently referenced in the literature.


Figure 2.1. Worldwide geographical distribution of key naturally fractured reservoirs (Sun and Pollitt, 2020).

The study of fluid flow and transport processes within fractured porous media has long captivated researchers, given the inherent complexity of these dual systems. Historically, seminal works like those of Barenblatt et al., (1960), Warren and Root (1963), and Kazemi (1969), along with subsequent studies by Pruess and Narasimhan (1985), Wu and Pruess (1988), Kazemi et al., (1992), and Nelson (2001), have significantly contributed to our understanding of subsurface reservoir dynamics. These studies collectively highlight the crucial importance of this research domain. The relevance of these studies extends beyond academic interest, encompassing a range of practical applications for the extraction of natural resources, nuclear waste storage and disposal, environmental remediation, and CO2 sequestration. Furthermore, these reservoirs are indispensable in the geothermal industry (Yu-Shu Wu, 2016).

In recent times, the interaction of geomechanics within fractured porous media has attracted increasing attention. This interest is driven by a need for deeper insights into stress-dependent fluid flow in hydraulically stressed fractured reservoirs, particularly where significant stress alterations occur during the reservoir depletion cycle.

This chapter aims to review the key processes governing naturally fractured reservoirs and explore the impact of geomechanics on their flow properties. The complex dynamics of fluid flow in these systems are influenced by several stress-dependent factors. These include the nonlinear characteristics of permeability within fractures, the inherent permeability and porosity of the rock matrix, relative permeability, capillary pressure, and the resulting interfacial tension between wetting and non-wetting fluid phases.

## 2.2. Literature Review

The influence of geomechanics on the flow properties of fractured porous media has been a focal point of research over recent decades. This body of work is crucial for understanding the dynamics of naturally fractured reservoirs under various stress conditions. One of the earliest studies in this area by Jones (1975) revealed that increases in confining pressures, similar to those seen during reservoir depletion, significantly reduce permeability in natural rocks. Building on this, McDonald et al., (1991) investigated the impact of stress on relative permeability in an oil-water system. They observed that increased stresses contracted fracture apertures, shifting the critical saturation points and altering fluid displacement dynamics due to a combination of viscous, gravitational, and capillary forces. Further exploring this domain, Pyrak-Nolte et al., (1991) developed a model to examine fluid flow through fractures, showing that stress increments can alter fracture geometry and, consequently, fluid flow patterns and relative permeability. Similarly, Zhu and Wong (1997) conducted experiments on Berea sandstone under triaxial compression, concluding that shear-enhanced compaction leads to a substantial decrease in permeability.

The study by Lian et al., (2012) on water-wet carbonate cores demonstrated that fractures facilitate early water breakthroughs and increase water relative permeability, significantly impacting waterflooding recovery. They also found that effective stress increases lead to higher irreducible water saturation and reduced permeability. Similarly, Moghadam et al., (2016) confirmed that gas permeability in shale is effectively stress-dependent. Extending this research, Huo and Benson (2016) examined the stress-dependency of relative permeability in fractured sandstone, finding that slight increases in water content dramatically reduce gas permeability, which could explain rapid production declines in gas wells in fractured rocks.

Most recently, Haghi et al., (2020) investigated the multiphase flow properties of Berea sandstone under varying effective stress levels. Their findings corroborate earlier studies, showing a decrease in porosity and permeability with increased stress, alongside shifts in relative permeability curves and capillary pressure.

The existing studies, as described earlier, provide significant insights into how stress alterations affect single-phase flow properties (porosity and absolute permeability) in both intact and fractured rocks. In the case of multiphase flow properties like relative permeability and capillary pressure, research has only considered isotropic stress for intact materials and normal stress for fractured rocks (see Figure 2.2). However, a significant knowledge gap exists in understanding behaviors under shear stresses, particularly regarding how shear stress affects multiphase flow properties in fractured porous media. By concentrating on intact materials or fractures with impermeable matrices, many of these previous investigations tend to overlook the matrix's contribution. Consequently, they do not comprehensively explain the flow dynamics in naturally fractured reservoirs. This deficiency is the primary focus of this research. The effect of shear stress on the multiphase flow properties (relative permeability and capillary pressure) is investigated with the objective of understanding the contributions of matrix and fracture fluid transfer. Figure 2.2 aims to summarize the main references from these important studies, highlighting the necessity for further exploration in this field.

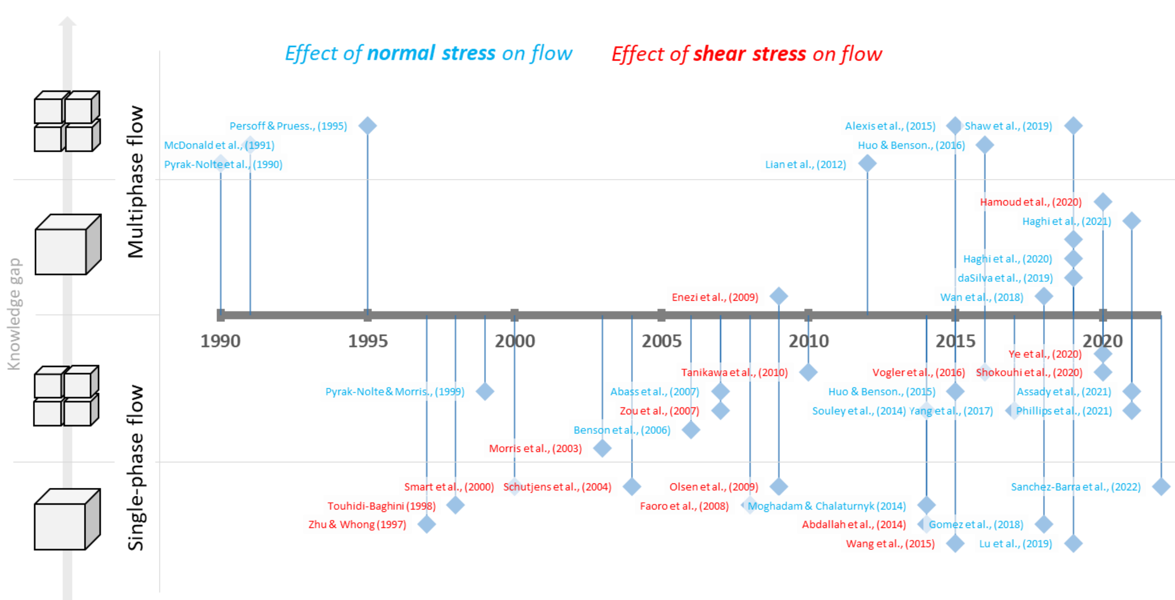


Figure 2.2. Literature review on the stress-dependent multiphase flow in fractures and porous media.

## 2.3. Governing Physics of Flow in Fractured Porous Media

The fundamental principles that govern fluid flow within naturally fractured reservoirs are critical for predicting the reservoir's behavior during injection or production operations. They encompass a thorough understanding of the interactions between the matrix and the fractures which can be described with concepts such as Darcy's Law, capillary pressure, relative permeability, fluid saturation, and pressure gradient, among others. These principles, in conjunction with the reservoir's unique geomechanical and lithological characteristics, determine how fluids, including oil, water, and gas, interact and move within the reservoir's matrix and fracture network.

### 2.3.1. Dual-Porosity System

Naturally fractured reservoirs exhibit a dual-porosity structure consisting of matrix blocks and fractures, each with distinct fluid storage and permeability characteristics. Warren and Root (1963) defined this system as comprising primary and secondary porosity. Primary porosity, which is intergranular in nature, is governed by processes like deposition and lithification. It is highly interconnected, often correlates with permeability, and is largely dependent on grain geometry, size, and spatial distribution. Conversely, secondary porosity is formed through fracturing, jointing, or solution activity in circulating water and is potentially altered by infilling due to precipitation. It is typically less interconnected and does not correlate well with permeability. This type of porosity is especially prevalent in carbonate rocks such as limestones or dolomites, where solution channels or vugular voids form during weathering or burial.

The dual-porosity concept was initially visualized as a stack of identical, rectangular parallelepipeds, similar to sugar cubes, intersected by fractures of constant widths oriented parallel to one or more principal axes of permeability, as illustrated in Figure 2.3 (Warren and Root, 1963; Rangel-German, 2002). This model has been fundamental in understanding fluid flow and storage mechanisms in fractured reservoirs, aiding in the development of more accurate predictive and simulation models for reservoir management.

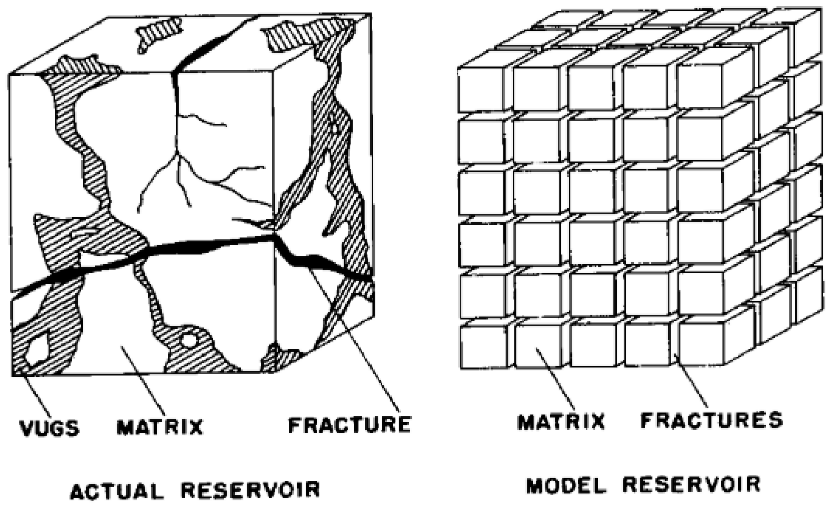


Figure 2.3. Idealized dual-porosity system as conceptualized by Warren and Root (1963).

### 2.3.2. Darcy's Law and the Definition of Permeability

The basic governing law of fluid flow through porous media is Darcy's law, which was originally formulated by the French civil engineer Henry Darcy on the basis of his experiments on vertical water filtration through sand beds. Darcy's law can be described by the following equation:

$$Q = \frac{CA\Delta(P - \rho gz)}{L}, \tag{2.1}$$

where $P$ is the pressure (Pa), $\rho$ is the fluid density (kg/cm$^3$), $g$ is the gravitational acceleration (m/s$^2$), $z$ si the vertical coordinate (in the downward direction) (m), $Q$ is the volumetric flow rate (m$^3$/s), $C$ is the constant of proportionality (m$^2$/Pa s), and $A$ is the cross-sectional area of the sample (m$^2$). Darcy's law is mathematically analogous to other linear phenomenological transport laws, such as Ohm's law for electrical conduction, Fick's law for solute diffusion, and Fourier's law for heat conduction.

In Darcy's law, the flow rate is dominated by the term $P - \rho gz$, which essentially embodies the "conservation of energy" of Bernoulli's equation,

$$\frac{P}{\rho} - gz + \frac{u^2}{2} = \frac{1}{\rho}\left(P - \rho gz + \frac{\rho u^2}{2}\right), \tag{2.2}$$

where $P/\rho$ is related to the enthalpy per unit mass, $-gz$ is the gravitational energy per unit mass, and $u^2/g$ is the kinetic energy per unit mass. Fluid velocities in a reservoir are usually very small, and so the third term is usually negligible, in which case the component $P - \rho gz$ represents an energy-type term. It seems reasonable that fluid would flow from regions of higher energy to lower energy; therefore, the driving force for flow should be the gradient (i.e. the rate of spatial change) of $P - \rho gz$. Subsequent to Darcy's initial discovery, it has been found that, all other factors being equal, $Q$ is inversely proportional to the fluid viscosity, $\mu$ (Pa s). It is therefore convenient to factor out $\mu$, and put $C = k/\mu$, where $k$ is known as the permeability, with dimensions (m$^2$). Equation 2.1 can be re-written as,

$$Q = \frac{kA\Delta(P - \rho gz)}{\mu L}. \tag{2.3}$$

Permeability is a function of rock type, and also varies with stress, temperature, etc., but does not depend on the fluid; the effect of the fluid on the flow rate is accounted for by the viscosity term. Permeability has units of m$^2$, but in the petroleum industry it is conventional to use "Darcy" units, defined by

$$1 \text{ Darcy} = 0.987 \text{ x } 10^{-12} \text{ m}^2 \approx 10^{-12} \text{ m}^2. \tag{2.4}$$

The original purpose of the "Darcy" unit was to avoid the need for using small prefixes such as $10^{-12}$, as would be needed if $k$ were measured in units of m$^2$ (Zimmerman, 2018).

### 2.3.3. Basic Principles Governing Fracture Fluid Flow

In many naturally fractured reservoirs, the rock structured of fractured porous media is composed of low permeability matrix blocks surrounded by a highly permeable fracture network, in which case the fluid flow takes place predominantly through the fractures. In some cases the flow takes place though a singe fracture or fault, while in other cases the flow occurs though a network of fractures.

The physics of flow of an incompressible Newtonian viscous fluid are governed by the following form of the Navier-Stokes equations (Zimmerman and Bodvarsson, 1996),

$$\frac{\partial \boldsymbol{u}}{\partial t} + (\boldsymbol{u} \cdot \nabla)\boldsymbol{u} = \boldsymbol{F} - \frac{1}{\rho}\nabla p + \frac{\mu}{\rho}\nabla^2 \boldsymbol{u}, \tag{2.5}$$

where $\rho$ is the fluid density, $\boldsymbol{F}$ is the body force vector (per unit mass), $p$ is pressure, $\mu$ is the fluid viscosity, $\boldsymbol{u}$ is the velocity vector, and $\nabla$ is the gradient operator. This equation ensures mass conservation of the fluid. The first term on the left, known as temporal acceleration, denotes the part of the acceleration of a fluid particle where, at a fixed point in space, the velocity changes with time. The term $\partial \boldsymbol{u}/\partial t$ could be understood as the rate of change of velocity with respect to time. It describes how the velocity of a fluid particle changes over time at a fixed position. The second term is the advective acceleration term, which represents the acceleration of a fluid particle as it moves along its flow path. In other words, it captures the change in velocity due to the fluid particle moving to a different location with a different velocity. Mathematically, it is given by the dot product of the velocity vector with its own gradient $(\boldsymbol{u} \cdot \nabla)\boldsymbol{u}$. Even in steady-state flow, a given fluid particle may change its velocity (i.e., be accelerated) by virtue of moving to a position at which there is a different velocity. The sum of these two terms represents the acceleration of a fluid particle along its trajectory. The terms on the right-hand side of Equation 2.5 represent the applied body force, the applied pressure gradient, and the viscous forces. The applied body force represents external forces per unit mass that act on the fluid. In many cases, this could be gravitational, electromagnetic, or centrifugal forces. The applied pressure gradient gives the rate of change of pressure in the fluid across space. The viscous forces are the fluid's internal resistance to flow — in simple terms, the "stickiness" or "thickness" of the fluid. The viscous term in the Navier-Stokes equation essentially models the internal friction within the fluid, which tends to oppose and slow down the motion.

Equation 2.5 represents one vector equation, or three scalar equations, containing four functions: three velocity components and the pressure field. In order to have a closed system of equations, they must be supplemented by the continuity equation, which represents conservation of mass. For an incompressible fluid, conservation of mass is equivalent to conservation of volume, and the equation takes the form,

$$div\, \boldsymbol{u} \equiv \nabla \cdot \boldsymbol{u} = 0. \tag{2.6}$$

This equation states that the divergence of the velocity field is zero, meaning fluid is neither being created nor destroyed at any point in the fluid. The assumption of incompressibility is acceptable for liquid fluids under typical reservoir conditions. For example, the compressibility of water is 4.9 x$10^{-10}$/MPa, meaning that a pressure change of 1 MPa will change the density by only 0.05% (Batchelor, 1967; Zimmerman and Bodvarsson, 1996). Since fracture and matrix flow are commonly studied under single phase steady-state flow, the fluid density will be assumed to be constant. This assumption would change under transient phenomena or multiphase flow problems.

The relevant boundary conditions for the Navier-Stokes equations include the "no-slip" conditions, which specify that at any boundary between the fluid and a solid, the velocity vector of the fluid must equal that of the solid. This implies that at the fracture walls, not only is the normal component of the velocity equal to zero, but the tangential component vanishes as well (Zimmerman and Bodvarsson, 1996).

In subsurface flow, the most common situation for the applied body force is that due to gravity, in which case $\boldsymbol{F} = \boldsymbol{g}$. Taking the z-direction to be vertically upwards, $\boldsymbol{g} = -g\boldsymbol{e}_z$, where $g$ = 9.81 m/s$^2$ = 9.81 N/kg, and $\boldsymbol{e}_z$ is a unit vector in the vertical direction. The gravitational term can be removed from the governing equations by defining a reduced pressure (Batchelor, 1999).

$$P = p + \rho g z, \tag{2.7}$$

in which case, the first two terms $\boldsymbol{F} - (1/\rho)\nabla p$ of the right-hand side of Equation 2.5 can be written as,

$$\boldsymbol{F} - \frac{1}{\rho}\nabla p = -g\boldsymbol{e}_z - \frac{1}{\rho}\nabla p = -\frac{1}{\rho}(\nabla p + \rho g\boldsymbol{e}_z). \tag{2.8}$$

Deriving Equation 2.8, we find,

$$\boldsymbol{F} - \frac{1}{\rho}\nabla p = -g\boldsymbol{e}_z - \frac{1}{\rho}\nabla, p \tag{2.9}$$

$$\boldsymbol{F} - \frac{1}{\rho}\nabla p = \frac{-\rho g\boldsymbol{e}_z - \nabla p}{\rho}, \tag{2.10}$$

$$\boldsymbol{F} - \frac{1}{\rho}\nabla p = -\frac{1}{\rho}(\nabla p + \rho g\boldsymbol{e}_z), \tag{2.11}$$

$$\boldsymbol{F} - \frac{1}{\rho}\nabla p = -\frac{1}{\rho}\nabla(p + \rho g z). \tag{2.12}$$

Then, if Equation 2.7 is substituted in Equation 2.12, the following equation is obtained,

$$\boldsymbol{F} - \frac{1}{\rho}\nabla p = -\frac{1}{\rho}\nabla(p + \rho g z) = -\frac{1}{\rho}\nabla P. \tag{2.13}$$

The governing equations can therefore be written without the gravitational term, in terms of the reduced pressure, $P$.

$$\frac{\partial \boldsymbol{u}}{\partial t} + (\boldsymbol{u} \cdot \nabla)\boldsymbol{u} = -\frac{1}{\rho}\nabla P + \frac{\mu}{\rho}\nabla^2 \boldsymbol{u}. \tag{2.14}$$

Flow in fractured porous media is generally defined under the assumption of steady-state flow under a uniform macroscopic pressure gradient. In the steady-state, the term $\partial \boldsymbol{u}/\partial t$ drops out, and the equation is reduced to the following,

$$(\boldsymbol{u} \cdot \nabla)\boldsymbol{u} = -\frac{1}{\rho}\nabla P + \frac{\mu}{\rho}\nabla^2 \boldsymbol{u}. \tag{2.15}$$

Simplying the equation,

$$\nabla P = \mu \nabla^2 \boldsymbol{u} - \rho(\boldsymbol{u} \cdot \nabla)\boldsymbol{u}. \tag{2.16}$$

The presence of the advective component of the acceleration, $(\boldsymbol{u} \cdot \nabla)\boldsymbol{u}$, generally causes the equations to be nonlinear, and consequently very difficult to solve. In certain cases this term is either very small, in which case it can be neglected, or else vanishes altogether.

### 2.3.4. Parallel Plate Model and Cubic Law

The study of fracture flow often employs the parallel plate model, particularly under steady flow conditions where the advective term is negligible, allowing for an exact solution. This approach is characterized by the cubic law, recognized as the only fracture model that permits an exact determination of hydraulic conductivity (Witherspoon et al., 1980; Zimmerman and Bodvarsson, 1996). When considering more complex and realistic geometries that incorporate a higher degree of roughness, typical of rock fractures, approximations become necessary. These approximations aim to linearize the Navier-Stokes equations or otherwise simplify them into a more manageable form.

The derivation of the cubic law begins by assuming that the fracture walls can be represented by two smooth, parallel plates, separated by an aperture $h$ (Figure 2.4).

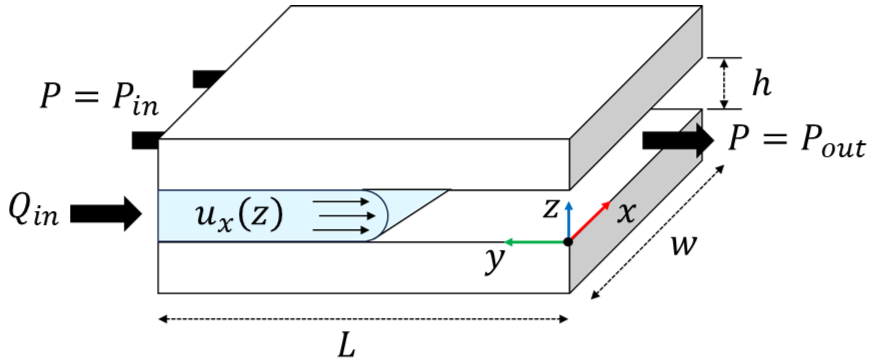


Figure 2.4. Representation of the parallel plate model. The fracture is represented by two smooth, parallel plates, separated by an aperture $h$, with uniform pressures $P_{in}$ and $P_{out}$ imposed on two opposing faces.

Considering a uniform pressure gradient within the plane of the fracture, the uniform pressures $P_{in}$ and $P_{out}$ could be expressed as,

$$|\overline{\nabla P}| = \left(\frac{P_{in} - P_{out}}{L}\right), \tag{2.17}$$

where the overbar denotes an average over the plane of the fracture. The geometry of the fracture could be expressed using a Cartesian coordinate system, where $x_1 \equiv x$ direction, parallel to $\nabla P$, $x_2 \equiv y$ direction, perpedicular to $x_1$ in the plane of the fracture, and $x_3 \equiv z$ direction (not necessarily vertical) perpedicular to the fracture walls. The top and bottom walls of the fracture correspond to $z = \pm h/2$.

The (reduced) pressure gradient lies entirely in the plane of the fracture, and has no $z$ component. It seems plausible that the velocity will also have no $z$ component, particularly since $u_z$ must not only vanish at the two walls of the fracture, $z = \pm h/2$, but must also have a mean value of zero. Since the geometry of the region between the plates does not vary with $x$ or $y$, the pressure gradient should also be uniform within the plane of the fracture. Hence, we assume that the velocity vector depends only on $z$. As all components of the velocity must vanish at $z = \pm h/2$, the velocity vector must necessarily vary with $z$. The components of the vector $(\boldsymbol{u} \cdot \nabla)\boldsymbol{u}$ can be written explicitly as,

$$(\boldsymbol{u} \cdot \nabla)\boldsymbol{u} = (\boldsymbol{u} \cdot \nabla)(u_x, u_y, u_z) = [\boldsymbol{u} \cdot (\nabla u_x), \boldsymbol{u} \cdot (\nabla u_y), \boldsymbol{u} \cdot (\nabla u_z)]. \tag{2.18}$$

The velocity components do not vary with $x$ or $y$, so any of the three velocity gradients that are not identically zero must be parallel to the $z$-direction. The velocity vector, on the other hand, is normal to the $z$-direction. Hence, each of the dot products in Equation 2.18 is zero. This serves to remove the nonlinear term from Equation 2.16, leaving

$$\nabla P = \mu \nabla^2 \boldsymbol{u}(z). \tag{2.19}$$

As $\nabla P$ lies parallel to the $x$-axis, it can be written as,

$$\nabla P = \left(\frac{\partial P}{\partial x}, \frac{\partial P}{\partial y}, \frac{\partial P}{\partial z}\right) = (|\overline{\nabla P}|, 0,0). \tag{2.20}$$

A comparison of Equations 2.19 and 2.20 shows that the three velocity components must satisfy the following three equations:

$$\text{a) } \nabla^2 u_x(z) = \frac{\overline{\nabla P}}{\mu}, \qquad \text{b) } \nabla^2 u_y(z) = 0, \qquad c) \; \nabla^2 u_z(z) = 0. \tag{2.21}$$

The boundary conditions for each velocity component are $u_i = 0$ when $z = \pm h/2$. Therefore, $u = 0$ will satisfy the governing equations for $u_y$ and $u_z$, and their associated boundary conditions. To find $u_x$, we integrate Equation 2.21a twice with respect to $z$, and make use of the boundary conditions, to find the velocity profile $u_x(z)$, expressed in Figure 2.4.

$$\int \nabla^2 u_x(z) dz = \int \frac{\overline{\nabla P}}{\mu} dz. \tag{2.22}$$

Then, the velocity profile is expressed as,

$$u_x(z) = \frac{|\overline{\nabla P}|}{2\mu}\left[z^2 - \left(\frac{h}{2}\right)^2\right]. \tag{2.23}$$

This velocity profile field satisfies the continuity Equation 2.6, because $u_y = u_z = 0$, and $u_x$ depends only on $z$, but not on $x$. The total volumetric flow through the fracture, for a width $w$ in the $y$-direction (perpedicular to the pressure gradient), is found by integrating the velocity across the fracture from $z = -h/2$ to $z = +h/2$:

$$Q_x = w \int_{-h/2}^{h/2} u_x(z) dz, \tag{2.24}$$

$$Q_x = w \int_{-h/2}^{h/2} \frac{|\overline{\nabla P}|}{2\mu} \left[ z^2 - \left(\frac{h}{2}\right)^2 \right] dz = \frac{-|\overline{\nabla P}| w h^3}{12\mu}. \tag{2.25}$$

Substituting $\overline{\nabla P}$ in Equation 2.3 for Darcy's law for flow through porous media in one dimension, and considering that the cross-sectional area $A$ is equal to $wh$, the permeability of the fracture can be expressed as,

$$k = \frac{h^2}{12}. \tag{2.26}$$

### 2.4. The Effect of Geomechanics on Fractured Porous Media

In fractured porous media, the interplay between geomechanical processes and reservoir characteristics critically influences reservoir performance. The matrix, typically less porous and permeable, deforms under stress, reducing pore volume, porosity, and permeability. This deformation is affected by factors such as mineral composition and the presence of microcracks (Zoback, 2007; Nur and Byerlee, 1971). Conversely, fractures, which serve as the main conduits for high permeability, exhibit a more variable and sensitive response to stress.

Normal stress tends to close fractures, reducing permeability, while shear stress might cause dilation or displacement, potentially increasing permeability. Excessive shear, however, can generate gouge material, which blocks the fracture (Barton et al., 1995; Olsson and Barton, 2001). The overall response of fractured porous media to stress involves a complex balance between matrix compaction and fracture behavior. The stress path, reflecting both shear and normal stresses, is crucial for understanding this dynamic, as it directly influences fluid flow properties and affects hydrocarbon recovery processes (Coussy, 2004; Jaeger et al., 2007). The collective impact on porosity and permeability, which is critical for reservoir management and modeling, depends on the mechanical properties of both matrix and fractures under *in-situ* stress conditions.

### 2.5. Reservoir Depletion in Naturally Fractured Reservoirs

Reservoir depletion, characterized by a decrease in pressure and an alteration of fluid distribution due to hydrocarbon extraction, significantly impacts the geomechanical properties of naturally fractured reservoirs. This process leads to compaction, stress redistribution, and potentially the formation or reactivation of fractures, thereby influencing fluid flow behavior and reservoir performance (Zoback, 2007). As reservoir pressure drops, the effective stress on the rock matrix increases, enhancing compaction, reducing porosity and permeability, and altering fracture orientation and aperture (Nur and Byerlee, 1971; Barton et al., 1995).

In certain reservoirs, especially those with weaker formations, compaction can be a substantial drive mechanism which helps to expel hydrocarbons and boost recovery. However, this may also lead to decreased permeability, potentially offsetting the benefits of increased drive (Coussy, 2004). To mitigate these effects, injection operations like waterflooding or gas injection are employed. While these operations help maintain reservoir pressure and minimize compaction, they must be managed carefully to prevent adverse effects like fracture reactivation or unintended stress field shifts (Witherspoon et al., 1980; Zimmerman and Bodvarsson, 1996).

Additionally, depletion can induce mechanisms such as fault reactivation or subsidence, potentially causing seismicity, well casing damage, or surface infrastructure issues (Jaeger et al., 2007). Understanding and managing these effects is crucial for optimizing production, maintaining reservoir integrity, and prolonging the lifespan of both the reservoir and its infrastructure. This necessitates a comprehensive geomechanical assessment that integrates knowledge of the reservoir’s initial state with the dynamic changes induced by production activities.

# 3. Akal Field Case Study: Geomechanical and Flow Properties in a Naturally Fractured Reservoir

## 3.1. Introduction

The Akal field, discovered in 1976, is a Naturally Fractured Carbonate Reservoir (NFCR) located approximately 80 km offshore in the Bay of Campeche, Mexico (see Figure 3.1). As an integral part of the Cantarell complex, which includes the Nohoch, Chac, Kutz, and the deeper Sihil blocks, Akal stands out as the most significant. It holds 91.4% of the complex's original oil in place, covering an area of about 191.8 km$^2$ (Leon-G et al., 2005; National Hydrocarbons Commission of Mexico, 2018).

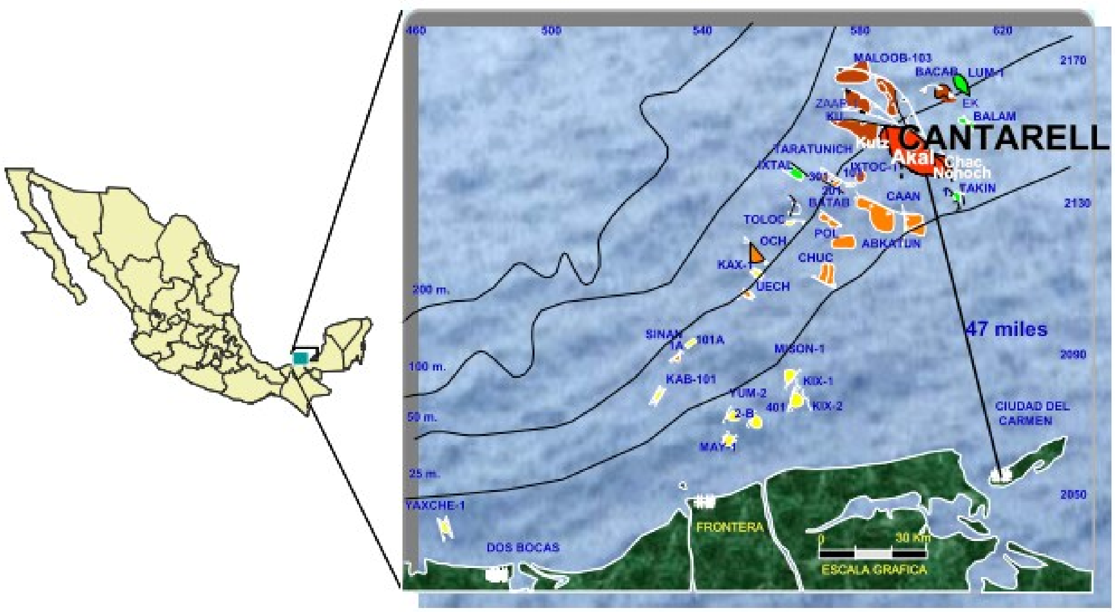


Figure 3.1. Offshore location of the Cantarell Complex (Sanchez-Bujanos et al., 2005).

The Akal reservoir is characterized by an asymmetric anticline structure, bounded by a normal fault on the west and an inverse fault on the northern and eastern sides. With an original oil volume of 32 billion stock tank barrels, it is classified as a supergiant reservoir (Arevalo et al., 1996). The principal pay zones, spanning a thickness of 1110 meters, consist of highly fractured and vuggy carbonate formations. The upper interval, about 290 meters thick, comprises breccia dolomite of upper Cretaceous Paleocene origin. In contrast, the lower interval, approximately 820 meters thick, is formed of dolomitic limestone from the medium and lower Cretaceous period (Rojas and Torres, 1994).

Exploitation began in June 1979 with the first well, Akal 1-A, producing 34000 barrels per day (BPD) of 22° API gravity oil. Initially, the oil was undersaturated, with a reference depth pressure of 26.4 MPa at 2300 meters subsea level (mssl), leading to a short initial production period driven by depletion and expansion of the rock-fluid system. The average porosity in the reservoir is 8%, with secondary porosity—comprising fractures, microfractures, and vugs—accounting for up to 35% of this value. Typical absolute permeability values for the matrix and fracture systems are 0.3 and 5000 millidarcies (mD), respectively, with an average reservoir temperature of 100.2°C (Arevalo et al., 1996). By June 1980, after reaching the bubble-point pressure, a secondary gravity drainage gas cap started forming.

A decade into production, studies highlighted the potential benefits of a gas cap pressure maintenance project for improving oil recovery in the Akal reservoir (Arevalo et al., 1996). These analyses indicated that without such intervention, by 2004, the reservoir would likely face significant reductions in both pressure and oil production rates. Operating under natural depletion conditions would have led to reduced oil recovery efficiency, necessitating longer production periods and frequent updates to production facilities. Additionally, this scenario would have posed the challenge of managing an increased influx of water.

To address these issues, it was decided that nitrogen injection would be the most effective method for maintaining gas cap pressure and thereby optimizing reservoir exploitation (Limón-Hernández et al., 1999). Analyses of various production-injection scenarios suggested that an optimal oil rate of 2 million barrels per day (MMBPD) for four years could be achieved with a nitrogen injection rate of 1200 million standard cubic feet per day (MMSCFD). This approach was projected to enhance oil and gas recoveries significantly (Sanchez-Bujanos et al., 2005). The project commenced in May 2000, starting with a nitrogen injection rate of 300 MMSCFD, and reached the planned 1200 MMSCFD by December of the same year. Nitrogen was injected through seven wells located at the top of the reservoir structure. This process was closely monitored to track pressure, nitrogen concentration, and the movement of the gas-oil contact.

Figure 3.2 illustrates the oil production history of the Akal field since its inception, in relation to Mexico's total oil production, represented by purple and orange curves, respectively. This graph highlights the substantial contribution of the Akal field to Mexico's energy mix. Initially, production stabilized at approximately 1 MMBPD. Following the implementation of the nitrogen injection project in 2000, production surged to nearly 2 MMBPD, accounting for about 60% of Mexico's total oil output. Post-2010, a significant decline in production was observed, reaching minimal levels and prompting the Mexican energy industry to explore diversification strategies to sustain production levels.

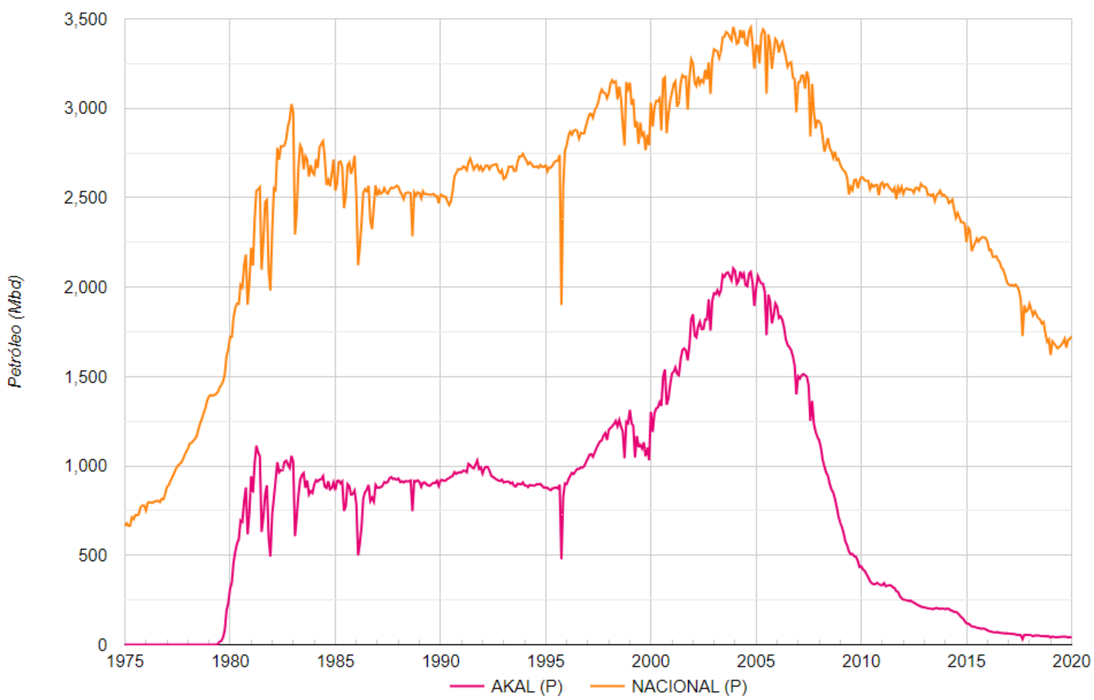


Figure 3.2. Historical oil production trends in the Akal field compared to Mexico's total oil production. This graph depicts Akal's production from its inception, highlighting its significant contribution to Mexico's energy sector (National Hydrocarbons Commission of Mexico).

### 3.2. Akal KL

Considering the extensive size of the Akal reservoir, a smaller section on its northwest side, known as Akal KL, was chosen for a detailed case study, as shown in Figure 3.3. This selection was specifically made to enable a more focused reservoir characterization, potentially suitable for pilot testing. The characterization process for Akal KL began with the collection of critical field data, provided by the National Hydrocarbons Commission of Mexico and the Mexican Petroleum Institute (IMP) in 2018.

Figures 3.3 and 3.4 were derived from a comprehensive geological model that included structural and stratigraphic data—such as surface horizons, faults, zones, and layers—of the Cantarell field. The case study was further enriched with specific data including drilling reports, well test data, well logs, reservoir core data, and geomechanical laboratory tests. Additionally, 3D geological grids and formation tops were also incorporated into the study.

The choice to focus on Akal KL was driven by its relative isolation from the main field, with its only connection being the gas cap. This isolation was confirmed through pressure measurements in wells located in the gas zone (Pemex Exploration and Production). Consequently, it is inferred that the dynamics of the larger field have a minimal impact on the oil column in Akal KL, meaning its behavior is predominantly influenced by localized extraction activities. Geologically, Akal KL is bounded to the east and west by normal faults, as shown in Figure 3.4.

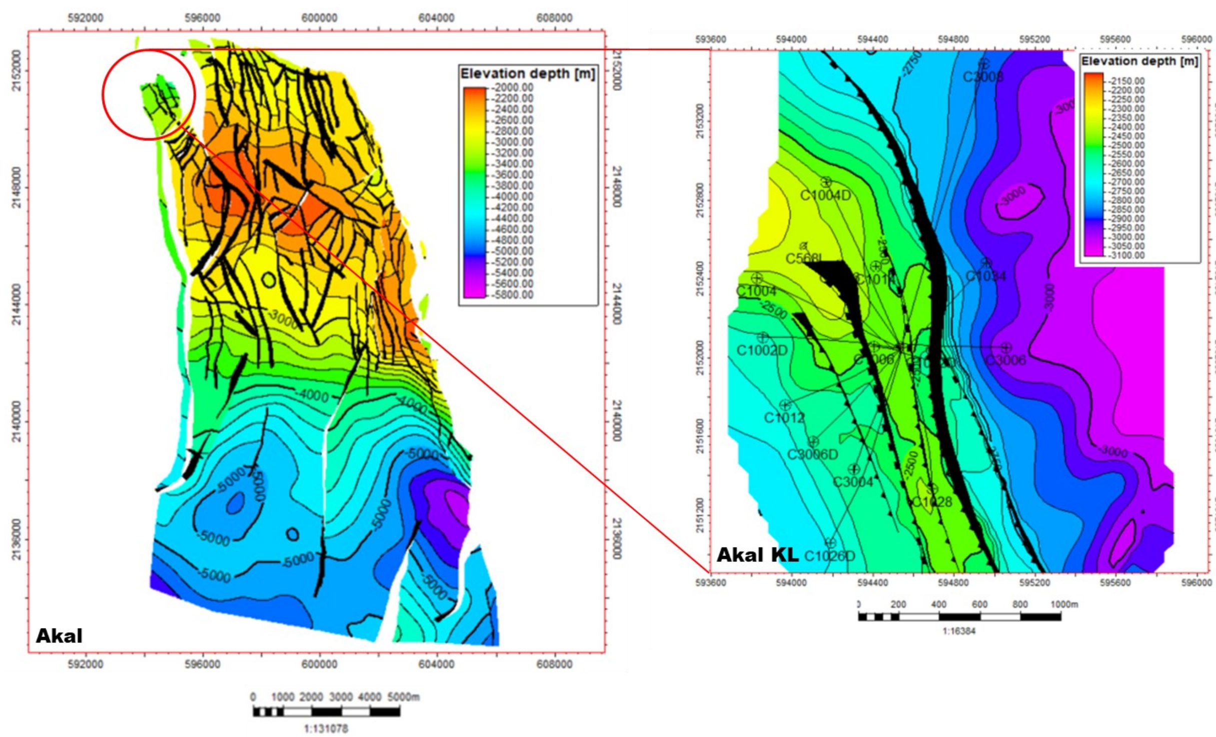


Figure 3.3. Akal KL area within the Akal reservoir. This map illustrates the elevation depth and the geographical boundaries of the Akal KL area.

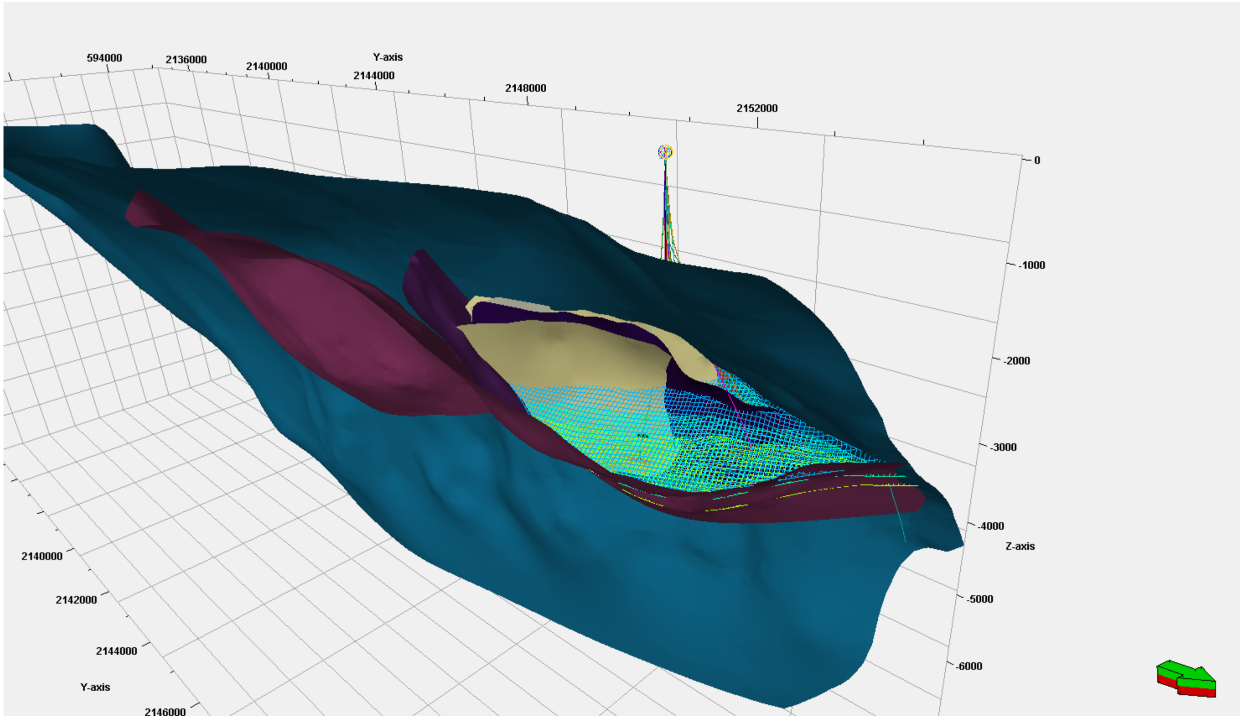


Figure 3.4. Geological boundaries of the Akal KL section, illustrating the normal faults on the east and west sides.

The exploitation of the Akal KL block began in 2000. Initially, the oil was saturated, with a reservoir pressure of 10.3 MPa at a reference depth of 2300 meters subsea level (mssl). This led to a production period predominantly driven by depletion and expansion of the rock-fluid system. The reservoir is characterized by an average total porosity of around 10%, with secondary porosity – comprising fractures, micro-fractures, and vugs – contributing up to 35% of this figure. Typical absolute permeabilities for the matrix and fracture systems are 5 and 5000 millidarcies (mD), respectively, and the reservoir temperature is recorded at 100°C (Arevalo et al., 1996).

In August 2005, the nitrogen injection initiative was launched to maintain reservoir pressure and enhance recovery efforts. This intervention led to a peak production rate of 270 MBPD, as shown in Figure 3.5. However, the nitrogen injection did not fully stabilize the reservoir pressure, primarily due to early breakthrough and migration through the fractured media. Production data indicates that about 60% of the gas produced during this period was nitrogen. Following 2010, there was a significant decline in oil production, mainly attributed to the sweeping of oil from the fractured system and the percolation of gas through the fracture network.

During the reservoir's production life, the pressure dropped from 10.3 MPa to approximately 6 MPa. The reservoir pressure data, presented at reference depths of 2300 meters and 2500 meters, are indicated in Figure 3.5 by the black line and circle markers, respectively. The circle marker data were extracted from well data, while the rest is from public records of the National Hydrocarbons Commission of Mexico. These evolving conditions highlight the need for continuous reassessment of the dynamic *in-situ* stress state within the reservoir. The depletion experienced has significantly altered the rock properties, impacting the overall flow characteristics of the reservoir.

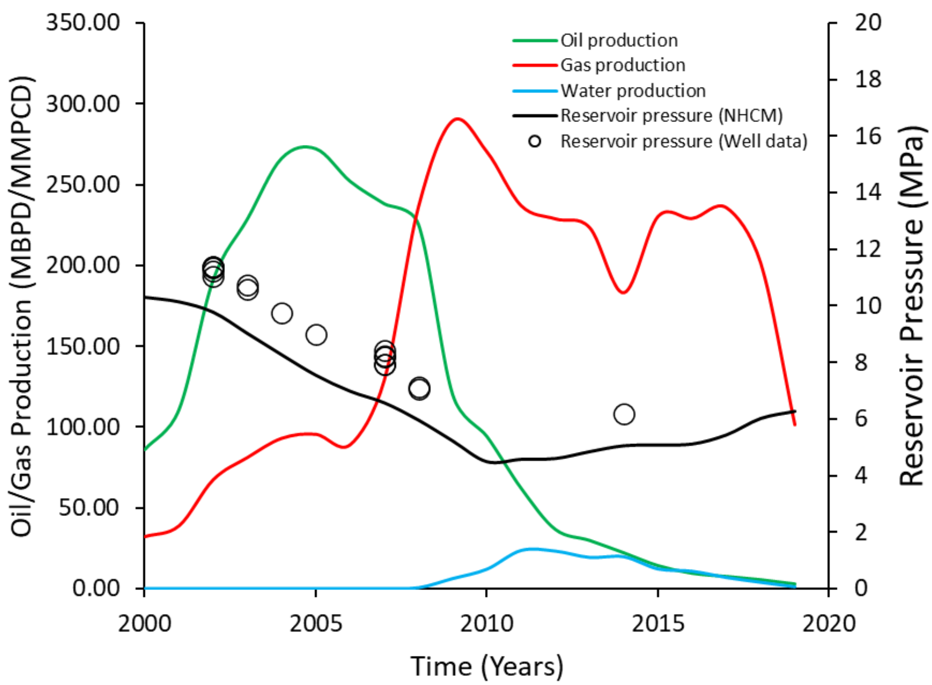


Figure 3.5. Pressure vs. production behavior in the Akal KL reservoir (year 2000–2019). Data source: National Hydrocarbons Commission of Mexico. Reservoir pressure data, represented by circle markers, was obtained from Pemex Exploration and Production well data at a reference depth of 2500 meters.

### 3.3. *In-situ* Stress State

A limited number of studies have been published regarding the stress state in the Akal field. The stress state at a certain depth is defined by stress vectors across three mutually perpendicular planes. These vectors' components form a stress tensor, which is a second-order Cartesian tensor with nine stress components. The Earth's surface, being a free surface, has no shear stresses, and thus can be considered a principal stress plane (Fairhurst, 2003). Consequently, one principal stress is typically normal to the Earth's surface, with the other two principal stresses operating within an approximately horizontal plane. Four parameters must be defined to comprehensively describe the stress state at depth: the overburden stress (Sv), the maximum principal horizontal stress (SHmax), the minimum principal horizontal stress (Shmin), and one stress orientation, typically the azimuth of the maximum horizontal compression (Zoback, 2007).

Celis et al., (2006) used image logs, caliper logs, leak-off tests (LOT), and pore pressure measurements to define the magnitude and orientation of the principal stresses and analyze potential fault leakage. Their analysis suggested that the reservoir pressure is below the hydrostatic pressure, an abnormal condition since the beginning of exploitation. The overburden stress was calculated by integrating the density log. Based on minifrac and LOT analysis, the magnitude of the minimum horizontal stress is less than the overburden, making Shmin the least principal stress. Wellbore failures in vertical wells, such as breakouts and drilling-induced tensile fractures, were used to determine the azimuth of the maximum horizontal stress. The most probable azimuth of SHmax was determined to lie between N10° and N30°. Their analysis indicated that the magnitude of SHmax is greater than Sv, aligning with a strike-slip regime (Shmax > Sv > Shmin) (Table 3.1).

Similarly, Cruz et al., (2009) defined the *in-situ* stress tensor (both orientation and magnitude) as a function of depth (Table 3.1). Their analysis focused on the critically-stressed-fault hypothesis to characterize and predict the orientation of the most permeable natural fractures (faults and fractures with high shear-to-normal stress ratios). Their study suggested that the most permeable natural fractures, and hence the pathways for early breakthrough, dip deeply and are oriented NNE-SSW. Their findings align with those of Celis et al., (2006), suggesting that the current stress regime in the northwest of Akal is strike-slip, and the most probable azimuth of SHmax ranges between N10° and N40°. The azimuth also showed a good match with different sources reported in the World Stress Map (WSM) (Figure 3.6). The average ratio of the horizontal to vertical stress ($k_{avg} = SHmax + Shmin/2Sv$) varies between 0.88 and 0.91.

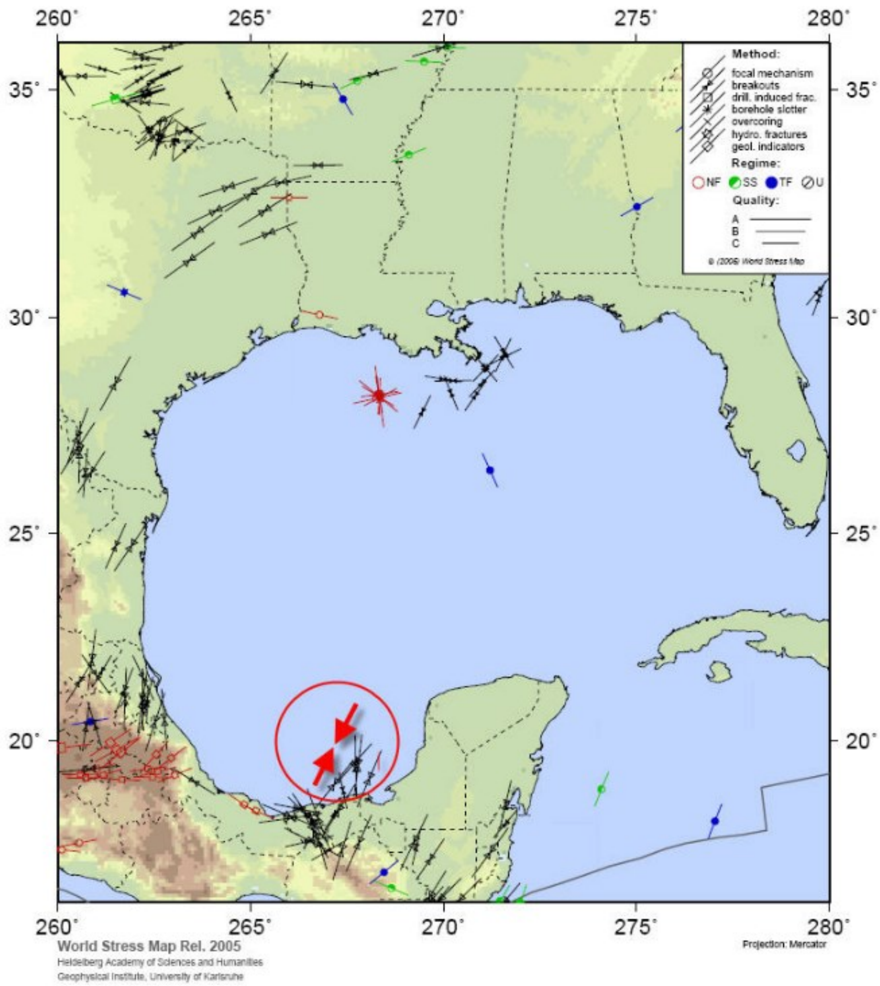


Figure 3.6. SHmax azimuth reported from different sources in the World Stress Map, from Cruz et al., 2009.

Table 3.1. *In-situ* stress characteristics and stress orientations in the Akal field at 2500 meters depth.

| | Sv | SH | SH | Shmin | Pp | $k_{avg}$ |
|---|---|---|---|---|---|---|
| **Celis et al., 2006** | | | | | | |
| Specific Gravity, (-) | 2.39 | 2.60 | - | 1.73 | 0.46 | 0.91 |
| Stress / Pressure, (MPa) | 58.61 | 63.77 | - | 42.43 | 11.28 | 0.91 |
| Orientation, (°) | - | - | N10°-N30° | - | - | - |
| | | | | | | |
| **Cruz et al., 2009** | | | | | | |
| Specific Gravity, (-) | 2.29 | 2.75 | - | 1.30 | 0.45 | 0.88 |
| Stress / Pressure, (MPa) | 56.16 | 67.44 | - | 31.88 | 11.04 | 0.88 |
| Orientation, (°) | - | - | N10°-N40° | - | - | - |

### 3.4. Effects of Reservoir Depletion

An evaluation of the *in-situ* stress state and geomechanical properties within the Akal KL reservoir was conducted using data from 14 wells provided by the National Hydrocarbons Commission of Mexico. This assessment aimed to estimate the evolution of the stress state within the reservoir and to determine the increase in effective stress throughout the reservoir's life cycle. The effective stress, a crucial concept in this analysis, is defined as the difference between the overburden (or total stress) and the pore pressure, as initially described by Terzaghi in 1943. In its simplest form, the effective stress can be mathematically expressed by the equation:

$$\sigma' = \sigma - P_P, \tag{3.1}$$

where $\sigma'$ represents the effective stress, $\sigma$ is the total stress, and $P_P$ denotes the pore pressure. This relationship is foundational in understanding how stress variations over the life cycle of the reservoir influence its geomechanical behavior and fluid flow properties.

The overburden stress was determined by integrating the rock densities from the surface to the depth of interest, as per Equation 3.2. For this analysis, the reference depth was set at 2500 meters.

$$S_v = \rho_w g z_w + \int_{z_w}^{z} \rho(z) g d_z \approx \rho_w g z_w + \rho_b g (z - z_w), \tag{3.2}$$

where $\rho(z)$ represents the density as a function of depth, $\rho_w$ denotes the density of water, $g$ stands for gravitational acceleration, and $\rho_b$ is the mean overburden density (Zoback, 2007). The average vertical principal stress gradient is 25.7 kPa/m. The maximum and minimum horizontal stress gradients, taken from the literature (Table 3.1), are 26.2 kPa/m and 14.9 kPa/m, respectively.

Pore pressure within the Akal KL reservoir was accurately determined through well testing operations. During these operations, reservoir pressure readings were systematically collected at various depths, with measurements taken at intervals of approximately every 250 meters. This approach enabled the construction of a detailed and precise profile of pore pressure at different depths within the reservoir. The observed pore pressure gradient in the reservoir is approximately 4.7 kPa/m, as depicted in Figure 3.7.

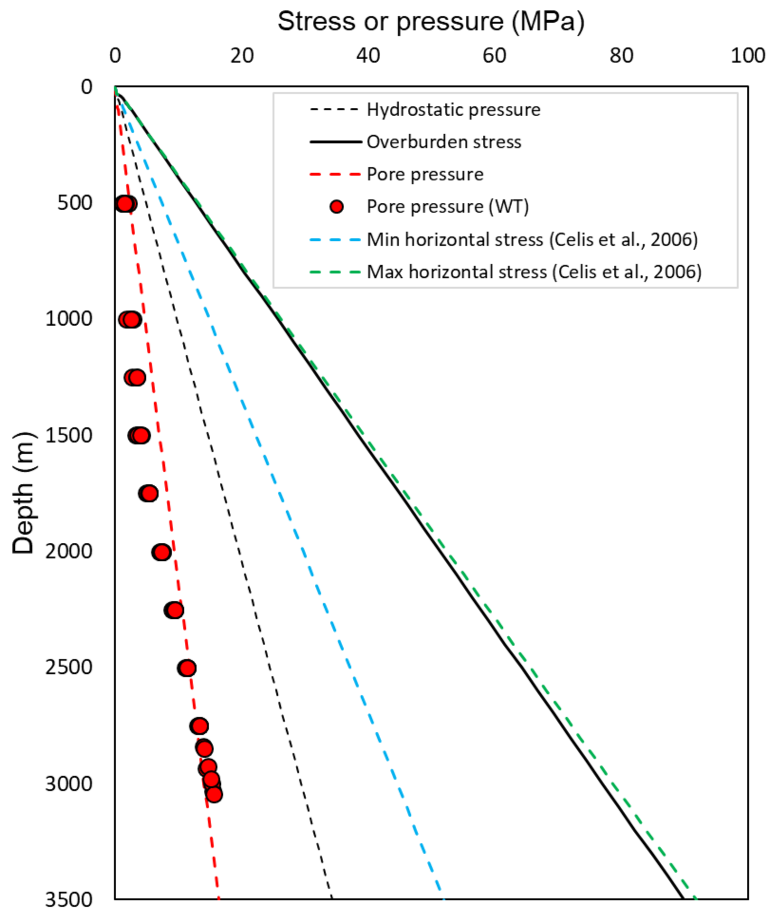


Figure 3.7. Variation of stress magnitudes in Akal KL. The current stress regime is strike-slip.

The Akal KL reservoir actively produced hydrocarbons for 20 years until it became economically unfeasible to continue, as depicted in Figure 3.5. Throughout this production period, the pore pressure experienced a notable decrease from 11.3 to 6 MPa—a drop of 5.3 MPa at the reference depth of 2500 meters. While this change in pressure might seem modest, it is significant considering the fractured nature of the reservoir's rock structure. The reduction in pressure and the corresponding increase in effective stress can induce notable deformations in the fractured media, thereby altering the reservoir's flow dynamics. Fractures are particularly sensitive to stress changes compared to the intact rock matrix. They can deform under both shear and normal stresses, leading to anisotropy within the reservoir. Figure 3.8 illustrates the increase in effective stress resulting from the decrease in pore pressure. The reservoir pressure decreased by 5.3 MPa, which consequently increased the effective stress by an equivalent amount, assuming the overburden stress as the total stress. This increase in effective stress is critical in understanding the geomechanical behavior of the reservoir and its impact on hydrocarbon production.

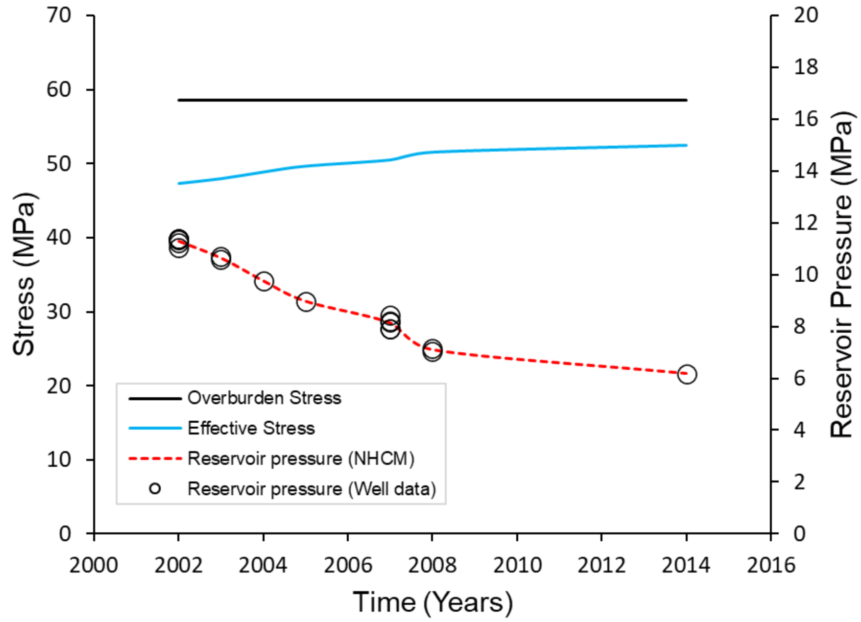


Figure 3.8. Effective stress increase in the Akal KL reservoir, demonstrating the relationship between pore pressure decrease and effective stress growth over the production period.

During the production period of the Akal KL reservoir, the effective stress increased from 47 MPa to 53 MPa. Geomechanical testing on core samples from the reservoir revealed that this increase in effective stress could result in deformation ranging from approximately 1 to 1.3%, translating to a total volumetric strain of about 0.3%. Although these deformation rates were observed in laboratory tests using intact core samples, it is important to consider that the reservoir rock is extensively fractured. Therefore, the *in-situ* impact of stress on the rock structure might have been more significant, potentially leading to more substantial alterations in the flow dynamics of the reservoir. The stress-induced changes in the fractured rock *in-situ* are likely to have had a more profound effect on the reservoir's flow characteristics compared to the laboratory observations.

Figure 3.9 illustrates the deformation of three core samples under different effective stress levels. The petrophysical analysis was conducted in 1999, around the commencement of production. The rock core sample C1006_1V exhibited a nonlinear response at initial loading, possibly reflecting the fractured nature of the rock. Initially, the microfractures close, causing deformation of the bulk rock, after which the behavior stabilizes and follows a more linear pattern. In contrast, core samples C1006_2V and C1006_3V displayed more linear trends, suggesting they were more intact and solid.

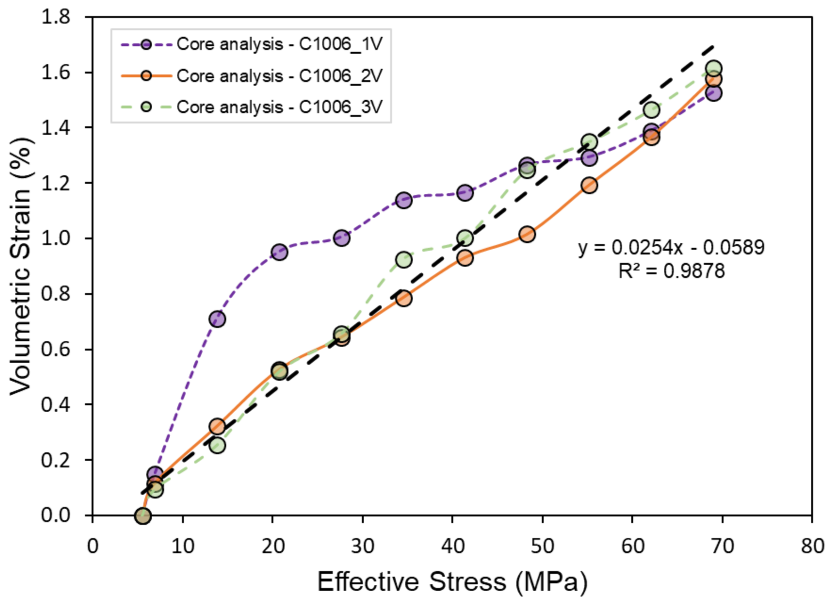


Figure 3.9. Deformation analysis of Akal KL core samples under varying effective stress levels, displaying non-linear and linear deformation patterns reflective of the fractured and intact nature of the rock samples. The geomechanical analysis was conducted in 1999 at the beginning of production.

### 3.5. Flow Properties

The flow properties of the Akal KL reservoir are determined by its dual-porosity structure, characterized by matrix blocks, vugs, and fractures, each exhibiting distinct fluid storage and permeability characteristics. This dual-porosity system comprises both primary and secondary porosity. Primary porosity is intergranular, originating from the initial rock formation process. In contrast, secondary porosity is developed through geological processes such as fracturing, jointing, and the formation of vugular cavities, which significantly contribute to the reservoir's overall porosity. The presence of this dual-porosity structure is evident in CT images obtained from the core samples C1006, as illustrated in Figure 3.10. These images provide a clear visualization of the intergranular and fractured nature of the reservoir rock, offering insights into its complex porosity and permeability attributes.

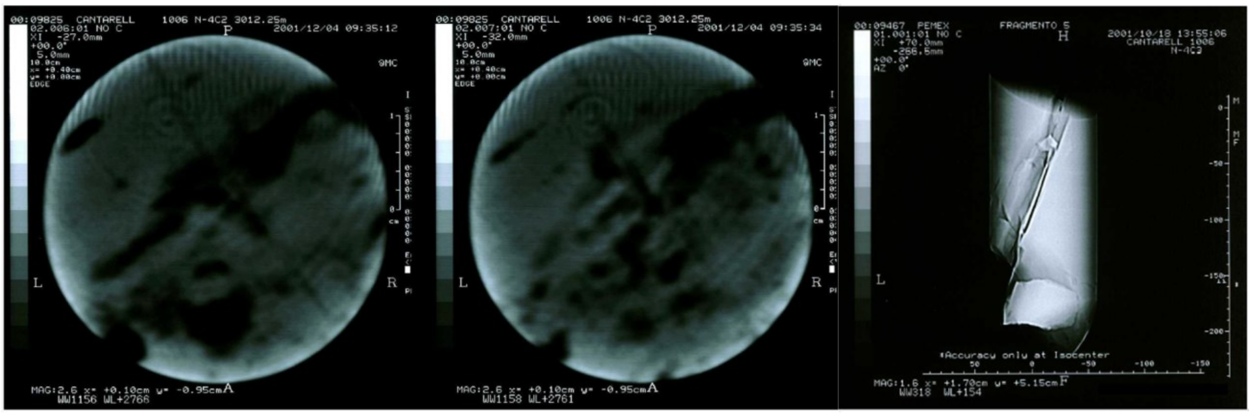

Figure 3.10. CT Imaging of core samples from Akal KL reservoir showing their dual-porosity structure. The images highlight the intergranular primary porosity and the secondary porosity characterized by fractures and vugular cavities.

### 3.5.1. Porosity-Permeability Relationship

The porosity-permeability relationship in the Akal KL reservoir is significantly influenced by its dual-porosity structure. Figure 3.11 depicts the relationships characterized by Pemex Exploration and Production. The blue curve represents the matrix permeability relationship ($k = 6E^{-5}\emptyset^{4.16}$), the red curve illustrates the vug permeability as a function of porosity ($k = 5.3E^{-5}\emptyset^{4}$), and the green curve denotes the fracture permeability ($k = 27.15\emptyset^{2}$). The data points from wellbores C1006 and C1016 predominantly align with the matrix and vug permeability relationships, tending more towards the matrix relationship. However, this should be interpreted with caution, as it depends on the characteristics of the available samples, often the more solid ones.

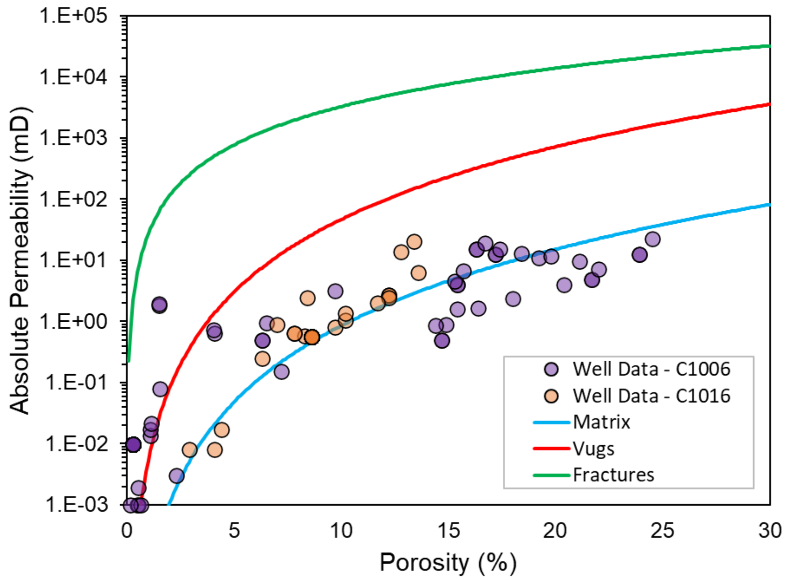


Figure 3.11. Porosity-permeability relationships in the Akal KL reservoir. The graph shows matrix, vug, and fracture permeability as functions of porosity. Data points from wellbores C1006 and C1016 illustrate the alignment with matrix and vug relationships.

As per Lucia (2007), these measurements mostly fall between Class 2 and Class 3 limestone and dolomite carbonates, as shown in Figure 3.12. These classes are part of the rock-fabric petrophysical classification system, which includes Class 1, Class 2, and Class 3. Class 1 encompasses grainstones, dolomitized grainstones, and large crystalline dolostones, typically with grain sizes ranging from 100 to 500 microns. Class 2 is characterized by grain-dominated packstones, fine to medium crystalline grain-dominated dolopackstones, and medium crystalline mud-dominated dolostones, with grain sizes from 20 to 400 microns. Class 3 mainly includes mud-dominated fabrics (such as mud-dominated packstone, wackestone, and mudstone) and fine crystalline mud-dominated dolostones.

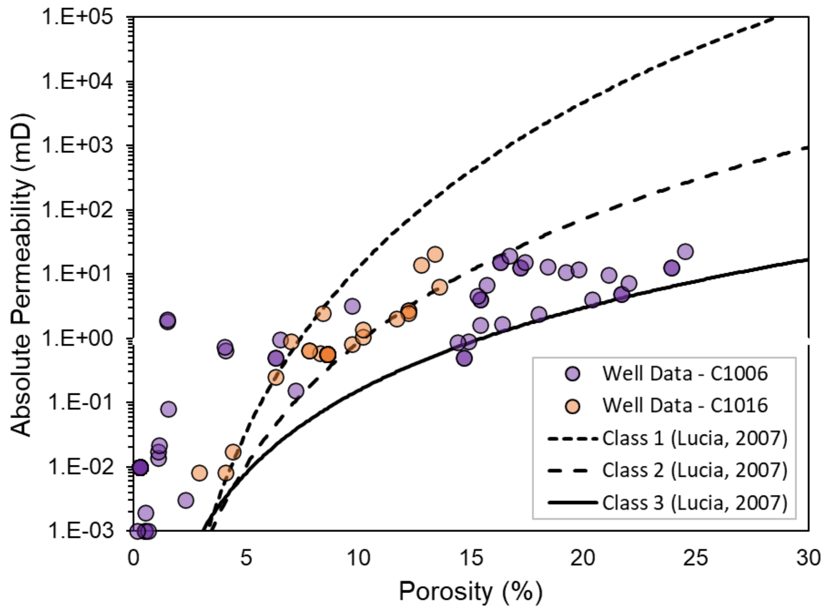


Figure 3.12. Rock-fabric petrophysical classification for the Akal KL reservoir. This diagram categorizes samples into Class 2 and Class 3 limestone and dolomite carbonates.

### 3.5.2. Relative Permeability and Capillary Pressure

The relative permeability measurements in the Akal KL reservoir were carried out using both water-oil and gas-oil systems. These measurements, conducted on samples extracted at 2350 meters from the wellbore C1006 in 1999, were performed at a confining stress of 21 MPa and a temperature of 96°C. Core Laboratories (Houston, TX, USA) carried out these tests under steady-state conditions, utilizing X-rays to determine the wetting phase saturation.

Figure 3.13 presents the relative permeability curves for the water-oil system from core samples C1006_5, C1006_14, and C1006_5. The data illustrates that the three core samples exhibit similar trends. The irreducible water saturation ranges between 22% and 31%, while the residual oil saturation lies between 39% and 45%. The crossover point, where the water and oil relative permeabilities are equal, is at a water saturation of about 43%. This crossover suggests a mixed-wettability condition. According to Craig's rule of thumb, a water saturation of approximately 35% indicates oil-wet cores, while around 65% points to water-wet samples (Craig, 1971).

The wettability of a system significantly impacts relative permeability. In a uniformly wetted system, the wetting fluid typically occupies the smaller pores and forms a thin film in the larger pores, while the non-wetting fluid is found in the centers of these larger pores. Generally, a fluid's relative permeability is higher when it is in the non-wetting phase. For example, in an oil-wet system, water (the wetting fluid) travels through smaller, less permeable pores, while the non-wetting fluid flows more easily in the larger pores. Additionally, at low non-wetting phase saturations, the non-wetting phase fluid can become trapped in the larger pores, reducing the wetting-phase's relative permeability.

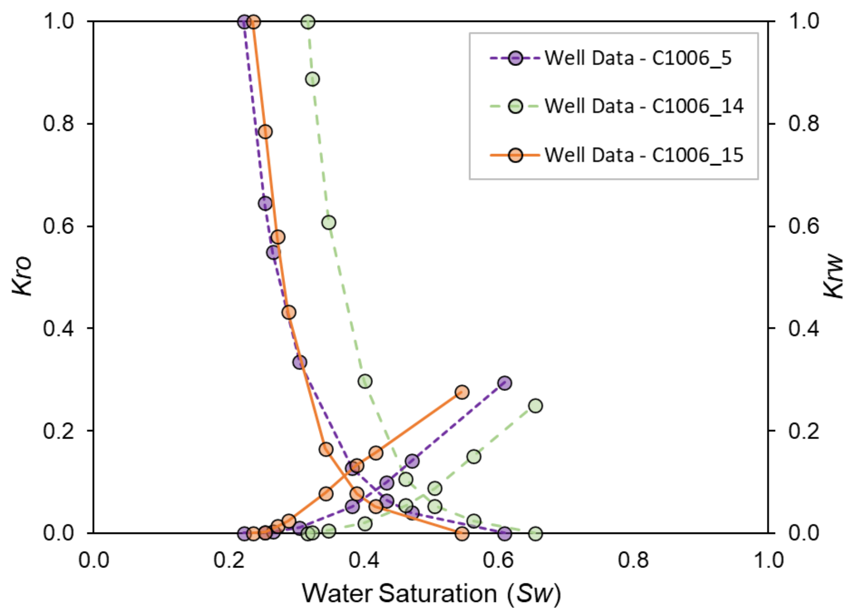


Figure 3.13. Water-oil relative permeability curves for Akal KL reservoir. This figure displays the relative permeability trends for water and oil in the Akal KL reservoir, using core samples C1006_5, C1006_14, and C1006_5. The graph illustrates the irreducible water saturation and residual oil saturation levels, highlighting the system's mixed-wettability.

Figure 3.14 illustrates the relative permeability in an oil-gas system. Here, the residual oil saturation varies between 72% and 78%, with the relative permeability to gas at residual oil saturation ranging from 18% to 26% of the absolute permeability. In an oil-gas mixture, gas typically acts as the non-wetting phase, occupying larger pore centers. Oil often shows higher relative permeability than gas due to its ability to occupy smaller pores and navigate more complex paths, especially in oil-wet or mixed-wet systems. Oil's higher viscosity compared to gas allows it to utilize a larger fraction of the pore space. Meanwhile, gas, being the non-wetting phase with lower viscosity, often flows through larger, more permeable channels, leaving much of the smaller pore space unused. This results in a lower relative permeability for gas. At maximum gas saturations, the relative permeability to gas is about 20% of the absolute permeability, as gas, filling mainly the larger pores, cannot completely displace oil from smaller pores due to capillary forces. Consequently, the full potential of the reservoir's absolute permeability is not fully utilized by the gas phase. These changes can either enhance oil mobility or lead to premature gas breakthrough, depending on the reservoir conditions and gas saturation levels. Therefore, the introduction of gas adds complexity to the phase behavior, flow dynamics, and recovery strategies in oil reservoirs.

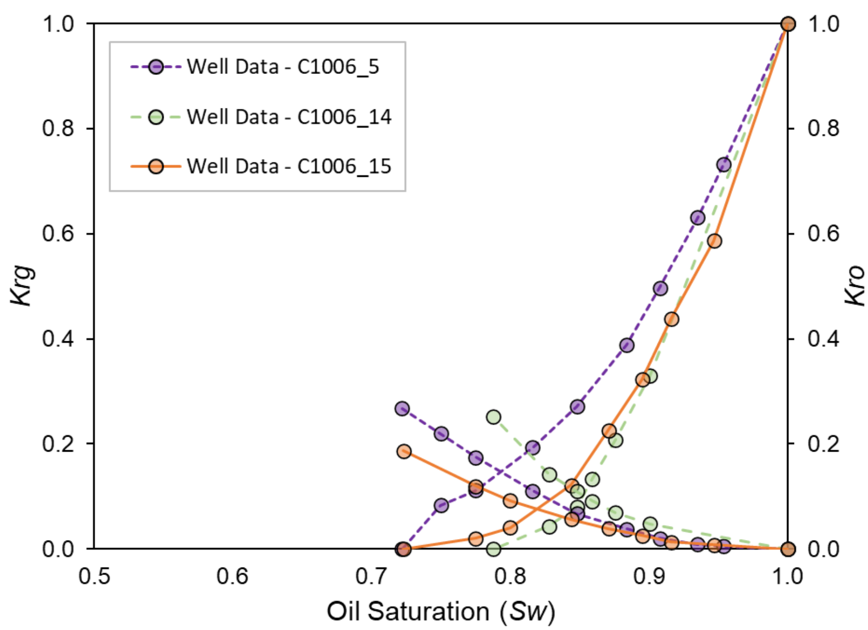


Figure 3.14. Oil-gas relative permeability in Akal KL reservoir. This figure shows the relative permeability characteristics of an oil-gas system in the Akal KL reservoir.

Figure 3.15 presents the capillary pressure data obtained through the Mercury Injection Capillary Pressure (MICP) method. MICP involves the injection of non-wetting mercury into a porous medium under controlled conditions to measure capillary pressures. This technique is widely used because of its accuracy in determining pore size distributions and capillary pressure relationships in reservoir rocks. The measurements were initially conducted at room temperature using a mercury-air mixture. Subsequently, the data were converted to represent gas-water, gas-oil, and oil-water systems. The graph shows that water saturation reaches residual levels at approximately 40%, beyond which the capillary pressure increases exponentially, indicating only minor reductions in water saturation even with significant pressure increments. This behavior reflects the resistance of the rock's pore network to mercury invasion, providing insights into the pore structure and fluid distribution within the reservoir.

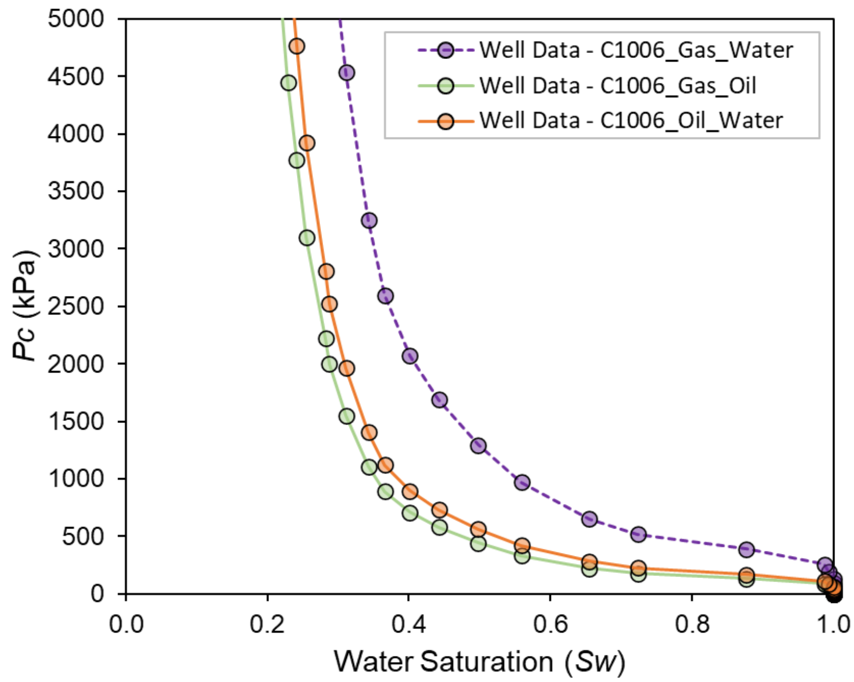


Figure 3.15. Capillary pressure curves for Akal KL reservoir rock, derived from Mercury Injection Capillary Pressure (MICP) measurements. The curves represent the conversion of mercury-air measurements to gas-water, gas-oil, and oil-water systems, illustrating the change in water saturation and corresponding capillary pressure.

### 3.6. Geomechanical Properties

The geomechanical properties of the Akal field present a unique challenge due to the limited data available from core testing. Recognizing this gap, researchers have turned to well logs as a practical and effective alternative for geomechanical modeling (Celis et al., 2006; Morales et al., 2006; Cruz et al., 2009). These logs, extending through both the overburden and the reservoir, offer a comprehensive dataset from which the rock mechanical properties can be inferred. This approach can be further enhanced by using empirical correlations that link static properties (obtained from laboratory measurements) with dynamic properties (derived from well logs).

In an elastic, isotropic, and homogeneous solid, elasticity moduli can be inferred from the velocities of compressional waves ($V_p$) and shear waves ($V_s$). Therefore, the shear modulus and bulk modulus for the Akal KL reservoir can be calculated using established relationships for isotropic materials (Zoback, 2007). Table 3.2 presents the average properties identified within the reservoir, with compressional and shear wave velocities derived from sonic logs and bulk density from density logs. In a collaborative effort, Pemex Exploration and Production and Core Laboratories analyzed cores from the Akal KL reservoir at a depth of 2551 meters. This analysis included measuring acoustic velocities on core samples to ascertain compressional and shear wave velocities, further enabling the calculation of mechanical properties. Compressibility measurements for both bulk and pore volumes were also conducted. The congruence between properties derived from well logs and core analysis indicates a reliable approximation of the reservoir rock's mechanical properties.

Table 3.2. Summary of reservoir rock properties obtained from well logs.

| Property | Mean | StDev | Method |
|---|---|---|---|
| $\boldsymbol{V_p}$, (m/s) | 4361.07 | 1311.06 | Sonic log* |
| $\boldsymbol{V_s}$, (m/s) | 2674.13 | 531.97 | Sonic log* |
| $\boldsymbol{\rho_b}$, (kg/m3) | 2565.34 | 369.00 | Density log* |
| $\boldsymbol{v}$, (-)* | 0.24 | 0.08 | $v = V_p^2 - 2V_s^2/2\left(V_p^2 - V_s^2\right)$ |
| $\boldsymbol{E}$, (GPa)* | 50.69 | 70.19 | $E = 2G(1 + v)$ |
| $\boldsymbol{G}$, (GPa)* | 19.41 | 8.73 | $G = \rho_b V_s^2$ |
| $\boldsymbol{K}$, (GPa)* | 32.59 | 21.53 | $K = E/3(1 - 2v)$ |
| $\boldsymbol{M}$, (GPa)* | 55.92 | 33.14 | $M = E(1 - v)/(1 + v)(1 - 2v)$ |
| $\boldsymbol{\emptyset_T}$, (%) | 10.48 | 3.46 | Neutron, sonic logs |
| $\boldsymbol{K_{m,f}}$, (mD) | 5.62-5000 | 47.79 | Evaluated logs |

* Properties calculated from relationships among elastic moduli in isotropic materials.

Table 3.3. Summary of reservoir rock properties obtained from core analysis.

| Property | Sample 1 | Sample 2 | Sample 3 | Mean | Method |
|---|---|---|---|---|---|
| $\boldsymbol{V_p}$, (m/s) | 4475.38 | 3735.63 | 4061.46 | 4090.82 | Acoustic velocity |
| $\boldsymbol{V_s}$, (m/s) | 2273.81 | 1945.84 | 2197.91 | 2139.19 | Acoustic velocity |
| $\boldsymbol{\rho_b}$, (kg/m3) | 2410.00 | 2320.00 | 2360.00 | 2363.33 | Direct measurement |
| $\boldsymbol{v}$, (-) | 0.33 | 0.31 | 0.29 | 0.31 | Elastic relationships |
| $\boldsymbol{E}$, (GPa) | 33.01 | 23.06 | 29.52 | 28.53 | Elastic relationships |
| $\boldsymbol{G}$, (GPa) | 12.45 | 8.78 | 11.42 | 10.88 | Elastic relationships |
| $\boldsymbol{K}$, (GPa) | 31.63 | 20.65 | 23.77 | 25.35 | Elastic relationships |
| **Cbc** (1/MPa) | 2.5E-4 | 2.18E-4 | 2.72E-4 | 2.47E-4 | Bulk compressibility |
| **Cb** (1/MPa)* | - | - | - | 2.54E-4 | Well test data |

* Bulk compressibility obtained from well test data.

## 3.7. Reservoir Fluid Properties

Fluid properties in the Akal KL reservoir were determined from well test data and Pressure-Volume-Temperature (PVT) analysis. Data were collected in 2002, at the beginning of reservoir exploitation, from various wells and at different depths within the reservoir. The average reservoir pressure at the time of these measurements was 10.3 MPa, and the temperature was 104°C.

Table 3.4. Fluid properties in the reservoir.

| T, °C | $\boldsymbol{P_b}$, (kg/cm$^2$) | $\boldsymbol{B_o}$, (-) | $\boldsymbol{\rho_o}$, (g/cm$^3$) | $\boldsymbol{\mu_o}$, (cP) | API° | $\boldsymbol{B_g}$, (-) | $\boldsymbol{\rho_g}$, (g/cm$^3$) | $\boldsymbol{\mu_g}$, (cP) | Method |
|---|---|---|---|---|---|---|---|---|---|
| 99.93 | 150.00 | 1.23 | 0.78 | 1.29 | 23.00 | 0.01 | 0.10 | 0.02 | WT1 |
| 101.19 | 150.00 | 1.24 | 0.81 | 2.47 | 23.00 | 0.01 | 0.13 | 0.02 | WT2 |
| 111.44 | 150.00 | 1.23 | 0.76 | 2.46 | 23.00 | 0.01 | 0.11 | 0.02 | WT3 |
| 107.26 | 150.00 | 1.24 | 0.80 | 2.29 | 23.00 | 0.01 | 0.13 | 0.02 | WT4 |
| 103.86 | 150.00 | 1.23 | 0.82 | 2.47 | 23.00 | 0.01 | 0.12 | 0.02 | WT5 |
| 105.00 | 142.20 | 1.29 | 0.78 | 1.98 | 22.90 | 0.01 | 0.29 | - | PVT1 |
| 106.10 | 128.90 | 1.24 | 0.80 | 2.30 | 22.20 | 0.009 | 0.29 | - | PVT2 |

WT: Well test analysis (Pemex E&P), PVT: Pressure-Volume-Temperature analysis (Core Laboratories).

# 4. Design and Execution of Multiphase Triaxial Testing[1]

## 4.1. Introduction

This chapter presents the design and functionality of the Multiphase Triaxial System, a sophisticated setup encompassing five key hydraulic and electrical components. The system is encased within an oven to ensure uniform isothermal conditions, a crucial aspect for the accuracy of experimental results.

The capabilities of the system are highlighted through initial testing on sandpack and Berea sandstone specimens. These tests not only demonstrate the system's effectiveness but also provide insights into the behavior of fluid flow under different stress conditions. The design and experimental procedures of this facility have wide-reaching applications, especially in fields that require an understanding of two-phase flow in variable effective stress environments, such as extraction of natural resources, geothermal energy, radioactive waste management, and carbon capture and storage.

This research focuses on the important role of triaxial stress in influencing fluid flow mechanisms, offering both theoretical and practical insights in geomechanics and fluid dynamics. It advances our understanding of subsurface fluid behavior under complex stress states, which is crucial for effective resource exploration, extraction, and environmental protection.

[1] This chapter was presented as a conference paper at the 56th US Rock Mechanics/Geomechanics Symposium in Santa Fe, New Mexico, USA, from 26-29 June 2022. The paper, authored by Sanchez-Barra, A.; Deisman, N.; Guerrero, F.; Brandl, J.; Chalaturnyk, R., is titled "Experimental Facility for Testing Unconventional Reservoirs: Effect of Geomechanics on Multiphase Flow Properties." It was published in the proceedings of the American Rock Mechanics Association, 2022. DOI: 10.56952/ARMA-2022-0543.

### 4.2. Experimental Facility for Multiphase Triaxial Testing

Designed and assembled at the University of Alberta, the Multiphase Triaxial System comprises five essential components: (1) a triaxial high-pressure cell, (2) a loading system, (3) a multiphase pore-pressure circuit, (4) a fluid phase separation system, and (5) a data logging system. To ensure the accuracy and reliability of experimental results, the entire system is encased within an oven, maintaining consistent isothermal conditions. A detailed render of the system's design, showing the complex arrangement and connectivity of these components, is presented in Figure 3.1. The 3D computerized model of the system was created using Inventor® software (Autodesk, San Francisco, CA, USA).

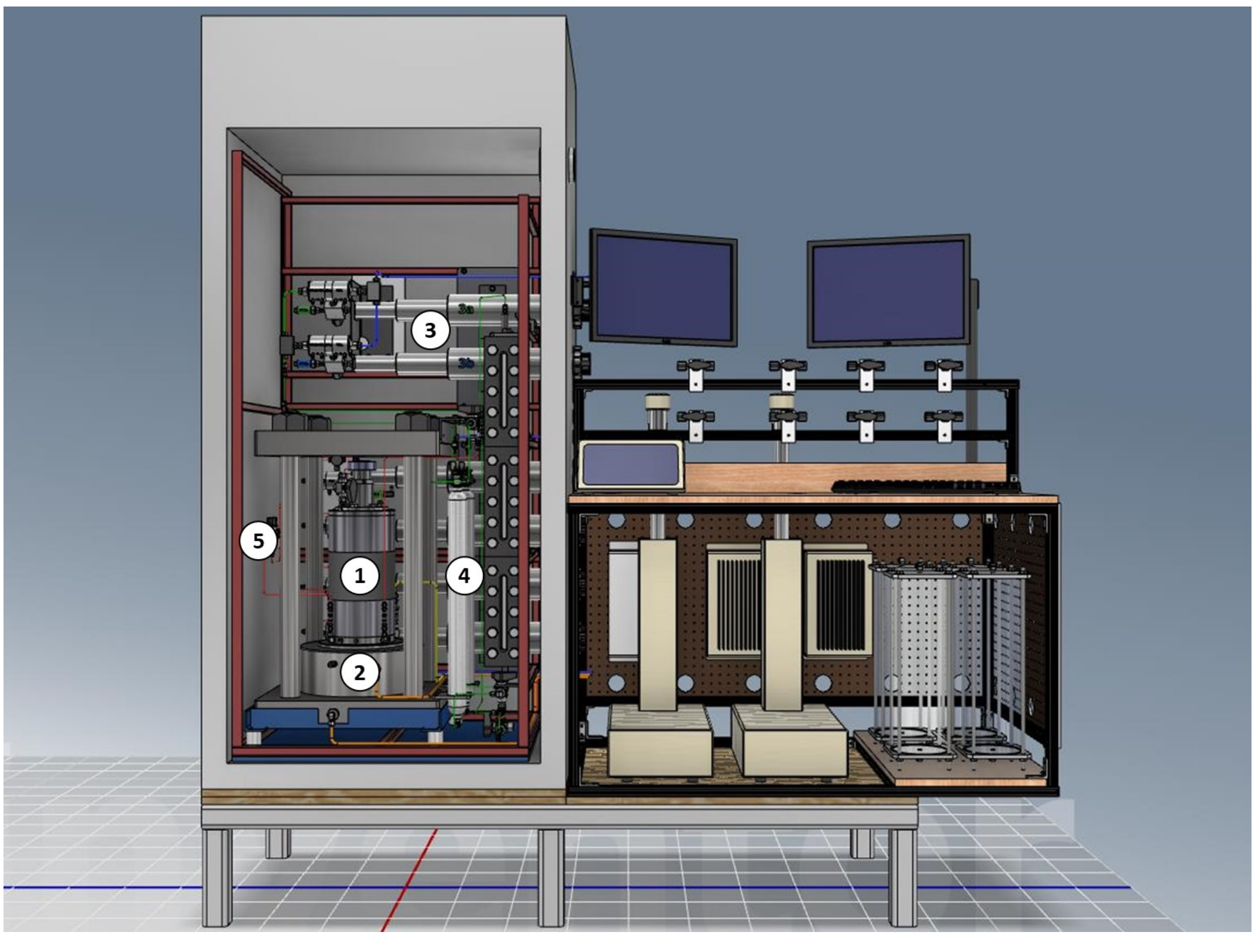


Figure 4.1. Detailed render of the Multiphase Triaxial Testing System. This image illustrates the primary components of the system and their arrangement.

The construction of this system involved a series of sequential steps. It began with the 3D model, followed by the acquisition of various components such as pumps, valves, High-Pressure High-Temperature (HPHT) cells and cylinders, sensors, and stainless steel tubing for the hydraulic lines. After gathering the necessary parts, they were meticulously assembled in accordance with the 3D model. The complete system was then built and calibrated before initiating testing, as shown in Figure 4.2. These images not only display the physical structure of the system but also highlight the intricate engineering and meticulous planning that went into developing this advanced experimental setup for multiphase triaxial testing.

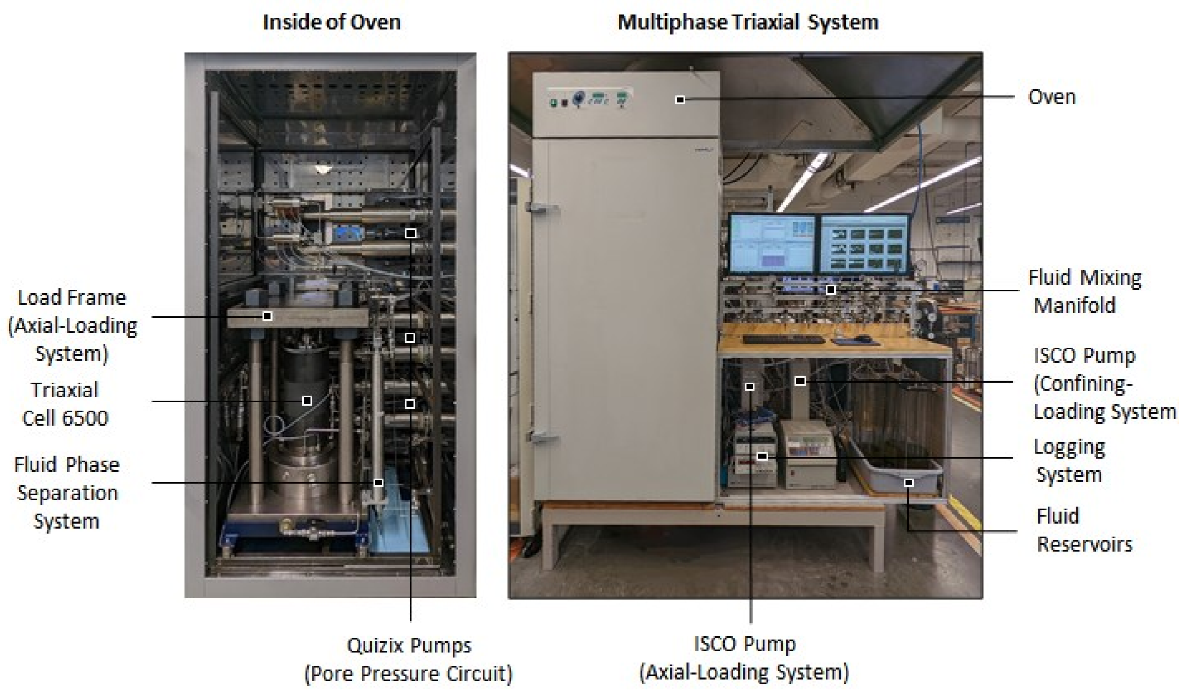


Figure 4.2. Assembled Multiphase Triaxial System by the Reservoir Geomechanics Research Group.

An outside manifold was built to distribute multiple fluids such as gas, oil, and water into the system. This manifold allows the mix of the fluids prior to entering the cell and during a test. The manifold also includes a separate flow line for air/vacuum to facilitate the purge of the lines when needed (Figure 4.3). The different color lines in Figure 4.3 indicate the general flow paths of the fluids for the different circuits, starting from the fluid reservoirs to the manifold, through the internal/external pumps, into the oven, to the loading system, through the specimen, and finishing in the fluid separation system.

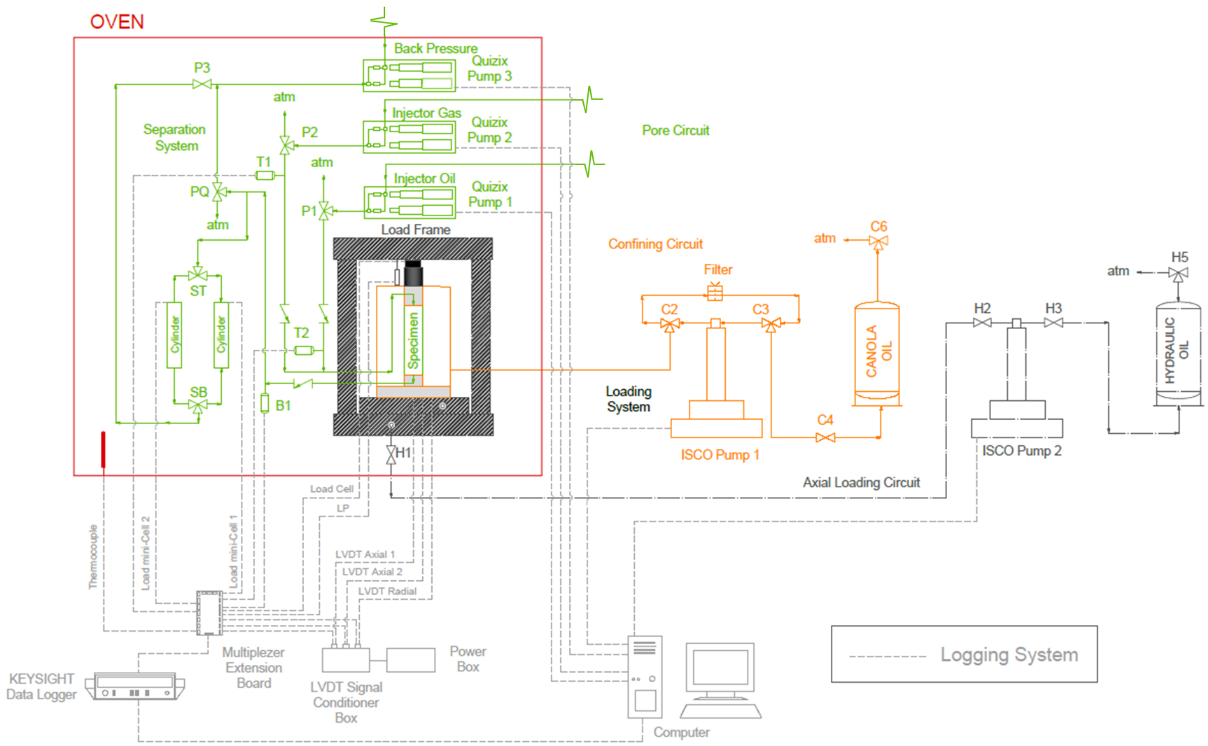


Figure 4.3. Flow diagram for the Multiphase Triaxial System. The different color lines indicate the general flow paths.

### 4.2.1. Triaxial High-Pressure Cell

The Deisman Triaxial Cell 6500 (Deisman et al., 2011) is a high-pressure and high-temperature cell capable of independently applying axial and confining stresses to the specimen. The cell has maximum operating stress of 45 MPa, maximum pore pressure of 20 MPa, and a maximum operating temperature of 60°C (Figure 4.4). The upper and lower platens are hollow, allowing for piezo electric crystal installation if required. The flow and pressure lines enter through the base of the cell. Two available ports are present on upper and lower platens, allowing the displacement of two different fluids through the specimen. This configuration provides the choice of flowing upwards or downwards through the specimen and allows the testing of absolute or relative permeability.

For this study, the flow lines for the injecting fluids are connected to the upper platen (top), while the drainage lines are connected to the lower platen (bottom). The top platen connects to the axial ram, which passes through the plug in the upper-end cap and connects to an external load cell. During the cell assembly, the ram is fixed to the upper-end cap using an isolation plate and threaded rods. This helps to minimize sample disturbance during installation.

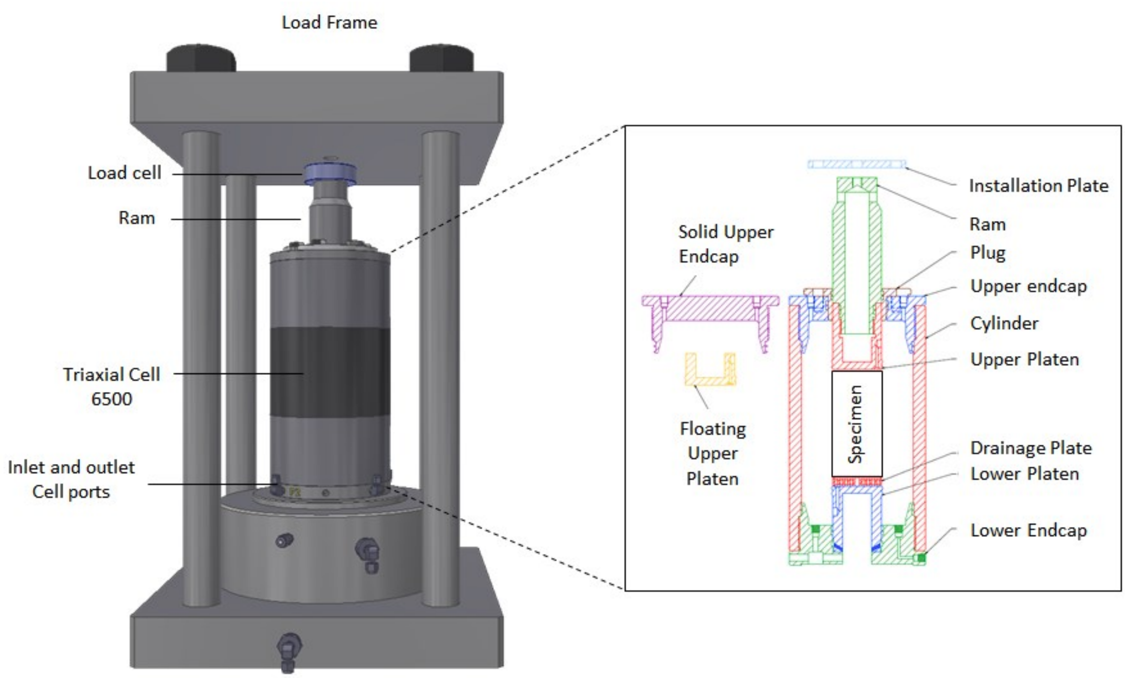


Figure 4.4. Load frame and cross-section of the triaxial high-pressure cell (modified from Deisman et al., 2011).

### 4.2.2. Loading System

The loading system of the Multiphase Triaxial System is divided into two main circuits: (a) the axial loading circuit and (b) the confining (radial) circuit, represented by black and orange lines, respectively, in Figure 4.3. The axial loading circuit is composed of a low-profile load frame with a 228.6 mm (9.0 in) diameter hydraulic piston located at the bottom of the frame and an external 260HP High-Pressure ISCO Syringe Pump (see Figure 4.4). The piston is connected to the pump, which uses hydraulic oil as the hydraulic fluid. The axial load is applied using constant flow rate mode on the pump, and it is measured with a 400 kN OMEGA load cell fixed between the top of the frame and the ram. The displacement of the ram is measured with an external linear potentiometer.

The confining circuit is composed of the Deisman Triaxial Cell 6500 and an external 260HP High-Pressure ISCO Syringe Pump. The isotropic or radial stress is applied by pumping canola oil (confining fluid) into the cell and measured with a Honeywell pressure transducer of 41 MPa. Two internal axial LVDT's are placed around the sample to measure vertical displacement and, an internal radial chain with a spring-loaded and LVDT is used to measure the change in specimen circumference.

### 4.2.3. Multiphase Pore-Pressure Circuit

The multiphase pore-pressure circuit, depicted by green lines in Figure 4.3, is an integral part of the system. It is controlled through an external fluid mixing manifold, operated by three HPHT Quizix Q5000 pumps. To ensure accuracy by preventing volumetric errors due to thermal expansion and contraction, the entire pump body of these Quizix pumps is situated inside the oven (Figure 4.5), maintaining the fluids, pistons, and cylinder barrels at a uniform temperature. The motors and controllers for these pumps, however, are located externally, outside the oven wall.

Figures 4.5a and 4.5b display the 3D computerized model and the actual constructed system, respectively. In both images, it is evident that all metal components are made of stainless steel to prevent corrosion. The 3D model initially included a HPHT glass cell designed for visualizing the separation of fluid phases. However, this component was not installed during the calibration phase as it was found to increase the dead pore volume of the circuit, adversely affecting the quality of the experiments. Thermocouples, pressure transducers, load cells, and other measurement devices are strategically distributed throughout the system, ensuring comprehensive data collection during testing.

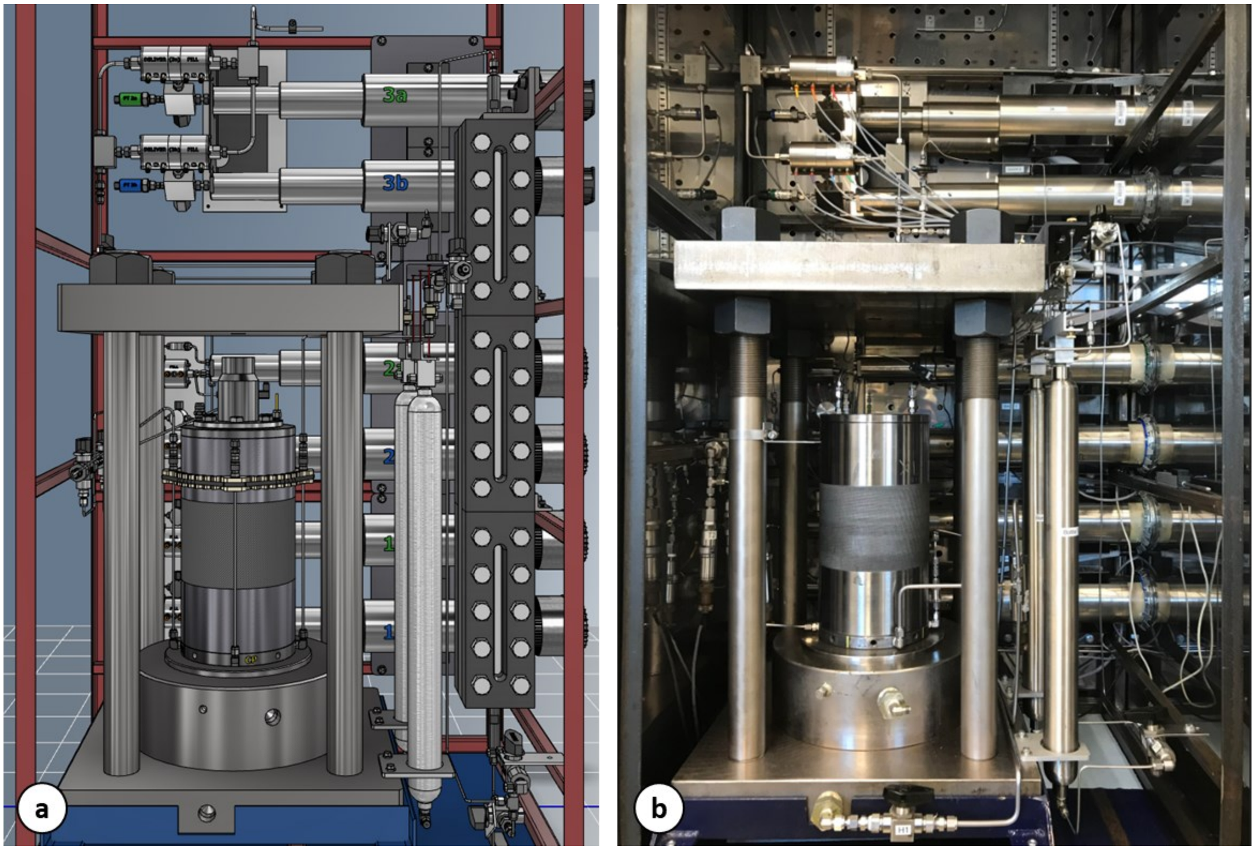

Figure 4.5. Comparison of the multiphase pore-pressure circuit. (a) 3D Computerized model of the system; (b) actual constructed system.

Within the system, two Quizix pumps are employed upstream to inject two distinct fluids simultaneously into the specimen, while a third pump is utilized downstream to maintain back pressure. The inlet flow lines from the injector pumps, each fitted with check valves to prevent backflow, converge before entering the top of the specimen. The outlet flow line coming from the specimen is diverted to the fluid phase separation system and to the backpressure pump. The inlet and outlet (upstream and downstream) flow pressures are measured independently for each fluid flow line with 20 MPa Honeywell high-precision transducers. This allows accurate measurements of the differential pressure across the specimen. The readings of the upstream and downstream pressure transducers are logged and continuously displayed with an Agilent data acquisition unit and a LabView-based data logging software.

### 4.2.4. Fluid Phase Separation System

The fluid phase separation system is a crucial component, featuring two HPHT vertical separation cylinders. These cylinders are continuously monitored for weight changes using ultra-sensitive Omega LC703-10 load cells (4.5 kgf) coupled with custom-built amplifiers, as depicted in Figure 4.6. This setup enables the precise estimation of wetting and non-wetting fluid phase saturations through real-time mass measurements of the fluids being produced.

When the two-phase flow downstream reaches a steady state, it is assumed that the fluid saturations are uniformly distributed throughout the specimen. At this stage, the fluid mixture exiting the specimen is directed to the phase separation system, which is equilibrated with the pore pressure. Here, the system effectively segregates the fluid volume fractions through gravity separation. The design of this system, with a 500 mL fluid capacity for each cylinder, allows for extended periods of fluid production, ensuring comprehensive data collection over the course of an experiment.

Figures 4.6 and 4.7 present the 3D model design and the actual assembled multi fluid phase separation system. This setup not only enables the separation of fluid phases but also provides valuable data for understanding the dynamics of multiphase flow within the specimen, contributing significantly to the study of fluid behaviors in various geomechanical contexts.

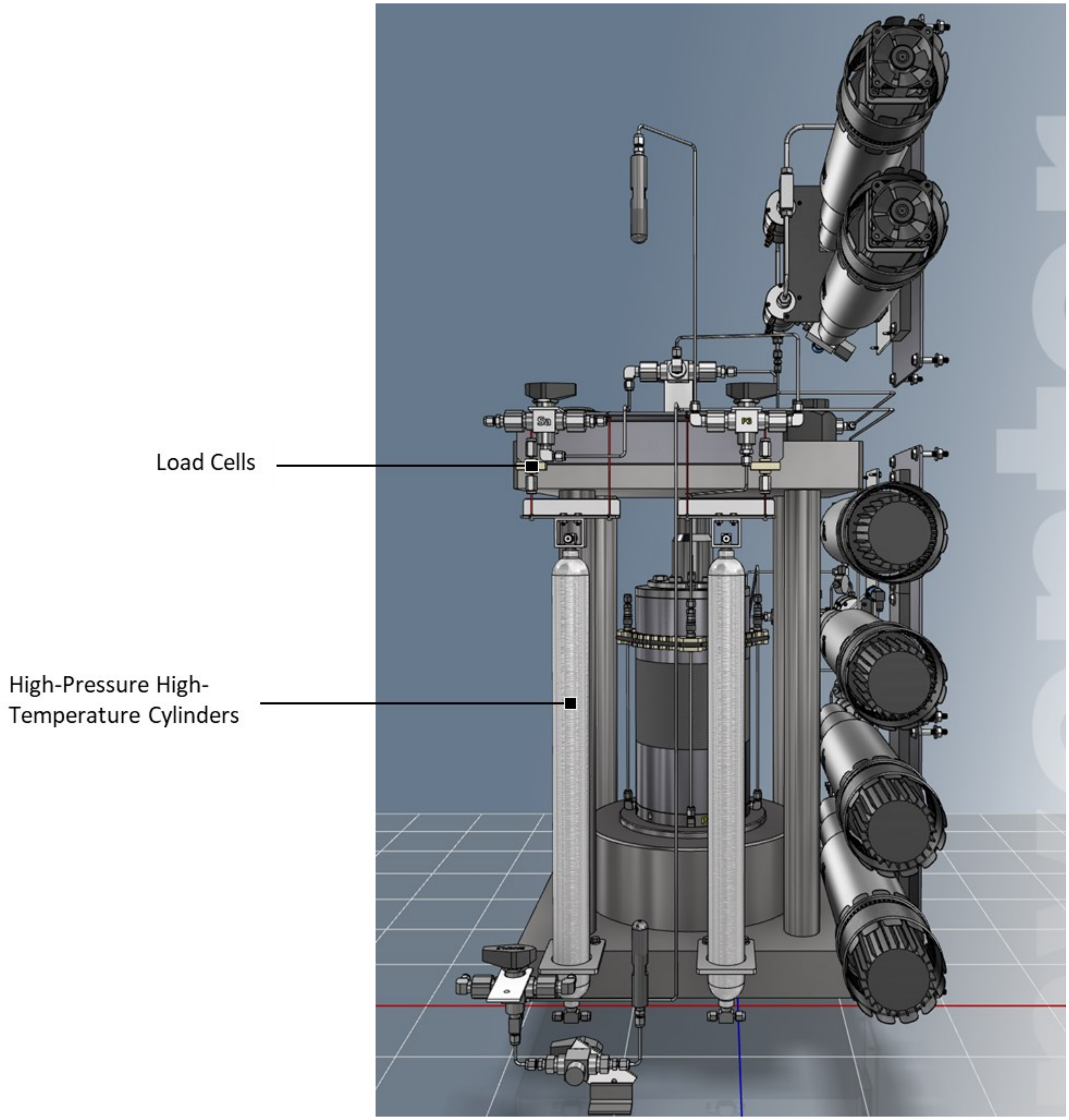


Figure 4.6. 3D Model of the HPHT fluid phase separation system. This detailed illustration showcases the vertical separation cylinders, monitored by ultra-sensitive load cells, crucial for precise phase saturation measurements in multiphase flow experiments.

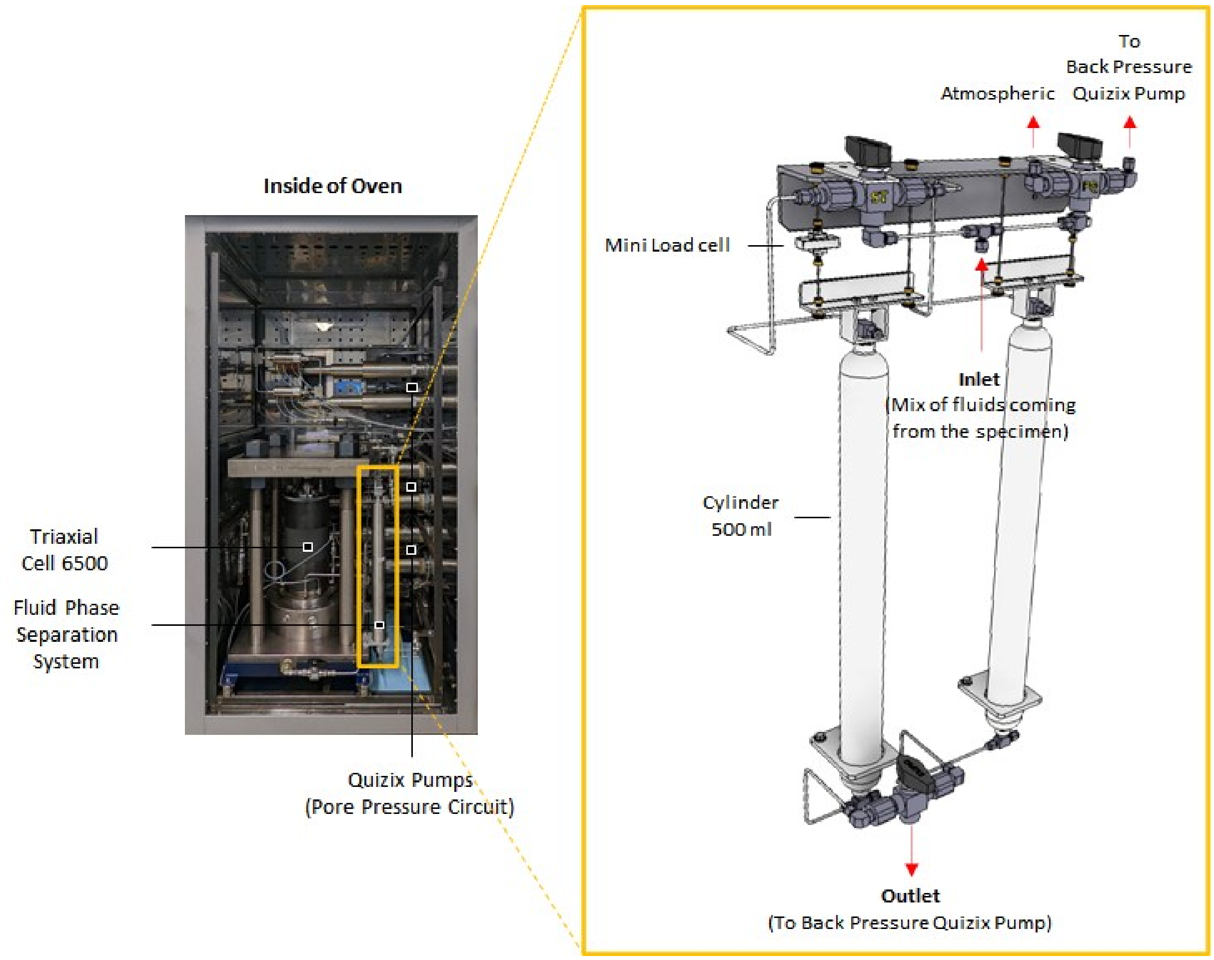


Figure 4.7. Assembled fluid phase separation system within the multiphase triaxial setup. This image showcases the actual (real) fluid separation system, featuring vertical separation cylinders and load cells, integrated into the broader Multiphase Triaxial System.

### 4.2.5. Data Logging System

The design of the data logging system is shown in Figure 4.8, where a close-up view of the system allows the visualization of the different sensors used to monitor the data during a triaxial test. The signal readings of the load cells, pressure transducers, axial/radial strains, and thermocouples are logged and continuously displayed on a LabView-based data logging software built by the Reservoir Geomechanics Research Group.

A KEYSIGHT® 34972A data acquisition unit is used to collect and process the signals coming from the different sensors in the system. The data acquisition unit allows the measurement of different signals such as ac/dc volts, thermocouple, thermistor and RTD temperature measurements, ac/dc current, frequency, and period. The unit is able to provide 6½ digits (22 bits) of resolution with 0.004% dcV accuracy. The unit comes with a configured 20-channel relay multiplexer. An outside multiplexer extension board is used to manage cables, signals and provide 10V power to the required sensors. The Quizix pumps also include in-house designed software and control systems to set and log pressures and flow rates for secondary or backup data acquisition.

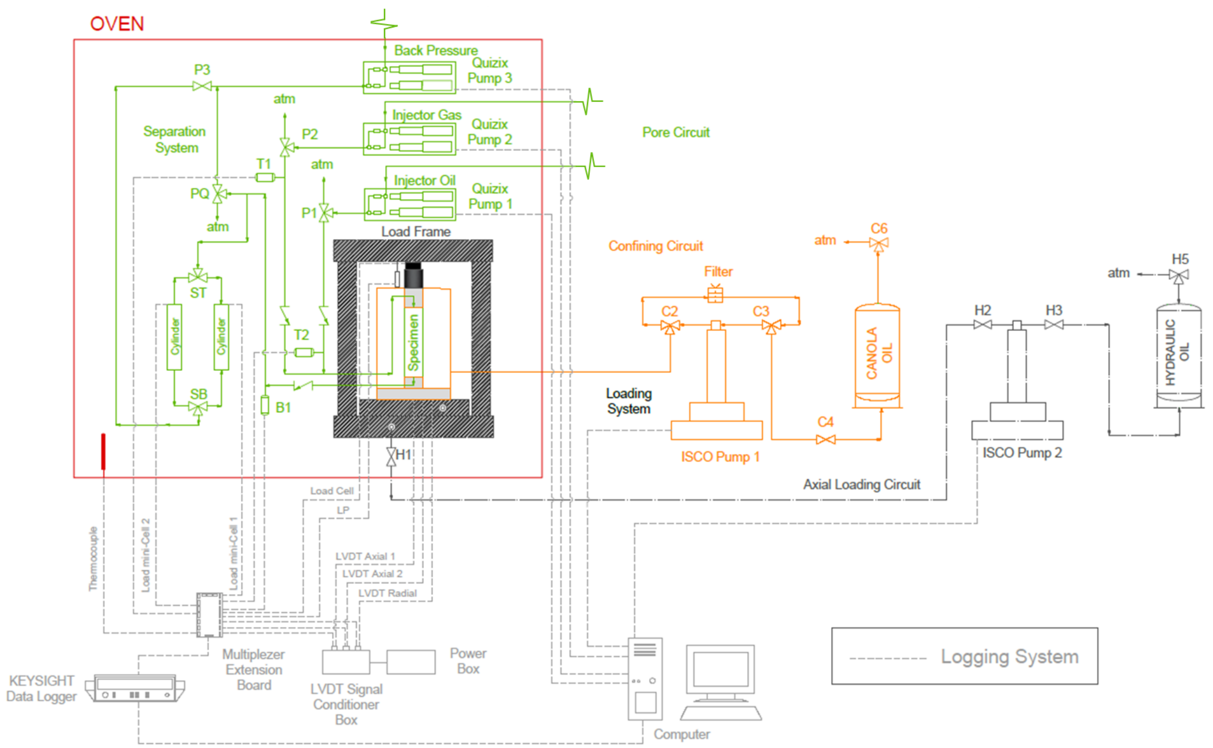


Figure 4.8. Data logging system for the Multiphase Triaxial System.

### 4.3. Experimental Procedure

This section outlines the design and execution of experimental procedures intended to thoroughly assess the capabilities of the Multiphase Triaxial System. These procedures target the precise measurement of several critical parameters, which in turn contribute to a comprehensive understanding of the system’s behavior under various conditions.

The parameters examined include volumetric strain, which indicates changes in the volume of the system or specimen under strain, and bulk compressibility, demonstrating volume changes under applied pressure. The bulk modulus is also assessed, reflecting the material's resistance to uniform compression, which is crucial for understanding its mechanical stability. Additionally, measurements of absolute permeability, the ability of a material to transmit fluids under an external driving force, and relative permeability, the capacity of multiple fluid phases to flow simultaneously through the system or material, are conducted.

The comprehensive data and insights derived from these procedures have the potential to inform a wide range of disciplines dealing with complex multiphase flow scenarios. This includes but is not limited to, enhanced oil recovery, geothermal processes, radioactive waste repositories, and carbon capture and storage operations. Each of these fields often confronts challenging conditions of varying effective stress, hence the value and applicability of the knowledge gathered from this study.

### 4.3.1. Materials

The laboratory testing program utilized two types of specimens: sandpacks and Berea sandstone. The sandpack specimens were meticulously prepared from silica sand, characterized by a monodisperse particle size distribution ($D_{50}$ = 175 μm). For the purpose of this study, two distinct types of sand mixtures were prepared. The first type used clean silica sand (control), while the second type employed silica sand coated with a binder (reclaimed), following the methodology outlined by Hodder and Chalaturnyk (2019). The contrasting characteristics of these sand mixtures are depicted in Figure 4.9.

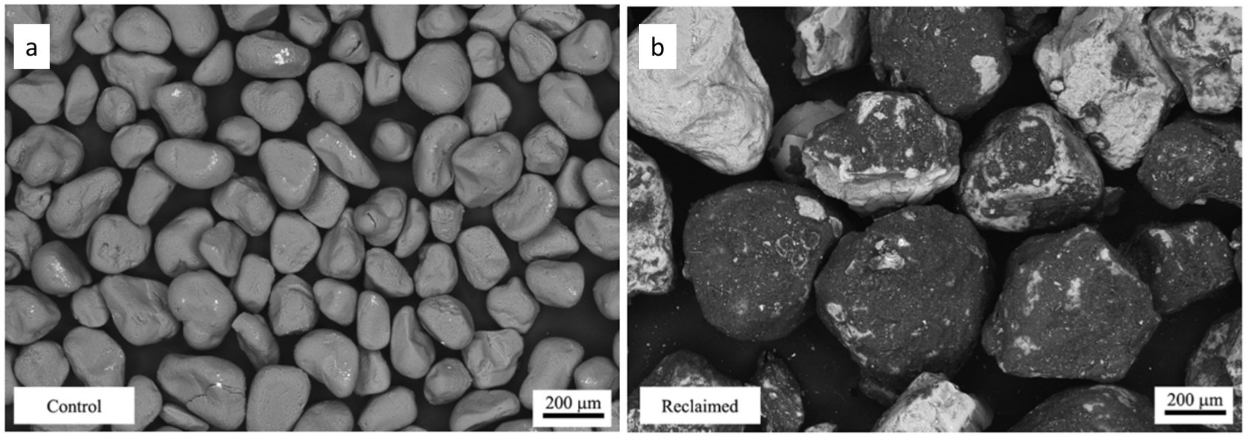


Figure 4.9. Comparative representation of sandpack specimens used in laboratory testing. (a) Clean silica sand specimen; (b) binder-coated sand specimen (modified from Hodder and Chalaturnyk, 2019).

Porosity and permeability were measured at 45% and 40%, and 5.6 D and 2.9 D, for each sandpack specimen, respectively. The sand was packed inside a stainless-steel tube with 9.11 mm in diameter and 128 mm in length, maintaining a 10:1 ratio to reduce capillary end effects (Hadley and Handy, 1956). The steel tube was then mounted in the system. The Berea sandstone specimen had a porosity of 17% and a permeability of 105 mD at 500 kPa effective confining stress. The core sample was 63.61 mm in diameter and 126.57 mm in length. The specimen was wrapped with a thin layer of cellophane, aluminum foil, and another layer of cellophane film to prevent gas diffusion through the membrane. Then, the specimen was inserted into a Viton fluoro-rubber membrane with porous stones in both ends. The whole package was then mounted into the triaxial cell.

The fluids used during the core flooding experiments were nitrogen gas and canola oil. The selection of the fluid pair was determined to be compatible with conditions in hydrocarbon reservoirs during forced gas drainage (gas flooding) and free gas gravity drainage. Canola oil was used as the wetting phase fluid and nitrogen was the non-wetting phase. At testing conditions (1 MPa and 40°C), the canola oil has a density of 0.88 g/cm$^3$ and a viscosity of ~34 cP and nitrogen has a density and viscosity of ~0.1g/cm$^3$ and ~0.184 cP, respectively.

### 4.3.2. Stress-strain Measurements

The volumetric strain was calculated using the real-time measurements of the axial and radial displacements sensor.

$$\varepsilon_v = \varepsilon_a + 2\varepsilon_r, \tag{4.1}$$

where $\varepsilon_v$, $\varepsilon_a$, and $\varepsilon_r$ are the volumetric strain, axial strain, and radial strain, respectively. The rock bulk compressibility was calculated using the changes in pore and confining pressures (Zimmerman et al., 1986) (Equation 4.2).

$$C_{bc} = \frac{1}{V_b^i}\left(\frac{\partial V_b}{\partial P_c}\right)_{P_p}, \tag{4.2}$$

where $V_b^i$ is the initial bulk volume of the rock, $\partial V_b$ is the change in bulk volume by the increase/decrease confining pressures ($\partial P_c$) under a constant pore pressure ($P_p$).

The bulk modulus $K$ was determined by calculating the reciprocal of the bulk compressibility, as outlined in Equation 4.3.

$$K = \frac{1}{C_{bc}}. \tag{4.3}$$

### 4.3.3. Absolute Permeability

Absolute permeability to oil was conducted at the beginning of each core-flooding experiment. The samples were continuously saturated with canola oil at low flow rates, typically 10 pore volumes for the sandpack samples and 40 to 80 pore volumes for the Berea sandstone, depending on the loading stage. When the porous media was completely saturated, the flow rate was increased, and the initial absolute permeability to oil was measured under steady-state single-phase incompressible fluid flow considerations. The constant flow was delivered by a Quizix pump, and the pressure drop across the specimen was recorded with upstream and downstream pressure transducers. Darcy's law for vertical flow was used to calculate permeability.

$$Q = \frac{kA\Delta P - \rho g L}{\mu L}, \tag{4.4}$$

where $\rho$ is the fluid density, $\mu$ is the fluid viscosity, $Q$ is the flow rate, $\Delta P$ is the differential pressure across the specimen, and $k$ the absolute permeability.

### 4.3.4. Relative Permeability

After the single-phase flow, the relative permeability was measured. When the oil flow rate was constant and the pressure drop across the specimen was stable, the nitrogen was co-injected into the samples through a second flow line. In step increments, the flow rate of nitrogen was increased while the oil flow rate was decreased by the same proportion to give a total flow rate of 2.5 mL/min. In the steady-state approach, a mixture of two or more fluids flows through the specimen until equilibrium is achieved. At equilibrium conditions, the saturation of the mixture of fluids is uniformly distributed across the specimen. Previous studies have suggested that the uniform saturation profile across the specimen is a valid assumption while injecting oil and gas phases simultaneously. However, the accuracy of the uniform saturation assumption has been questioned when the total flow rate is dominated by the gas phase and the oil phase is immobile (Haghi et al., 2020). This effect was discarded during the present study for the sandpack specimens with high permeability (>2.9 D) and a well-connected flow path (inlet to outlet). These conditions minimize slip flow and non-continuum flow regimes (Moghadam and Chalaturnyk, 2016). However, the non-continuum flow effect was considered for the Berea sandstone, which presented a low permeability matrix and significant phase interference. Relative permeability was calculated from individual fluid flow rates and pressures using Darcy law at different saturations.

$$kr_i = \frac{\mu_i Q_i L}{kA\Delta P_i + \rho_i g L}, \tag{4.5}$$

where $kr_i$ ($i$ = oil or gas) defines each fluid phase's relative permeability.

The fluid saturations were measured as described in Section 4.2.4. When the two-phase flow was at steady-state, the fluids drained from the specimen were separated, and the mass of the wetting phase fluid (canola oil) was measured and recorded in real-time. Then, with mass-balance calculations, the wetting phase fluid saturation was estimated.

The individual data points of the relative permeability versus saturation were fit using the X-curve model and the Brooks-Corey model. Several authors have conceptualized and simplified the relative permeability curves using models that correlate with the wetting phase saturation (Huo and Benson, 2016). The X-curve model assumes that the pore structure is well-connected (Bertels et al., 2001). The X curve is described by:

$$kr_w = s_w, \tag{4.6}$$

$$kr_{nw} = s_{nw} = 1 - s_w, \tag{4.7}$$

where $kr_w$ is the wetting phase relative permeability, $kr_{nw}$ is the non-wetting phase relative permeability, $s_w$ is the wetting phase saturation, and $s_{nw}$ is the non-wetting phase saturation. The X-curve model considers there is no interference between the two flowing phases. Therefore, the sum of the wetting and non-wetting phase relative permeability equals one at all saturations. In addition to the X-curve approach, the modified Brooks-Corey model accounts for phase interference and estimates the relative permeability curve as a power-law function of wetting phase saturation (Brooks and Corey, 1966; Huo and Benson, 2016; Haghi et al., 2020). The modified Brooks-Corey model is commonly used to describe the multiphase flow in porous media:

$$kr_w = k_{rw} - max\left(\frac{s_w - s_{wir}}{1 - s_{wir} - s_{nwr}}\right)^{n_w}, \tag{4.8}$$

$$kr_{nw} = k_{rnw} - max\left(\frac{1 - s_w - s_{wir}}{1 - s_{wir} - s_{nwr}}\right)^{n_{nw}}, \tag{4.9}$$

where, $s_{wir}$ is the irreducible wetting phase saturation, and $s_{nwr}$ is the residual non-wetting phase saturation. The powers $n_w$ and $n_{nw}$ are fitting constants to calibrate the equations with the experimental data.

## 4.4. Experimental Results

The testing program was developed to assess the performance of the experimental facility. The first case evaluates the multiphase flow system. Nitrogen gas and canola oil were used to measure the relative permeability of the sandpack specimens. The second case on Barea sandstone was used to test the entire Multiphase Triaxial System. This case shows the evolution of volumetric strain during loading and the effect of geomechanics on single-phase fluid flow. In addition, the gas-oil relative permeability was measured at maximum rock deformation.

### 4.4.1. Case 1. Sandpack Specimens

The sandpack specimens were used to evaluate the multiphase flow system performance and gas-oil relative permeability techniques. For this testing case, two different sandpacks were made. Specimen A was prepared with clean silica sand and specimen B with binder-coated sand similar to the one used in the foundry industry. The rationale for these mixtures is that different grain morphology induces different flow behaviors. Previous studies have shown that if the surfaces of the grains are modified through the bonding of residual binders, friction between grains increases and changes the pore structure (Hodder and Chalaturnyk, 2019).

Relative permeability for samples A and B was measured following the procedure described in Section 4.3.4. The test was conducted at room temperature for simplicity. After the absolute permeability to oil, the nitrogen was co-injected into the specimens through a second flow line. In step increments, the flow rate of nitrogen was increased while the oil flow rate was decreased by the same proportion to give a total flow rate of 2.5 mL/min. This process ensured that the two phases flowed simultaneously at the set flow fraction ($Q_o/Q_g$). Figure 4.10 shows the relative permeability measurements for sample A for each nitrogen/oil fraction flow. The data points were curve-fitted with the X-curve model (dotted lines) and the Brooks-Corey model (continuous and dashed lines). The results showed that oil relative permeability measurements followed the X-curve model, which can be attributed to a well-connected porous media. The gas relative permeability curve increased gently until the nitrogen was flowing at residual oil saturation. The assumption of matrix connectivity is reflected by the efficient drainage displacement of the wetting phase (oil phase), a typical behavior when there is low phase interference (Huo and Benson, 2016). At 100% nitrogen fractional flow ($Q_g$ = 2.5 mL/min), the nitrogen effective permeability was 22% of the absolute permeability.

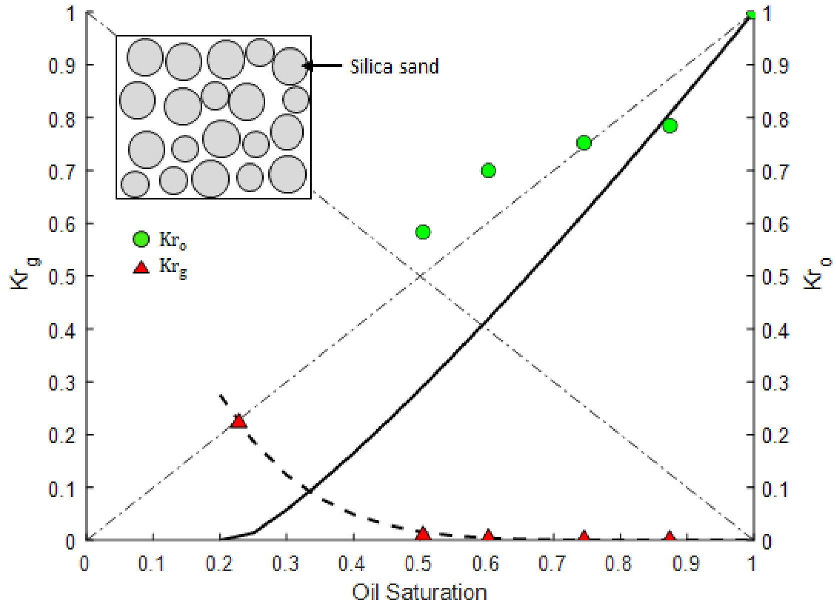


Figure 4.10. Nitrogen-oil relative permeability curves for sandpack A. The measurements reflect a well-connected porous media with very low phase interference.

Figure 4.11 shows the relative permeability measurements for sample B. For this case, the relative permeability data points deviated from the X-curve model and were best curve-fitted by the Brooks-Corey model. This tendency may have occurred due to the presence of capillary barriers. The pore structure for sample B had a better packing arrangement than sample A, which may have reduced the pore space and developed flow obstruction. When capillary barriers are present, the small pores are filled with the wetting phase and restrain the flow paths to the non-wetting phase (Huo and Benson, 2016). This observation was validated by the higher pressure drops across the specimen. At 100% nitrogen fractional flow ($Q_g$ = 2.5 mL/min), nitrogen effective permeability was 24% of the absolute permeability.

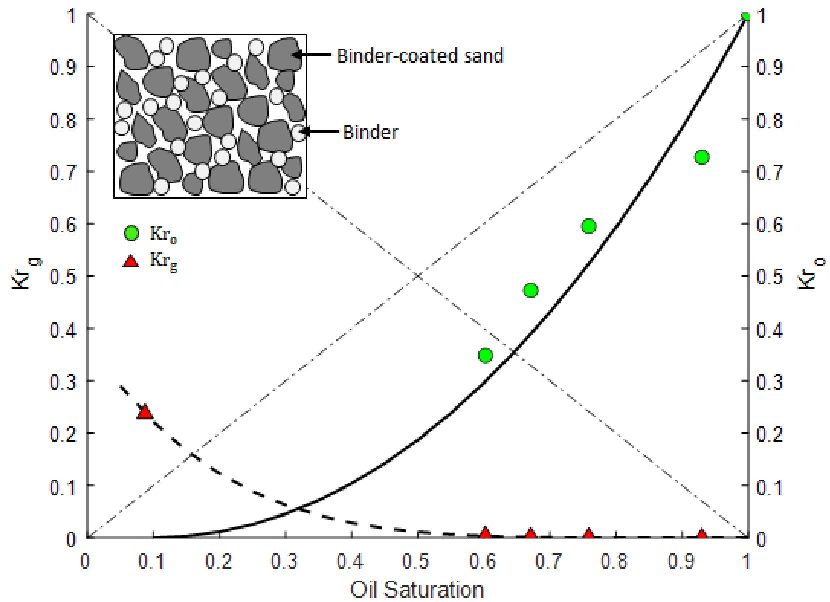


Figure 4.11. Nitrogen-oil relative permeability curves for sandpack B. The pore structure for sample B had a reduced pore space and high flow interference.

The experimental results presented in this section showed similar behavior to previous studies on the effects of stress-dependent drainage relative permeability (McDonald et al., 1991; Huo and Benson, 2016; Haghi et al., 2020). As the pore space was reduced, the wetting phase residual saturation (oil saturation) decreased from 23% to 9%. When the pore space is reduced and the flow conditions remain constant, the viscous pressure gradient increases. If the pressure drop becomes significant, the non-wetting phase flow path widens and invades marginal regions, enhancing the drainage sweep efficiency (Longeron et al., 1994).

### 4.4.2. Case 2. Berea Sandstone

A Berea sandstone specimen was used to determine the performance of the entire Multiphase Triaxial System. The specimen was dried at 60°C for 24 hrs and weighed with a precision scale. Then, the core was saturated with canola oil using a vacuum chamber at -80 kPa. During the oil saturation process, several mass measurements were taken until no further change was observed. At this point, the core specimen was weighed for porosity estimation. The Berea sandstone was prepared for testing and mounted in the triaxial cell. The temperature of the system was increased to 40°C, and the core specimen was saturated using pump circulation at 0.5 mL/min under 500 kPa effective confining stress. The effects of stress and strain on fluid flow were investigated by loading the specimen from 1 MPa to 20 MPa effective stress by increasing the confining stress from 2 to 21 MPa with pore pressure constant at 1 MPa. The isotropic triaxial stress was increased ($\sigma_1 = \sigma_2 = \sigma_3$) using the independent loading circuits, axial and radial, respectively. However, the loading system can be used to apply triaxial compression ($\sigma_1 > \sigma_2 = \sigma_3$) and triaxial extension ($\sigma_1 < \sigma_2 = \sigma_3$) conditions if required. Figure 4.12 shows the accuracy of the stress path followed during testing (black dots). The red line is an isotropic stress path line plotted for reference.

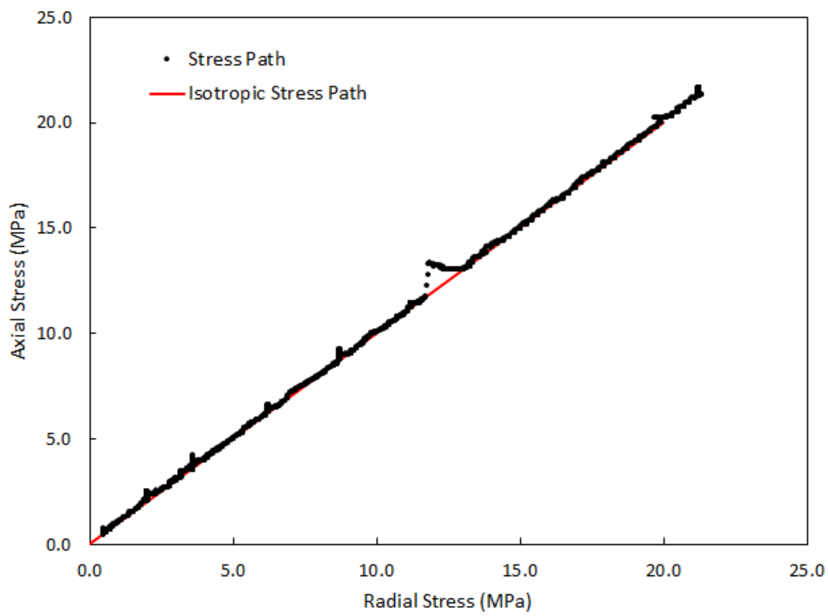


Figure 4.12. Isotropic stress path during loading. The isotropic triaxial stress was increased using the independent axial and radial loading circuits.

During the loading stage, the volumetric deformation was measured in real-time to track the poroelastic response of the rock (Figure 4.13). At various stress levels (every 2.5 MPa increments), the confining stress was maintained constant to allow core flooding measurements. At these levels, inelastic deformation or creep was observed, typically 0.02% over 48 hrs periods. The bulk compressibility was plotted as a function of the effective stress (Figure 4.14) and showed a non-linear reduction with respect to effective stress increase. The behavior is expected because, as porosity decreases, more grains are brought into contact.

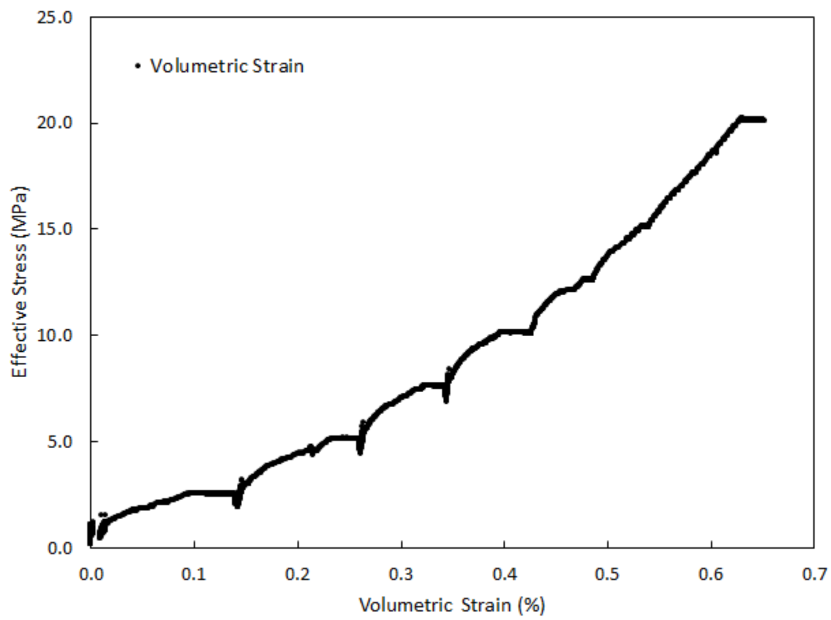


Figure 4.13. Volumetric deformation of the Berea sandstone. At various stress levels, effective stress was maintained constant to evaluate the poroelastic response of the rock.

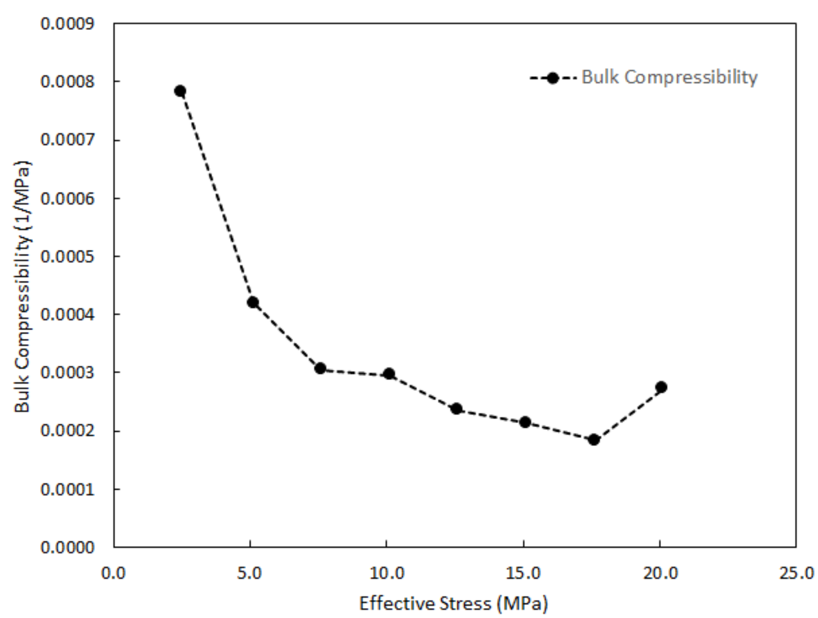


Figure 4.14. Drained bulk compressibility of the Berea sandstone. The curve shows the evolution of the bulk compressibility at different stress levels.

The evolution of the bulk modulus (reciprocal of the drained bulk compressibility) was tracked during the loading stage (Figure 4.15). The variation in the bulk modulus can be attributed to changes in the pore volume. The lower the pore volume, the stiffer the rock becomes, and therefore, the higher the bulk modulus. At the last confining stress, the bulk modulus behaved anomalously and is being explored. However, this effect may be due to grain crushing.

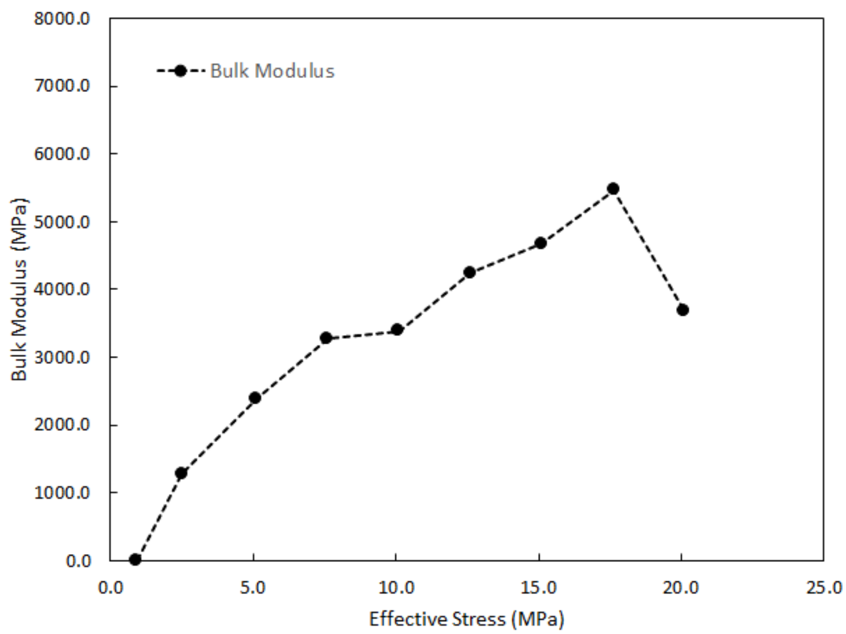


Figure 4.15. Bulk modulus of Berea sandstone during the isotropic confining stress.

During the constant effective stress states, the stress-dependent single-phase flow properties were measured. Figure 4.16 shows the stress-dependent absolute permeability and porosity. The permeability tests were conducted at a constant flow rate of 0.5 mL/min for all effective stress levels. The results showed that permeability decreased from 83.5 mD at 1 MPa of effective stress to 49.7 mD at 20 MPa effective stress, a total reduction of 59%. The total volumetric deformation associated with this range of effective stress was 0.67%.

Porosity was calculated from the real-time volumetric deformation measurements using the initial porosity measurement as the reference. According to previous studies, porosity can be calculated from the volumetric deformation assuming grain compressibility is negligible in comparison to pore compressibility (Haghi et al., 2020). In this test, porosity was reduced from 16.98% to 16.43% over the loading sequence.

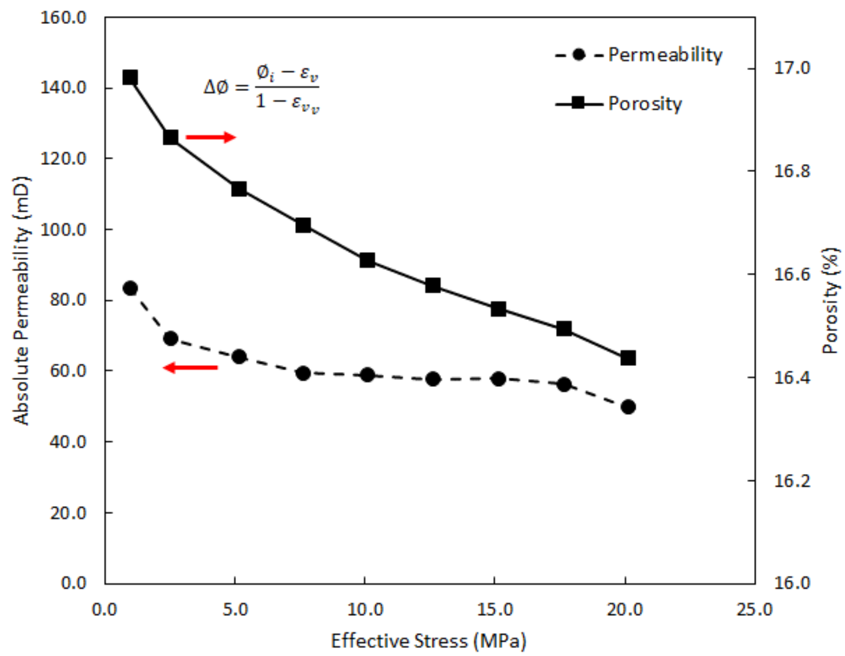


Figure 4.16. Stress-dependent porosity and absolute permeability.

In addition to the single-phase flow measurements, the gas-oil relative permeability was measured for the Berea sandstone. The multiphase flow tests were conducted at 20 MPa effective stress and volumetric deformation of 0.67%, where the same procedure was followed as described for the sand packs. The absolute permeability test was conducted at 2.5 mL/min, then the oil flow rate was decreased to 2 mL/min, and the nitrogen was co-injected at 0.5 mL/min into the specimen. In increments, the flow rate of nitrogen was increased, and the oil flow rate decreased, always maintaining a total flow rate of 2.5 mL/min. Figure 4.17 shows the nitrogen-oil relative permeability curves. The absolute permeability to oil at the initial core flooding test was 72.97 mD. When the nitrogen (non-wetting phase) was injected, the differential pressure across the specimen increased twofold, and the effective permeability to oil decreased to 15.83 mD. At this point, the relative permeability to oil was 21% of the absolute permeability. The sharper decline in the oil relative permeability may be explained by the high interfacial tension (ITF) between the two fluid phases. Previous studies have shown that relative permeability to oil decreased rapidly as ITF increased (Asar and Handy, 1989). The gas phase relative permeability remained very low until residual wetting phase saturations ($kr_g = 0.1$). The effective permeability to gas was corrected for non-continuum flow using the slope of the pressure drop vs the gas flow rate. At the end of the relative permeability test, the residual oil saturation was 61%. Therefore, a relatively small volume of gas in the porous media can dramatically reduce the relative permeability to oil.

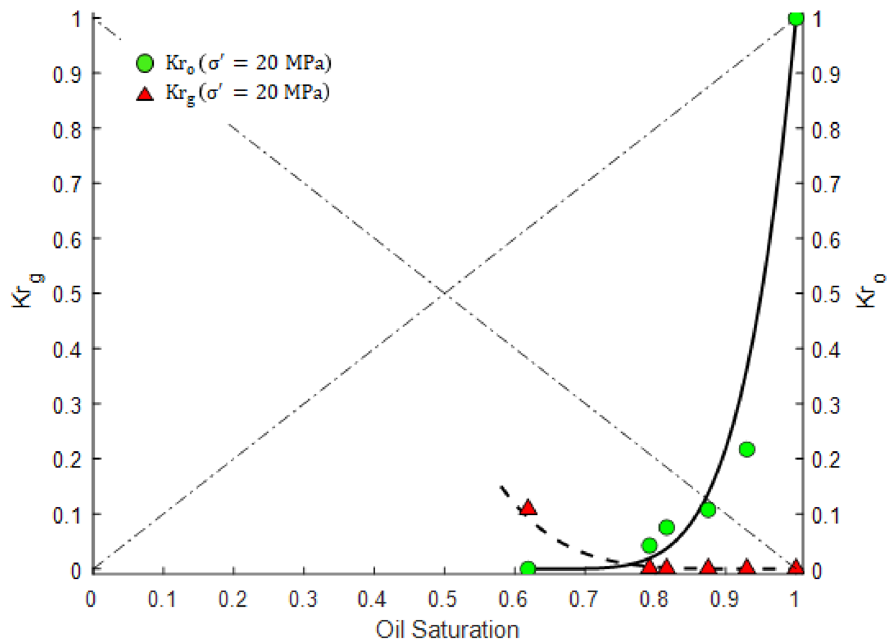


Figure 4.17. Nitrogen-oil relative permeability curves for Berea sandstone.

## 4.5. Conclusion

An integrated laboratory testing facility was developed to investigate the effects of triaxial stress on the governing mechanisms of multiphase fluid flow. The study presented the main components of the system and its performance. The individual components were tested on sandpack and Berea sandstone specimens to study the effect of geomechanics on fluid flow properties. The Deisman triaxial cell 6500 was used to independently apply axial and confining stresses to the specimen, where isotropic triaxial stress, triaxial compression, and triaxial extension conditions can be implemented. The multiphase pore pressure system and phase separation system were accurately tested for the injection of multiple fluids and the measurement of real-time wetting phase saturation. In addition, experimental results for volumetric deformation, bulk compressibility, bulk modulus, absolute permeability, and relative permeability were presented.

# 5. Advancements in 3D-Printed Sandstone Analysis: Exploring Strength, Stiffness, and Densification in Geomechanical Applications[2]

## 5.1. Introduction

Experimental studies play a crucial role in the development of numerous projects in geoscience and engineering. Laboratory testing of geomechanical and transport properties is essential for validating numerical analyses during the project design stage. However, experiments conducted on core samples from reservoir formations typically involve a degree of uncertainty due to the heterogeneous characteristics of rock samples (Hodder et al., 2018). Additionally, core sampling from wellbores, core handling, and laboratory testing procedures can increase uncertainty and introduce inherent property variability. Previous studies have demonstrated that uniaxial compressive strength (UCS) tests for homogeneous rocks may result in standard deviations ranging from 2 to 25 MPa, while those for heterogeneous rocks range from 33 to 53 MPa (Bewick et al., 2015). The UCS test is one of the most commonly used rock engineering parameters for strength determination in geomechanical studies. The broad range of standard deviation values for natural rocks encompasses a variety of failure modes that impact the prediction of the rock's mechanical behavior. To account for the variability in rock properties, the standard deviation is often used to characterize the reliability of the rocks' mechanical properties. For instance, studies focused on the mechanical properties of sedimentary rocks extracted from various depths have found that the standard deviation from UCS tests approximates 24 MPa for Fell sandstones (Bell, 1978). Furthermore, UCS tests conducted on commonly studied sandstones revealed standard deviation values of 9.7 MPa for Berea, 41.1 MPa for Rockwell, and 60.4 MPa for Tuscarora sandstones (Hale and Shakoor, 2003). This broad range of standard deviation values

[2] This chapter is based on research findings that have been published in two articles in the 'Energies' journal:
(1) Sanchez-barra, A.; Zambrano-narvaez, G.; Chalaturnyk, R. An In-Depth Analysis of Strength and Stiffness Variability in 3D-Printed Sandstones : Implications for Geomechanics. energies 2023, 16 (14). https://doi.org/10.3390/en16145406.
(2) Hodder, K. J.; Sanchez-Barra, A. J.; Ishutov, S.; Zambrano-Narvaez, G.; Chalaturnyk, R. J. Increasing Density of 3D-Printed Sandstone through Compaction. energies 2022, 15 (5). https://doi.org/10.3390/en15051813.

highlights the anisotropic nature of natural rocks, which introduces challenges in replicating experimental results and poses questions regarding the feasibility of validating numerical analyses.

Binder-jet additive manufacturing (3D printing) has emerged as a promising technology for characterizing rock properties across diverse engineering fields, such as petroleum and geothermal reservoirs, mining, and underground tunnels (Osinga et al., 2015; Primkulov et al., 2017; Vogler et al., 2017; Ardila et al,. 2018; Gomez et al., 2018; Ziaee and Crane, 2019; Hodder et al., 2020; Santiago et al., 2022). Binder-jet additive manufacturing (BJ-AM) is the process of joining materials to make objects from 3D model data, usually layer upon layer, as opposed to subtractive manufacturing and formative manufacturing methodologies, as defined by ASTM ISO/ASTM52900-15. This technology allows for the creation of 3D-printed proxy models that serve as analogues to natural rock, offering greater control over properties and boundaries during experimental testing. The capability to create analogues of natural porous media with high repeatability, homogeneity, and at low manufacturing costs offers a promising avenue for geosciences and engineering. Considering that natural rocks consist of mineral grains and cement, binder-jet technology provides the ability to manufacture rock analogues using similar components: mineral grains and organic binders. In a binder-jet system, a liquid binder is dispensed onto powder, forming a two-dimensional pattern on a layer. These layers are subsequently stacked to produce a 3D volume. This system can adapt to nearly any powder type with high production rates (Ziaee and Crane, 2019), with material options ranging from sand and polymers to metals and ceramics. Silica sand, in particular, enables an accurate reproduction of porous media, with resolution comparable to natural sandstones. 3D-printed sandstones, which possess physical and chemical properties similar to natural sandstones, serve as excellent models for laboratory experiments and numerical modeling calibration (Vogler et al., 2017; Gomez et al., 2018). Previous studies have investigated the use of 3D-printed sandstones and their implications for geomechanics. Primkulov et al., (2017) demonstrated that 3D-printed sandstones, when cured at an optimal temperature of 80°C, could achieve a consistent UCS of 19.0 MPa. They further provided guidelines on the minimal number of UCS test repetitions required for reliable results. Gomez et al., (2018) explored the utility of 3D-printed sandstones in emulating the behavior of natural rocks, particularly under consolidated drained triaxial tests. Their conclusions indicated that while the 3D-printed analogues closely mirrored the mechanical behavior of natural rocks, they were more compressible and permeable than commonly studied natural reservoirs such as Berea Sandstone.

Perras and Vogler (2019) created 3D-printed sandstone analogues using sand and furan binders. These analogues exhibited mechanical behavior closely resembling that of natural, particularly weak, sandstone in terms of compressive and tensile strength ratios, as well as stiffness. This finding suggests the potential for these 3D-print materials to effectively replicate the behavior of natural rock specimens in geomechanical testing. Song et al., (2020) explored the potential of 3D-printed rocks for simulating geomechanical and transport properties of natural rocks. These 3D-printed rocks, produced using binder jetting and selective laser curing, underwent uniaxial and triaxial compression tests. Their microstructural characteristics were comparable to natural sandstones, although they exhibited higher permeability. Yu et al., (2021) investigated the mechanical properties and crack propagation modes of 3D-printed sandstone under high-temperature conditions. Their study revealed that both mechanical properties and crack propagation modes of 3D-printed sandstone significantly change under such conditions, primarily due to changes in the furan resin. The maximum UCS and splitting tensile strength were achieved at 150°C when the resin transitions from a solid to a liquid state. However, the furan resin's bonding capability and the sandstone's structural integrity deteriorated significantly when heated to 300°C.

Hodder et al., (2022) explored the densification of 3D-printed sandstones. By adjusting printing parameters and using compaction rollers, the authors increased the samples' density by approximately 15% and the UCS by around 65%. Song et al., (2023) examined the heterogeneous mechanical properties of 3D-printed samples made from silica sand, gypsum powder, and coated silica beads, using binder-jetting and selective laser curing technologies. Their findings suggested that the strength of the 3D-printed samples was significantly lower compared to natural rock, resulting in distinct regional fracture bands during failure, and the onset of failure at weak cementing points. The research also reported heterogeneity in mechanical properties due to inconsistent cementing conditions, with measurements of Young's modulus and peak strength showing slight discrepancies from experimental data.

Although 3D-printed materials are generally considered to be homogeneous and isotropic, the physical properties of a single 3D-printed specimen may exhibit variability when compared to other specimens printed from the same batch (Cone et al., 2017; Ardila, 2018). Prior studies have examined the average values of the mechanical properties of 3D-printed sandstones, located randomly within the 3D printing build volume (Osinga et al., 2015; Primkulov et al., 2017; Vogler et al., 2017; Ardila et al,. 2018; Gomez et al., 2018; Hodder et al., 2020; Santiago et al., 2022; Perras and Vogler, 2019; Song et al., 2020; Yu et al., 2021; Hodder et al., 2022; Song et al., 2023). However, the statistical spatial distribution of sandstone strength has not been thoroughly explored.

This chapter introduces a novel methodology to assess the variability of mechanical properties inherent in binder-jet additive manufacturing, with a focus on how the location of samples within the print bed influences the strength of 3D-printed sandstones. Key parameters such as grain size distribution, porosity, binder content, bedding orientation, and sample dimensions were consistently maintained. Additionally, the chapter proposes a densification approach for 3D printing compacted sandstone analogues. This involves an analysis of bimodal sand grain size distributions and the implementation of two distinct compacting rollers in the printing process. The primary aim is to examine the effects of sand size distribution and roller size on porosity, adding mechanical compaction to sand layers after each deposition and exploring its impact on the material properties of the printed sandstones.

## 5.2. 3D Printing and Post-Processing Procedure

The present study utilized binder-jet additive manufacturing to produce the 3D-printed rock samples, created using an M-Flex® 3D-printer (ExOne, North Huntingdon, PA, USA). The experiments were conducted at the GeoPRINT facilities at the University of Alberta. The M-Flex® is a multipurpose tool capable of printing with a variety of materials, including sand, metal, ceramics, and composites. The binder-jetting process involves depositing layers of powder material and selectively applying a liquid binder onto the powder bed to bind the particles together. This process is repeated layer by layer until the part is complete.

To produce the 3D-printed rock samples, silica sand ($D_{50}$ = 175 μm) was mixed with p-toluene sulphonic acid (activator) to coat the sand grains, which were then added to a hopper atop the printer. The hopper deposited the sand onto a vibrating spreader that moved parallel to the job box, spreading a thin layer of 250 μm of silica sand. A roller was used to even out and compact the sand layer, which was then jetted with furfuryl alcohol (binder) by a print-head system moving in accordance with the pre-loaded digital file until the 3D volume was complete (see Figure 5.1).

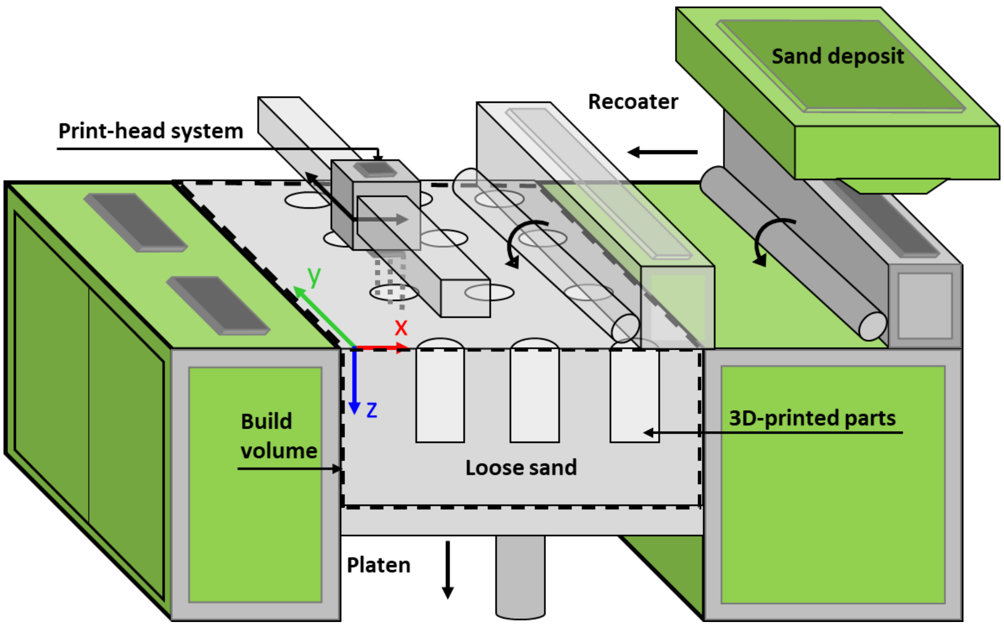


Figure 5.1. Schematic of the M-Flex® 3D-printer illustrating its principal components and the main 3D-printing process.

The binder saturation was fixed at 20% for all samples, a crucial parameter controlling the strength of the sandstones (Primkulov et al., 2017). Binder saturation refers to the volume of binder occupying the pore space. To achieve full strength, the 3D-printed sandstones were thermally cured at 80°C for 24 hours to reduce moisture resulting from the polymerization reaction between the binder and the activator (Hodder et al., 2018). The polymerization is an exothermic reaction that releases energy in the form of heat and creates the bonds or binder necks between the sand particles. Figure 5.2 displays the grain morphology of the 3D-printed sandstone under UV light at high magnification. The binder necks between sand particles are identified by the darker regions, while the porous space appears in areas back-filled with fluorescent epoxy (gradient blue).

Additional information on the 3D-printing process can be found in previous studies (Hodder et al., 2022).

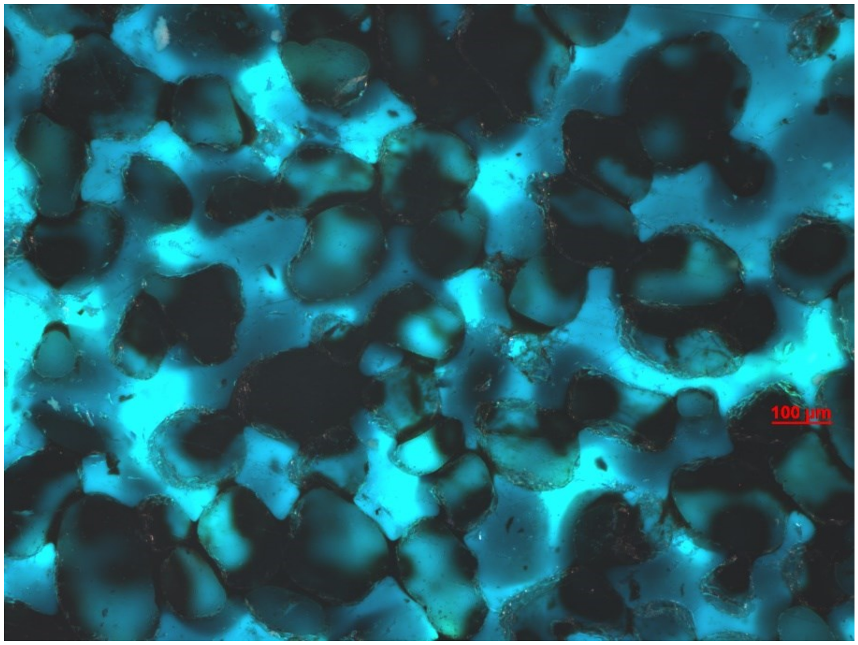


Figure 5.2. High-magnification, optically transmitted bright field image of the grain morphology of the 3D-printed sandstone.

### 5.3. Microstructure of 3D-printed Sandstones

The microstructure of the 3D-printed sandstones was analyzed using the Zeiss Xradia Versa 620 X-Ray Microscope (Zeiss, Oberkochen, BW, Germany) located in the nanoFAB laboratories at the University of Alberta. This advanced imaging system employs X-rays to generate high-resolution images, capable of rendering voxel sizes as small as 50 nanometers. The microscope was employed to investigate the anisotropy of the pore network within the 3D-printed rocks and to understand its potential impact on the rock strength. The specimen analyzed had a diameter of 22.29 mm and a 0.5:1 height-to-diameter ratio. Figure 5.3 illustrates the Micro-CT image of the cross-sectional area of the rock. This image was used to estimate the aspect ratio of the pores and the orientation of the pore network through a Python routine. The microstructure exhibits a degree of anisotropy, as evidenced by an average pore shape that is elliptical, with an aspect ratio predominantly around 1.7. The pore network is oriented in two main directions that reflect the layering during printing. Generally, an aspect ratio close to 1 would denote nearly spherical (or circular in 2D) pores, suggesting greater isotropy. For comparison, the aspect ratio of a carefully selected Berea sandstone ranges between 1.11 and 4.90 and can reach up to 12.7 for other commonly used sandstones (Sui et al., 2020). The porosity was also calculated to be 41.6%. Microstructural analysis is crucial, as the pore structure may undergo changes during the printing process. The 3D-printer can create samples with different pore networks, depending on the compaction effectiveness, thereby influencing the strength of the rocks.

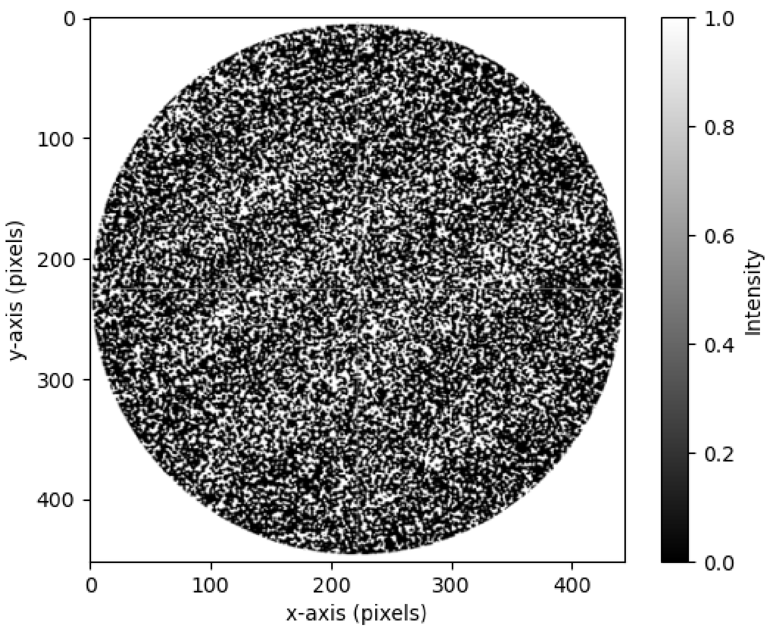


Figure 5.3. Cross-sectional Micro-CT image of a 3D-printed sandstone sample, captured using the Zeiss Xradia Versa 620 X-Ray Microscope, highlighting the internal microstructure and pore network of the sample.

## 5.4. Test Measurements

### 5.4.1. Porosity

Porosity, a critical parameter in reservoir rock studies, represents the proportion of void or pore spaces in a rock or sediment, typically expressed as a percentage of the total volume. This property is crucial for determining a rock's fluid storage capacity. In our study, we measured porosity using helium pycnometry. For this process, we utilized the Quantachrome Pentapyc 5200e instrument (Anton-Parr, Ashland, VA, USA) to measure the solid volume of the specimens, placed in a 10 $cm^3$ cylindrical cell (24 mm × 23 mm). Ultra-high purity helium gas (99.9% pure, Praxair, Danbury, Connecticut, USA) was employed. Knowing the total volume of the samples, we calculated the pore volume by subtracting the solid volume from the measured helium volume. Porosity was then derived by dividing this pore volume by the sample's total volume.

### 5.4.2. Uniaxial Compressive Strength

During compressive testing, the specimen is loaded axially with no radial stress until it fails, at which point the failure value is defined as the uniaxial compressive strength (UCS). Failure in compression occurs when the stresses acting on the rock exceed its compressive strength. The failure of rock in compression is a complex process involving microscopic failures, which manifest as the creation of small tensile cracks that eventually coalesce into a through-going shear plane (Zoback, 2007). In this study, an Instron 400 kN loading system (Instron, Norwood, MA, USA) was used to perform UCS testing on the 3D-printed specimens. The samples were manufactured with a recommended height-to-diameter ratio of 2:1.

The printed samples were preloaded to 0.5 kN to establish contact between the specimen and the loading platens. Subsequently, the 3D-printed sandstones were compressed axially until failure. The loading rate was fixed at 0.25 mm/min, resulting in an average time-to-failure of seven minutes. Strain was measured using an external linear variable differential transformer (LVDT) mounted on two parallel rigid metallic discs. The Young's modulus, $E$, was determined using the slope of the straight-line portion of the stress-strain curve. The average slope was calculated by dividing the change in stress by the change in strain (ASTM D7012-14).

## 5.5. Analysis of Strength and Stiffness Variability in 3D-Printed Sandstones

Natural rocks are highly heterogeneous due to various geological processes that constantly alter their properties. The accumulation, deposition, and cementation of mineral and organic particles continuously modify the spatial characteristics of rock properties. Property variability or anisotropy is commonly observed in most rock types and influences strength, transport, and thermal conductivity behavior. On the other hand, 3D-printed materials are generally considered to be homogeneous and isotropic. However, a single 3D-printed specimen may display variability in its physical properties compared to others printed from the same batch, presenting a significant challenge for laboratory testing. This section proposes a methodology to evaluate the variability and repeatability of mechanical properties of 3D-printed sandstones during binder-jet additive manufacturing.

### 5.5.1. 3D-Printer Repeatability Testing

The experiment aimed to investigate the inherent variability and repeatability during binder-jet additive manufacturing. The laboratory testing program involved manufacturing 3D-printed sandstones uniformly distributed within the build volume of the M-Flex™ 3D-printer. For each specimen, the location inside the printer build volume was marked using x, y, and z coordinates. During the experiment preparation, the STL digital files of the parts to be printed were imported into the 3D-printer software according to the predefined x, y, and z coordinates (see Figure 5.4). The x-y direction represents the coordinates or areas of interest in the powder bed, while the z-direction represents the printed samples in the lower ($z_1$), middle ($z_2$), and upper ($z_3$) sections of the build volume. For each elevation ($z_1$, $z_2$, and $z_3$), a total of 15 specimens were evenly distributed in the x-y direction of the build platform. The layout configuration was printed three times, one above the other, resulting in a total of 45 specimens. Figure 5.4 illustrates the distribution of the 3D-printed samples in the build volume.

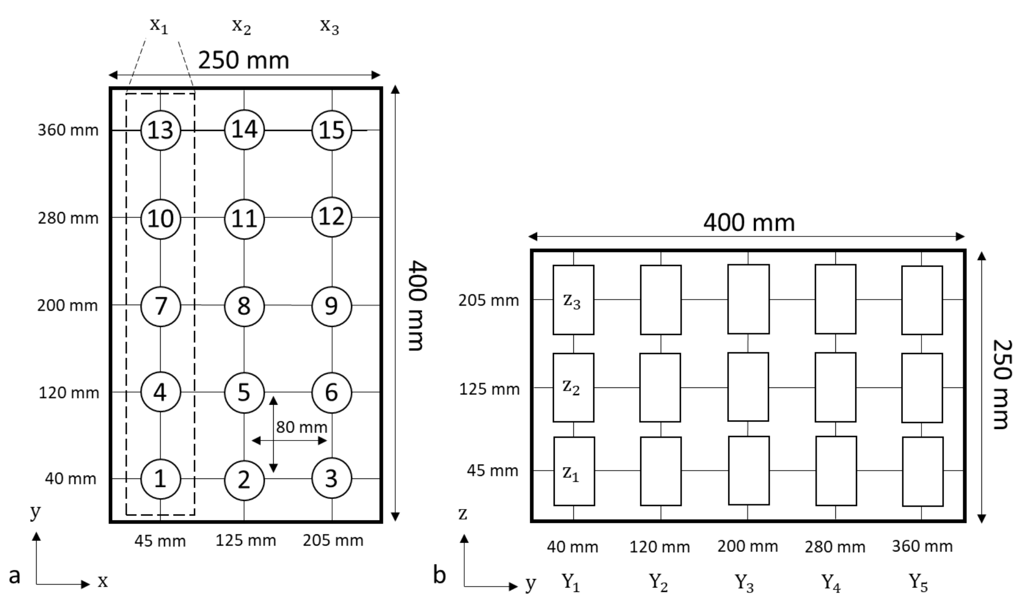


Figure 5.4. Distribution of 3D-printed samples within the M-Flex® 3D-printer build volume. (a) Top view illustrating the sample placement in the x and y axes of the build volume. (b) Lateral view showing the sample positioning along the z-axis.

### 5.5.2. Strength and Stiffness Characteristics

The experiments focused on assessing the mechanical properties (UCS, Young's modulus and bulk density) of samples printed simultaneously and under the same conditions. This workflow clarified the inherent variability during binder-jet additive manufacturing. The quantitative investigation was based on how the mechanical properties diverged from the mean values and how the resulting uncertainty can be reduced.

Mechanical properties of rocks play a crucial role in characterizing rock masses for diverse engineering applications. Generally, natural rocks exhibit variability in their strength and stiffness properties, which is attributable to the natural processes implicated in their formation (Vogler et al., 2018). An example of this is the influence of weak bedding planes, a phenomenon often identified as strength anisotropy (Zoback, 2007). Compared to natural rocks, 3D-printed sandstones are generally more isotropic and homogeneous. However, the existence of property variability among specimens printed in the same batch has been noted, though often overlooked as average values are typically employed for analyses. To quantify this variability during the 3D printing process, measurements of UCS, Young's modulus, and bulk density were collected from a population of 45 3D-printed sandstones produced in a single batch. The 3D-printed sandstones were tested under axial compression without confining stress until they failed. This failure typically occurred in a brittle mode, marked by an abrupt loss of cohesion as the material's compressive strength gave way to shear fracture formation. The predominant failure mode observed in most samples involved two distinct phenomena: the emergence of a cone-shaped structure at one end of the specimen, and axial splitting originating from the apex of this cone. This behavior aligns with the findings reported in previous studies (Osinga et al., 2015; Primkulov et al., 2017; Vogler et al., 2017; Gomez et al., 2018; Hodder et al., 2022).

The experimental results, illustrated in Figure 5.5, highlight significant variation in the strength and stiffness properties of 3D-printed sandstones. The UCS ranged from a minimum of 23 MPa to a maximum of 38 MPa, with an average value of 29 MPa. Young's modulus varied from 1.50 GPa to 4.05 GPa, with an average value of 2.33 GPa. The dry bulk density showed a strong correlation with the UCS results, suggesting non-uniformity in the 3D printer's compaction mechanism across the building volume. A higher bulk density was generally associated with increased strength. The range of results highlights the critical need for improved homogeneity in 3D printing. While 3D-printed sandstones offer numerous advantages, careful control and deeper exploration of the printing process are necessary to reduce variability and optimize these specimens' potential for applications in rock mechanics and engineering.

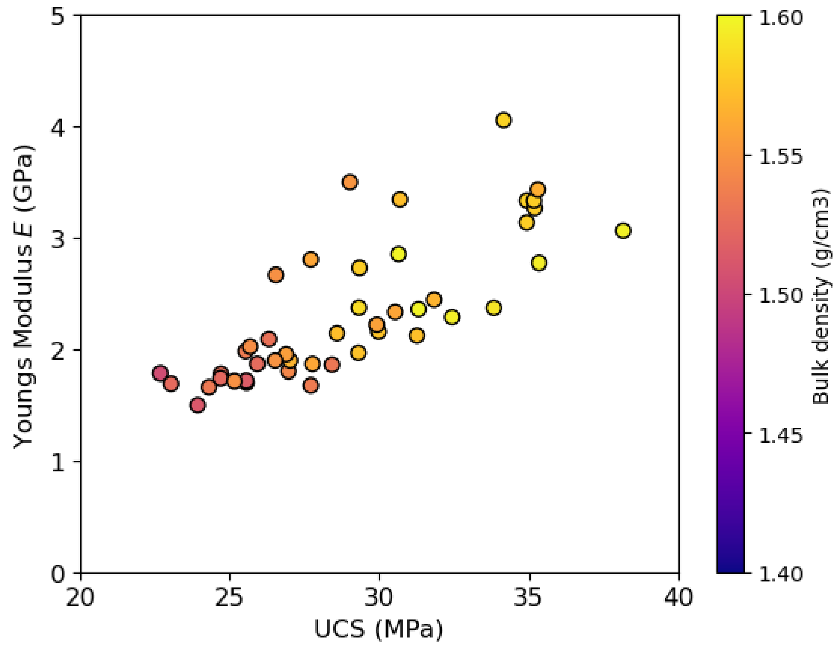


Figure 5.5. Variability of strength and stiffness among 3D-printed sandstones produced in a single batch.

### 5.5.3. Variability of Uniaxial Compressive Strength, Young's Modulus, and Bulk Density

To develop a deeper understanding of the variability observed during 3D printing, the experimental results were divided into distinct groups drawn from the entire population of samples. Figure 5.6 illustrates the mechanical properties of the 3D-printed samples, highlighting their variability across the build platform area, with color intensity representing variation in magnitude. The samples were divided by their level in the build volume (platform elevation, denoted as $z_1$, $z_2$, and $z_3$). Subsequently, each level was discretized to represent the left ($x_1$), center ($x_2$), and right ($x_3$) sections of the powder bed. This categorization enabled the identification of areas where significant changes were observed.

The results indicated that the sandstones printed on the lower elevation of the build box (level $z_1$) exhibited superior mechanical properties (UCS, Young's modulus, and bulk density) compared to the sandstones printed on the higher levels ($z_2$ and $z_3$). Moreover, samples located at $z_1$-$x_2$ (the center of the powder bed on level 1) displayed higher mechanical properties than those in areas $z_1$-$x_1$ and $z_1$-$x_3$ (refer to Figure 5.6). This trend could possibly be due to the higher compaction of the roller in that particular area, which would lead to a reduction in the pore volume of the samples, thereby increasing their bulk density. Interestingly, when the same configuration was replicated on levels $z_2$ and $z_3$, the 3D-printed sandstones exhibited higher mechanical properties on the right side of the powder bed (areas $z_2$-$x_3$ and $z_3$-$x_3$). This pattern could be interpreted as a rightward shift in the roller's compacting force as the platform elevation increased. A similar pattern was observed for Young's modulus values, where samples from level $z_1$ exhibited stiffer properties than those from $z_2$ and $z_3$. The dry density showed a correlation directly proportional to the UCS results, which can be attributed to the fact that the strength of the specimen was determined by the compaction performance during 3D printing. Greater compaction density facilitated superior grain packing arrangements, leading to the generation of stronger specimens.

**Unconfined Compressive Strength (MPa)**

| (MPa) | Z1 X1 | Z1 X2 | Z1 X3 | Z2 X1 | Z2 X2 | Z2 X3 | Z3 X1 | Z3 X2 | Z3 X3 |
|---|---|---|---|---|---|---|---|---|---|
| 40 | 30.65 | 33.83 | 34.16 | 25.57 | 26.32 | 30.54 | 26.55 | 27.72 | 31.27 |
| 35 | 29.98 | 34.94 | 35.31 | 22.69 | 23.94 | 27.72 | 23.05 | 24.32 | 29.04 |
| 30 | 30.70 | 35.18 | 29.36 | 24.72 | 24.71 | 28.43 | 25.70 | 26.52 | 27.78 |
| 25 | 29.34 | 38.16 | 31.32 | 25.55 | 25.94 | 29.93 | 25.17 | 26.89 | 28.60 |
| | 34.94 | 35.35 | 35.20 | 25.58 | 26.97 | 31.84 | 27.02 | 29.32 | 32.45 |

**Young's Modulus (GPa)**

| (GPa) | Z1 X1 | Z1 X2 | Z1 X3 | Z2 X1 | Z2 X2 | Z2 X3 | Z3 X1 | Z3 X2 | Z3 X3 |
|---|---|---|---|---|---|---|---|---|---|
| 4.0 | 2.85 | 2.37 | 4.05 | 1.72 | 2.09 | 2.33 | 2.67 | 2.80 | 2.12 |
| 3.5 | 2.16 | 3.14 | 3.43 | 1.78 | 1.50 | 1.68 | 1.69 | 1.66 | 3.50 |
| 3.0 | 3.34 | 3.33 | 2.73 | 1.78 | 1.74 | 1.86 | 2.02 | 1.90 | 1.87 |
| 2.5 | 2.37 | 3.06 | 2.36 | 1.98 | 1.87 | 2.22 | 1.71 | 1.95 | 2.14 |
| 2.0 | 3.33 | 2.77 | 3.27 | 1.70 | 1.80 | 2.45 | 1.90 | 1.97 | 2.29 |

**Dry Density (g/cm3)**

| (g/cm3) | Z1 X1 | Z1 X2 | Z1 X3 | Z2 X1 | Z2 X2 | Z2 X3 | Z3 X1 | Z3 X2 | Z3 X3 |
|---|---|---|---|---|---|---|---|---|---|
| 1.60 | 1.60 | 1.59 | 1.58 | 1.52 | 1.53 | 1.56 | 1.55 | 1.56 | 1.57 |
| 1.58 | 1.57 | 1.58 | 1.56 | 1.50 | 1.51 | 1.53 | 1.52 | 1.53 | 1.55 |
| 1.55 | 1.57 | 1.58 | 1.58 | 1.53 | 1.52 | 1.53 | 1.55 | 1.55 | 1.56 |
| 1.53 | 1.59 | 1.60 | 1.60 | 1.54 | 1.52 | 1.56 | 1.55 | 1.55 | 1.57 |
| 1.50 | 1.58 | 1.60 | 1.58 | 1.55 | 1.54 | 1.57 | 1.57 | 1.57 | 1.59 |

Figure 5.6. Variability of strength and stiffness among 3D-printed sandstones at different locations in the build volume.

The influence of property variability was further explored using statistical analysis. Frequency distribution, mean, and standard deviation were calculated for the entire set of 3D-printed sandstone samples. The data, depicting the total population of 3D-printed sandstones, yielded a histogram indicative of a normal distribution (Figure 5.7a). The mean and standard deviations of the UCS values were computed to be 29.11 MPa and 3.85 MPa, respectively. When dividing the complete population of 3D-printed sandstones into smaller subgroups, a significant decrease in variability (as quantified by the standard deviation) was observed. The sample groups representing the elevation of the build platform ($z_1$, $z_2$, and $z_3$) exhibited narrower normal distributions (delineated by dashed lines) than the total population, with standard deviations of 2.65 MPa, 2.47 MPa, and 2.40 MPa, respectively (refer to Figure 5.7). Further division of these samples, based on each elevation into smaller groups located in the left, center, and right sections of the printing area (e.g., $z_1$-$x_{123}$, $z_2$-$x_{123}$, $z_3$-$x_{123}$), resulted in an additional decrease in standard deviation. Figures 5.7b, 5.7c, and 5.7d illustrate the normal distribution of UCS values for the lower, middle, and upper elevations of the build platform, respectively. For the lower and middle elevations of the build platform, the center of the powder bed had minimal property variability. Conversely, the higher elevation showed reduced variability on the left side of the powder bed ($z_3$-$x_1$). Overall, the optimal location for minimizing property variability is at the center of the powder bed at the middle elevation ($z_2$-$x_2$). These graphs expose changes in the compacting performance of the M-Flex® 3D-printer as the building platform transitioned along the z-axis.

For samples printed at the lower elevation of the printer build volume ($z_1$), the highest strength specimens were observed in the center of the platform (e.g., sample $z_1$-$x_2$ (green curve)), where compaction reached its maximum (Figure 5.7b). As the platform's elevation increased to $z_2$ and $z_3$, the samples on the right section of the powder bed exhibited higher compaction (e.g., samples $z_2$-$x_3$ and $z_3$-$x_3$ (blue curves)). The alteration in compaction might result in samples with different pore networks or aspect ratios, potentially affecting the flow properties of the rock. As such, it underscores the necessity of acknowledging and adjusting for these variations when utilizing 3D-printed sandstones in reservoir geomechanical studies, as these differences can have significant implications for both predictive modeling and empirical data analysis.

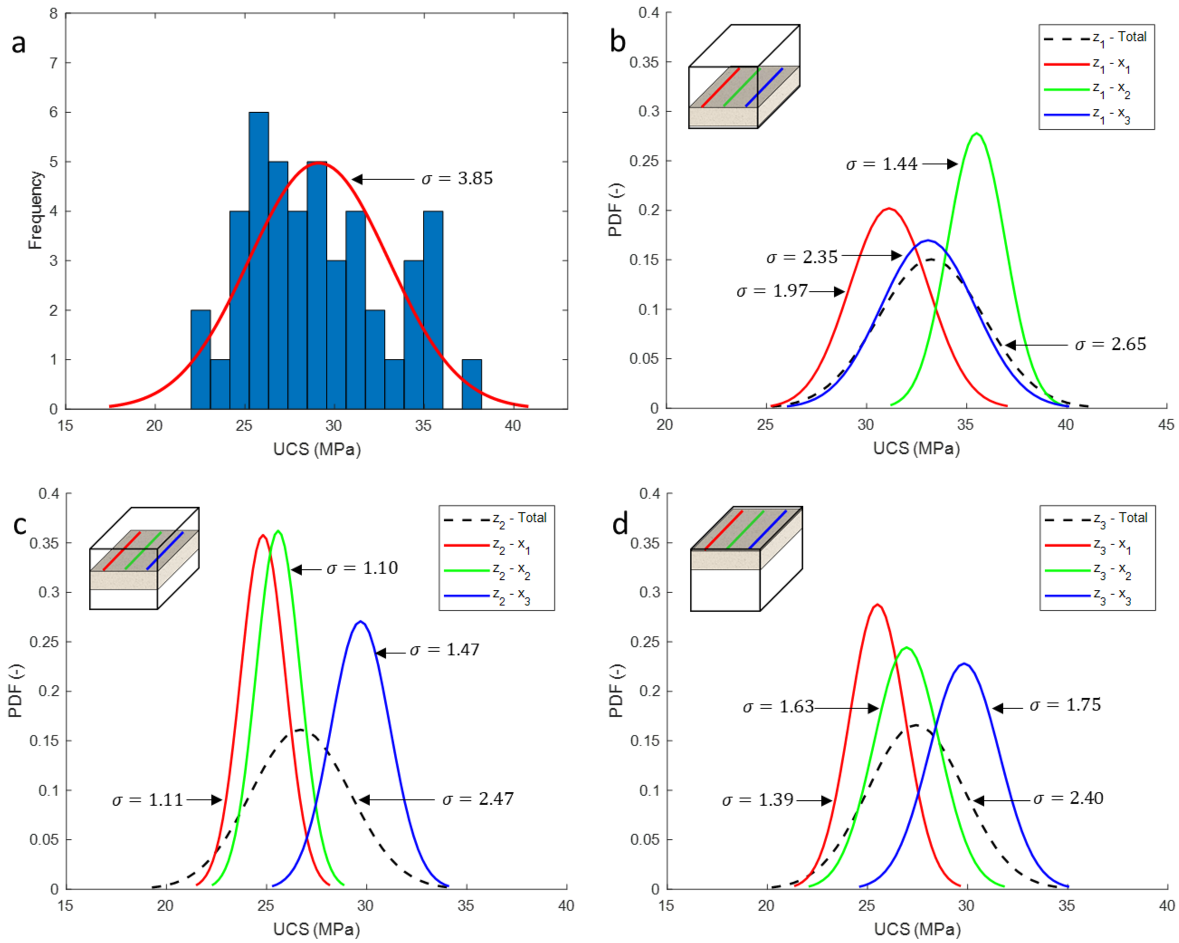


Figure 5.7. Distribution and variability of UCS in 3D-printed sandstones: (a) illustrates the normal distribution of the total population, (b) displays the normal distribution at the lower elevation ($z_1$), emphasizing maximum compaction in the platform's center ($z_1$-$x_2$), (c) portrays the normal distribution at the middle elevation ($z_2$), where samples exhibited reduced variability, and (d) presents the normal distribution at the higher elevation ($z_3$), both (c) and (d) highlight enhanced compaction in the right section of the powder bed.

Figure 5.8 illustrates the normal distribution of Young's modulus values for each group of 3D-printed sandstone samples. The displayed graphs exhibit a clear pattern. The modulus values of the samples from the lower elevation ($z_1$) were noticeably higher than those from levels $z_2$ and $z_3$. Notably, the stiffest specimens were consistently located in the right section of the powder bed across all three elevations ($z_1$, $z_2$, and $z_3$). The observed trends in Young's modulus across the build platform are significant as they suggest that the printing process may result in spatial variability in material stiffness. This could have implications for the design and use of 3D-printed sandstone structures, as different regions of the build platform may produce parts with different mechanical properties.

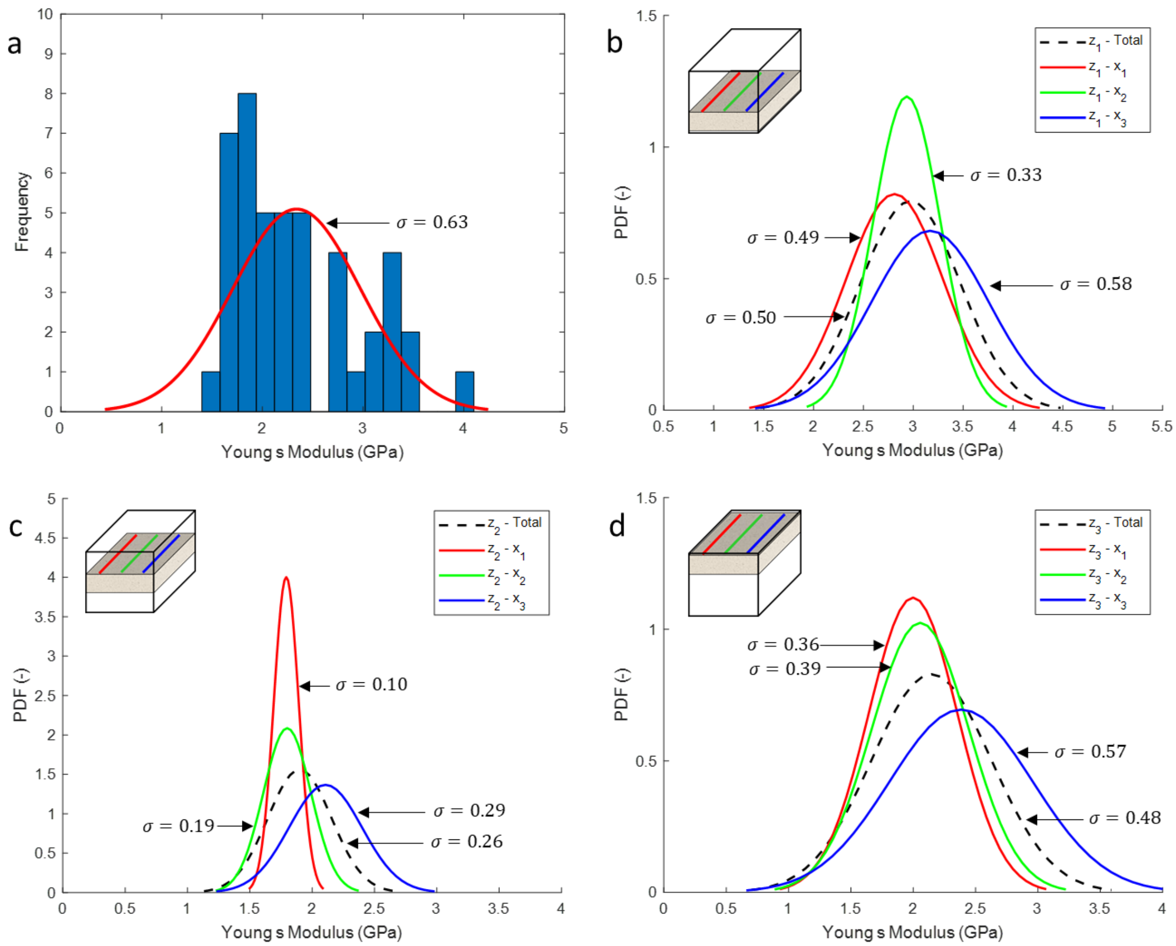


Figure 5.8. Distribution and variability of Young's modulus in 3D-printed sandstones: (a) normal distribution for the total population, (b) normal distribution at lower elevation ($z_1$), (c) normal distribution at middle elevation ($z_2$), and (d) normal distribution at higher elevation ($z_3$).

### 5.6. Densification Approach during the 3D-Printing Process

This section introduces a densification approach designed for 3D-printed compacted sandstones. The approach involves analyzing bimodal sand grain size distributions, utilizing mixtures of both coarse and fine silica grains. Specifically, the mixtures consist of grains with median diameters ($D_{50}$) of 175 μm and 105 μm, respectively. Moreover, we integrate two distinct compacting rollers into the 3D-printing process. The objective is to apply mechanical compaction to the sand layers after each sand deposition. We specifically examine the relationships between sand size distribution and roller size and investigate how they influence changes in porosity in each grain mixture.

### 5.6.1. Sand Mixtures

Silica sand was used as the printing media (Figure 5.9), with different blends of fine ($D_{50}$ = 105 μm) and coarse grains ($D_{50}$ = 175 μm). The $D_{50}$ was determined via sieving for both grain sizes. The fine sand was purchased from Badger Mining, (Badger Mining, Berlin, WI, USA), while the coarse sand was purchased from ExOne, (ExOne, North Huntingdon, PA, USA), which is the standard sand used with the printer. Both sands were composed of ~99% quartz silica, according to vendor datasheets. The coarse sand was whole-grained, which ensured greater flowability compared to highly angular grains, and had a unimodal and narrow size distribution (Figure 5.9). The fine sand had the smallest diameter that was commercially available in whole grain form. To achieve smaller grain sizes, the sand grains need to be crushed, which results in angular grains. Angular grains have poor flowability and are not suitable for 3D printing. High flowability is required so that the sand can be fluidized by the recoater through vibration and deposited efficiently on the sand bed. In order to quantify the effect of different diameters of sand grains, several mixtures are selected (Table 5.1). The ratios of sand percentages are defined by weight fraction.

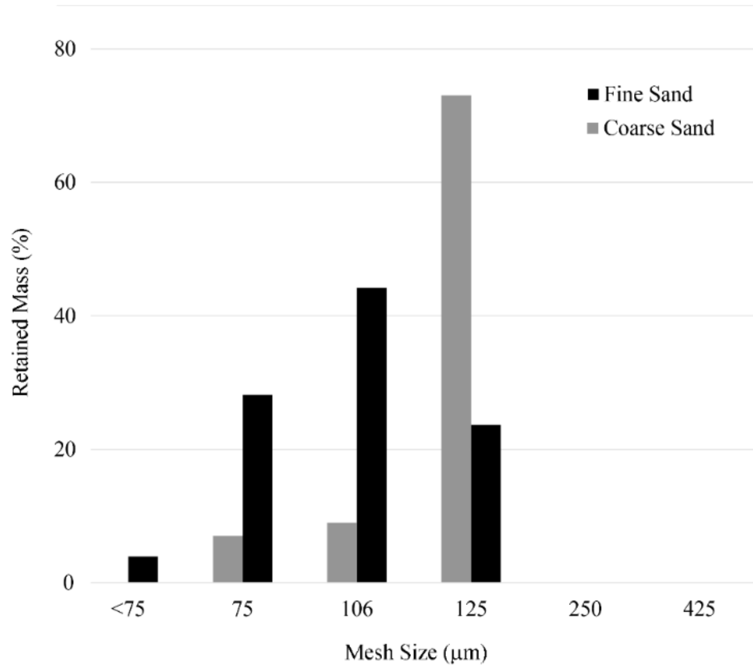


Figure 5.9. Size distributions (retained mass) of the fine and coarse sands used to create the samples in this study.

Table 5.1. Grades of sand mixtures used to 3D-print specimens. Percentage indicates total weight of fine (F) or coarse (C) sand within the blend.

| **Sand Mixture** | **Coarse Sand (wt.)** ($D_{50}$ = 175 µm) | **Fine Sand (wt.)** ($D_{50}$ = 105 µm) |
|---|---|---|
| 100C | 100% | 0% |
| 75C/25F | 75% | 25% |
| 50C/50F | 50% | 50% |
| 25C/75F | 25% | 75% |
| 100F | 0% | 100% |

### 5.6.2. Porosity and Density Analysis

Helium pycnometry is a widely used method in geoscience for estimating porosity and the apparent density of the solid phase. This technique is advantageous as it allows for obtaining measurements regardless of the specimen's heterogeneity (Andreola et al., 2000). On the other hand, one of the strengths of 3D-printed samples is their ability to be fabricated with a high degree of homogeneity and repeatability (Gomez et al., 2017; Hodder et al., 2018). This enables the application of a simplified approach to achieve an accurate approximation of porosity. By incorporating the density of water, the specific gravity of solid grains, and the void ratio in the calculations (Das and Sobhan, 2014), the dry density can be determined using the following equation:

$$\rho_d = \frac{G_s \rho_w}{1 + e}, \tag{5.1}$$

where $\rho_d$ is the dry density of the rock, $\rho_w$ is the density of water, $G_s$ is the specific gravity of solid grains (2.65 for silica), and $e$ is the void ratio, the volume of voids to the volume of solids. Considering that the 3D-printed samples need to pass through a heated curing process to achieve a full strength, the finished specimens are completely dry. This allows for the calculation of dry density by weighing and measuring the samples. Thus, Equation 5.1 can be arranged to estimate the void ratio (Equation 5.2).

$$e = \frac{G_s \rho_w}{\rho_d} - 1. \tag{5.2}$$

Finally, the ratio of the volume of voids to the total volume of the specimen (porosity, $\emptyset$) can be calculated using Equation 5.3:

$$\emptyset = \frac{e}{1 + e}. \tag{5.3}$$

To verify the validity of the previous approach, a comparison of the helium porosity and the porosity calculated by Equation 5.3 is presented in Table 5.2. The results show a porosity difference ranging from 0.25% to 1.63% for the samples manufactured with the small roller, and 0.1% to 3.3% for the samples printed with the large roller. The approximation of results between the two methods validates the use of this simple approach to porosity determination.

Table 5.2. Porosity and dry density calculations for sandstones printed with a bimodal distribution of sand.

| Sand Mixture | Porosity (%)—He | Porosity (%)—C (Equation 5.3) | Dry Density (g/cm$^3$) |
|---|---|---|---|
| | | **Small Roller (29 mm)** | |
| 100%C | 44.40 | 44.15 | 1.48 |
| 75%C/25%F | 47.30 | 45.67 | 1.44 |
| 50%C/50%F | 48.41 | 46.99 | 1.40 |
| 25%C/75%F | 49.10 | 48.67 | 1.36 |
| 100%F | 51.09 | 49.93 | 1.33 |
| | | **Large roller (48 mm)** | |
| 100%C | 40.23 | 40.13 | 1.59 |
| 75%C/25%F | 41.33 | 44.71 | 1.47 |
| 50%C/50%F | 42.34 | 43.20 | 1.51 |
| 25%C/75%F | 41.11 | 42.71 | 1.52 |
| 100%F | 45.36 | 46.27 | 1.42 |

To increase the packing density of the grains, the sand distribution needs to go beyond the unimodal packing limit into a bimodal distribution, allowing for fine grains to be placed into the pore space between larger grains (Ziaee and Crane, 2019). The effect of a bimodal distribution of sand and compaction on the porosity and density is observed graphically in Figure 5.10, where porosity and dry density calculations are carried out using the helium pycnometry measurements and Equation 5.3. The 3D-printed sandstones fabricated with a higher volume of fine grains show higher porosities and lower densities. Between the two compacting rollers, the larger roller is more effective for reducing porosity during printing (Figure 5.10). It is suggested that the larger mass and radius of curvature for the large roller produce greater compaction by applying more pressure towards the sand layers during 3D printing.

In terms of sand grade distributions, as fine grains are introduced, porosity begins to increase. It is suggested that the grain packing is not efficient, since the fine sand ($D_{50}$ = 105 μm) has a unimodal grain size distribution. On the contrary, the coarse sand itself has a broader distribution, meaning that the diameter ratio between the smallest and largest grain is increased, which provides denser packing. This suggestion is in line with random packing theory; when the diameter ratio between the grains increases, the density increases (Bertei and Nicolella, 2011). Therefore, a higher ratio between the smallest and the largest grains in the mixture should result in a more heterogeneous distribution of grains within the pore space. This phenomenon is similar to grain sorting in natural materials, where moderately or poorly sorted rocks contain a higher portion of fine-to-coarse grains, and can result in lower porosity (Friedman, 1964; Nelson, 1994).

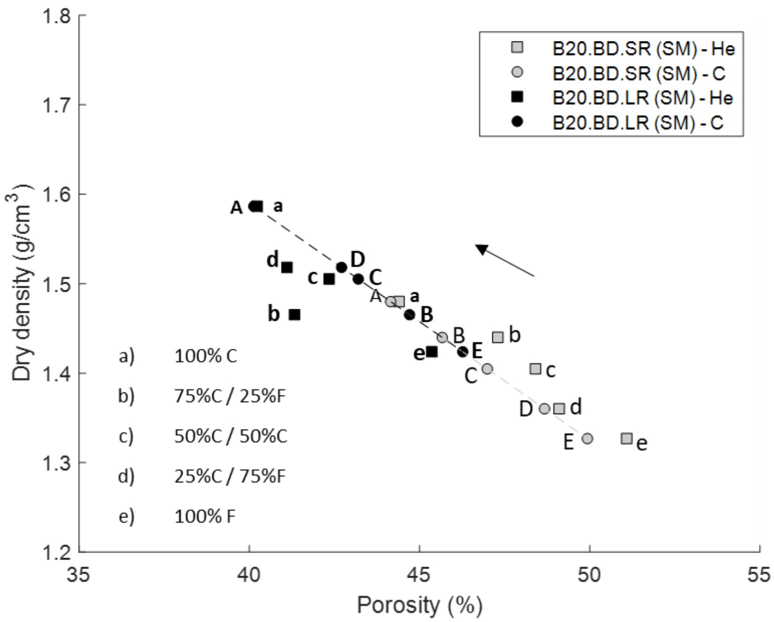


Figure 5.10. Effect of the bimodal distribution of sand and compacting rollers in the porosity–density relationship of 3D-printed sandstones. Letters a, b, c, d, and e represent grade sand distributions 100%C, 75%C/25%F, 50%C/50%F, 25%C/75%F, and 100%F, respectively. The lowercase letters correspond to the helium measurements, while the capital letters represent the calculations by Equation 5.3. The correlation coefficient of the linear trend covering all data points shows an $R^2$ value of 0.9.

### 5.6.3. Unaxial Compressive Strength

A bimodal distribution of sand grains resulted in a strength reduction of the 3D-printed sandstone that was proportional to the weight fraction of fine sand grains. Additionally, it was observed that the samples fabricated using the small roller experienced a decrease of 15% in strength for each 25% increment of finer grain weight fraction (Figure 5.11). The previous behavior was less pronounced when using the larger, 48 mm diameter roller. It is suggested that the larger radius and weight of the roller provides greater compaction, which combats the detrimental effect of fine grains in the sand mixture. Across almost all sand blends, the larger diameter roller achieved more compaction and increased the strength of the 3D-printed sandstones. It is unclear at this time why the 100% coarse sand blend specimens (control) are the only samples to see a decrease in strength from the larger roller.

The decrease in UCS with an increase in the volume of fine sand was not expected, as the increased packing density (from small grains filling the larger pores) was expected to create a stronger specimen. Upon investigation it was found that for a grain mixture to benefit from a bimodal distribution, the fine-grained grains must have been at least seven times smaller than the coarser grains (Gregorski, 1996). Since a grain size of ~25 µm would be needed, the optimum grain packing is not achievable for 3D printing, as the fine powder would be airborne and have poor flowability. Thus, compaction is limited to the type of roller used, where it is shown that the larger diameter roller produces higher compaction, leading to a greater strength.

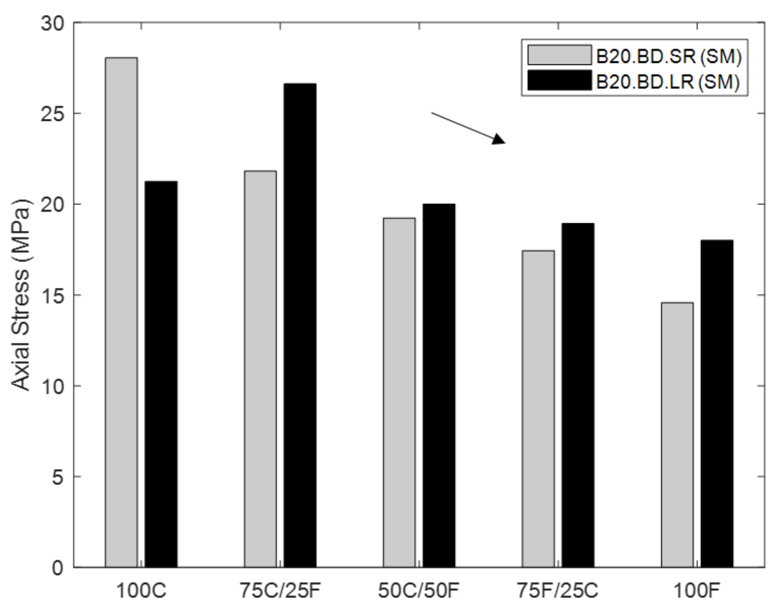


Figure 5.11. Effect of the bimodal distribution of sand and compacting rollers in the strength of 3D-printed sandstones. Gray bars show the peak UCS of samples 3D-printed with the smaller (29 mm) roller, while black bars represent samples 3D-printed with the larger (48 mm) roller.

### 5.6.4. Strength and Stiffness Characteristics

The diverse configurations of grain structures led to distinct mechanical responses. There is a direct correlation between pore space, density, and the specimen's strength, which resulted in observed variations in UCS. There was an increase in UCS when transitioning from the small to the large roller, as well as an increase in Young's modulus, respectively. The UCS of the large roller resulted in a similar deviation with regard to UCS of the smaller roller, but a much larger deviation with regard to Young's modulus (Figure 5.12). The increase in UCS from the larger roller is suggested to be caused by the additional packing caused by the larger radius of the curvature. However, the distribution of Young's modulus with a larger roller is much more variable. It is suggested that the larger surface area of the roller may cause additional perturbations during printing that are unaccounted for. The results also showed that the mechanical properties differed for samples printed in different locations of the powder bed. Figure 5.13 shows the measurements for 15 specimens evenly distributed in the powder bed. The value in each cell represents the mechanical properties of one specimen. This behavior was observed with both rollers, which implies that compaction was not even across the printing area, regardless of the roller used. Ultimately, the large roller has shown better performance in the densification of 3D-printed sandstone (Figure 5.13). The large roller achieved better compaction in the powder bed and created a smaller difference between the physical properties of the printed samples.

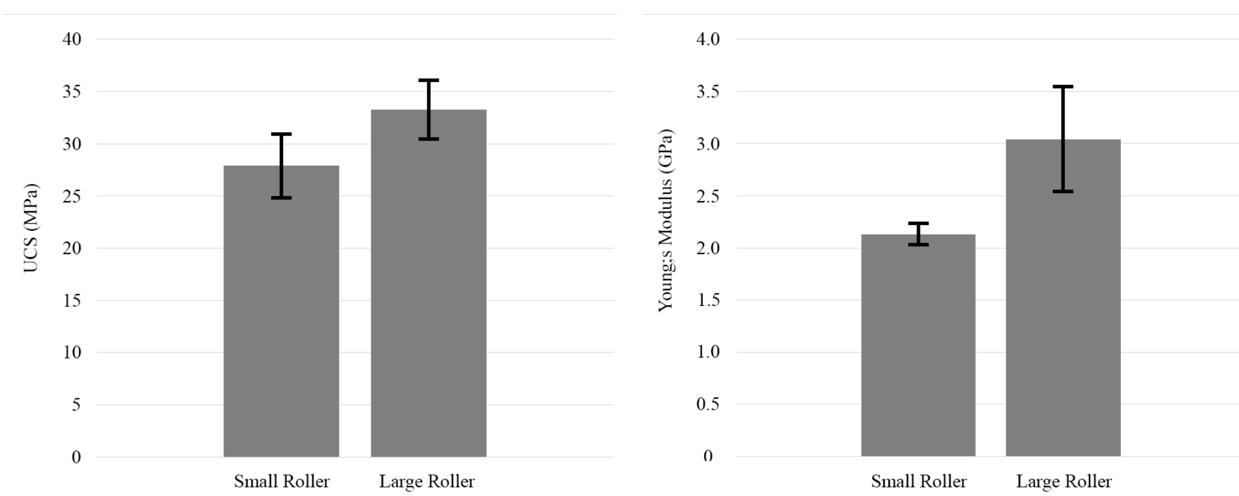


Figure 5.12. (a) Uniaxial compressive strength (UCS) and (b) Young's modulus values of the small and large roller, respectively.

a

**Small roller (29 mm)**

| (MPa) | Compressive strength (MPa) | | | Young's Modulus (GPa) | | | (GPa) |
|---|---|---|---|---|---|---|---|
| 40 | 27.86 | 31.74 | 28.93 | 2.10 | 2.28 | 2.17 | 4 |
| 35 | 23.42 | 32.19 | 29.38 | 2.01 | 2.23 | 2.12 | 3.5 |
| 30 | 22.65 | 31.27 | 29.33 | 1.92 | 2.26 | 2.08 | 3 |
| 25 | 23.86 | 29.33 | 25.35 | 2.11 | 2.17 | 1.97 | 2.5 |
| | 25.04 | 30.08 | 27.73 | 2.14 | 2.28 | 2.14 | 2 |

b

**Large roller (48 mm)**

| (MPa) | Compressive strength (MPa) | | | Young's Modulus (GPa) | | | (GPa) |
|---|---|---|---|---|---|---|---|
| 40 | 30.65 | 33.83 | 34.16 | 2.85 | 2.37 | 4.05 | 4 |
| 35 | 29.98 | 34.94 | 35.31 | 2.16 | 3.14 | 3.43 | 3.5 |
| 30 | 30.70 | 35.18 | 29.36 | 3.34 | 3.33 | 2.73 | 3 |
| 25 | 29.34 | 38.16 | 31.32 | 2.37 | 3.06 | 2.36 | 2.5 |
| | 34.94 | 35.35 | 35.20 | 3.33 | 2.77 | 3.27 | 2 |

Figure 5.13. (a) Effect of placement of 3D-printed samples on the compressive strength and Young's modulus for the smaller roller and (b) large roller, respectively. The tables represent a normal view of the powder bed, where increased properties can be observed in the middle column of the powder bed.

The effect of a higher fraction of fine grains in the size distribution resulted in a decrease in strength, a decrease in density, and an increase in porosity. This is in contrast to what the previous literature suggests, where higher packing density and strength are achieved when the fraction volume of fine grains is increased (Bertei and Nicolella, 2011). However, the sand mixture of coarse and fine grains is sub-optimum, as the grain size ratio between the largest and smallest grains is only 1.5. A recommended ratio of 7 was unobtainable with the current equipment, as it would require a fine grain sand size of approximately 25 μm, which would not be possible with the current parameters of the sand printer (Gregorski, 1996).

The analysis of compacting rollers revealed that the large roller resulted in a higher strength and increased densification, mostly in the middle of the powder bed, where compaction was at its maximum. For example, attempts to reproduce 3D-printed sandstone have reported values of ~20 MPa, which results in an increase of ~65% for this study (Primkulov et al., 2017). Figures 5.14 and 5.15 show the results from the effect of a bimodal distribution of sand and compacting rollers in the 3D printing process. In addition, the results of how properties varied depending on the location of the powder bed are presented. The geomechanical and transport properties tend to improve when the large roller and coarse sand are used during printing. The data points inside the red areas in Figures 5.14 and 5.15 show the properties for samples with higher compaction. This group of printed sandstones achieved better results in terms of reservoir-like properties. Previous experimental tests from samples manufactured with 10% binder saturation and no roller were included. The contrast between samples 3D-printed with standard parameters and samples printed with this workflow supports the densification approach.

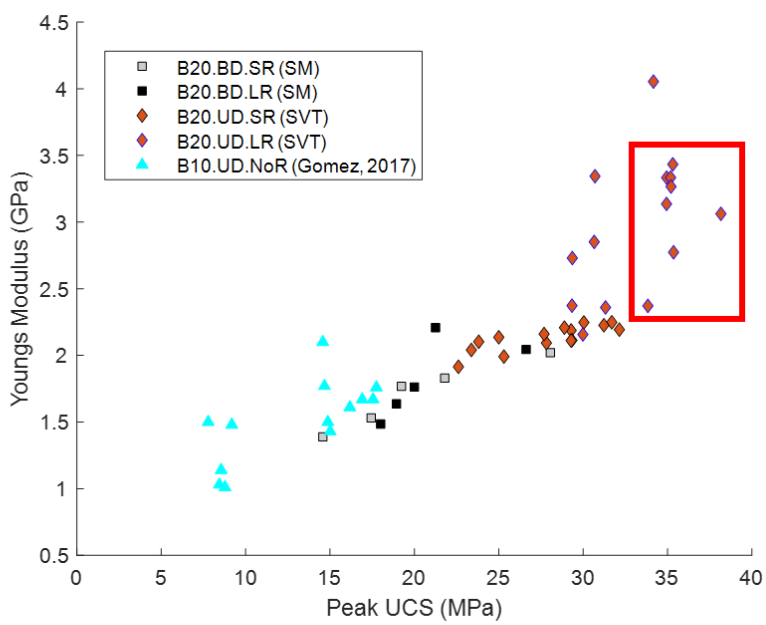


Figure 5.14. Effect of a bimodal distribution of sand and compacting rollers on the geomechanical properties of the 3D-printed sandstones. The legend described the test code for each experiment. B represents the amount of binder used during 3D printing (10 or 20%). UD and BD denote the unimodal or bimodal grain size distribution used during the sand mixing (SM) process. SVT represents the strength variability tests. All tests were conducted using the small and large rollers, SR and LR, respectively.

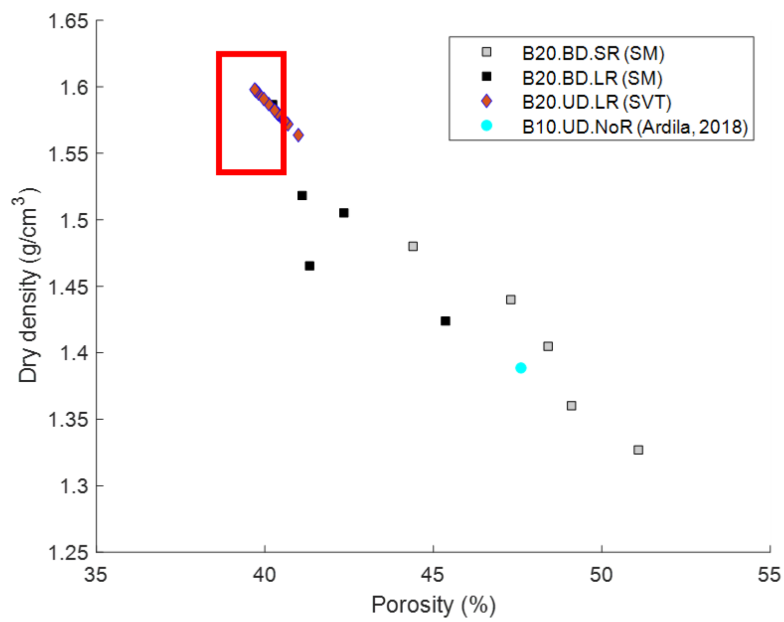


Figure 5.15. Effect of a bimodal distribution of sand and compacting rollers on the transport properties of the 3D-printed sandstones.

### 5.6.5. Morphological and Microstructural Analysis

Scanning electron microscopy (SEM) was used to observe the grain arrangement of the 3D-printed sandstone. Figure 5.16 contains a collage of SEM images collected across the samples at 75X magnification using backscatter detection. There is a clear distinction between the microstructure of the specimens fabricated with the smaller roller versus the larger roller, where the number of large pores decreases. A better grain arrangement and packing are observed with the 100% coarse sand ($D_{50}$ = 175 µm) and the larger roller. It is suggested that the extra compaction decreased the pore space of the 3D-printed sandstones, thus increasing density. Figure 5.17 is an image captured via optical microscopy and ultra-violet light, where the polished grains are translucent and the binder (dark) is opaque. Figure 5.17 allows for the identification of the binder necks between grains, which also contributes to reducing porosity. It was observed during SEM that the finer grains promoted the grouping of the binder in discrete areas, most likely due to the surface tension and capillary actions of a higher surface area (Figure 5.18). These areas of binder accumulation were observed throughout the specimen, which may have resulted in the reduced performance of compressive strength since the binder was not spread uniformly throughout the sample.

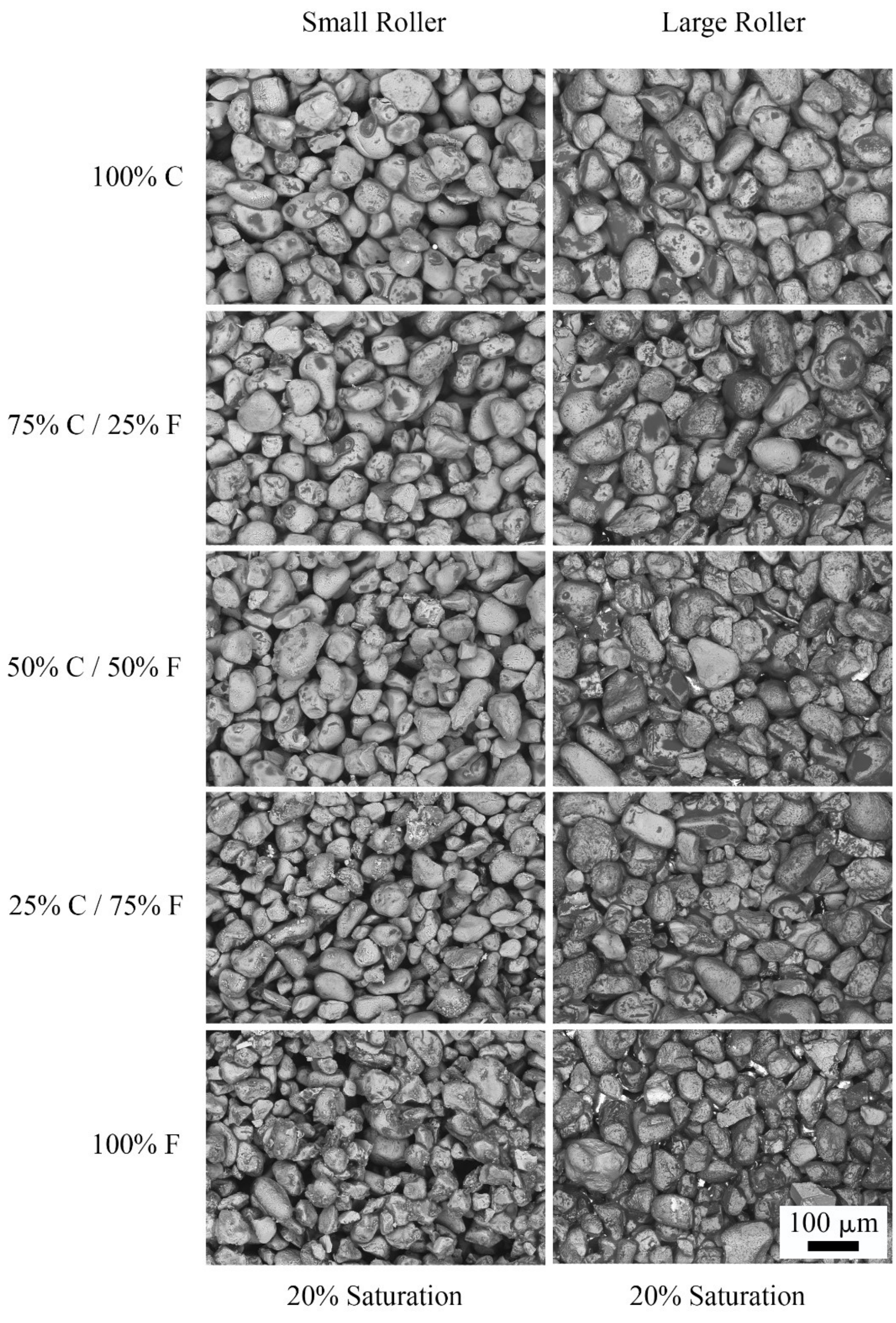


Figure 5.16. Scanning electron microscopy images of 3D-printed sandstone using the small roller (a) and large roller (b). Better packing and higher density are achieved with the large roller and 100% coarse sand.

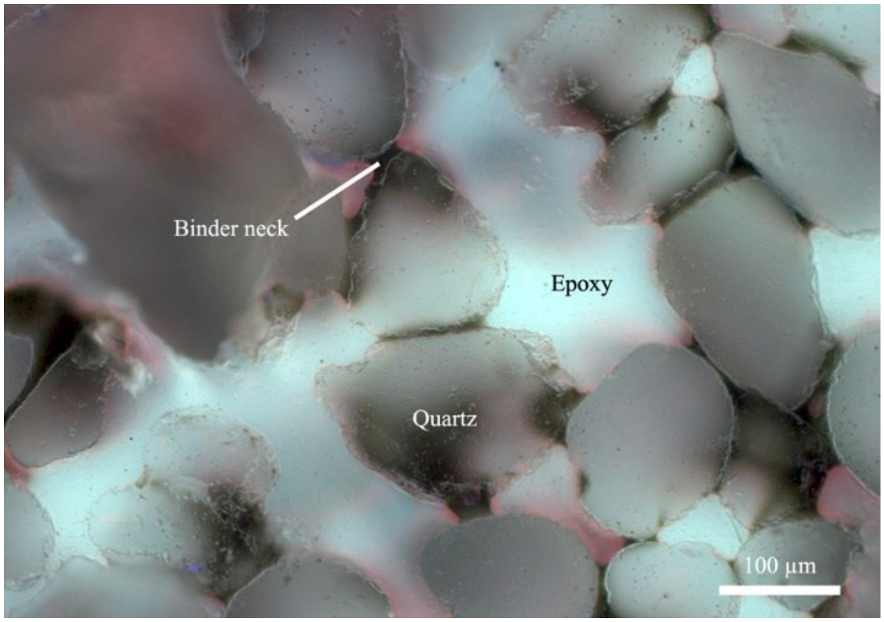


Figure 5.17. Optical microscopy image captured under ultra-violet light, highlighting the binder necks between sand grains. These binder necks contribute to reducing porosity and enhancing the strength of the 3D-printed specimens (from Hodder et al., 2018).

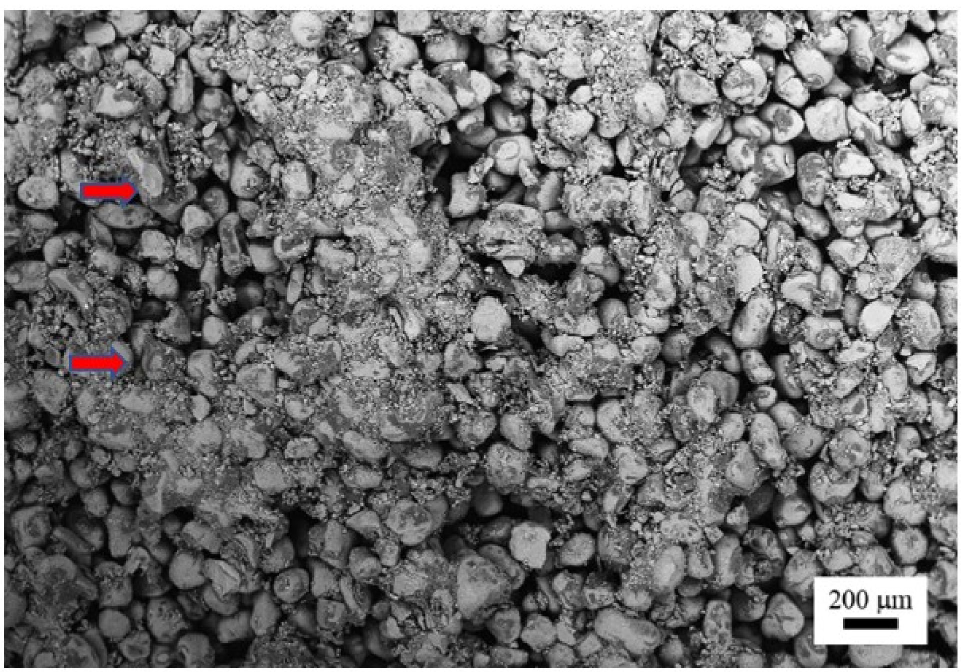


Figure 5.18. Scanning electron microscopy image illustrating finer grains leading to binder accumulation at discrete locations (indicated by red arrows). The constant volume fraction of binder throughout specimen production means that localized binder concentration can decrease the compressive strength of the samples.

## 5.7. Conclusion

This study provides a comprehensive analysis of the inherent variability in mechanical properties of 3D-printed sandstones and the effectiveness of a densification approach in the 3D printing process. Our findings indicate that while individual 3D-printed sandstones exhibit isotropy and homogeneity, there is notable variability among specimens from the same batch. This variability is mitigated by segregating the samples based on their specific locations within the build platform and further within the powder bed. Strength and stiffness properties are influenced by the positioning, with samples printed at lower elevations and centrally in the powder bed demonstrating superior mechanical characteristics.

Additionally, the study explores the impact of varying sand grain size distributions and different compacting rollers on the physical properties of 3D-printed sandstones. The introduction of a bimodal sand distribution, especially with a higher fraction of fine grains, resulted in decreased strength and increased porosity, contrary to previous studies. This effect is further impaired when using smaller rollers, emphasizing the importance of roller size in achieving desired compaction and density levels. The larger roller proved to be more effective, enhancing the density and strength of the sandstones by applying greater pressure during the printing process.

These findings highlight the complexities of 3D printing in geomechanics, emphasizing the critical role of material composition, printing position, and post-processing techniques. Understanding these variables is vital for optimizing 3D-printing processes, particularly in applications such as petroleum engineering and construction, where the predictability and reliability of material properties are paramount.

# 6. Geomechanical and Flow Characterization of 3D-Printed Reservoir Rock Analogues

## 6.1. Introduction

Binder-jet additive manufacturing has emerged as a promising technology for characterizing rock properties across diverse engineering fields. This technology allows for the creation of 3D-printed proxy models that serve as analogues to natural rock, offering greater control over properties and boundaries during experimental testing.

Despite the current technological advances in experimental testing using 3D-printed rocks, geomechanical and flow properties, such as Young's modulus, bulk modulus, porosity and permeability, differ from those of natural reservoir rocks by two to three orders of magnitude, rendering them unrepresentative of reservoir rocks. The use of 3D-printed rocks for reservoir modeling and simulation requires the rocks to have similar geomechanical and petrophysical properties to natural reservoir rocks.

This study presents a comprehensive investigation into the geomechanical and flow properties of 3D-printed reservoir rock analogues. A methodology was developed for customizing the geomechanical and petrophysical properties of standard 3D-printed rocks, such as the ones described in Chapter 5, to resemble reservoir rock analogues. This includes a sodium silicate-carbon dioxide treatment to reduce porosity and permeability, thereby altering the rocks' petrophysical properties. The results provide valuable insights into the properties of 3D-printed reservoir rock analogues and may have important implications for reservoir modeling and simulation.

## 6.2. Experimental Approach

This section presents a comprehensive investigation into the geomechanical and flow properties of 3D-printed reservoir rock analogues. A methodology was developed for customizing the petrophysical properties of standard 3D-printed rocks to resemble reservoir rock analogues. The methodology involves saturating the rocks with sodium silicate and injecting carbon dioxide for a specified duration. The findings offer significant understanding of the characteristics of 3D-printed reservoir rock analogues and could play a crucial role in enhancing reservoir modeling and simulation techniques.

### 6.2.1. Densification Approach Utilizing the Sodium Silicate-Carbon Dioxide Process

Since the petrophysical characteristics, such as porosity and permeability, of 3D-printed sandstones differ from those of typical reservoir rocks, a post-printing process is necessary to achieve greater similarity (Hodder et al., 2022; Santiago et al., 2022). The applied procedure involves reducing the pore space, which in turn reduces porosity and permeability. To accomplish this, we saturated the pore system with sodium silicate ($Na_2SiO_3$) using a vacuum suction of -80 kPa. Sodium silicate was selected because of its affinity with the silica sand used in the 3D-printing process. After completely saturating of the samples with sodium silicate, we placed them in a high-pressure cell and injected carbon dioxide ($CO_2$) at 1 MPa confining pressure to promote diffusion through the porous media. The carbon dioxide reacted with the sodium silicate in the presence of silica sand ($SiO_2$) through a process known as carbonation (Castañeda-Herrera et al., 2018). In this process, $CO_2$ dissolved in water to form carbonic acid ($H_2CO_3$), which reacted with sodium silicate to produce sodium carbonate ($Na_2CO_3$) and silica gel ($SiO_2 \cdot nH_2O$), as indicated by the overall chemical reaction (Equation 6.1).

$$Na_2SiO_3 + CO_2 + H_2O \rightarrow Na_2CO_3 + SiO_2 \cdot nH_2O. \qquad (6.1)$$

The introduction of silica gel into the pore system effectively reduced both porosity and permeability by filling the void spaces and obstructing flow pathways. Initially, the silica gel was in a soft state and required curing to harden and securely adhere to the porous media. To facilitate this, the samples were subsequently placed in an oven at 80°C for 24 hours. This step was crucial to complete the crystallization process, remove any excess water, and ensure that the silica gel attained its full strength.

We investigated the effect of the sodium silicate-carbon dioxide process on the petrophysical and geomechanical properties of printed rock samples by varying the duration of sodium silicate saturation and carbon dioxide injection. The primary objective was to evaluate the feasibility of this approach and identify the optimal testing conditions for the rock samples to accurately simulate reservoir rock properties. Two main components of the process were varied: (1) the duration of sodium silicate saturation, and (2) the exposure time of the samples to carbon dioxide. Figure 6.1 displays the geomechanical properties of the samples, including UCS, Young's modulus ($E$), and bulk density.

The Young's modulus was determined by calculating the slope of the linear section of the stress-strain curve. We observed a decrease in the strength and stiffness properties of the samples as the duration of sodium silicate saturation increased, with the carbon dioxide exposure time held constant at one hour (samples A, B, and C). Moreover, when the carbon dioxide exposure time was extended to eight hours, while maintaining the same saturation duration, the geomechanical properties deteriorated significantly (samples A', B', and C'). Interestingly, we observed an unexpected relationship between bulk density and strength: the stronger samples had lower bulk density. One possible explanation for this is that the carbon dioxide injection induced tensile stress to the binder necks between the grains during depressurization, weakening the bonds and ultimately reducing the strength of the samples. Consequently, the reference samples without post-treatment, and thus no carbon dioxide injection, had higher UCS and lower bulk density (Figure 6.1).

The porosity of the samples decreased by nearly 50% after the first iteration of the process. For most of the tests, it remained constant at an average of 21.6% with a standard deviation of 1.2%. Samples 2C and 2C' were subjected to two cycles of the process reported for C and C', respectively. After careful inspection, it was determined that the method used to create sample C yielded the best performance, providing optimal testing conditions for manufacturing analogues of reservoir rocks using 3D-printed rock. This selection was made by prioritizing petrophysical properties, while sacrificing geomechanical properties. Therefore, sample C was chosen for further testing in terms of flow, geomechanical, and microstructural analysis. Table 6.1 presents the results for each sample, with reported values representing the average of three samples for the reference 3D-printed rock and two samples for all post-treated rocks.

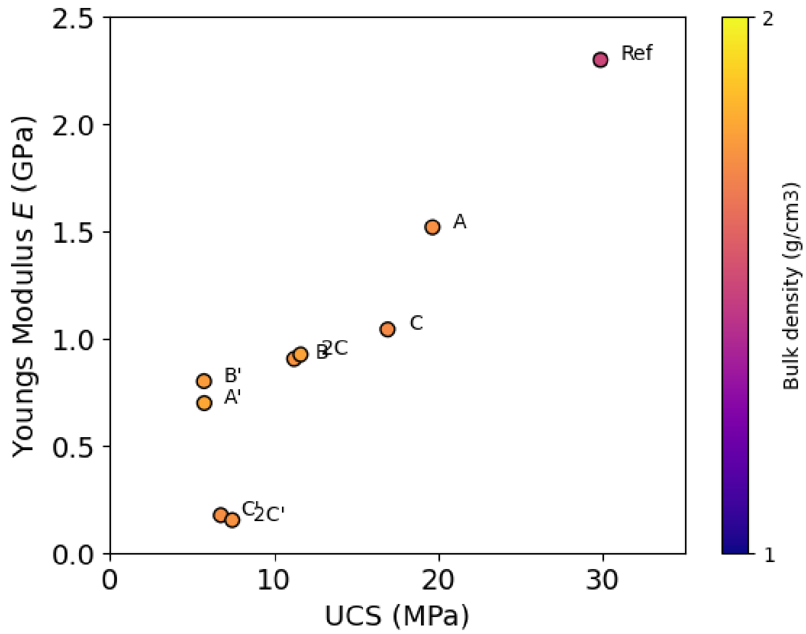


Figure 6.1. The impact of the sodium silicate-carbon dioxide process on the mechanical properties of 3D-printed rock samples.

Table 6.1. Average petrophysical properties of the 3D-printed rocks after the sodium silicate-carbon dioxide processing.

| **Sample** ID | **$Na_2SiO_3$ Saturation** (hr) | **$CO_2$ Injection** (hr) | **UCS** (MPa) | ***E*** (GPa) | $\rho_b$ (g/cm$^3$) | **Φ** (%) |
|---|---|---|---|---|---|---|
| Ref | - | - | 29.85 | 2.30 | 1.50 | 40.13 |
| A | 1 | 1 | 19.63 | 1.52 | 1.73 | 22.63 |
| A' | 1 | 8 | 5.74 | 0.70 | 1.80 | 19.99 |
| B | 8 | 1 | 11.21 | 0.90 | 1.75 | 21.67 |
| B' | 8 | 8 | 5.72 | 0.80 | 1.77 | 20.58 |
| C | 24 | 1 | 16.90 | 1.04 | 1.72 | 22.51 |
| C' | 24 | 8 | 6.75 | 0.17 | 1.73 | 23.64 |
| 2C | 24 | 1 | 11.61 | 0.92 | 1.79 | 20.47 |
| 2C' | 24 | 8 | 7.45 | 0.15 | 1.74 | 21.79 |

### 6.2.2. Morphology and Microstructure

The morphology of grains in the porous media was examined using a Zeiss Sigma Field Emission Scanning Electron Microscope (FESEM) located in the nanoFAB laboratories of the University of Alberta. The FESEM was utilized in conjunction with Energy Dispersive X-ray Spectroscopy (EDX) and Electron Backscatter Diffraction (EBSD) techniques. The FESEM uses an electron beam to generate high-resolution images of samples at magnifications of up to 1,000,000x. The narrow electron beam, produced by a field emission electron source with high current density, facilitates imaging of very small features, down to the nanometer scale. In this study, the FESEM was used to investigate the infilling of silica gel in the pore throats and the bonding necks between the silica gel, furfuryl binder, and sand grains.

For microstructural analysis of the 3D printed rocks, we used the Zeiss Xradia Versa 620 X-Ray Microscope, which is an advanced imaging system that employs X-rays to produce high-resolution 3D images. The system is equipped with a 4X objective lens and offers a large field of view. Using tomographic imaging, it can produce images with voxel sizes as small as 50 nanometers. The X-Ray Microscope was employed to determine the connected pore network of the 3D-printed rocks, which enabled us to gain insights into fluid propagation through the porous media impregnated with silica gel.

## 6.3. Laboratory Testing Program

The laboratory testing program focused on evaluating intact 3D-printed reservoir rock analogues to ascertain their geomechanical and flow properties. This involved using samples to measure porosity and permeability under low effective stress conditions. Isotropic stress testing was also carried out, which helped determine key parameters such as volumetric strain, bulk compressibility, and bulk modulus. Furthermore, triaxial stress testing was performed at various confining stress stages (effective stresses of 1, 3.75, 7.5, and 17.5 MPa), as outlined in Table 6.2. These tests were instrumental in identifying several vital geomechanical parameters, including Poisson’s ratio, Young’s modulus, shear modulus, bulk modulus, friction angle, and cohesive strength.

Table 6.2. Overview of stress testing stages in 3D-printed reservoir rock analogues. This table outlines the different effective stress levels applied during isotropic and triaxial testing and specifies the stress conditions for each testing stage on the 3D-printed reservoir rock analogues.

| **Case** | **Rock type** | **Stress-path** | $\boldsymbol{\sigma_1'}$ (MPa) | $\boldsymbol{\sigma_3'}$ (MPa) | $\boldsymbol{\sigma_1' - \sigma_3'}$ (MPa) | **Test** |
|---|---|---|---|---|---|---|
| CS1 | Intact | Isotropic | 1 | 1 | $-$ | $\emptyset, k$ |
| CS2 | Intact | Isotropic | 1 | 1 | $-$ | $\varepsilon v$, $C_b, K$ |
| CS2 | Intact | Isotropic | 3.75 | 3.75 | $-$ | $\varepsilon v$, $C_b, K$ |
| CS2 | Intact | Isotropic | 7.5 | 7.5 | $-$ | $\varepsilon v$, $C_b, K$ |
| CS2 | Intact | Isotropic | 17.5 | 17.5 | $-$ | $\varepsilon v$, $C_b, K$ |
| CS3 | Intact | Triaxial | 8.13 | 1.00 | 7.13 | E, $v$, $\varepsilon a$, $\emptyset'$ |
| CS4 | Intact | Triaxial | 12.42 | 3.75 | 8.67 | E, $v$, $\varepsilon a$, $\emptyset'$ |
| CS5 | Intact | Triaxial | 18.07 | 7.50 | 10.57 | E, $v$, $\varepsilon a$, $\emptyset'$ |
| CS6 | Intact | Triaxial | 29.30 | 12.50 | 16.80 | E, $v$, $\varepsilon a$, $\emptyset'$ |
| CS7 | Intact | Triaxial | 35.24 | 17.50 | 17.74 | E, $v$, $\varepsilon a$, $\emptyset'$ |

## 6.4. Porosity-Permeability Relationship

The relationship between porosity and permeability is a crucial factor in reservoir development, as it enables the prediction of hydrocarbon productivity and flow rates from reservoir rocks. However, this relationship is complex and varies depending on factors such as rock type, pore structure, and fluid flow characteristics (Ma, 2019). It is essential to understand these relationships to accurately model reservoir behavior and optimize production strategies. Figure 6.2 displays the porosity and permeability measurements obtained from the 3D-printed reservoir rock analogues (blue markers). The average porosity and permeability were 23.2%, and 140 mD, respectively. The porosity was calculated based on mass measurements, and the absolute permeability was measured using canola oil at a confining effective stress of 1 MPa. The absolute permeability tests were conducted using the Multiphase Triaxial System (as described in Chapter 4) under steady-state single-phase incompressible fluid flow conditions. Darcy’s law for vertical flow at a constant flow rate was used to calculate absolute permeability (Equation 6.2).

$$Q = \frac{kA\Delta P - \rho g L}{\mu L}. \tag{6.2}$$

In this equation, $Q$ represents the flow rate, $k$ is the absolute permeability, $A$ is the cross-sectional area, $\Delta P$ is the differential pressure across the specimen, $\mu$ is the fluid viscosity, and $L$ is the specimen length. The term $\rho g L$ represents the hydrostatic pressure exerted by the pore fluid.

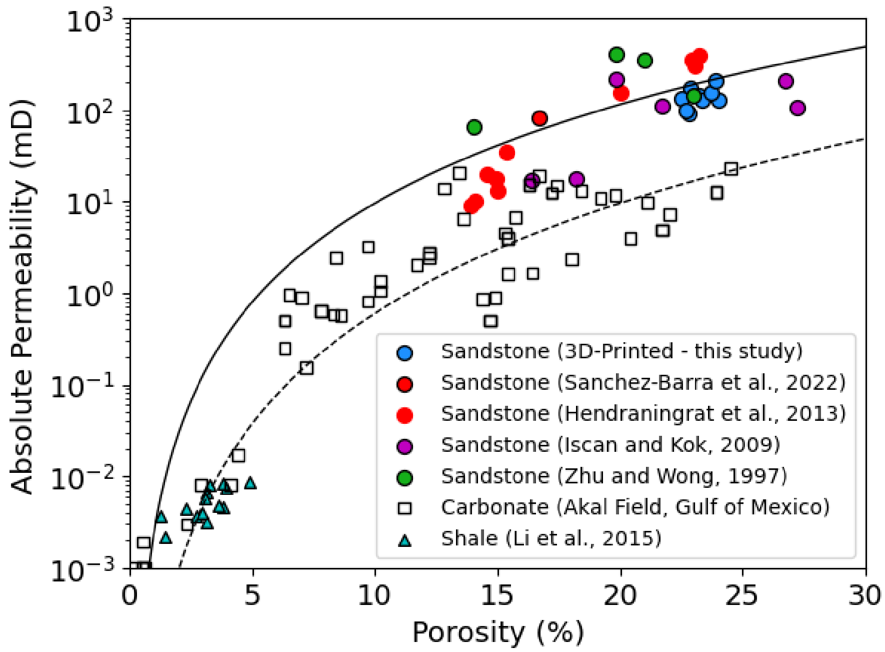


Figure 6.2. Porosity-permeability relationship comparison between 3D-printed reservoir rock analogues and typical sedimentary reservoir rocks.

To validate the experimental results, we compared them with those of typical sedimentary reservoir rocks, including sandstones, carbonates, and shales. The sandstone samples analyzed were Berea, Adamswiller, Boise, Darley Dale, and Rothbatch. Berea sandstone data were obtained from Sanchez-Barra et al., (2022) and Hendraningrat et al., (2013), while data for the other sandstones were from Zhu and Wong (1997) and Iscan and Kok (2009). The data for the carbonate samples presented in this study corresponds to dolomite core samples extracted from the Akal KL reservoir located in the Gulf of Mexico, detailed in Chapter 3. This data was provided by the National Hydrocarbons Commission of Mexico in 2018.

Our results indicate that the porosity-permeability relationships of these typical intact reservoir rocks can be described by two main power-law fitting curves (see Figure 6.2). The lower curve describes the relationship for tight and low-permeability reservoir rocks ($k = 6^{-5}\varphi^{4}$), while the upper curve describes the relationship for moderate-permeability rocks ($k = 0.0025\varphi^{3.584}$). We observed that the porosity-permeability relationship of the 3D-printed reservoir rock analogues matched well with that of the moderate-permeability reservoir rocks. The variation in these curves is typically associated with various factors such as grain size, sorting, and cementation (Lucia, 2007).

### 6.5. Isotropic Stress Testing

Understanding the impact of stress on the geomechanical properties of reservoir rock is crucial for comprehending the deformation resulting from changes in effective stress during hydrocarbon production and stimulation operations. This section presents the results of geomechanical testing conducted on 3D-printed reservoir rock analogues subjected to isotropic stress. The samples were fully saturated with canola oil and placed in the triaxial cell as described in Chapter 4, where canola oil was used to apply the confining stress. The pore pressure was held constant at 1 MPa, and the isotropic confining stress increased gradually from 1 MPa to 18.5 MPa at 40°C. Figure 6.3 shows the volumetric strain of the 3D-printed reservoir rock analogues at different effective stress levels (blue markers).

To ensure the repeatability of the results, multiple measurements were taken at certain effective stresses. All data points fall within the filled area, representing the confidence intervals. The volumetric strain was calculated using the axial and radial displacement sensor measurements as follows:

$$\varepsilon_v = \varepsilon_a + 2\varepsilon_r, \tag{6.3}$$

where $\varepsilon_v$, $\varepsilon_a$, and $\varepsilon_r$ are the volumetric strain, axial strain, and radial strain, respectively. The stress-strain experimental data points indicate a linear relationship ($\varepsilon_v = 0.14\sigma' - 0.07$), which differs from the non-linear behavior observed in natural reservoir rock. Compared to Berea sandstone, the 3D-printed reservoir rock analogue showed three times more deformation, and six times more deformation compared to dolomite intact rocks.

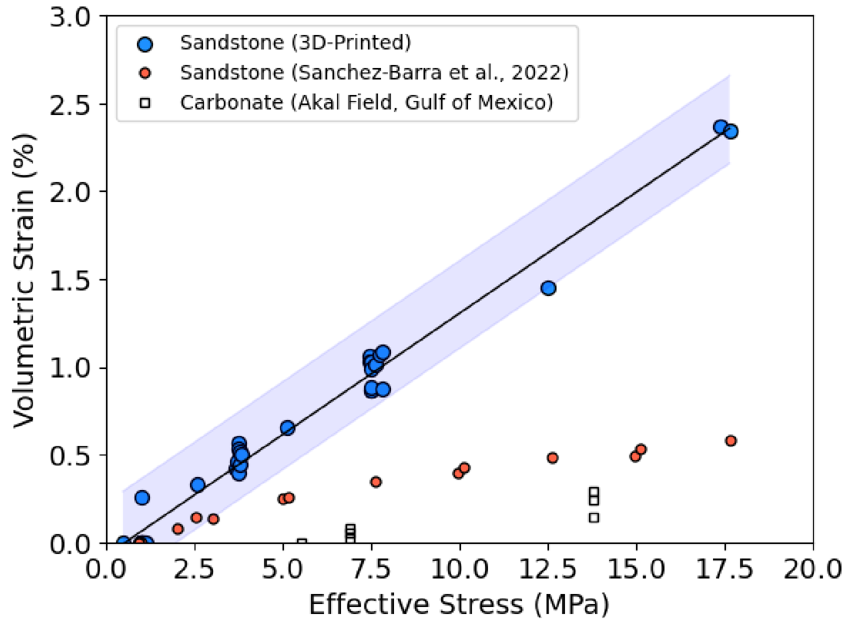


Figure 6.3. Relationship between effective stress and volumetric strain in 3D-printed reservoir rock analogues under isotropic stress.

Figure 6.4 illustrates the relationship between the effective stress and bulk compressibility of the 3D-printed reservoir rock analogues. Bulk compressibility is a measure of the rock's response to external forces and is defined as the changes in rock volume ($\partial V_b$) with respect to variations in confining effective stress ($\partial P_c$) (Zimmerman et al., 1986). The equation for bulk compressibility ($C_{bc}$) is given by:

$$C_{bc} = \frac{1}{V_b^i}\left(\frac{\partial V_b}{\partial P_c}\right)_{P_p}, \tag{6.4}$$

where $V_b^i$ is the initial bulk volume of the rock, and $\partial V_b$ represents the change in bulk volume in response to a change in confining effective stress ($\partial P_c$) at a constant pore pressure ($P_p$). The results show a non-linear reduction in bulk compressibility as the effective stress increases, as illustrated by the power-law fitting curve $C_{bc} = 0.0023\sigma'^{-0.27}$ (black line). This trend is consistent with prior research and is attributed to decreased pore volume resulting in increased grain contact and reduced compressibility (Gomez et al., 2018). Notably, the 3D-printed rocks showed approximately five times higher compressibility compared to natural reservoir rocks.

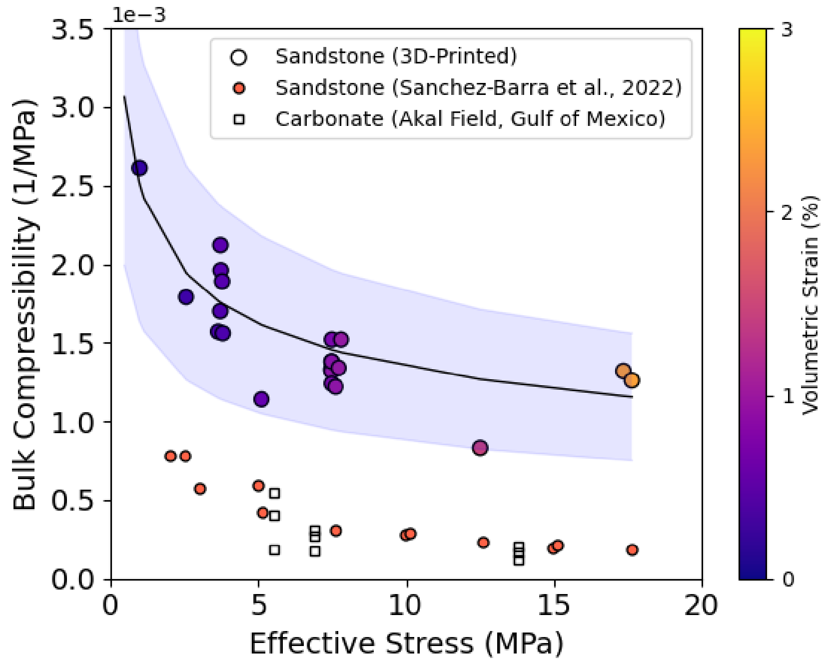


Figure 6.4. Relationship between bulk compressibility and effective stress for 3D-printed reservoir rock analogues.

The evolution of the bulk modulus of the 3D-printed rock analogues was monitored as isotropic effective stress increased, as shown in Figure 6.5. Bulk modulus is a fundamental property of rocks that reflects their ability to resist deformation under pressure (Duncan and Bursey, 2013). The change in bulk modulus observed in this study is attributed to variations in pore volume. As pore volume decreases, the rock becomes stiffer, resulting in a higher bulk modulus. The bulk modulus ($K$) was calculated using the reciprocal of the bulk compressibility, as described in Equation 6.5, and the modulus behavior can be approximated using a logarithmic relationship $K = 327.6 ln\sigma' + 117.6$ (black trend line). These results were compared to the sandstone and carbonate rocks, which showed five to seven times greater stiffness and a more pronounced trend.

$$K = \frac{1}{C_{bc}}. \tag{6.5}$$

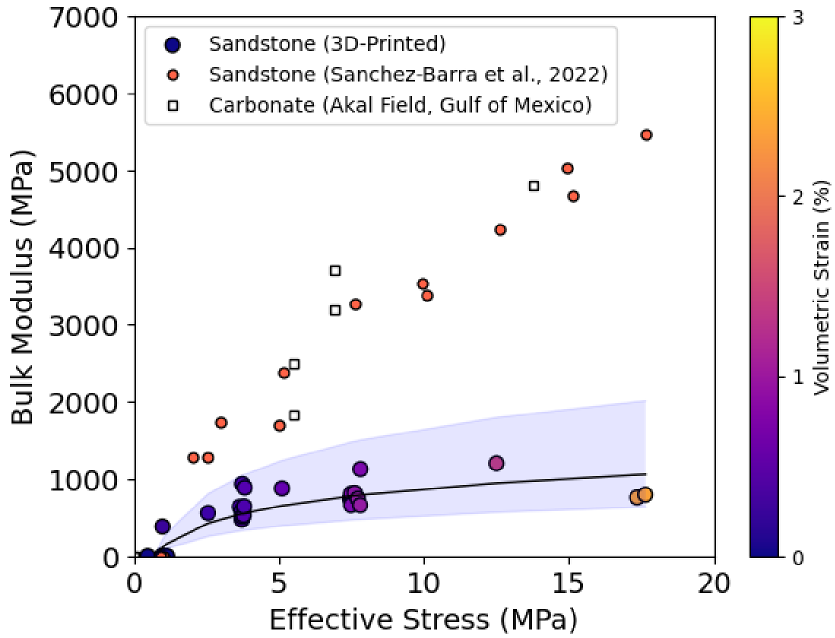


Figure 6.5. Variation of bulk modulus with effective stress for 3D-printed rock analogues.

## 6.6. Triaxial Stress Testing

This section presents the results of drained triaxial stress testing conducted on 3D-printed reservoir rock analogues. Triaxial testing is a widely used method in geomechanics to determine the strength and deformation characteristics of rocks under controlled axial and confining stresses. The 3D-printed rock samples were placed in the triaxial cell, as described in Chapter 4, and were subjected to axial loading until failure occurred under triaxial compression. The samples were tested at different confining effective stresses to investigate their strength and deformation behavior (Figure 6.6).

The testing sequence indicated that the initial linear-elastic response of the deviator stress was similar for both the axial and radial strains. The shear strength of the 3D-printed rock analogues increased with increasing confining stress. For all samples, the deviator stress increased until it reached the peak strength, after which the strength gradually decreased with further deviator stress increase (see Figure 6.6a). At low confinement levels (1 MPa effective stress), the 3D-printed rocks became brittle, which was consistent with prior research (Gomez et al., 2018). However, with an increase in confining effective stress beyond 1 MPa, the rocks exhibited ductility and strain hardening. All the samples exhibited volumetric contraction in response to axial strain (Figure 6.6b). The failure mode for low confinement resulted in a subtle deformation with no apparent fractures. On the other hand, the rocks tested under higher confinement exhibited lateral expansion or barreling with no visible cracks.

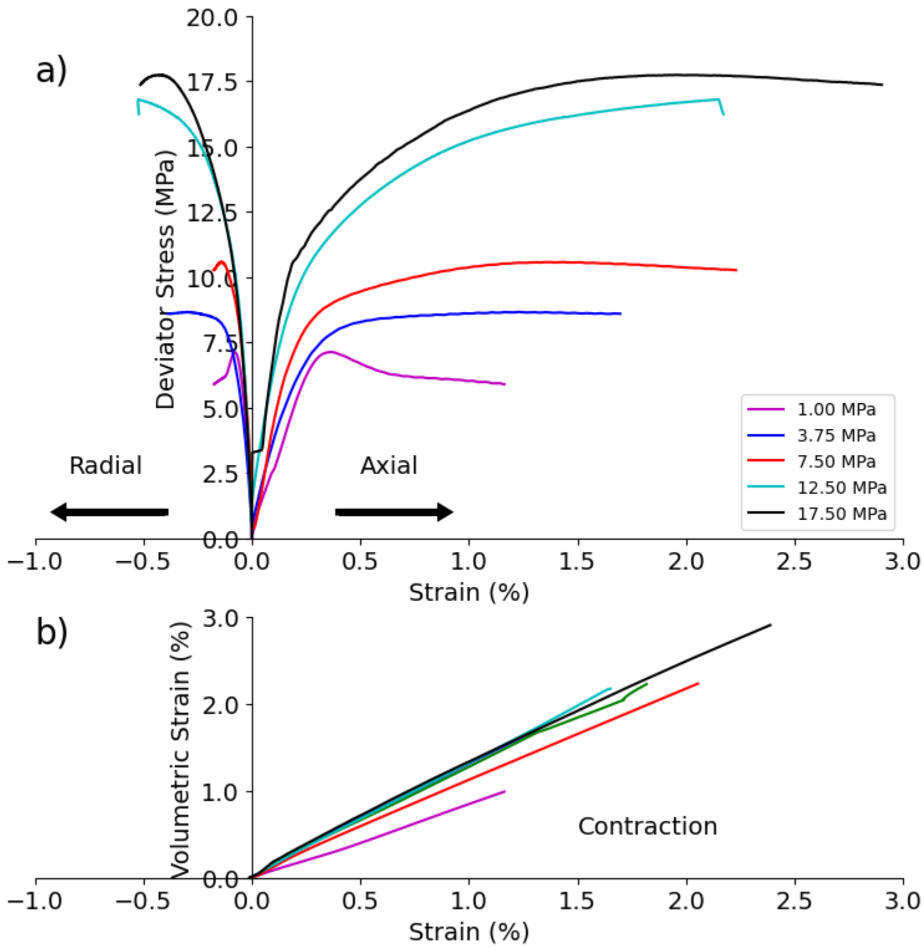


Figure 6.6. Deviator stress-strain behavior for 3D-printed reservoir rock analogues under varying confining stresses.

Young's modulus and Poisson's ratio were calculated from the linear-elastic portion of the stress-strain curves in Figure 6.6a, and were used to calculate the elastic shear modulus ($G$) and bulk modulus ($K$). These geomechanical parameters increased as the confining stress increased, which is expected due to the closure of micro-cracks and pores under high confining stresses (see Table 6.3). In addition, Figure 6.7 displays the stress path or failure envelope in p-q space for the 3D-printed reservoir rock analogues under triaxial compression. The figure shows that the failure envelope followed a linear path, described by the equation $q = 0.25p + 2.54$. This stress path can be used to predict the strength and deformation behavior of rocks under similar loading conditions. The observed behavior is consistent with previous studies on conventional reservoir rocks and provides further evidence of the reliability of 3D-printed rock analogues for geomechanical testing (Arias-Buitrago et al., 2021).

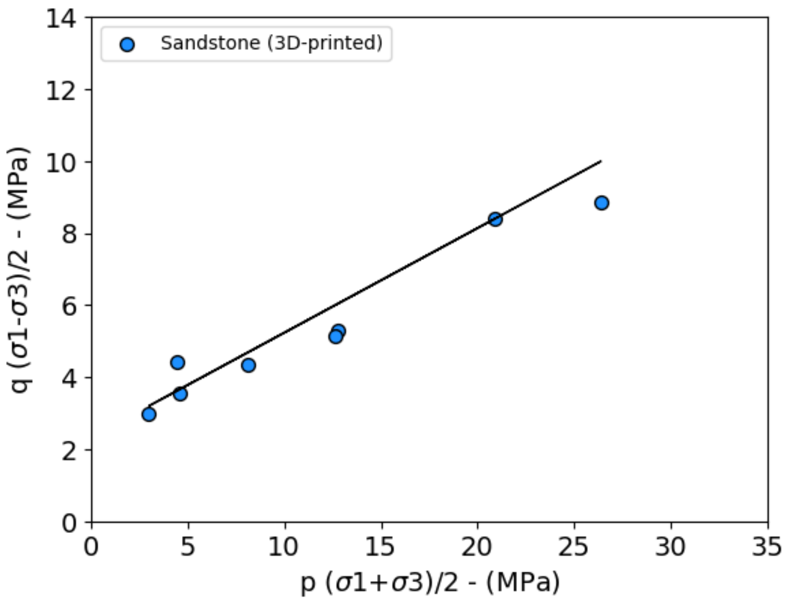


Figure 6.7. Stress path in p-q space for 3D-printed reservoir rock analogues subjected to triaxial loading.

Table 6.3 summarizes the principal stresses at failure, the deviatoric and mean stresses, and the geomechanical parameters obtained from the stress-strain curve analysis.

Table 6.3. Geomechanical parameters and stress values at failure for 3D-printed reservoir rock analogues.

| **Rock ID** | **σ1'** (MPa) | **σ3'** (MPa) | **(σ1'- σ3')** (MPa) | **q** (MPa) | **p** (MPa) | **ν** - | ***E*** (MPa) | ***G*** (MPa) | ***K*** (MPa) |
|---|---|---|---|---|---|---|---|---|---|
| CS3 | 8.13 | 1.00 | 7.13 | 3.57 | 4.57 | 0.12 | 2955.70 | 1315.76 | 1307.35 |
| CS4 | 12.42 | 3.75 | 8.67 | 4.33 | 8.08 | 0.15 | 3311.60 | 1441.05 | 1572.56 |
| CS5 | 18.07 | 7.50 | 10.57 | 5.29 | 12.79 | 0.16 | 4606.50 | 1982.46 | 2270.20 |
| CS6 | 29.30 | 12.50 | 16.80 | 8.40 | 20.90 | 0.15 | 4792.00 | 2085.07 | 2276.19 |
| CS7 | 35.24 | 17.50 | 17.74 | 8.87 | 26.37 | 0.19 | 5343.80 | 2254.41 | 2829.10 |

Figure 6.8 shows the principal stress plot of the peak strength of the 3D-printed rock samples. The peak strength envelope was estimated using the generalized Hoek-Brown criterion for shear failure. The Hoek-Brown failure criterion is a widely used empirical rock failure criterion that describes the non-linear increase in peak strength and deformation behavior of intact isotropic rock and rock masses (Hoek and Brown, 1980; Hoek and Brown, 1997; Hoek and Brown, 2019). The generalized Hoek-Brown failure criterion is expressed as the following equation:

$$\sigma_1' = \sigma_3' + \sigma_{ci}\left(m_b\frac{\sigma_3'}{\sigma_{ci}} + s\right)^a, \tag{6.6}$$

where $\sigma_1$ and $\sigma_3$ are the major and minor effective principal stresses at failure, and $\sigma_{ci}$ is the uniaxial compressive strength of the intact rock material. $m_b$ is a reduced value of the material constant $m_i$ and is given by:

$$m_b = m_i \exp\left(\frac{GSI - 100}{28 - 14D}\right). \tag{6.7}$$

GSI is the Geological Strength Index, established as 100 to represent intact material without discontinuities or fractures. $s$ and $a$ are constants for the rock mass, given by the following relationships:

$$s = \exp\left(\frac{GSI - 100}{9 - 3D}\right), \tag{6.8}$$

$$a = \frac{1}{2} + \frac{1}{6}\left(e^{-GSI/15} - e^{-20/3}\right). \tag{6.9}$$

The material constants for intact rock are $s = 1$, and $a = 0.5$. The Hoek-Brown failure envelope (red line) fitted well with the peak strength experimental data of the 3D-printed rock analogues (blue markers). The intact uniaxial compressive strength was 6.08 MPa, and the $m_b$ was 2.05, which is lower than the values obtained for natural sandstones (~9-24 MPa) and carbonate rocks (~5-8), according to Hoek and Brown (1997). The thresholds for crack initiation and crack damage were found to be approximately 39% and 69% of the peak strength, respectively. These thresholds are consistent with those observed in natural rocks and were determined based on the point where axial and radial strain deviated from linearity (Hoek and Martin, 2014).

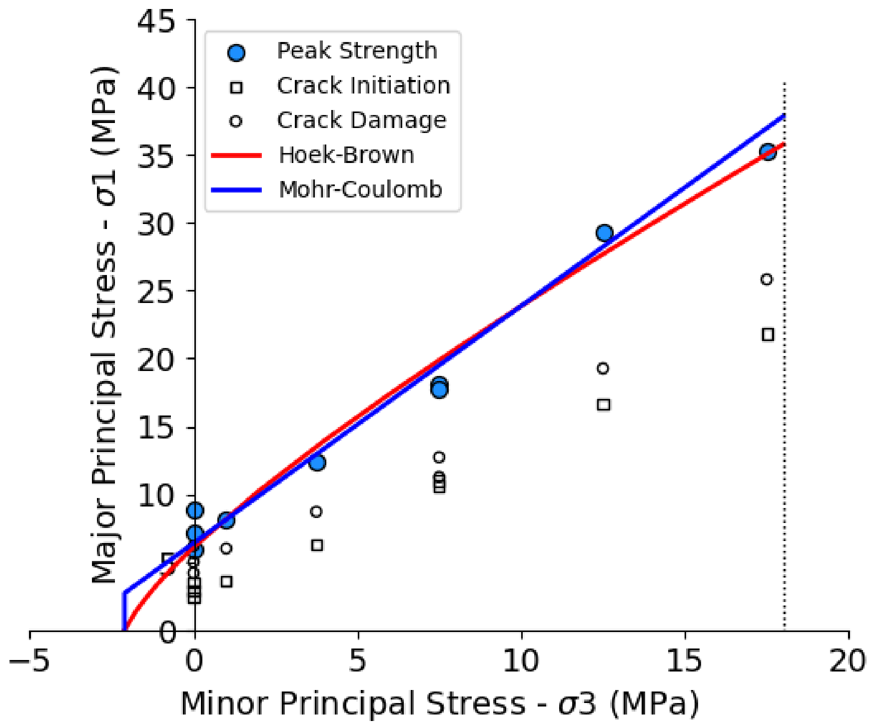


Figure 6.8. Principal stress plot of 3D-printed rock analogues showing the relationships between principal stresses for the Hoek-Brown and equivalent Mohr-Coulomb criteria.

The equivalent friction angle (φ') and cohesive strength (c') of the rock samples were determined using the Mohr-Coulomb failure criterion, with values of φ' = 16° and c' = 2.5 MPa. This was achieved by fitting the linear Mohr-Coulomb relationship for principal stresses (blue line) to the Hoek-Brown failure envelope for a range of minor principal stress values defined by $\sigma_t < \sigma_3' < \sigma_{3max}'$ (see Figure 6.8). The fitting process involved balancing the areas above and below the Mohr-Coulomb failure envelope, as described by Hoek et al., (2002). The Mohr-Coulomb relationship for principal stresses is defined by the following equation:

$$\sigma_1' = \frac{2c' cos\emptyset'}{1 - sin\emptyset'} + \frac{1 + sin\emptyset'}{1 - sin\emptyset'} \sigma_3'. \tag{6.10}$$

The equivalent friction angle and cohesive strength of the rock samples can be calculated using Equations 6.11 and 6.12, respectively:

$$\emptyset' = sin^{-1}\left[\frac{6am_b(s+m_b\sigma'_{3n})^{a-1}}{2(1+a)(2+a)+6am_b(s+m_b\sigma'_{3n})^{a-1}}\right], \tag{6.11}$$

$$c' = \frac{\sigma_{ci}[(1+2a)s+(1-a)m_b\sigma'_{3n}](s+m_b\sigma'_{3n})^{a-1}}{(1+a)(2+a)\sqrt{1+[6am_b(s+m_b\sigma'_{3n})^{a-1}]/[(1+a)(2+a)]}}, \tag{6.12}$$

here, $\sigma'_{3n}$ is given by $\sigma'_{3n} = \sigma'_{3max}/\sigma_{ci}$.

The resulting friction angle and cohesive strength were found to be lower than those of natural sandstones. Typical friction angles for Berea, Athabasca, and Ottawa sandstones range between 20° and 40° (Agar, 1984; Touhidi-Baghini, 1998; Bareither et al., 2008), while cohesive strength for typical sandstones ranges between 8 and 20 MPa (Carmichael, 1982; Zoback, 2007).

### 6.7. Morphological and Microstructural Analysis

This section presents the results of the morphological and microstructural analysis conducted on 3D-printed reservoir rock analogues. Figure 6.9 compares the porous matrix of a 3D-printed rock before and after the post-treatment process. Figure 6.9a shows the porous matrix of a rock printed with default properties and no post-treatment, while Figure 6.9b shows the infilled matrix of sample C after post-treatment. The results indicate that the post-treatment process filled nearly 50% of the pore space available in the 3D-printed rock, including pores and pore throats, with silica gel. This infilling led to a reduction in pore space, resulting in decreased porosity and, consequently, lower permeability.

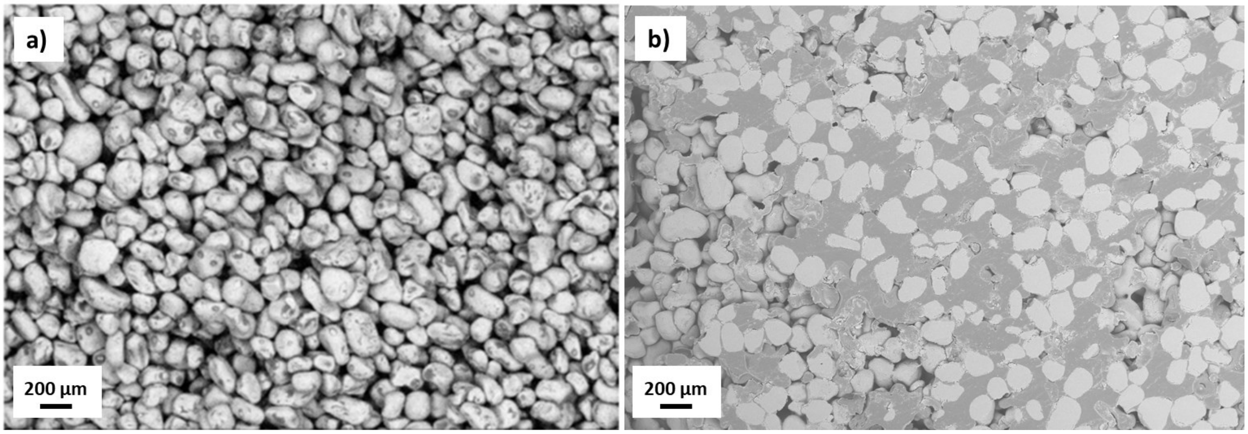


Figure 6.9. Comparison of the porous matrix of a 3D-printed rock before (a) and after post-treatment with sodium silicate and carbon dioxide (b). Figure (a) was modified from Gomez et al., 2017.

Figure 6.10 presents a collage of FESEM images at various magnifications, showing the grain arrangement, pore and pore throat infilling, and bonding necks between silica grains with the binder and silica gel. Our observations reveal that the silica gel has a strong affinity for the surface area of silica grains and can readily occupy the larger pores. This is consistent with the known high wettability of silica-based materials (Rostami et al., 2020). As a result, the silica gel rapidly spreads and forms a uniform wetting front upon contact with silica grains (see Figure 6.10a and 6.10b). However, the adhesion between the silica gel and the cured binder was limited. Figure 6.10c and 6.10d show a distinct boundary between the silica gel and binder, reducing the linkage between the two, and ultimately the strength of the binder neck. Our findings are consistent with previous research studies that have shown that 3D-printed sandstones exhibit mixed wettability characteristics due to the high preference of silica grains for polar fluids and the affinity of the binder to organic fluids (Ardila et al., 2018).

The microstructure of the 3D-printed reservoir rock analogues was further analyzed using the Zeiss Xradia Versa 620 X-Ray Microscope. This instrument allowed us to observe changes in pore space and the pore network resulting from infiltration with silica gel. The 2D scan images were segmented into binary images using Otsu's thresholding algorithm based on a histogram analysis in the Dragonfly® software (ORS, Montréal, QC, Canada), as described by Sahoo et al., 1988. Figure 6.11a and 6.11b present a cross-sectional view of the pore space of a rock sample before and after post-treatment with silica gel. The 2D images show a significant reduction in pore space after infiltration, which results in decreased porosity and lower permeability. This finding is consistent with those obtained from the FESEM analysis.

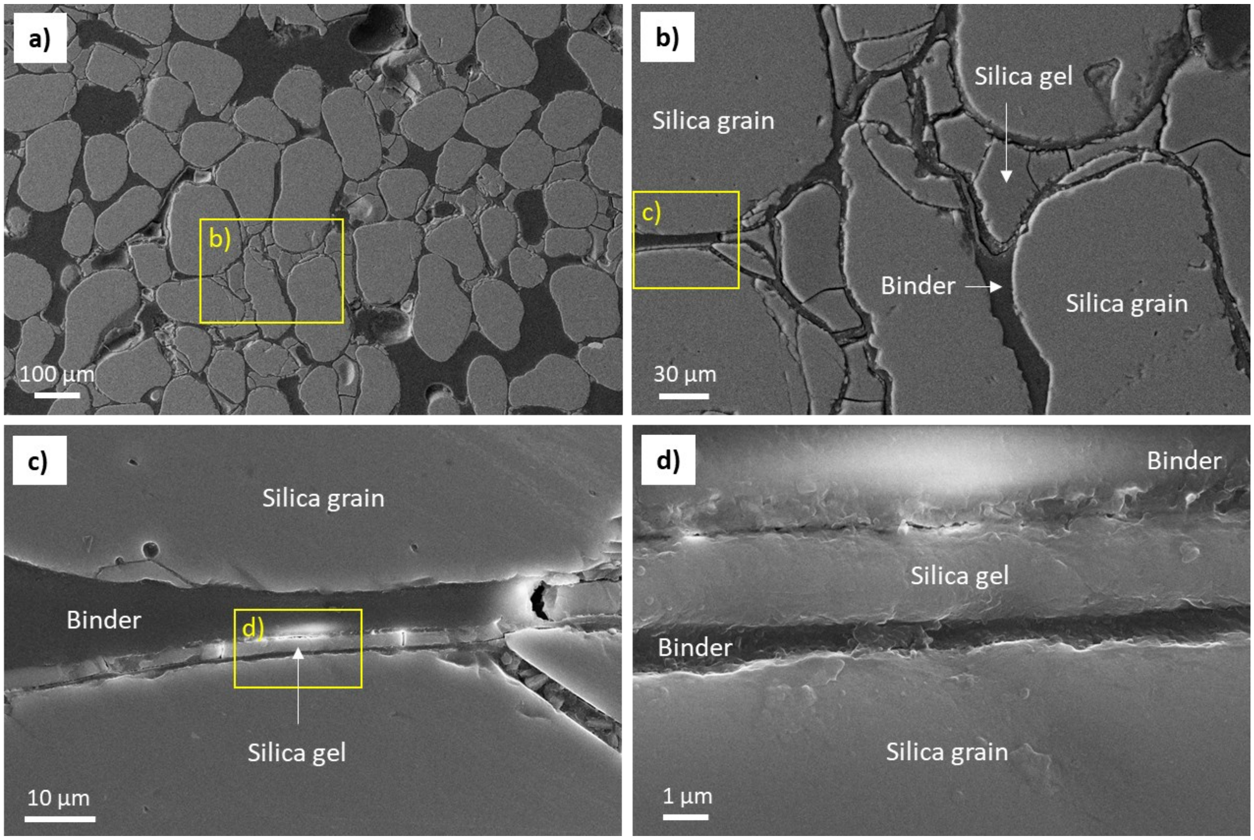


Figure 6.10. FESEM images showing the grain arrangement, pore infilling, and bonding between silica grains with silica gel and cured binder.

Furthermore, the 2D images were reconstructed, rendering a 3D visualization that enabled us to gain insights into the connectivity of the pore network in the 3D-printed rocks (see Figure 6.11c and 6.11d). This analysis revealed that the infilling of silica gel led to a substantial decrease in the connected pore network, resulting in decreased flow paths and thus, permeability. These segmentations facilitated the quantitative analysis of the pore network in terms of pore size, shape, and connectivity. Overall, the combination of FESEM and X-Ray Microscope images provided a comprehensive understanding of the morphology and microstructure of the 3D-printed rocks. Such knowledge is critical for the design and optimization of 3D-printed reservoir rock analogues.

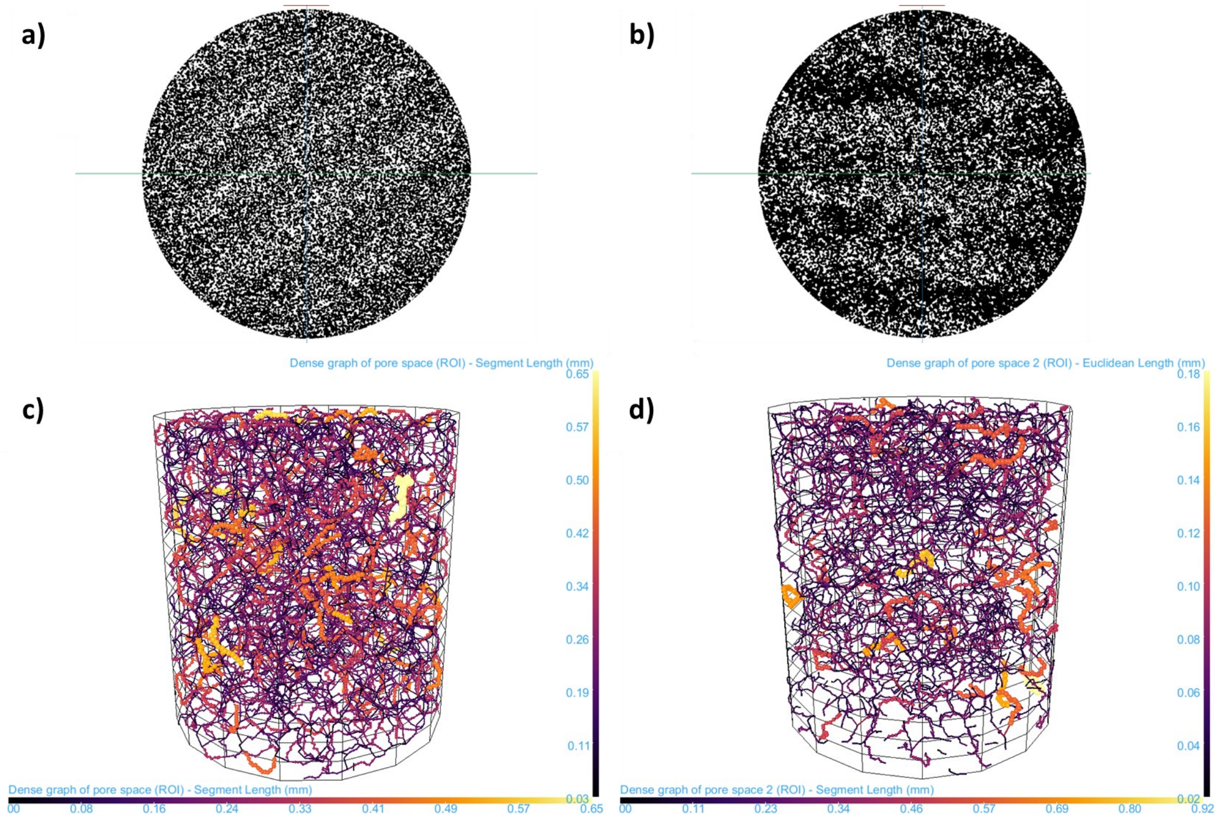


Figure 6.11. Effects of silica gel infiltration on pore space and network in 3D-printed reservoir rock analogues.

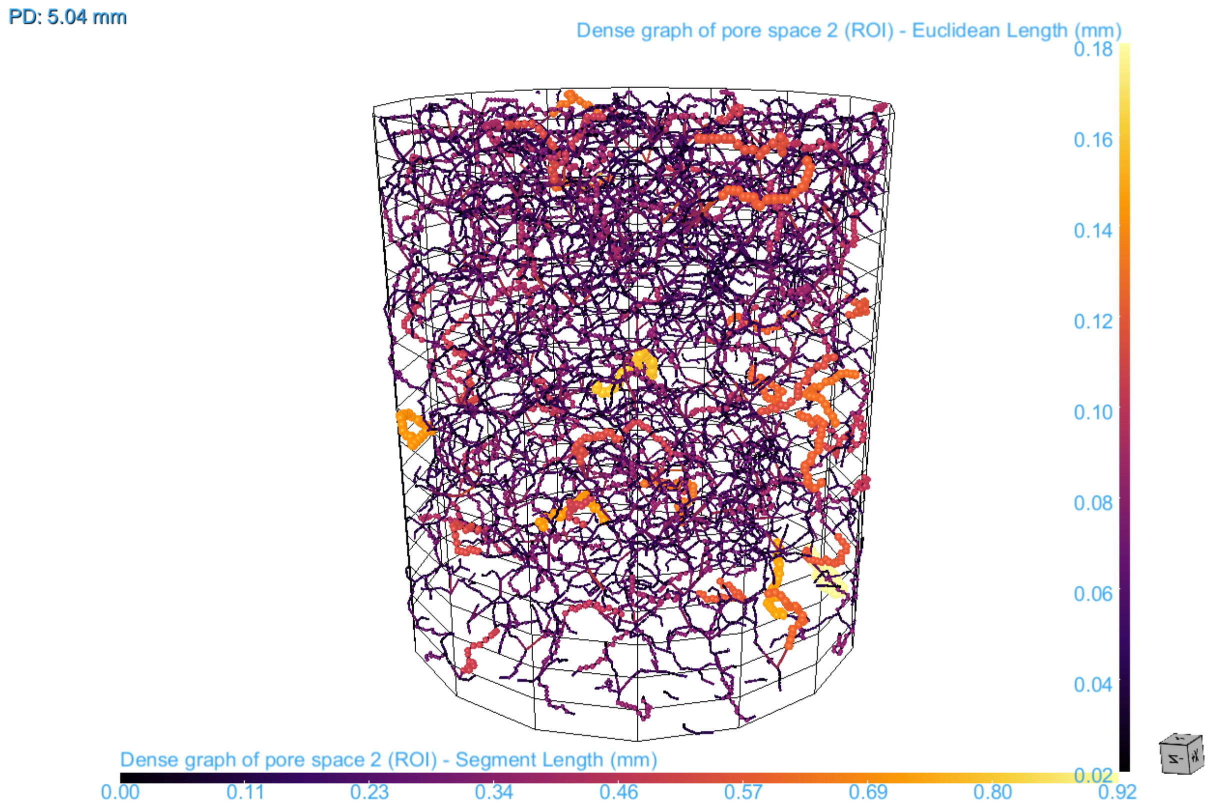


Figure 6.12. 3D visualization of pore network connectivity in 3D-printed reservoir rock analogues. This image illustrates the interconnectedness of pores within the 3D-printed rock samples, highlighting the complexity of the pore structure.

### 6.8. Conclusion

This study aims to investigate the geomechanical and flow properties of 3D-printed reservoir rock analogues. The research demonstrates a methodology for adjusting the geomechanical and petrophysical characteristics of standard 3D-printed rocks to resemble reservoir rock analogues. The approach involves saturating the 3D-printed rocks with sodium silicate and injecting carbon dioxide for a particular duration. The study indicates that the silica gel efficiently occupies the larger pores of the rocks, but there is limited adhesion between the silica gel and the cured binder. Consequently, the infilling process reduces the porosity by 50%, which leads to an 86% decrease in permeability. The relationship between porosity and permeability of the 3D-printed reservoir rock analogues is similar to moderate-permeability reservoir rocks. Additionally, geomechanical testing revealed that the 3D-printed reservoir rock analogues had three times more deformation than Berea sandstone and six times more deformation than dolomite intact rocks. The compressibility of the 3D-printed rocks was approximately five times higher than natural reservoir rocks, with decreasing pore volume resulting in an increase in bulk modulus. The axial and radial strains of the 3D-printed rocks showed similar initial linear-elastic responses. The shear strength of the rocks increased with an increase in confining stress, resulting in a transition from brittle behavior to ductility and strain hardening at 1 MPa effective stress. The friction angle and cohesive strength of the 3D-printed rocks were $\varphi' = 16°$ and $c' = 2.5$ MPa, respectively, which were lower than those of natural sandstones. The results provide valuable insights into the geomechanical and flow properties of 3D-printed reservoir rock analogues and may have important implications for reservoir modeling and simulation.

# 7. Effects of Triaxial Stress and Strain on Multiphase Flow Properties Using 3D-printed Fractured Reservoir Rock Analogues

## 7.1. Introduction

In the field of petroleum engineering and reservoir management, comprehending the dynamics of multiphase fluid flow within reservoir rocks under different stress conditions is crucial. This chapter examines the complex relationship between triaxial stress and strain and its impact on multiphase flow in 3D-printed fractured reservoir rock analogues. The development of 3D printing technology has facilitated the creation of reservoir rock analogues that closely resemble natural rock formations, offering a controlled setting to study the behaviors of reservoirs under simulated conditions.

The aim of this chapter is to investigate how various stress regimes, particularly triaxial stresses, affect the flow properties of both intact and artificially fractured reservoir rock analogues. Subjected to conditions that replicate the underground stress environment typical in hydrocarbon reservoirs, these analogues provide critical insights into changes in porosity, permeability, relative permeability, capillary pressure and fracture behavior under normal and shear stresses.

The importance of this study extends to practical applications in hydrocarbon extraction. Natural reservoirs often feature complex networks of fractures and experience changing stress conditions throughout their production life. The findings from this research are vital for improving extraction techniques, enhancing recovery processes, and making more accurate predictions of reservoir behavior. Thus, this chapter contributes to both the theoretical understanding of stress-related rock mechanics and fluid dynamics, and offers valuable practical insights for industry professionals managing naturally fractured reservoirs.

## 7.2. Experimental Approach

The experimental approach adopted in this study focuses on understanding the impact of stress on multiphase flow properties during reservoir depletion. To appreciate the basis of the experiments conducted, one must understand the fundamental concepts related to the state of stress. Within any material, the state of stress at a specific point is represented by the stress tensor, commonly denoted as $\sigma_{ij}$. This stress tensor can be divided into two main components.

The first is the Mean Normal Stress, sometimes termed the Mean Hydrostatic Stress. This represents the uniform normal stress acting on a point within the material and is expressed as $\sigma = \sigma_{kk}/3$. Under the influence of this stress, every direction evolves into a principal direction, and no shear stresses emerge. This means that the same normal stress, $\sigma$, is omnipresent and acts uniformly in every conceivable direction.

The second component is the Deviatoric Stress, also referred to as the Stress Deviator Tensor. This component represents the distortion or shape alteration of a material element due to the stresses applied. It is mathematically expressed as:

$$s_{ij} = \sigma_{ij} - \frac{1}{3}\sigma_{kk}\delta_{ij}, \tag{7.1}$$

where $\sigma_{kk}$ is the trace of the stress tensor and $\delta_{ij}$ represents the Kronecker delta, which takes the value of 1 when $i = j$ and 0 otherwise.

When combined, these two components give us the total stress tensor:

$$\sigma_{ij} = s_{ij} + \sigma\delta_{ij} = s_{ij} + \frac{1}{3}\sigma_{kk}\delta_{ij}. \tag{7.2}$$

The implications of these stresses on materials are profound. The Hydrostatic or Normal Stress primarily induces volumetric changes, causing materials to either compress or expand uniformly while preserving their original shape. On the other hand, the Deviatoric or Shear Stress results in distortional changes, leading to a transformation in shape without a uniform change in volume (Chou and Pagano, 1992). In the context of this study, a thorough understanding of these stress components, both normal and shear, is essential. The multiphase flow experiments focus on how materials respond to these two foundational aspects of the state of stress.

As depicted in Figure 7.1, the stress path followed during the experimental program is outlined by the blue and red arrows. Initially, the experiments focused on the behavior of mean stress, as evidenced by the isotropic compression path from Point A to Point B. Subsequently, shear stresses were introduced during the triaxial compression phase, transitioning from Point B to Point C.

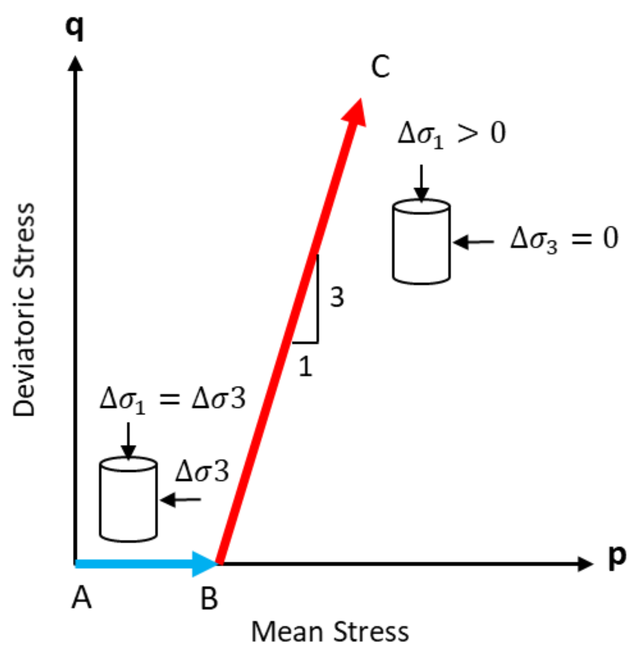


Figure 7.1. Stress path illustration of the experimental program highlighting isotropic compression and triaxial compression phases.

In fractured porous media, the direction of the stress path elicits varying responses in permeability sensitivity. Mean normal stresses cause the fractured porous media to contract, decreasing both the matrix and fracture permeability (Figure 7.2a). Typically, this does not affect fracture asperities unless there have been prior displacements on rough fractures. On the other hand, shear stress results in both contraction and dilation (Figure 7.2b). This can lead to dilatant microcracking, fracture dilation, and displacement. In these scenarios, fractures initially contract, but as shearing progresses, high-permeability conduits form and gouge is produced. If both stress and deformation are significant, and there is extensive engagement of the fracture surface, the asperities may progressively fill the aperture space, creating a barrier to permeability (Smart et al., 2001).

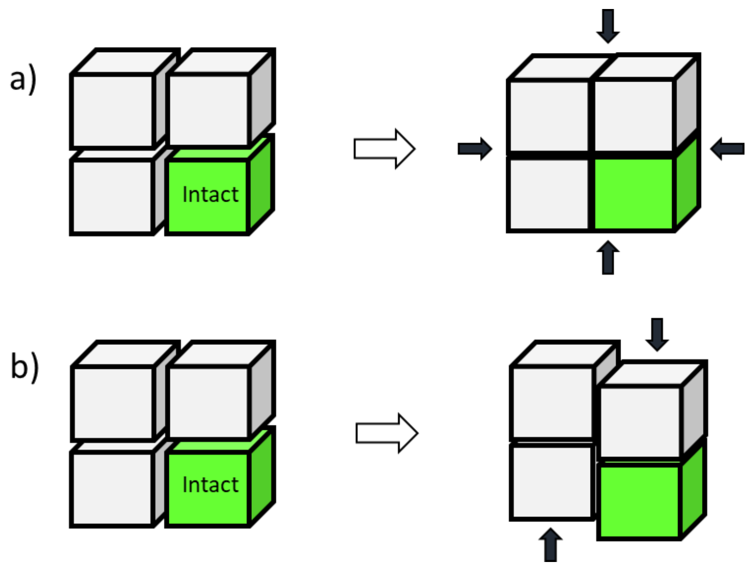


Figure 7.2. Schematic illustrating the effects of normal and shear stresses on fractured porous media.

In the context of multiphase fluid flow, the dependency on the stress-path is significant because it can alter the multiphase flow properties of a reservoir. Naturally fractured reservoirs are generally distinguished by a highly heterogeneous distribution of porosity and permeability. This is attributed to the typical structure composed of low porosity and low permeability matrix blocks, surrounded by a highly permeable fracture network. When stresses interact with this rock structure, they alter its geometry. This, in turn, affects its multiphase flow properties, consequently influencing the reservoir flow physics.

Previous studies have indicated that, in the case of intact matrix blocks, normal stresses reduce the pore space, porosity, and absolute permeability. These changes predominantly affect the wetting phase saturation of the rock, leading to increased capillary pressure and shifts in the relative permeability curves. Haghi et al., (2020) explored these effects using Berea sandstone across three effective stress levels. Employing steady-state flow considerations for nitrogen and water, they determined that an increase in effective stress resulted in reductions in porosity and permeability, from 13.16% and 58 mD to 12.24% and 36 mD, respectively. This shift in conditions caused the relative permeability curves to move to the left, indicating a decrease in the irreducible wetting phase saturation (Figure 7.3a).

In the case of fractures, observations have shown a similar behavior. Huo and Benson (2016) examined the stress-dependency of relative permeability in rock fractures using fractured Zenifim sandstone with an impermeable matrix in a nitrogen-water system under different effective stress conditions. They found that under constant flow rate experiments, an increase in isotropic effective stress led to a marked reduction in irreducible water saturation (Figure 7.3b). Conversely, when experiments maintained a constant capillary number (i.e., constant pore pressure conditions), irreducible water saturation increased with higher effective stress, aligning with findings by Lian et al., (2012).

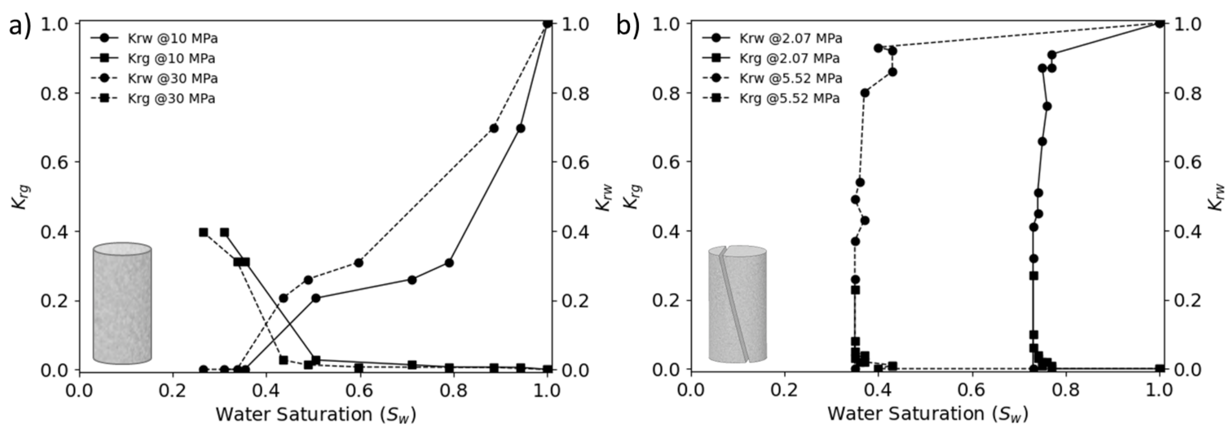


Figure 7.3. Stress-dependent relative permeability curves under isotropic compression: (a) intact Berea sandstone (adapted from Haghi et al., 2020) and (b) fractured Zenifim sandstone (modified from Huo and Benson, 2016).

The effects of shear stress on fractured porous media are complex due to the variable distortions it induces. These distortions, whether contraction or dilation, can lead to diverse interactions within the fracture (Smart et al., 2001). When a fracture closes, the primary flow path becomes obstructed, likely leading to an increase in capillary pressure. Conversely, when fractures open, a significant decrease in capillary pressure can occur. Regarding relative permeability curves, early breakthrough or channelling of the invading fluid can affect the drainage displacement, and therefore the recovery of the wetting phase fluid. Depending on whether there is contraction or dilation, the wetting phase saturation of the rock might either increase or decrease.

### 7.2.1. Laboratory Testing Program

The experimental program was designed to investigate the effects of both normal and shear stress on the multiphase flow properties of 3D-printed fractured reservoir rock analogues. To achieve this objective, four distinct cases were established. These cases measured single and multiphase flow properties, including porosity, absolute permeability, relative permeability, and capillary pressure, under both isotropic (normal stress) and triaxial (shear stress) conditions. Samples for Case 1 and Case 2 were tested under isotropic stress: Case 1 featured an intact 3D-printed reservoir analogue rock, while Case 2 involved a fractured reservoir analogue rock. For Cases 3 and 4, tests were conducted under triaxial stress conditions, with Case 3 being intact and Case 4 being fractured. Table 7.1 delineates the specific conditions under which each case was tested and highlights the measured flow properties for each respective scenario.

Table 7.1. Experimental cases and corresponding test conditions for the samples tested under normal and shear stress.

| **Case ID** | **Rock type** | **Stress-path** | $\boldsymbol{\sigma_1'}$ | $\boldsymbol{\sigma_3'}$ | $\boldsymbol{\sigma_1' - \sigma_3'}$ | **Test** |
|---|---|---|---|---|---|---|
| | | | MPa | MPa | MPa | |
| Case 1 | Intact | Isotropic | 7.5 | 7.5 | - | $\varphi$, k, kr, Pc |
| Case 1 | Intact | Isotropic | 17.5 | 17.5 | - | $\varphi$, k, kr, Pc |
| Case 2 | Fractured | Isotropic | 7.5 | 7.5 | - | $\varphi$, k, $e_h$, kr, Pc |
| Case 2 | Fractured | Isotropic | 17.5 | 17.5 | - | $\varphi$, k, $e_h$, kr, Pc |
| Case 3 | Intact | Triaxial | 7.5 | 7.5 | 0 | $\varphi$, k, kr, Pc |
| Case 3 | Intact | Triaxial | 12.5 | 7.5 | 5 | $\varphi$, k, kr, Pc |
| Case 3 | Intact | Triaxial | 17.5 | 7.5 | 10 | $\varphi$, k, kr, Pc |
| Case 4 | Fractured | Triaxial | 7.5 | 7.5 | 0 | $\varphi$, k, $e_h$, kr, Pc |
| Case 4 | Fractured | Triaxial | 12.5 | 7.5 | 5 | $\varphi$, k, $e_h$, kr, Pc |
| Case 4 | Fractured | Triaxial | 17.5 | 7.5 | 10 | $\varphi$, k, $e_h$, kr, Pc |

### 7.2.2. Experimental Cases and Stress Conditions

Building upon the experimental framework previously described, this section provides a detailed examination of the case studies and their corresponding testing conditions. Using the 3D printing technology discussed in Chapter 6, each case has been crafted to represent the behavior of the 3D-printed reservoir rock analogues under different stress scenarios. The specific cases for testing are shown in Figure 7.4.

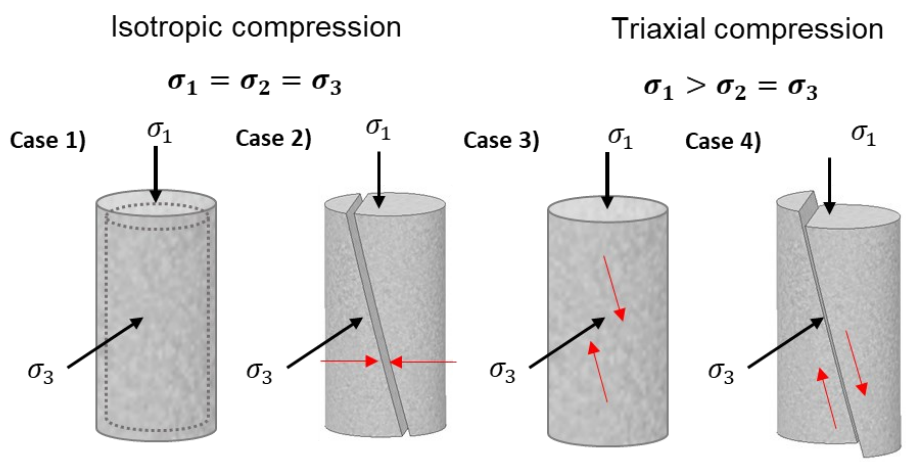


Figure 7.4. Overview of the test samples and their corresponding stress conditions: (a) Case 1 – Intact 3D-printed reservoir rock analogue under isotropic stress, (b) Case 2 –3D-printed fractured reservoir rock analogue under isotropic stress, (c) Case 3 – Intact rock analogue under triaxial stress, and (d) Case 4 – Fractured rock analogue under triaxial stress.

The experimental stress conditions were designed to match the stress and strain conditions of the field case presented in Chapter 3 (Akal KL). Located at a depth of 2500 TVD, the reservoir's stress state was determined from a mean total stress valued at 58 MPa. The mean value mitigated sensitivity between the principal stresses. The initial pore pressure was 11.3 MPa and decreased to 6 MPa during the reservoir's life cycle. It is assumed that the reservoir depletion induced geomechanical changes and increased the effective stress from 47 MPa to 53 MPa as illustrated in Figure 7.5a. To emulate these reservoir conditions in the experiments, the rock's bulk compressibility was used as a reference. Combining field observations and laboratory analyses, the reservoir rock's bulk compressibility was determined to be $2.4E^{-4}$/MPa, as shown in Figure 7.5b. For the tests, the 3D-printed specimens were subjected to an effective stress range of 7.5 to

17.5 MPa, in which greater compressibility (7E$^{-4}$/MPa) led to a volumetric deformation equivalent to that during the reservoir depletion (refer to Figure 7.5b, points A' to B').

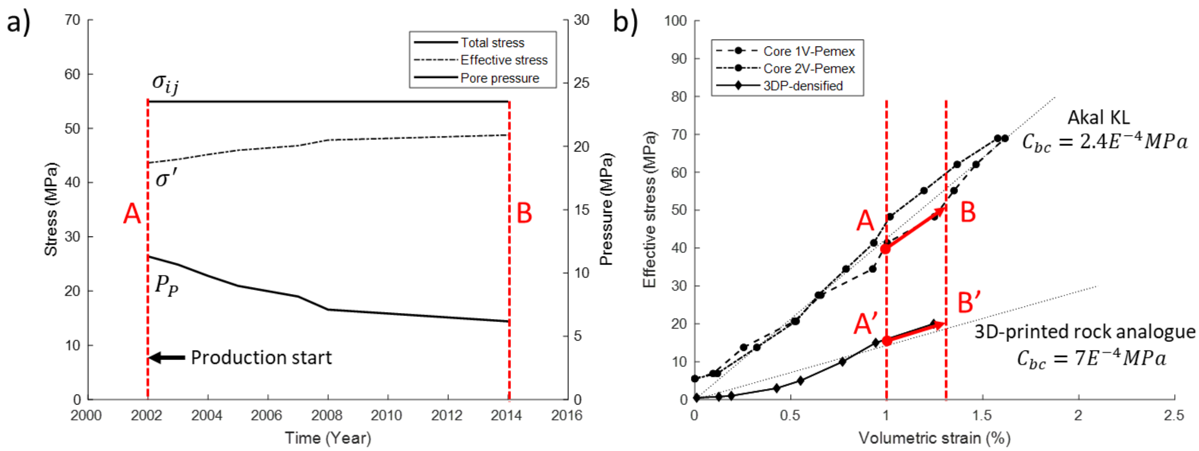


Figure 7.5. Matching reservoir conditions: (a) *in-situ* stress evolution during reservoir depletion, and (b) comparative relationship between volumetric deformation of the reservoir rock and 3D-printed rock analogues.

## 7.3. Materials and Equipment

### 7.3.1. 3D-printed Reservoir Rock Analogues

The use of 3D printing technology in geoscience studies has surged because it is an excellent alternative to manufacture precise and customizable reservoir rock analogues. As detailed in Chapter 6, the 3D-printed reservoir rock analogues were the focus of the present laboratory testing program. These samples exhibit an average porosity of 22.5%. The absolute permeability is 150 mD under an effective confining stress of 1 MPa. In terms of dimensions, these core samples have a diameter of 63.61 mm and a length of 126.57 mm (Figure 7.6).

Figure 7.6. 3D-printed reservoir rock analogue used in the multiphase triaxial experiments, featuring a diagonal fracture oriented at an angle of 15 degrees relative to the vertical direction.

The manufacturing process of these analogues was complex, involving multiple stages designed to generate petrophysical properties emulating those of the reservoir case study presented in Chapter 3. This approach facilitated the modification of the geomechanical and petrophysical attributes of standard 3D-printed rocks, enabling them to mimic their natural reservoir counterparts more closely. Such advancements not only enhance the accuracy of the experimental data but also support the relevance of 3D printing in petroleum reservoir studies.

The primary objective in fabricating the 3D-printed samples was to guarantee their repeatability (Sanchez-Barra et al., 2023). Moreover, mechanical compaction was employed to improve the rock mechanical properties of the samples. This method, on its own, failed to achieve the required flow properties. As a remedy, an auxiliary treatment was introduced to decrease pore space, consequently lowering both porosity and permeability. During this stage, sodium silicate was introduced into the rock matrix, where it crystallized to decrease the available void space. The complete process was described in Chapter 6. The intact matrix of the 3D-printed samples revealed a consistent structure, with a variance of 2% in the pore space. The microstructure of the pore space was extracted using the Zeiss Xradia Versa 620 X-Ray Microscope. This instrument facilitated observations of alterations in the pore space and network of the 3D-printed reservoir rock analogue, as depicted in Figure 7.7.

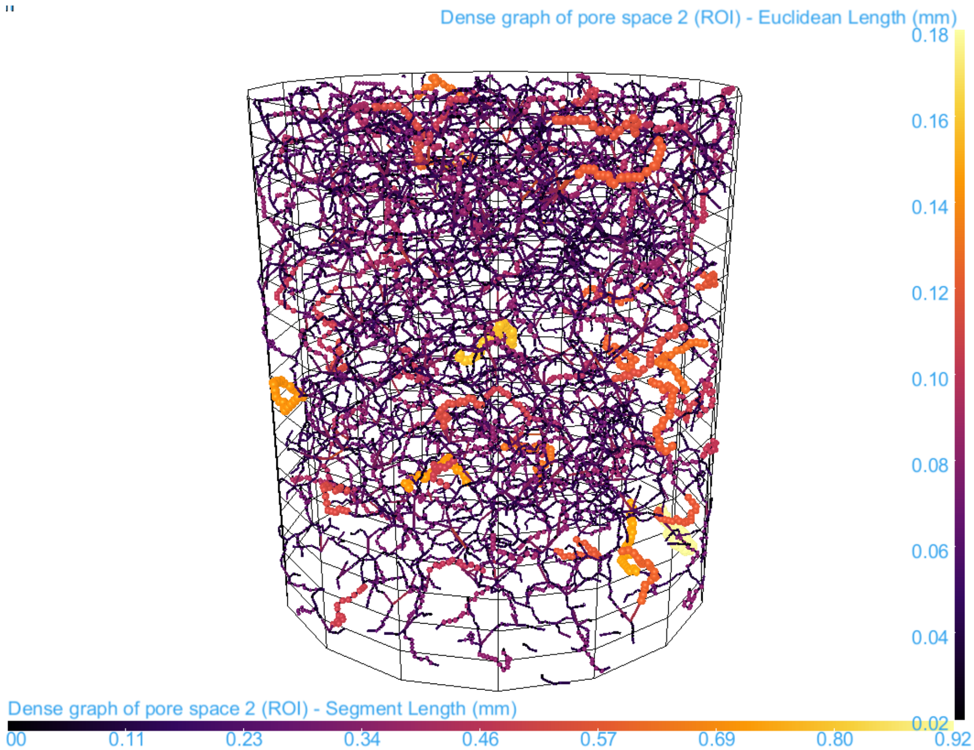


Figure 7.7. Microstructural analysis of the intact 3D-printed reservoir rock analogue. This image captures the intricate pore space and network, highlighting the consistent structure.

The 3D-printed rocks, which incorporate both intact and fractured components, were meticulously crafted to match the characteristics of fractured reservoir rocks. A distinct diagonal fracture was integrated to reflect the inherent nature of these reservoir rock fractures. This fracture was oriented at an angle of 15 degrees relative to the vertical direction and features a smooth surface with texture mean heights ranging between 50 to 90 microns, as illustrated in Figure 7.8. Furthermore, the 3D-printed reservoir rock analogue demonstrates a significant degree of isotropy. The orientation of its pore structure aligns at 82.47% with the grain structure direction, as depicted in Figure 7.9. To achieve an accurate assessment of the fracture surface, a JR-50 profilometer (Nanovea, Irvine, CA, USA) was employed. The scan speed was set to acquire data at 10 µm intervals in the x-direction and 10 µm in the y-direction. The resolution was chosen due to a good balance between the quality of the data received and the speed of the scan. This state-of-the-art instrument, is equipped with Chromatic Confocal optical technology. It measures physical wavelengths corresponding to specific heights without the need for complex algorithms, ensuring reliable and precise results irrespective of a sample's reflectivity. After the index testing, the 3D-printed sandstones were aged in canola oil under vacuum pressure for several days to improve the sample's affinity with the saturating fluid.

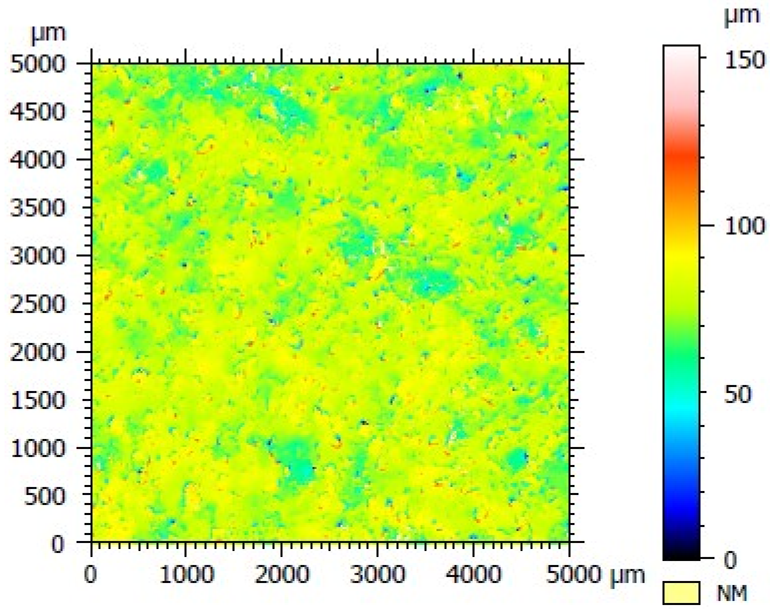


Figure 7.8. Representation of the 3D-printed rock's fracture surface. The scanned profile shows an area of 5 x 5 mm in which the texture's mean heights range between 50 to 90 microns.

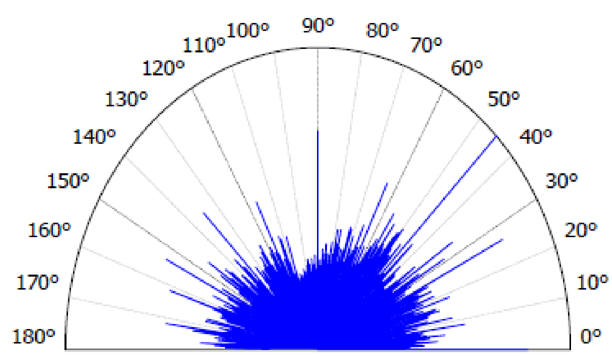


| Parameters | Value | Unit |
|---|---|---|
| Isotropy | 82.477 | % |
| First Direction | 44.988 | ° |
| Second Direction | 0.294 | ° |
| Third Direction | 26.445 | ° |

Figure 7.9. Isotropic nature of the 3D-printed reservoir rock analogue. The pore structure orientation demonstrates an 82.47% alignment with the grain structure direction.

### 7.3.2. Fluids

In the conducted multiphase flow experiments, canola oil and nitrogen gas were selected as the test fluids. This pairing aligns with the conditions found in hydrocarbon reservoirs during processes such as forced gas drainage and free gas gravity drainage, comparable to scenarios observed in Akal KL.

The significance of forced gas drainage and gas gravity segregation is underscored in the context of enhanced oil recovery. Forced gas drainage involves the artificial injection of gas into the reservoir to increase pressure and displace oil towards production wells, enhancing extraction efficiency. Gas gravity segregation, on the other hand, leverages the natural propensity of gas to rise above oil due to its lower density. This gravity-induced separation forms a gas cap, applying pressure that drives oil towards the wells and facilitating efficient extraction. Both mechanisms involve the meticulous monitoring and control of the concurrent flow of oil and gas to maximize oil recovery, with the oil and gas categorized as the wetting and non-wetting phases respectively.

In these specific experiments, canola oil is utilized as the wetting phase fluid, complemented by nitrogen as the non-wetting phase. These tests are executed at a pore pressure of 1 MPa and a temperature setting of 40°C. Under such parameters, canola oil displays a density of 0.90 g/cm$^3$ and a viscosity nearing 34 cP, as referenced in the work of Sahasrabudhe et al., (2017). In contrast, nitrogen possesses a lighter density of approximately 0.01 g/cm$^3$ and a viscosity of around 0.0186 cP. The attributes of nitrogen are determined utilizing PyFluids, a renowned open-source Python library, which is endorsed under the MIT license and assures the accuracy and dependability of the extracted data.

### 7.3.3. Core Flooding System

The experimental tests were performed using a multiphase triaxial system consisting of a triaxial high-pressure cell, a loading system, a multiphase pore pressure circuit, a fluid phase separation system, and a measurement/logging system. To maintain isothermal conditions, the system was installed inside an oven, as shown in Figure 7.10. The triaxial high-pressure cell is capable of independently applying axial and confining stresses to the specimen. The cell has a maximum operating stress of 45 MPa, maximum pore pressure of 20 MPa, and a maximum operating temperature of 60°C (Deisman et al., 2011). The flow and pressure lines enter through the base of the cell. For this study, the flow lines for injecting fluids are connected to the upper platen, while the drainage lines are connected to the lower platen. The back pore pressure was fixed at 1 MPa for all experiments. The top platen connects to the axial ram, which passes through the plug in the upper-end cap and connects to an external load cell.

The loading system comprises an axial loading circuit and a confining (radial) circuit, Isco Pump 1, and Isco Pump 2, respectively. The axial loading circuit consists of a low-profile load frame with a 228.6 mm (9.0 in) diameter hydraulic piston located at the bottom of the frame and an external 260HP High-Pressure ISCO Syringe Pump. The piston is connected to the pump, which uses hydraulic oil as the hydraulic fluid. The axial load is applied using a constant flow rate mode on the pump and is measured with a 400 kN OMEGA load cell fixed between the top of the frame and the ram. The displacement of the ram is measured using an external linear potentiometer (LP). The confining circuit consists of the triaxial high-pressure cell and an external 260HP High-Pressure ISCO Syringe Pump. The isotropic or radial stress is applied by pumping canola oil (confining fluid) into the cell and is measured with a Honeywell pressure transducer of 41 MPa. An internal axial LVDT is placed around the sample to measure vertical displacement, and an internal radial chain with a spring-loaded LVDT is used to measure the change in specimen circumference.

The multiphase pore pressure circuit is controlled by an external fluid mixing manifold and three HPHT Quizix Q5000 pumps, as shown in Figure 7.10. The fluid separation system consists of two high-pressure vertical separation cylinders that are continuously weighed with ultra-sensitive Omega LC703-10 load cells (4.5 kgf) and custom built amplifiers. The wetting and non-wetting fluid phase saturations are estimated using the real-time mass measurements of the producing fluids. When the two-phase flow (downstream) reaches a steady state, the saturation of fluids is assumed to be uniformly distributed across the specimen. At this point, the mixture of fluids coming out of the specimen is diverted to the phase separation system (equilibrated with the pore pressure), which collects and separates the fluid volume fractions by gravity segregation. The cylinders have a 500 mL fluid capacity, allowing longer periods of production.

The logging system includes signal readings of the load cells, pressure transducers, axial/radial strains, and thermocouples, which are logged and continuously displayed on a LabView-based data logging software. A KEYSIGHT® 34972A data acquisition unit is used to collect and process the signals coming from the different sensors in the system. A comprehensive description of the Multiphase Triaxial System, including its functional aspects and technical specifications, was previously detailed in Chapter 4 and in the publication by Sanchez-Barra et al., 2022.

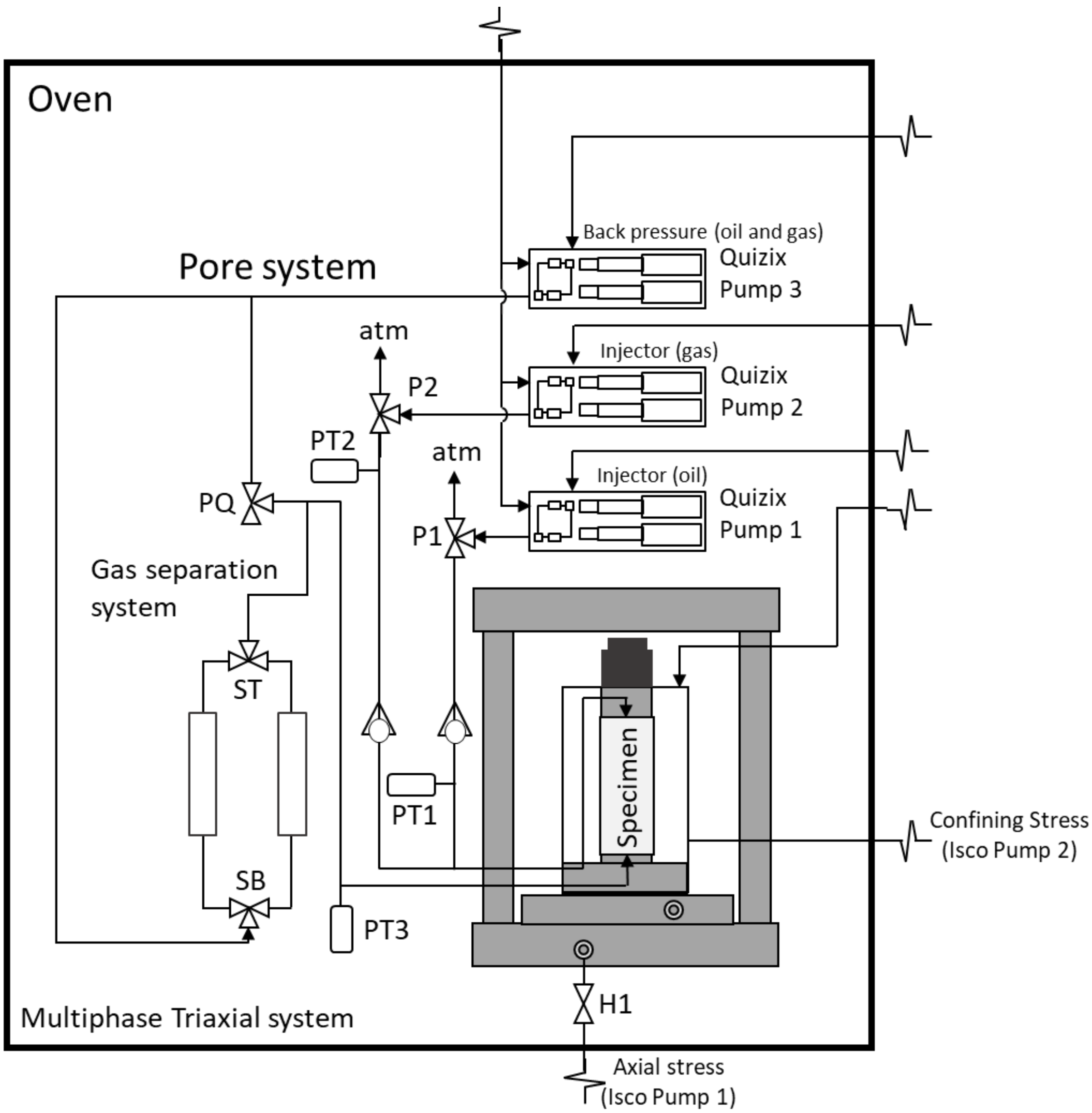


Figure 7.10. Schematic representation of the Multiphase Triaxial System, showing its primary components. The entire setup is contained within an oven to maintain isothermal conditions.

### 7.4. Methodology

The experimental methodology described in this section allows the simultaneous determination of porosity, absolute permeability, fracture aperture, drainage relative permeability, and drainage capillary pressure for the 3D-printed reservoir rock analogues under different stress conditions. Following the oil saturation process, the samples were weighed using a high-precision scale to determine their initial porosity. Each sample was then wrapped in a thin layer of cellophane, covered by aluminum foil, and further sealed with another cellophane layer to inhibit gas diffusion through the membrane. Subsequently, the specimen was encased within a Viton fluoro-rubber membrane and flanked by porous stones at both ends. This entire assembly was then installed within the triaxial cell.

The samples were saturated inside the multiphase core flooding system under an initial isotropic effective stress of 500 kPa, displacing approximately 80 pore volumes to ensure full saturation. The initial absolute permeability to oil was then measured under constant flow steady-state conditions at an effective stress of 1000 kPa. Following this, the effective stress was adjusted to the targeted levels, and the absolute permeability measurements were conducted once again. After completing the absolute permeability measurements, the drainage relative permeability tests were conducted. Then, canola oil was injected into the core over several pore volumes, displacing the nitrogen entirely and re-saturating the specimen. Subsequently, the drainage capillary pressure at the core's inlet face was measured by introducing nitrogen gas at varying flow rates. Once this was complete, the specimen was re-saturated, the effective stress adjusted, and the entire procedure was repeated. The specifics of this process are explained in the following sections.

#### 7.4.1. Porosity

Porosity, which refers to the measure of the void $V_p$, or pore spaces within the bulk volume of the rock, $V_b$, is highly dependent on the stress to which it is subjected. The 3D-printed reservoir rock analogues respond to both internal and external effective stresses, leading to deformations in their pore geometry and internal pore network. The stress-dependent poroelastic response of the rock can be approximated using poroelastic constitutive principles for fluid-saturated porous media. These principles are based on assumptions of strain and strain linearity, as well as the reversibility of the media deformation (Biot, 1941; Haghi et al., 2020).

The initial porosity was measured using mass balance considerations, based on the volume of oil saturating the pore space. The stress-dependent porosity was then determined using the initial porosity as a reference and the measured volumetric strain of the rock. The volumetric strain, $\varepsilon_v$, is defined as the change in bulk volume of the rock, $\Delta V_b$, divided by the original bulk volume, $V_b$. This relationship is expressed in Equation 7.3:

$$\Delta V_b = \varepsilon_v V_b. \tag{7.3}$$

Based on Zhang (2019), the strain-dependent porosity of intact porous media can be represented by the following equation:

$$\emptyset = \frac{(V_b + \Delta V_b) - (V_s + \Delta V_s)}{V_b + \Delta V_b} = \frac{(V_b + \varepsilon_v V_b) - (V_s + \Delta V_s)}{V_b + \varepsilon_v V_b} = \frac{V_p + V_b \varepsilon_v - \Delta V_s}{V_b(1 + \varepsilon_v)}. \tag{7.4}$$

When simplifying Equation 7.4 by dividing both the numerator and denominator by the bulk volume, we get:

$$\emptyset = \frac{\emptyset_i + \varepsilon_v - \frac{\Delta V_s}{V_b}}{(1 + \varepsilon_v)}. \tag{7.5}$$

Assuming that the change in solid volume is negligible compared to the change in pore volume, Equation 7.5 can be expressed as:

$$\emptyset = \frac{\emptyset_i + \varepsilon_v}{1 + \varepsilon_v}. \tag{7.6}$$

Strain-dependent porosity is a fundamental attribute in the study of reservoir rocks as it influences the storage capacity for fluids such as water, oil, or gas.

### 7.4.2. Absolute Permeability

Absolute permeability is a critical property in geosciences studies as it impacts how easily fluids can move through the pore spaces within the rock. In this study, the absolute permeability to oil was determined at the beginning of each core-flooding experiment. The samples were consistently saturated with canola oil at low flow rates, with displacements typically ranging from 40 to 80 pore volumes, depending on the loading stage. Once the porous medium reached full saturation, the flow rate was increased, and the initial absolute permeability to oil was measured under steady-state conditions, considering single-phase incompressible fluid flow. The constant flow was delivered by a Quizix pump. The pressure drop across the specimen was recorded using both upstream and downstream pressure transducers, as illustrated in Figure 7.10. Darcy's law for vertical flow (Equation 2.3), representing the absolute permeability, can be re-written as:

$$k = \frac{Q\mu L}{A(\Delta P + \rho g L)}, \tag{7.7}$$

where $\rho$ is the fluid density, $\mu$ is the fluid viscosity, $Q$ is the flow rate, $\Delta P$ is the differential pressure across the specimen, and $k$ is the absolute permeability.

### 7.4.3. Drainage Relative Permeability

Following the absolute permeability test, the drainage relative permeability experiment was conducted. In multiphase flow through porous media, the relative permeability represents the ratio of the effective permeability of a fluid phase to the absolute permeability of the rock ($kr = k_e/k$). During drainage displacements, the non-wetting phase (in this case, nitrogen gas) displaces the wetting phase (canola oil). Once the oil flow rate stabilized and the pressure drop across the specimen became consistent, nitrogen gas was co-injected into the top inlet of the samples through a secondary flow line. The nitrogen flow rate was increased in steps, and correspondingly, the oil flow rate was decreased by the same proportion, maintaining the total flow rate consistent with that used to measure absolute permeability, as illustrated in Figure 7.11.

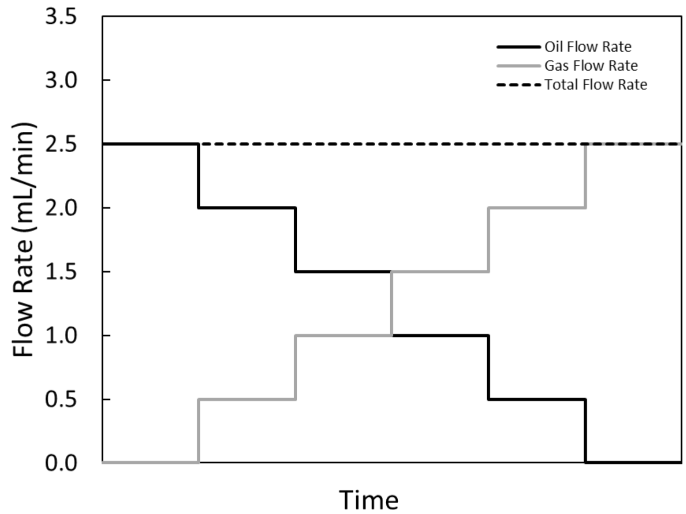


Figure 7.11. Schematic representation of the flow rates used during the simultaneous injection of gas and oil in the relative permeability tests.

The simultaneous flow of both phases at the set flow fraction ($Q_o/Q_g$) is kept constant until equilibrium is reached. It is then assumed that a uniformly distributed saturation profile is established across the specimen (Sanchez-Barra et al., 2022). The liquid saturation of the rock, represented by $Sw$, denotes the wetting phase saturation, which in this case is canola oil. Therefore, it should not be confused with the traditional nomenclature for water, "$Sw$". The gas saturation is expressed as $Snw$, representing the saturation of the non-wetting phase, which in this case is nitrogen gas. The rationale for using $Sw$ and $Snw$ is to facilitate the comparison of drainage relative permeability and capillary pressure behaviors with other drainage multiphase flow experiments, even if they are conducted using different fluid systems like natural gas and water. The mixture of fluids exiting the specimen is channeled into the phase separation system. This system, equilibrated with the pore pressure, segregates the fluid volume fractions using gravity segregation. This process is repeated at several flow fractions in order to complete at least six relative permeability points. Relative permeability is calculated using Darcy's law from individual fluid flow rates and pressures at various saturations, as detailed in Equation 7.8.

$$kr_i = \frac{\mu_i Q_i L}{kA\Delta P_i + \rho_i g L}, \tag{7.8}$$

where $kr_i$ ($i$ = oil or gas) defines each fluid phase's relative permeability.

### 7.4.4. Drainage Capillary Pressure (Porous Plate Method)

Capillary pressure is integral to the study of multiphase fluid flow within porous media. It represents the pressure differential existing between two immiscible fluids contained within this environment. The dynamics of this pressure differential are heavily influenced by the pore geometry and the medium's wettability characteristics, playing a key role in dictating the fluid distribution and flow patterns within naturally fractured reservoirs. Capillary pressure curves are often characterized by a distinct hysteresis pattern, observable during the imbibition and drainage processes. The imbibition process usually occurs when a wetting fluid (typically water or oil in the context of petroleum reservoirs) displaces a non-wetting fluid (commonly oil or gas). Conversely, the drainage process is controlled by the displacement of the wetting fluid by a non-wetting counterpart. A comprehensive understanding of the complex dynamics governing capillary pressure is critical for accurately predicting and enhancing recovery mechanisms operational within naturally fractured reservoirs.

The drainage capillary pressure was measured using the Porous Plate Method, a variation of the permeable plate method introduced by Hassler and Brunner (1945). This approach was used to increase the capillary pressure, subsequently impacting the saturation fraction within the sample during the core flooding experiment. The procedure initiates with the injection of the non-wetting phase (nitrogen gas) at a constant flow rate, $Q_{inj}$, into a rock sample already saturated with the wetting phase fluid (canola oil). As the non-wetting phase fluid invades the flow path saturated with the wetting phase fluid, the injection pressure builds up. This pressure continues to rise until a gas breakthrough occurs. After the non-wetting phase fluid exits the core specimen, the saturation of the wetting phase reduces, and the injection pressure starts to decrease until a steady-state condition is reached. At this stage, the wetting phase saturation becomes immobile. Both the pressure and saturation profiles stabilize, transitioning from the injection pressure, $P_{in}$ ,to the back pressure, $P_{out}$, as illustrated in Figure 7.12.

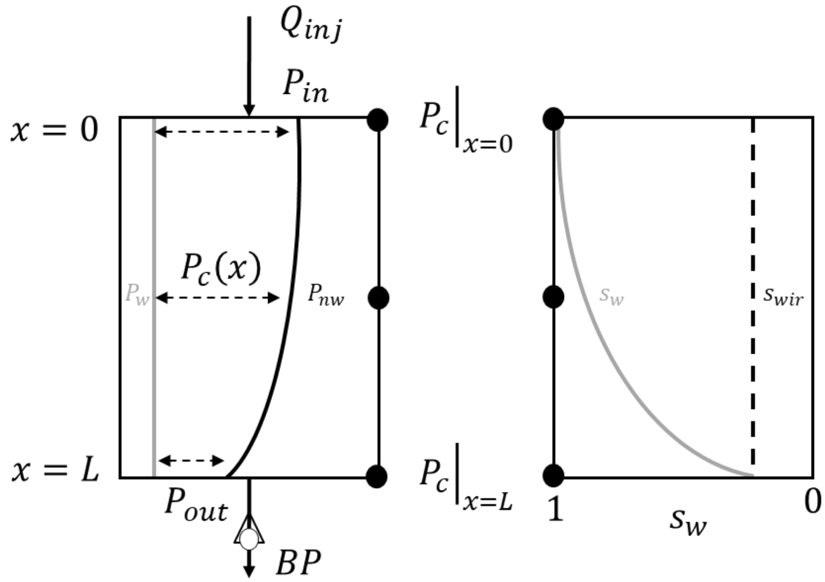


Figure 7.12. Graphical representation of the drainage capillary pressure measurement. The non-wetting phase ($nw$) gas is injected at a constant flow rate ($Q_{inj}$) into a core specimen saturated with the wetting phase fluid ($w$), all while maintaining a constant back pressure ($BP$).

Since the upstream and downstream pressures are measured outside the inlet and outlet faces of the core sample, and considering the porous stones with negligible capillary pressure located between the sample and the top and bottom platens, the boundary conditions for injecting the non-wetting phase can be summarized as follows:

$$Inlet = P_{in} = P_{nw}|_{x=0}, \quad (7.9)$$

$$Outlet = P_{out} = P_w|_{x=L}\,.$$

This indicates that the non-wetting phase gas injected is continuous across the inlet face of the core, while the wetting phase is prevalent at the downstream end. Consequently, the capillary pressure, defined as $P_c = P_{nw} - P_w$, maintains a finite value at the core's end-faces until it is reduced to zero outside of the core, that is, $P_c|_{x=0}$, $P_{nw}|_{x=L} \neq 0$ (Pini and Benson, 2013). In the steady state, the flow of the wetting phase fluid ceases, as described in Equation 7.10.

$$\frac{dP_w}{dx} = 0 \cong P_w|_{x=L} = P_w|_{x=0}\,. \quad (7.10)$$

The drainage capillary pressure can be calculated by measuring the pressure difference across the core specimen:

$$\Delta P = P_{in} - P_{out} = P_c|_{x=0} \,. \tag{7.11}$$

Each change in capillary pressure, induced by injecting at a constant flow rate, $Q_{inj}$, results in the immobilization of the wetting phase fluid's saturation. As the flow rate, and consequently the capillary pressure, increases, the saturation of the wetting phase decreases until it reaches an irreducible stage. This inverse relationship results in an ascending curve when capillary pressure is plotted against the wetting phase saturation, as depicted in Figure 7.13.

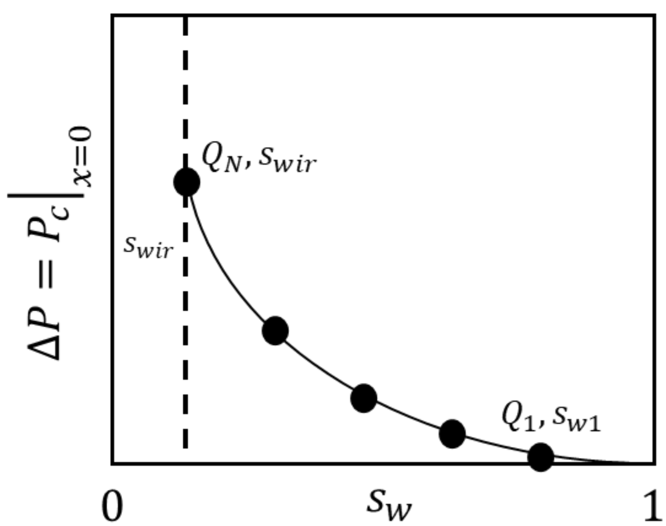


Figure 7.13. Illustration of the relationship between capillary pressure and wetting phase saturation. As the flow rate and associated capillary pressure increase, there is a corresponding decrease in wetting phase saturation, resulting in an upward-trending curve.

### 7.4.5. Fracture Aperture Measurement

The steady-state, incompressible flow of Newtonian viscous fluids through fractures is typically modeled using the Navier-Stokes equations (Zimmerman and Bodvarsson, 1996). However, solving these nonlinear partial differential equations can be complex, especially when dealing with irregular rock fracture geometries. Simplifications are often necessary and applicable in scenarios where fracture roughness is minimal, and the fracture can be approximated as two parallel, smooth plates. In such cases, the parallel plate model or cubic law becomes a viable approach for estimating fracture flow. The cubic law is important as it offers an exact solution for hydraulic conductivity, a feat achievable by neglecting the inertial terms of fluid flow through the fractures (Witherspoon et al., 1980).

The derivation of the cubic law begins with the assumption that the fracture walls can be represented as two smooth, parallel plates. These plates are separated by an aperture, $h$, and have a width, $w$, with uniform pressures, $P_{in}$ and $P_{out}$, applied on two opposing faces (see Figure 2.4 in Chapter 2). Under these conditions, the total volumetric flow through the fracture can be calculated using a simplified version of Equation 2.25.

$$Q = \frac{-|\overline{\nabla P}| w b_h^3}{12\mu}. \tag{7.12}$$

In Equation 7.12, $Q$ represents the volumetric flow rate, $\overline{\nabla P}$ denotes the average pressure gradient, $w$ is the fracture width, $b_h$ is the hydraulic aperture, and $\mu$ symbolizes the fluid viscosity. $Q$ is linearly related to the hydraulic aperture taken to the third power. The linear relationship between $Q$ and $\overline{\nabla P}$ is contingent upon the assumption that the effects of nonlinear flow are minimal, and thus can be neglected. It is crucial to note that these assumptions hold true under conditions of sufficiently laminar flow (Yin et al., 2017). Subsequently, this equation can be reformulated to express in terms of the hydraulic aperture as follows:

$$b_h = \sqrt[3]{\frac{12\mu Q}{|\overline{\nabla P}| w}}. \tag{7.13}$$

In this research, the hydraulic aperture of the 3D-printed fractured reservoir rock analogues was evaluated during the absolute permeability tests. These assessments were performed under steady-state conditions with a constant flow rate, initiated after ensuring the complete saturation of the fractures. The tests revealed a consistent linear relationship between $Q$ and $\overline{\nabla P}$ throughout all isotropic stress stages. This consistency indicates the negligible impact of nonlinearity, thereby validating the use of this approach for measuring the hydraulic aperture. These findings are visually illustrated in Figure 7.14.

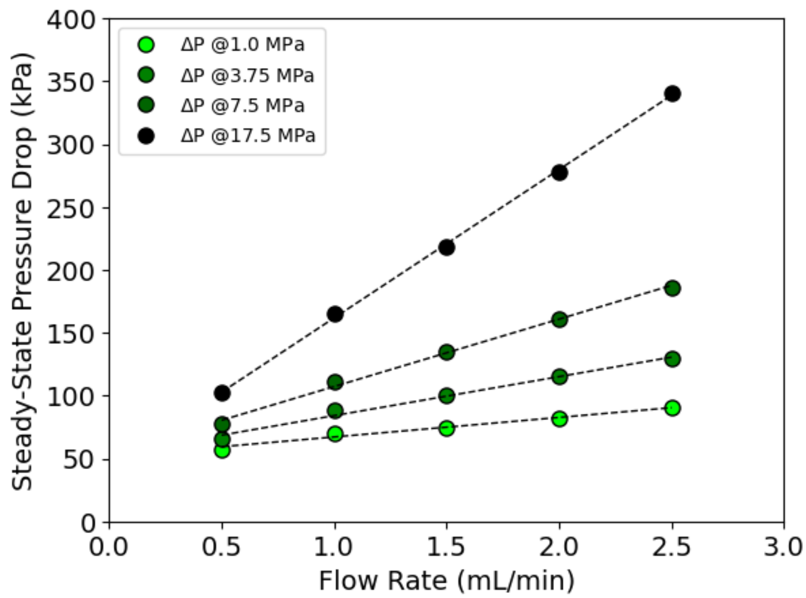


Figure 7.14. Linear relationship between the volumetric flow rate $Q$ and the average pressure gradient $\overline{\nabla P}$ across all isotropic stress stages. The consistent linearity validates the negligible impact of nonlinearity in the flow tests, confirming the accuracy of the hydraulic aperture measurements in 3D-printed fractured reservoir rock analogues.

### 7.5. Deformation of Fractured Porous Media

This section delineates the deformation patterns observed in 3D-printed fractured reservoir rock analogues under the influence of isotropic effective stress. As outlined earlier, the samples, saturated with canola oil, were encased in the triaxial cell, with the entire system maintained at a constant 40°C. Isotropic confining stress was systematically increased in steps from 1 MPa to 18.5 MPa, with the pore pressure consistently held at 1 MPa. Notably, during intervals of 1, 3.75, 7.5, and 17.5 MPa effective stress, a pause was instituted to allow the stabilization of volumetric strain. Deformation under such stress is typically characterized by two distinct yet consecutive phases: immediate deformation and creep. Immediate deformation occurs rapidly under the applied stress, accounting for approximately 90% of the total deformation. This is primarily attributed to the rapid reorientation and displacement of grains and fractures within the rock, leading to a significant yet transient deformation phase. Following this initial phase is the creep — a slower, time-dependent deformation that continues even when the applied stress is held constant. This phase contributes to the remaining 10% of the total deformation. During the creep, micro-cracking and the sliding of grains at the microscopic level contribute to the ongoing deformation. However, this process diminishes over time as the rock structure attains a new equilibrium state under the constant stress.

The measurements of deformation versus stress were specifically taken at a steady state, where the rate of deformation was reduced to a minimum, and the rock was considered stable. This steady state was achieved when the immediate and creep deformations had largely occurred, and further deformation was minimal. It is at this point that the structural and mechanical changes within the rock under the applied stress are deemed to be adequately stable for measurement. This ensures that the recorded deformation is representative and reproducible, offering insights into the rock's mechanical behavior under varying isotropic stresses. Figure 7.15 illustrates the volumetric strain of the 3D-printed fractured reservoir rock analogues at varying effective stress levels, with blue markers representing the intact rock and green triangles indicating the fractured rock.

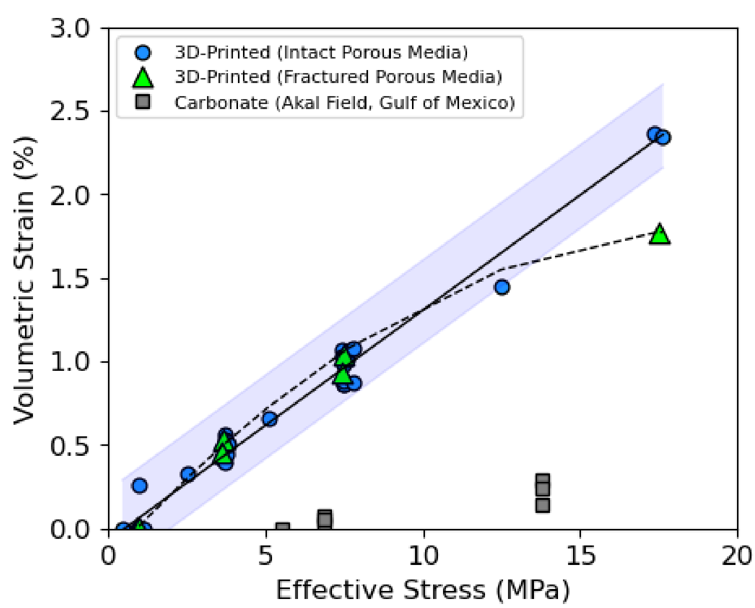


Figure 7.15. Volumetric strain responses of 3D-printed fractured and intact reservoir rock analogues at varying effective stress levels.

Both the intact and fractured rocks exhibited linear behavior up to 12 MPa effective stress. Beyond this point, the intact rock continued its linear deformation, whereas the fractured rock's deformation slope decreased. This divergence is attributed to the assumption that the fracture closes at this stress level, limiting further deformation of the fractured medium. The stress-strain experimental data for the intact rock showcased a linear relationship, expressed by the equation $\varepsilon_{vm} = 0.1373\sigma' - 0.0743$. In contrast, the fractured samples displayed non-linear behavior, characterized by a polynomial fitting curve $\varepsilon_{vf} = -0.0054\sigma'^2 + 0.2064\sigma' - 0.1866$. When compared to carbonate rock, the 3D-printed reservoir rock analogue underwent five times more deformation.

The evaluation of bulk compressibility, $C_{bc}$, was conducted using Equation 6.4, as proposed by Zimmerman et al., (1986). A non-linear decrease in bulk compressibility was observed, correlating with an increase in effective stress. This pattern is evident in both intact and fractured samples. This trend is graphically demonstrated through a power-law fitting curve for the intact sample $C_{bcm} = 0.0025\sigma'^{-0.269}$(represented by the black solid line), and the exponential decay curve for the fractured sample $C_{bcf} = 0.0022e^{-0.068\sigma'}$(dashed line). The contrasting behaviors of the intact and fractured samples under varying levels of effective stress provide critical insights into the inherent mechanical and structural complexities of these distinct rock forms.

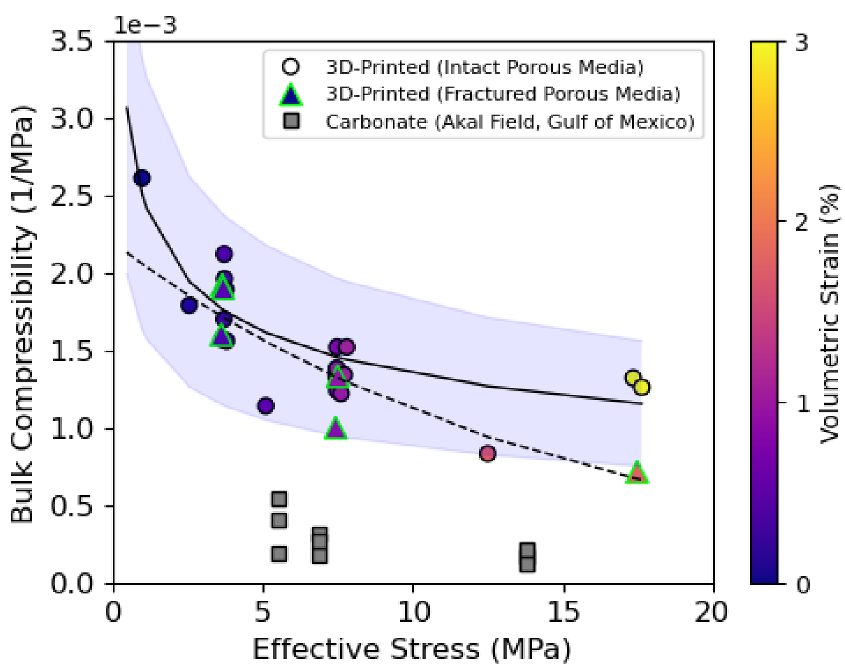


Figure 7.16. A comparative analysis of the bulk compressibility for the intact and fractured rock samples under varied effective stress levels.

## 7.6. Effects of Normal Stress on Flow Properties of Fractured Porous Media

### 7.6.1. Porosity and Absolute Permeability of Intact Rock

This section examines the impact of isotropic stress on the single-phase flow properties, namely porosity and absolute permeability, of the 3D-printed reservoir rock analogues. The stress-strain dependent porosity for the intact rock sample was preliminarily estimated at an average of 22.5%, derived from mass measurements conducted prior to testing. Dynamic porosity was subsequently calculated using Equation 7.6, yielding results as functions of both effective stress (Figure 7.17a) and volumetric strain (Figure 7.17b). These calculations were performed for multiple samples at the stress stages outlined in Section 7.5, corresponding to points where volumetric deformation exhibited consistency relative to the effective stress. It is noteworthy that the data points displayed a 2% scatter in porosity values, reflecting the margin of error or uncertainty associated with measuring the pore space of the 3D-printed rock analogue. This variance equates to an approximate fluid volume of 2 mL, serving as a quantifiable measure of the assessment's precision and reliability. The depicted solid lines in the figures represent linear trends that capture the dynamic porosity variations effectively, expressed as $\emptyset = -0.1059\sigma' + 22.722$, in relation to effective stress, and $\emptyset = -0.7642\varepsilon_v + 22.675$, concerning volumetric strain. These linear models provide a simplified yet accurate portrayal of the intricate interactions between effective stress, volumetric strain, and dynamic porosity in the context of intact 3D-printed reservoir rock analogues.

The initial absolute permeability of the intact rock samples was measured at an average of ~150 mD at the initial 1 MPa effective stress. Since the volumetric strain at this stage was minimal, it was considered negligible, aiding in reducing the sensitivity of the rocks during the initial saturation process. Figure 7.18a illustrates the relationship between dynamic absolute permeability and effective stress, with the color in the data points indicating the volumetric strain. Conversely, Figure 7.18b displays the permeability in relation to the volumetric strain. The data indicates a reduction in absolute permeability from approximately 150 to 40 mD, occurring at a rate of 7 mD/MPa (as seen in Figure 7.18a) or 45 mD per 1% volumetric deformation (Figure 7.18b). The solid lines in the figures delineate the trends that encapsulate the dynamic nature of the stress-strain dependent permeability, represented by equations $k_{m(\sigma')} = 139.19e^{-0.059\sigma'}$ and $k_{m(\varepsilon_v)} = 135.55e^{-0.438\varepsilon_v}$, respectively. Both curves exhibit an exponential fit, and the filled areas delineate the certainty regions. When these results were compared with data from a Berea sandstone rock—tested under analogous conditions and using identical equipment—a notable correlation was evident, particularly in the context of absolute permeability relative to volumetric strain (Sanchez-Barra et al., 2022).

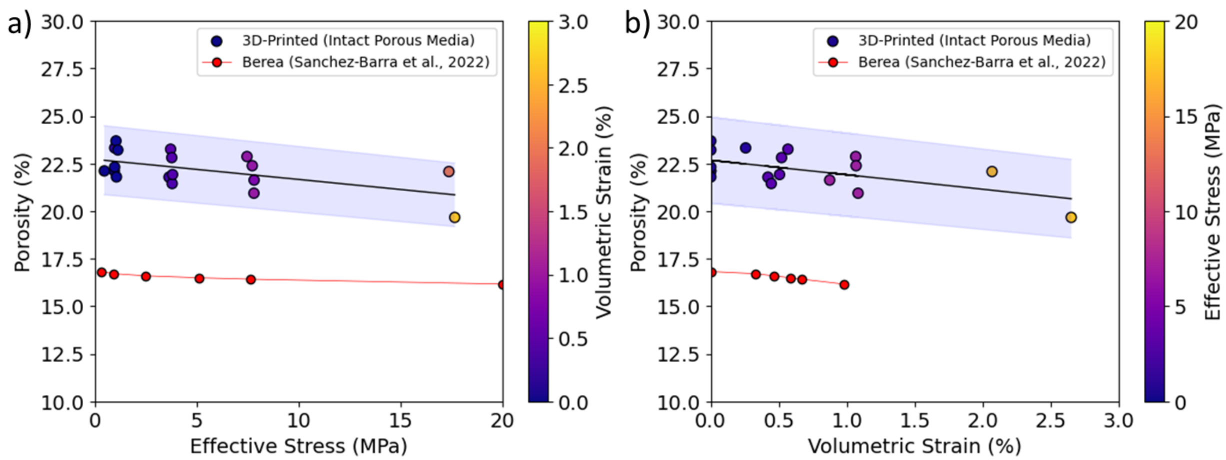


Figure 7.17. Dynamic porosity of the 3D-printed fractured reservoir rock analogues calculated as a function of effective stress (a), and volumetric strain (b).

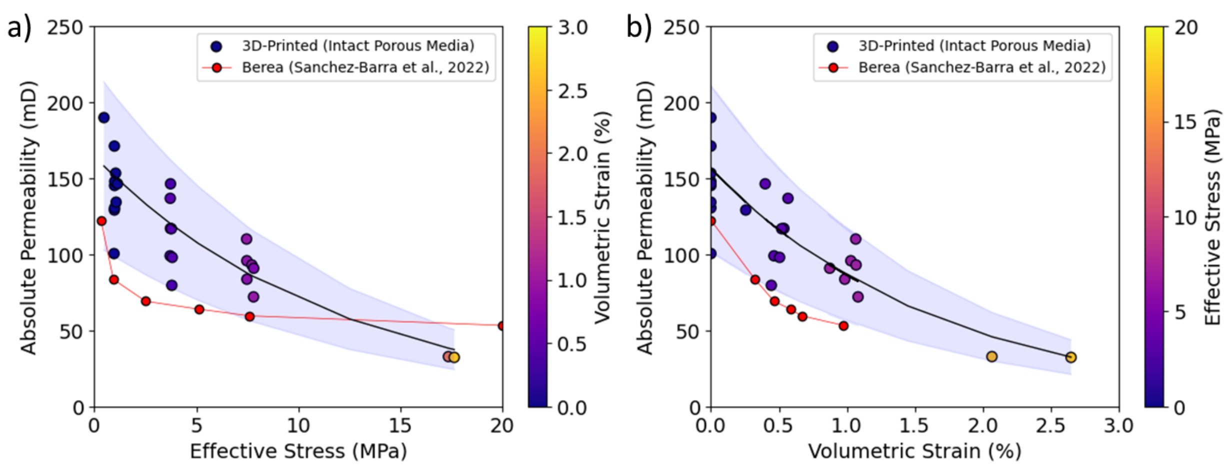


Figure 7.18. Dynamic absolute permeability of 3D-printed reservoir rock analogues illustrated in relation to effective stress (a) and volumetric strain (b).

The absolute permeability was normalized to facilitate a more effective comparison with the properties of natural rock, in this case, Berea sandstone. The data revealed similar patterns between the Berea sandstone and the 3D-printed rock analogues under stress-strain increments (Figure 7.19). However, the former exhibited higher sensitivity during initial increments but eventually stabilized into a constant behavioral pattern. In contrast, the 3D-printed rock analogue demonstrated a progressive, gradual response to the applied stresses and strains. This finding underscores the potential applicability of 3D-printed rock analogues in geoscientific research. Researchers can subject these analogues to deformations that mirror those occurring naturally in the field, yet, these tests can be conducted under laboratory conditions optimized for precision and control, such as those at lower effective stresses.

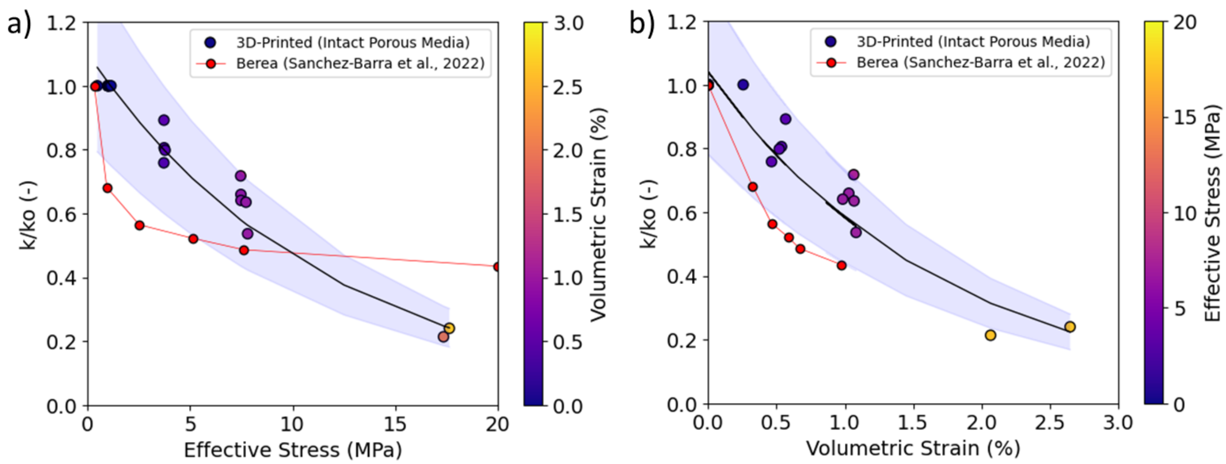


Figure 7.19. A comparison of normalized absolute permeability for Berea sandstone and 3D-printed rock analogues, illustrating their distinct responses to varying stress-strain increments.

### 7.6.2. Absolute Permeability of Fractured Rock

The fractured rock samples exhibited a higher sensitivity to stress and strain compared to their intact counterparts. At a low effective stress of 1 MPa, permeability was approximately 3000 mD, but it decreased to 250 mD at 17.5 MPa effective stress, following a power-law trend as depicted in Figure 7.20. The equations $k_{f(\sigma')} = 2715.8\sigma'^{-0.918}$ and $k_{f(\varepsilon_v)} = 492.79\varepsilon_v{}^{-0.309}$ represent the permeability in relation to effective stress and volumetric strain, respectively. Initially, the fracture contributed to 95.3% of the flow of the bulk behavior of the fractured porous media, which was later reduced to 84% at higher stress levels. Interestingly, the fractured rock analogues exhibited only 1.7% deformation across the examined stress levels, which was unexpectedly lower than the

2.5% deformation observed in intact rocks. This anomaly could be explained by the early closure of the fracture under initial stress levels, leading to a state of equilibrium. In this state, the fracture surface area was in complete contact, and the applied stress was insufficient to further reduce or deform it, or affect the intact portion of the rock.

The fracture's sensitivity plays a critical role in reservoir geomechanics as it can cause a drastic increase or decrease in the permeability of fractured porous media during typical hydrocarbon production processes. When a fracture is initiated or reactivated, the flow regime shifts from being dominated by the porous matrix to being fracture-dominated, with the matrix or intact portion contributing only 5-15% to the overall flow.

This scenario is typical in naturally fractured reservoirs, such as the case study depicted in Chapter 3, where the presence of fractures can significantly enhance overall permeability and fluid flow paths. Naturally fractured reservoirs are characterized by networks of such fractures, which can be open or filled with mineral deposits that affect the storage and migration pathways of hydrocarbons. The behavior of these reservoirs is complex due to the dual-porosity system in which the primary porosity is in the matrix and the secondary porosity is in the fractures (Lucia, 2007). In these systems, the fractures provide high-permeability conduits, while the matrix accounts for the majority of the pore volume, thus holding significant amounts of hydrocarbons.

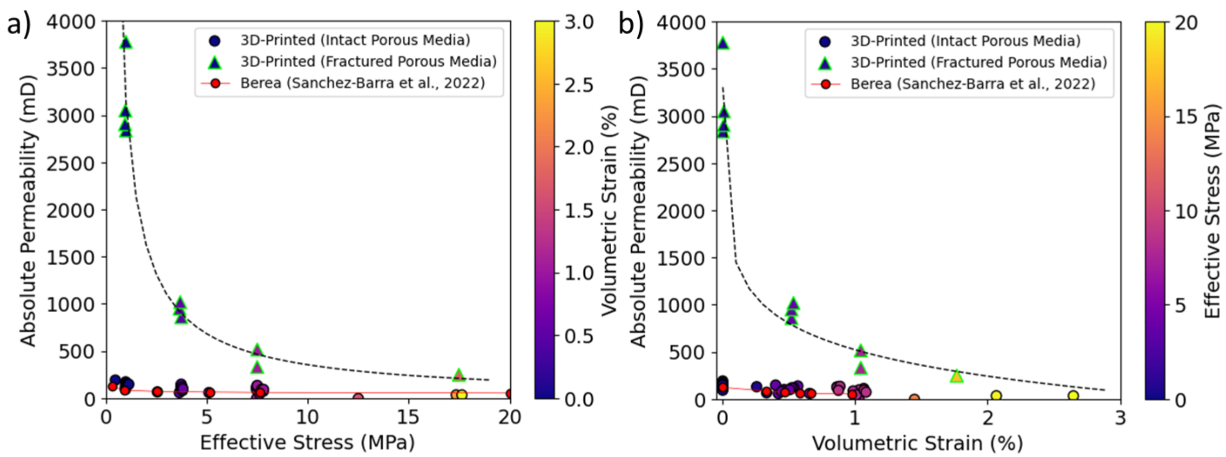


Figure 7.20. Dynamic permeability of the 3D-printed fractured reservoir rock analogues. The figure illustrates the variation in permeability under different levels of effective stress, highlighting the substantial impact of fractures on the rocks' permeability and deformation characteristics.

### 7.6.3. Sensitivity of Fracture Aperture

The hydraulic aperture was measured during the absolute permeability test at the same effective stress levels as in previous flow tests. This measurement followed the principles of the parallel plate model, or cubic law, as detailed in Equation 7.13. Initially, the hydraulic aperture was calculated to be 0.27 mm. This value decreased to 0.08 mm across the various stress stages, as illustrated in Figure 7.21. Notably, the hydraulic aperture was most sensitive to stresses below 5 MPa; beyond this threshold, it remained nearly constant. Figure 7.21 also depicts the progressive closing of the hydraulic aperture as the deformation of the bulk fractured porous media advanced. This decrease occurred at a rate of 0.19 mm/MPa, or 0.11 mm per 1% increase in volumetric strain. Furthermore, the reduction in hydraulic aperture followed a power-law relationship, depicted by the dashed line in the graph and mathematically expressed by the equation $b_h = 0.153x^{-0.182}$.

These findings show that once a fracture forms within an intact rock, the overall flow becomes predominantly governed by the fracture, a concept elaborated in the previous section. A fracture, even with a minor hydraulic aperture of 0.27 mm, can dictate up to 95.3% of the flow dynamics within a fractured porous medium. This insight is crucial for processes such as hydraulic fracturing, enhanced oil recovery, and shale gas production. The significant role of even small fractures in controlling flow underscores the necessity for precise fracture management to optimize extraction processes. Effective management ensures not only increased efficiency in oil and gas extraction but also reduced environmental impact. It also contributes to the enhancement of fluid injections and oil displacement optimization.

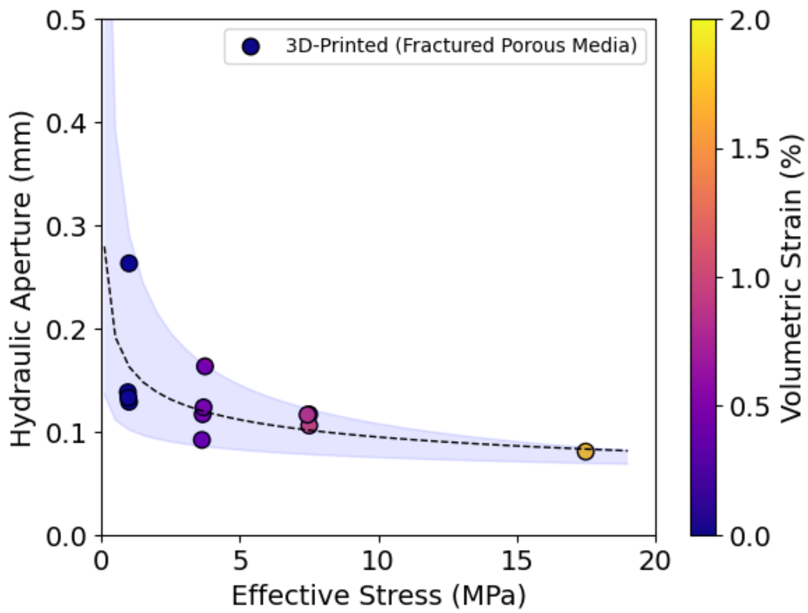


Figure 7.21. The stress- and strain-dependent hydraulic aperture of 3D-printed fractured reservoir rock analogues.

### 7.6.4. Drainage Relative Permeability

Transitioning from single-phase to multiphase flow reveals a layer of complexity in the behavior of 3D-printed fractured reservoir rock analogues. Drainage relative permeability tests were performed using canola oil and nitrogen gas at effective stress levels of 7.5 and 17.5 MPa, as detailed in Figure 7.22. These levels induced deformations of 1% and 2.5% in the intact rock, and 1% and 1.7% in the fractured rock, respectively. The aim was to ascertain the fracture's contribution to flow and its impact on the displacement of two immiscible fluid phases and to understand how this contribution is influenced by varying normal stresses. The individual relative permeability points versus the saturation of the wetting phase were fit using the modified Brooks-Corey model (Brooks and Corey, 1966), which estimates the relative permeability curve as a power-law function of the wetting phase saturation.

$$kr_w = k_{rw} - max\left(\frac{s_w - s_{wir}}{1 - s_{wir} - s_{nwr}}\right)^{n_w}, \tag{7.14}$$

$$kr_{nw} = k_{rnw} - max\left(\frac{1 - s_w - s_{wir}}{1 - s_{wir} - s_{nwr}}\right)^{n_{nw}}, \tag{7.15}$$

where $s_{wir}$ is the irreducible wetting phase saturation and $s_{nwr}$ is the residual non-wetting phase saturation. The powers $n_w$ and $n_{nw}$ are fitting constants to calibrate the equations with the experimental data.

This study revealed a prominent leftward shift in the drainage relative permeability curves as stresses increased in the intact material (Figure 7.22a). This shift indicated a reduction in the irreducible wetting phase saturation from 0.68 to 0.58, equivalent to 10% volume of the saturating fluid. This decrease was attributed to the rock's deformation under increased stress, leading to reduced porous media. As the pore space is reduced, the viscous pressure gradients increased and the non-wetting phase (nitrogen gas) flow path expanded, invading additional regions and enhancing the displacement of the wetting phase fluid (canola oil) through a drainage process. The dynamic behavior of these pressure gradients was observed in the pressure drop across the specimen (Figure 7.22b), where the lower curve represents the pressure drop at the initial stress condition. As the stress level increases, a proportional increase in the pressure drop across the specimen occurs, driving the physical process previously described.

The drainage relative permeability curves for the fractured porous media exhibited a similar yet more pronounced behavior, as depicted in Figure 7.22c. Initially, at 7.5 MPa and with 1% volumetric deformation, the relative permeability curves indicated that the injection of nitrogen gas displaced merely 8.58% of the volume of the saturating fluid. Considering that the fracture volume under these stress conditions represented 0.82% of the total rock volume, the drainage displacement effectively swept oil from the fracture and an additional 7.76% from the matrix. Subsequently, under higher stress and strain conditions—at 17.5 MPa and 1.7% volumetric deformation—the endpoints of the relative permeability curves demonstrated a marked reduction in the wetting phase saturation of the fractured porous media. The irreducible wetting phase saturation decreased to 0.73, signifying a reduction of 18.04% from the lower stress conditions. In this instance, the nitrogen gas displaced 26.62% of the oil within the rock, of which only 0.68% was attributed to the fracture, leaving 25.94% extracted from the matrix. These changes occurred due to structural alterations, specifically in the distribution of the largest apertures and the critical paths within the fractured porous media.

During the simultaneous injection of the two fluid phases, the immiscible non-wetting phase (nitrogen gas) first occupies the largest fracture apertures before moving to progressively smaller ones. As the non-wetting phase permeates these narrower pathways, it forms a continuous flow channel. This allows both the wetting and non-wetting phases to traverse the fracture network. The wetting phase is then relegated to a "critical path"—the narrowest aperture in the network of larger apertures that remains open. This critical path sustains a percolating area until it is filled by the non-wetting phase, at which point the flow of the wetting phase is obstructed, as explained by Pyrak-Nolte et al., (1991).

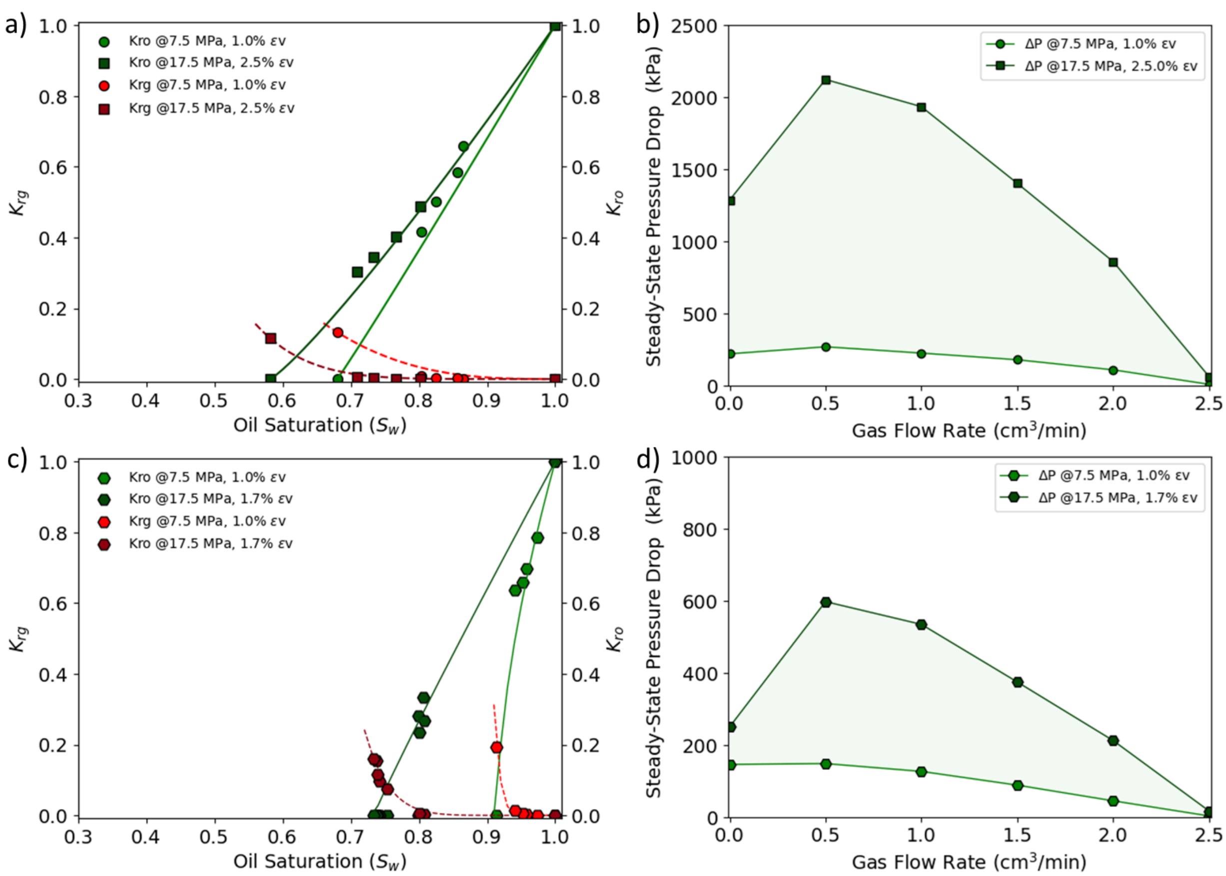


Figure 7.22. Evolution of the relative permeability in intact and fractured porous media under different normal stress conditions. These curves contrast the initial state with that expected after two decades or more of hydrocarbon production.

Furthermore, Figure 7.23 illustrates the progression of oil recovery from the fractured porous media as a function of the nitrogen gas flow rate. The darker regions in the figure reflect the increase in oil recovery concurrent with the increasing stresses. The selected stress and strain conditions aim to reflect the evolution of the fractured porous media's drainage relative permeability curves, from the commencement of hydrocarbon production to the conditions observed in the reservoir after two decades or more, consistent with the Akal KL case study presented in Chapter 3. This long-term perspective captures the typical alterations observed during the extensive timeline of hydrocarbon production.

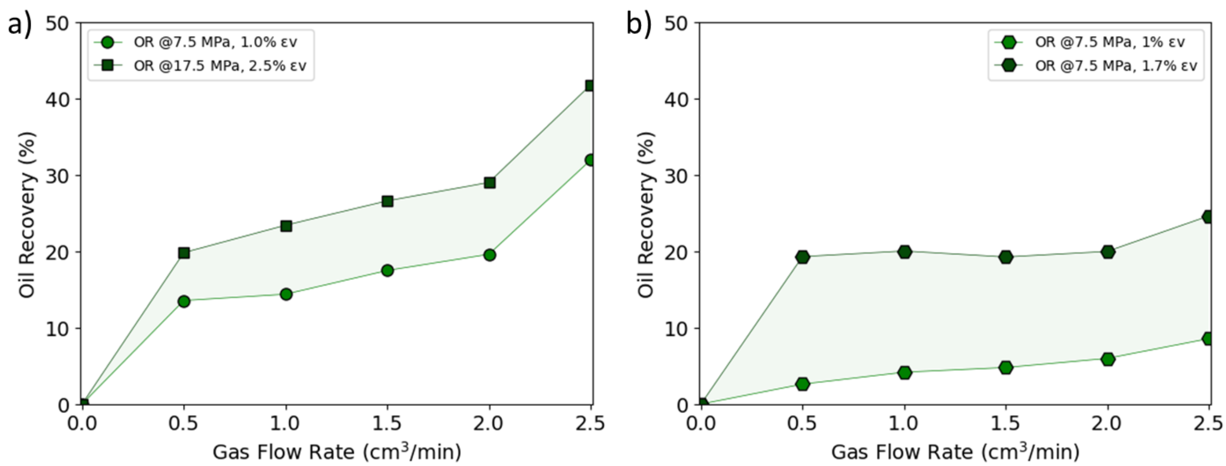


Figure 7.23. Progressive evolution of oil recovery from the fractured porous media as a function of nitrogen gas flow rate. The figure highlights the correlation between increased nitrogen gas injection and oil displacement. Darker regions indicate the enhanced oil recovery associated with the progression of applied stresses.

### 7.6.5. Drainage Capillary Pressure

The drainage capillary pressure tests (in which the non-wetting phase displaces the wetting phase) were performed at the same stress and strain levels as the relative permeability tests. The procedure, as detailed in Section 7.4.4, utilized the Porous Plate Method. After full saturation of the samples with canola oil, nitrogen gas was injected at a consistent flow rate. As the gas permeated the pore spaces, the injection pressure increased until a breakthrough occurred, after which the nitrogen pressure decreased and stabilized (see Figure 7.24). At this point, the flow of the wetting phase fluid ceased, allowing the steady-state drainage capillary pressure to be measured. Figure 7.24 captures the transient behavior of the breakthrough pressure prior to stabilization in the intact material. Initially, at 7.5 MPa and with 1% volumetric deformation, the gas pressure reached 45 kPa before breaking through the core specimen. Upon exiting at the downstream end, it displaced the oil saturating the rock's pore space (refer to Figure 7.24a). At the higher stress condition of 17.5 MPa and 2.5% volumetric deformation, the breakthrough pressure increased to ninefold (400 kPa) compared to the lower stress level, resulting in an additional 19% oil displacement (see Figure 7.24c). This results indicates that during the transient phase, a significantly larger fraction of oil was displaced than at steady-state conditions. This distinction is vital as it offers a more accurate representation of reservoir conditions compared to other conventional laboratory tests that do not utilize analogous procedures.

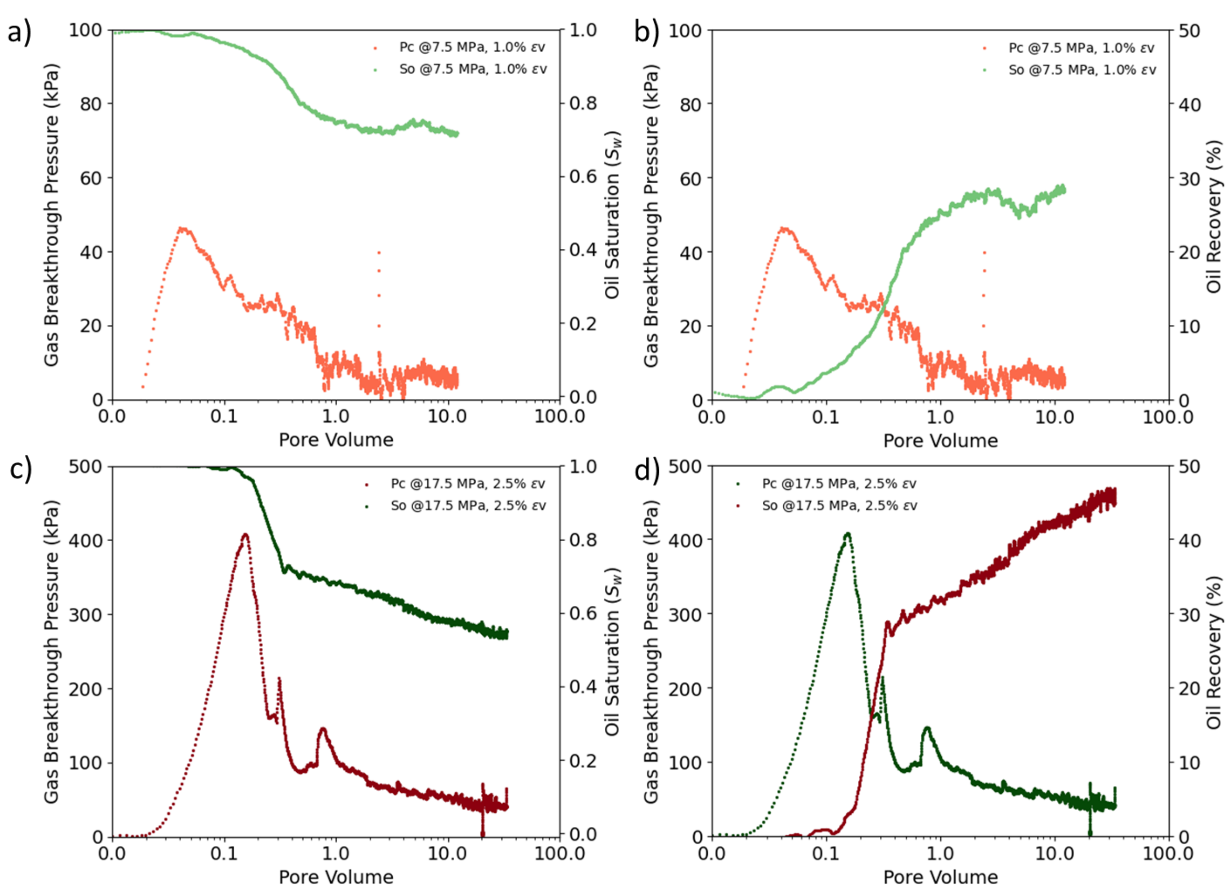


Figure 7.24. Sensitivity of breakthrough pressure and oil displacement in intact porous media. This figure illustrates the response of gas breakthrough pressures and consequent oil displacement under varying normal stress conditions, with red curves representing gas pressure evolution and green curves depicting the volume of oil displaced from the core specimen.

Figure 7.25a illustrates the steady-state drainage capillary pressure. Following the breakthrough, the nitrogen pressure decreased and eventually stabilized, indicating the attainment of steady-state conditions. The differential pressure across the specimen stabilized after 12 pore volumes at the lower effective stress level and after 30 pore volumes at the higher stress stage. At steady-state conditions, the flow of the wetting phase became immobile, and the drainage capillary pressure at the upstream face of the specimen was recorded. As the effective stress increased, so did the drainage capillary pressure, which indicated a reduction in pore space. These changes provided additional energy, lowering the residual wetting phase saturation and resulting in a leftward shift of the curves. It was also observed that the initial point exhibited a greater displacement of the wetting phase compared to subsequent points, which was attributable to the transient effects previously described.

Measuring capillary pressure within fractured porous media presented distinct challenges. At the applied stress levels of 7.5 and 17.5 MPa, the fracture apertures were reduced to 0.11 and 0.08 mm, respectively. These narrow openings produced differential pressures that were too fine to discern within the uncertainty range of the pressure transducers. Consequently, Figure 7.25b presents the drainage capillary pressure measurements derived from the relative permeability curves. This particular data point corresponds to 100% gas injection at irreducible wetting phase saturation. The capillary pressure points for the fractured porous media closely aligned with those of the intact media, yet, as anticipated, indicated lower residual saturations of the wetting phase due to the majority of oil being displaced from the fractures and their adjacent areas. The drainage capillary pressure points versus the saturation of the wetting phase were fit using the modified Brooks-Corey model (Brooks and Corey, 1966). This model predicts the capillary pressure curve as a power-law function of wetting phase saturation, represented by the equation:

$$P_c = P_e \left( \frac{1 - s_w - s_{wir}}{1 - s_{wir} - s_{nwr}} \right)^{\beta}, \tag{7.16}$$

where $P_c$ is the drainage capillary pressure, $P_e$ is the entry capillary pressure, $s_{wir}$ is the irreducible wetting phase saturation, and $s_{nwr}$ is the residual non-wetting phase saturation. The exponent $\beta$ serves as a fitting parameter to align the model with the experimental data.

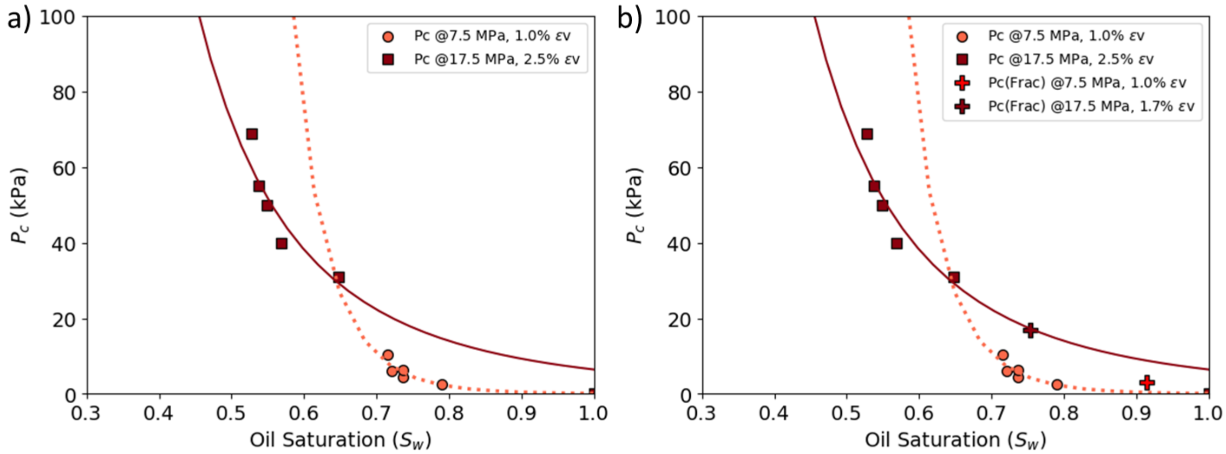


Figure 7.25. Comparison of steady-state drainage capillary pressure in intact and fractured porous media across varied normal stress conditions.

Figure 7.26 depicts the progression of oil recovery as a function of the nitrogen gas flow rate during the drainage capillary pressure tests. The darker region in the figure represents an increase in oil recovery corresponding to escalating stress levels. Unlike the relative permeability tests, which were conducted under full steady-state conditions, the capillary pressure tests revealed an initial transient phase. This phase led to a more substantial displacement of the wetting phase at the beginning of the nitrogen injection.

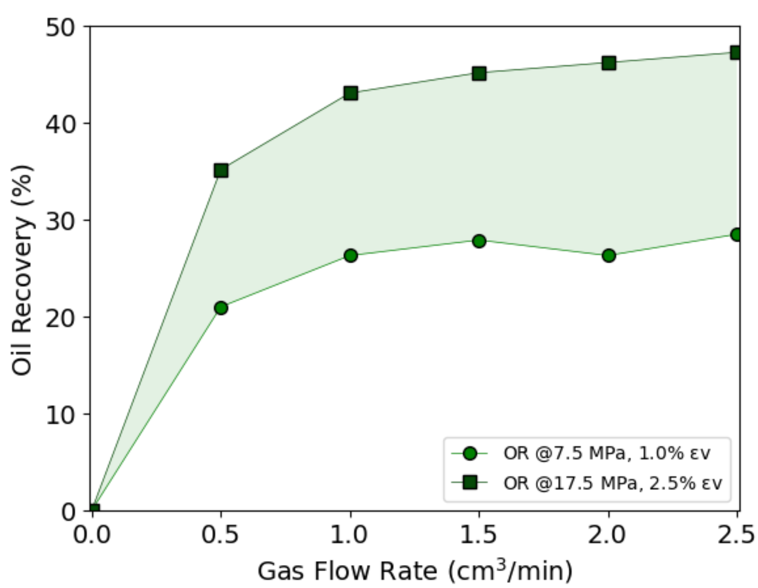


Figure 7.26. Oil recovery during drainage capillary pressure testing at increasing stress levels.

### 7.6.6. Matrix-to-fracture Mass Transfer

The mass transfer from the matrix to the fracture under stress conditions in fractured porous media shows distinct behaviors, as revealed through the analysis of drainage relative permeability curves. At a moderate stress of 7.5 MPa, combined with a volumetric deformation of 1%, the data suggests that nitrogen gas injection managed to displace a modest 8.58% of the saturating fluid's volume. This displacement encompasses oil swept from both the fractures, which accounted for 0.82% of the rock volume, and an additional 7.76% from the matrix, highlighting the interaction between matrix and fracture during the drainage process. However, this interaction becomes more pronounced under higher stress and strain. At 17.5 MPa stress and 1.7% volumetric deformation, there was a substantial decrease in irreducible wetting phase saturation, highlighting an enhanced oil displacement of 26.62% from the rock. A smaller fraction (0.68%) of this displacement was due to the fracture volume, with the majority (25.94%) being extracted from the matrix. This significant shift, suggests notable structural changes within the fractured porous media, affecting the distribution and connectivity of apertures and critical paths that facilitate mass transfer. Figures 7.27a and 7.27b present the changes in mass transfer from the matrix to the fracture for lower and higher stresses, respectively.

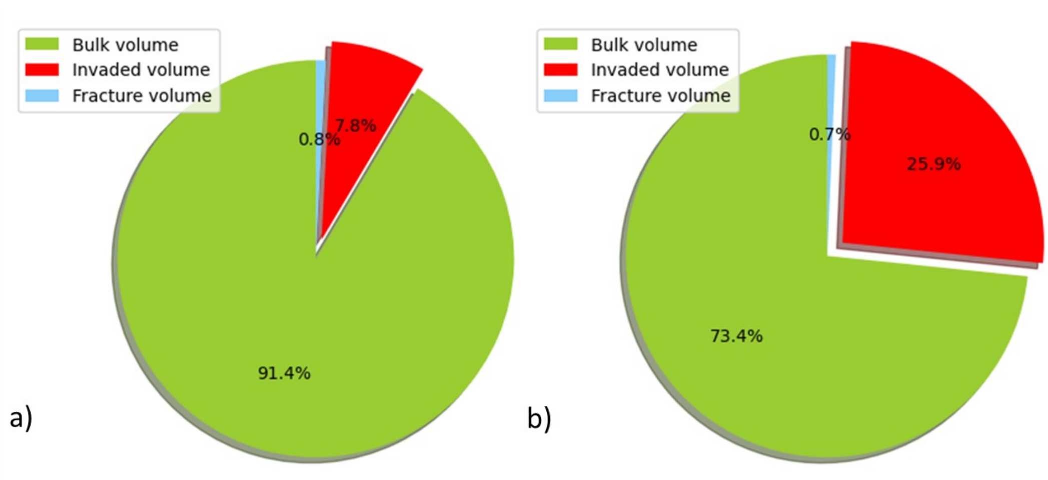


Figure 7.27. Mass transfer from matrix to fracture under different stress conditions.

### 7.7. Influence of Shear Stress on Flow Properties of Fractured Porous Media

This section examines the effects of shear stress and strain on the multiphase flow properties of 3D-printed intact and fractured reservoir rock analogues. The samples were placed within the triaxial cell, and the confining effective stress was isotropically increased to 7.5 MPa, while maintaining the pore pressure at 1 MPa. At this stage, axial loading was incrementally applied to evaluate the multiphase flow properties under triaxial compression. Figure 7.28 presents the principal stress plot indicating the peak strength of the 3D-printed rock samples. The peak strength envelope was estimated using the generalized Hoek-Brown criterion for shear failure, complemented by the Mohr-Coulomb failure criterion, as elaborated in Chapter 6, Section 6.6. Crack initiation and crack damage thresholds were identified at approximately 39% and 69% of the peak strength, respectively, discerned by the deviation of axial and radial strains from linearity (Hoek and Martin, 2014). The green data points in Figure 7.28 illustrate the stress path undertaken during the core flooding experiments. After isotropically increasing the effective stress to 7.5 MPa, the first series of multiphase flow tests were performed. Subsequently, axial loading was increased to 50% and then 87% of the average peak strength, at which points additional multiphase flow tests were executed.

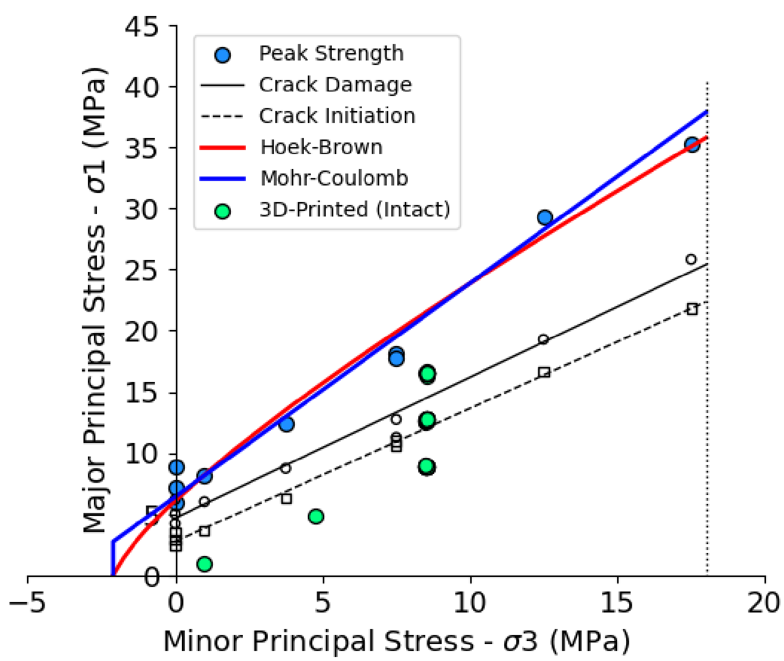


Figure 7.28. Principal stress plot and peak strength envelope of 3D-printed reservoir rock analogues.

### 7.7.1. Absolute Permeability of Intact Rock

The absolute permeability of the intact rock samples was assessed in relation to the evolution of deviator stress as a function of axial loading, as depicted in Figure 7.29. Initially, permeability was determined under a deviator stress of 1.42 MPa and 0.05% axial strain, closely approximating the isotropic effective stress conditions at 7.5 MPa (Stage 1). Subsequently, the deviator stress was increased to 5.2 MPa with a corresponding axial strain of 0.28%, equivalent to 50% of the average peak strength (Stage 2), at which point the absolute permeability was measured again. The final measurement was taken when the deviator stress reached 87% of the average peak strength, corresponding to a deviator stress of 9.03 MPa and an axial strain of 0.76% (Stage 3). These measurements indicate that the permeability change is likely due to axial compression of the pore network, without the formation of new fractures that could lead to fracture flow or an increase in permeability.

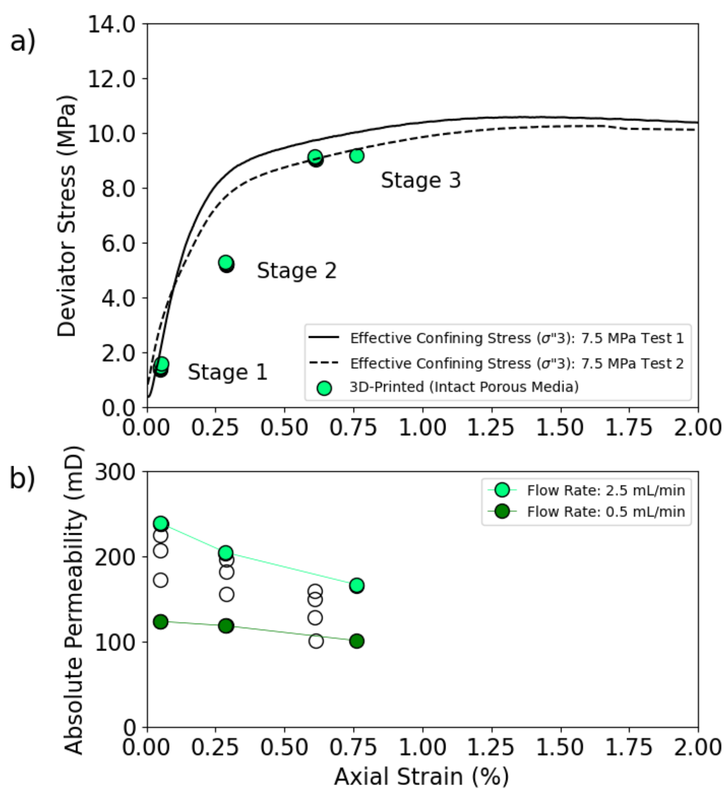


Figure 7.29. Evolution of absolute permeability with deviator stress and axial strain in intact rock. Permeability was measured at key stages of axial loading, reflecting isotropic conditions, 50% of average peak strength, and 87% of peak strength.

The absolute permeability exhibited a decrease as a function of axial loading, which was also influenced by the flow rate due to resultant changes in pore pressure, as shown in Figure 7.30. At approximately 0% axial strain, representing isotropic conditions, absolute permeability was recorded at 123 mD and 238 mD for flow rates of 0.5 mL/min and 2.5 mL/min, respectively. As the axial strain increased, permeability values declined to 100 mD at a flow rate of 0.5 mL/min and to 166 mD at 2.5 mL/min. These variations in permeability can be attributed to the alterations in pore pressure that accompanied the axial loading process. As the pore pressure adjusted in response to the flow rates, it exerted a dynamic impact on the pore spaces within the rock matrix. This fluctuation in pore pressure slightly reduced the effective stress acting on the rock structure. The reduction in effective stress, even though marginal, was sufficient to modify the pore geometry, leading to a measurable change in permeability. This interplay between pore pressure and effective stress is a critical factor in determining the flow characteristics of the rock, as it directly influences the ease with which fluids can navigate through the pore network.

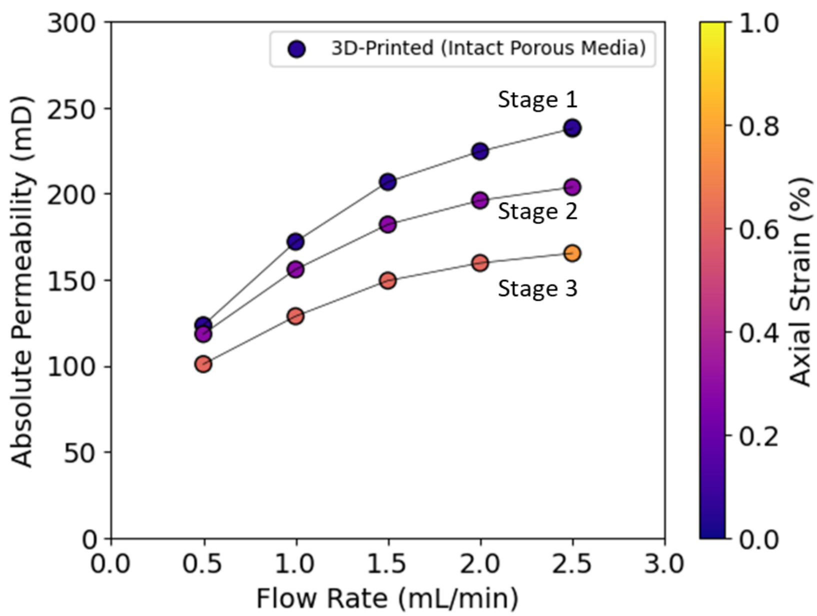


Figure 7.30. Impact of axial loading and flow rate on absolute permeability. The figure illustrates the reduction in permeability as a function of increased axial strain, highlighting how variations in pore pressure due to differing flow rates influence the effective stress within the rock matrix.

### 7.7.2. Absolute Permeability of Fractured Rock

The absolute permeability of the fractured rock samples was measured under the influence of shear stress, as depicted in Figure 7.31, which plots the evolution of deviator stress as a function of the rock's axial strain. The stress path followed during these permeability measurements was consistent with that used in the intact rock testing. Initially, at Stage 1, permeability was assessed under nearly isotropic conditions. Subsequently, at Stage 2, the deviator stress was elevated to 4.25 MPa, resulting in an increase in axial strain to 0.167%. At this stage, the permeability was determined at 41% of the average peak strength observed in the intact material. The deviator stress was further increased to 8.05 MPa at Stage 3, with the axial strain of the fractured rock rising to 0.37%, which corresponded to 77% of the average peak strength of the intact material. During Stage 1, the fractured porous media exhibited an absolute permeability of 2933 mD and a hydraulic aperture of 0.14 mm, consistent with the properties outlined in Section 7.6.2.

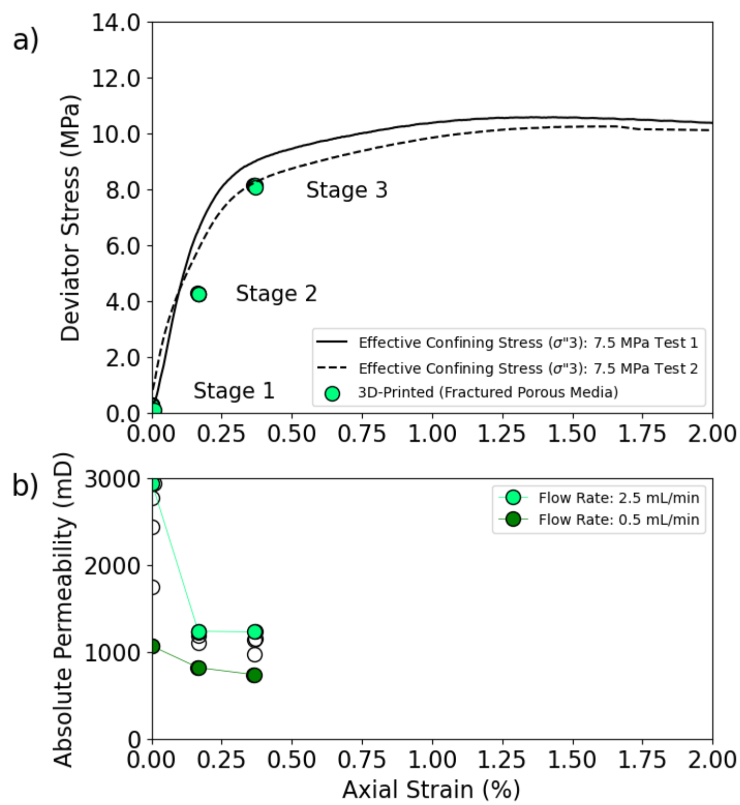


Figure 7.31. Evolution of absolute permeability with deviator stress and axial strain in fractured rock. Permeability was measured at key stages of axial loading, reflecting isotropic conditions, 41% of average peak strength, and 77% of peak strength.

Fractured rock samples exhibited less axial deformation compared to intact samples under similar stress conditions, as demonstrated in Figure 7.31a. This disparity in deformation can be primarily attributed to differences in stress distribution and concentration, fracture behavior, and interactions between the rock and fractures. In intact rock, stress is distributed more uniformly, leading to more significant deformation. In contrast, fractured rock experiences stress concentration around fracture edges, resulting in reduced overall deformation. The vertical fractures, like those used in these tests, often act as slip planes, allowing relative movement under stress, which absorbs energy and further reduces deformation in the rock matrix. This intricate interplay significantly affects the rock's response to deformation under various loading conditions.

Furthermore, fractured rock samples showed increased sensitivity to absolute permeability changes compared to intact samples. At Stage 1, the average absolute permeability was 2033 mD, which decreased to 1026 mD in Stage 2 and further to 987 mD in Stage 3. During these stages, the fracture greatly influenced flow behavior, contributing 91%, 84.3%, and 86% of the total flow for each stage, respectively. The permeability of fractured rocks was highly responsive to stress variations, especially as shearing progressed, which likely affected the fracture geometry. Under shear stress, fractured rocks undergo significant changes in permeability, influenced by factors like fracture aperture, surface roughness, and the development of new flow paths. Such stress-dependent permeability variations are more pronounced in fractured rocks due to their adaptability to stress variations, unlike intact rocks, which have more uniform porosity and less variable flow paths, resulting in less dramatic permeability changes under similar stress conditions (refer to Figure 7.29). Shearing can modify the aperture of fractures, either widening or narrowing them, and directly impact fluid flow. The roughness of fracture surfaces might also change due to shearing, either creating more complex pathways or smoothing surfaces for easier flow. Moreover, shear stress can lead to the formation of new micro-fractures or alter existing ones, creating varied flow paths that enhance or restrict permeability.

A critical observation was the fracture's sensitivity to changes in flow rate during absolute permeability measurements. Figure 7.32 highlights the absolute permeability's sensitivity to flow rate variations. During Stage 1, under isotropic conditions, a notable increase in absolute permeability was observed as the flow rate rose. However, as shearing proceeded, permeability dropped, showing less sensitivity to flow rate changes. The results indicated that increasing the flow rate from 0.5 cm$^3$/min to 1.5 cm$^3$/min led to an apparent opening of the fracture. But as the flow rate further increased to 2.0 and 2.5 cm$^3$/min, permeability decreased slightly and then remained almost constant, suggesting that the fracture may have slid once the threshold of 1.5 cm$^3$/min in flow rate was reached.

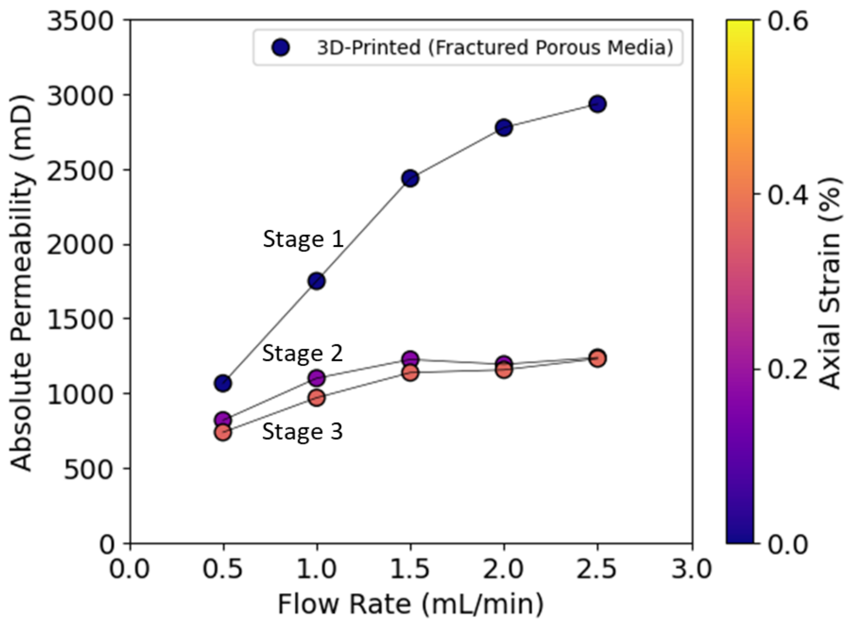


Figure 7.32. Impact of axial loading and flow rate on the absolute permeability of fractured rock samples. The figure demonstrates how permeability varies as a function of flow rate, emphasizing the combined influence of shear stress, strain, and variations in fracture aperture due to different flow rates on the overall flow behavior.

### 7.7.3. Drainage Relative Permeability

The multiphase flow properties of the 3D-printed reservoir rock analogues were also investigated under the influence of shear stress. Drainage relative permeability tests, utilizing canola oil and nitrogen gas, were performed in a manner similar to the procedures previously described, aligning with the same stages as in the absolute permeability testing. Following the completion of the absolute permeability test, the drainage relative permeability test was conducted. Figure 7.33 illustrates the evolution of the relative permeability of the intact rock samples under triaxial stress. Initially, at Stage 1, relative permeability was measured under near-isotropic conditions. Subsequently, the shear stress was increased to 5.2 MPa while the radial stress was kept constant. This increase in shear stress led to an axial strain of 0.28% (0.3% for simplicity), equating to 50% of the peak strength. The relative permeability test was then repeated at this stage. Following this, the shear stress was elevated further to 9.03 MPa, resulting in an axial deformation of 0.76% (0.8%), at which point the relative permeability was measured once more.

The relative permeability exhibited subtle variations across the different stages of axial strain, as depicted in Figure 7.34. The test results indicated that with an increase in axial strain, the differential pressure across the specimen also increased. This increase in pressure suggests a contraction in pore space, leading to reduced permeability (refer to Figure 7.34b). Interestingly, the residual wetting phase saturation appeared to increase with the induction of shearing, transitioning from isotropic conditions to an axial deformation of 0.3%. This increase may imply the formation of a fracture (see Figure 7.34a). The rationale behind this is that the non-wetting phase fluid, nitrogen in this case, tends to flow preferentially through the path of least resistance, such as the largest aperture or a high-conductivity flow path, thereby interacting less with the saturation of the matrix. It is proposed that the generation of a fracture during shearing caused the relative permeability curves to shift to the right, resulting in an increased residual wetting phase saturation. Then, at Stage 3, the axial strain increased from 0.3% to 0.8%. At this stage, the relative permeability curves shifted to the left, suggesting a closure of the potentially recently created fracture. This observation aligns with previous findings where fracture closure led to a reduction in the residual wetting phase saturation, as discussed in Section 7.6.4. The closing of the fracture under increased axial strain further indicates the dynamic nature of fracture behavior under varying stress conditions and its significant impact on the fluid flow characteristics within the rock matrix.

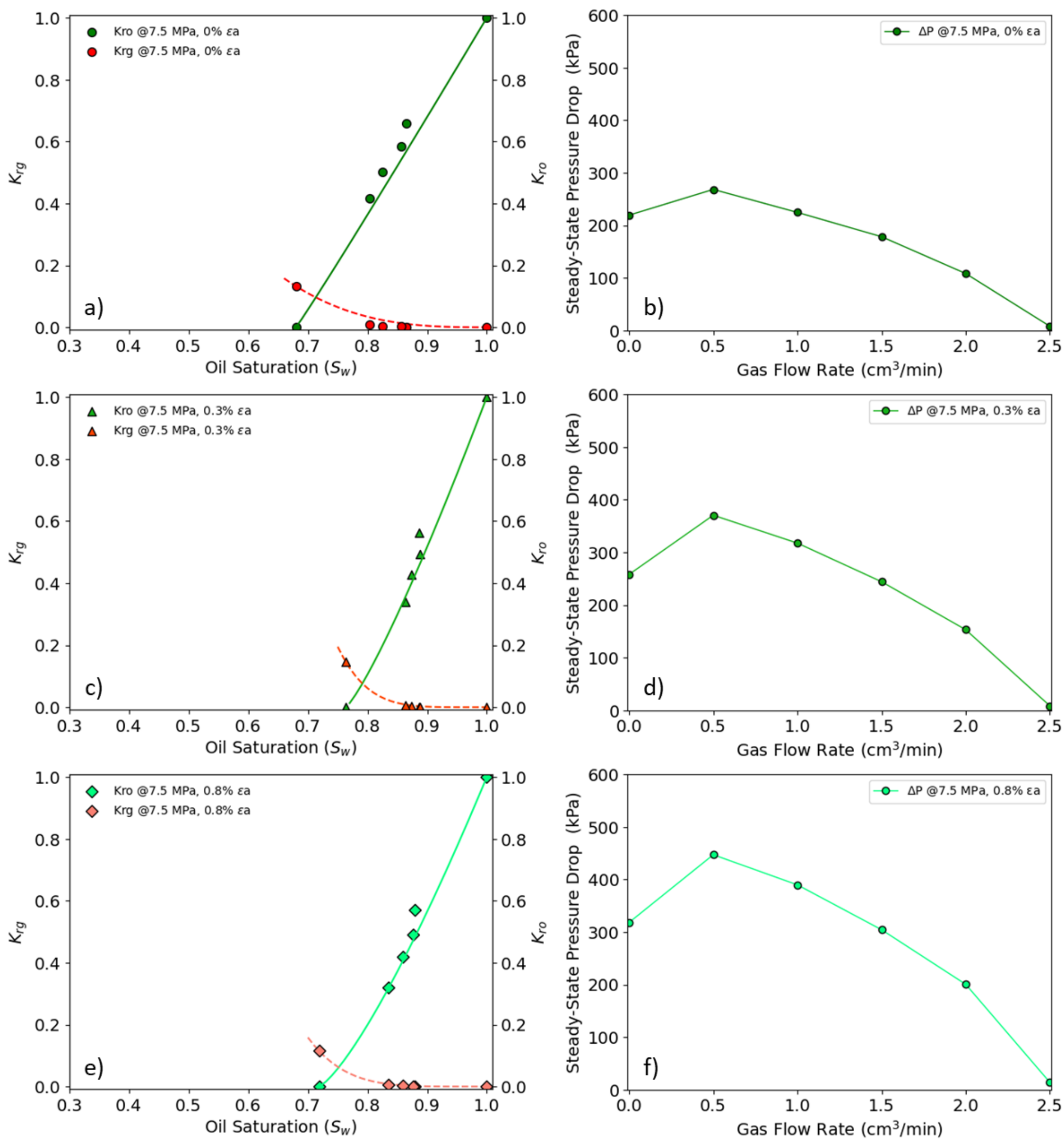


Figure 7.33. Evolution of relative permeability in intact rock under triaxial stress. This graph illustrates how relative permeability changes at different stages of axial strain.

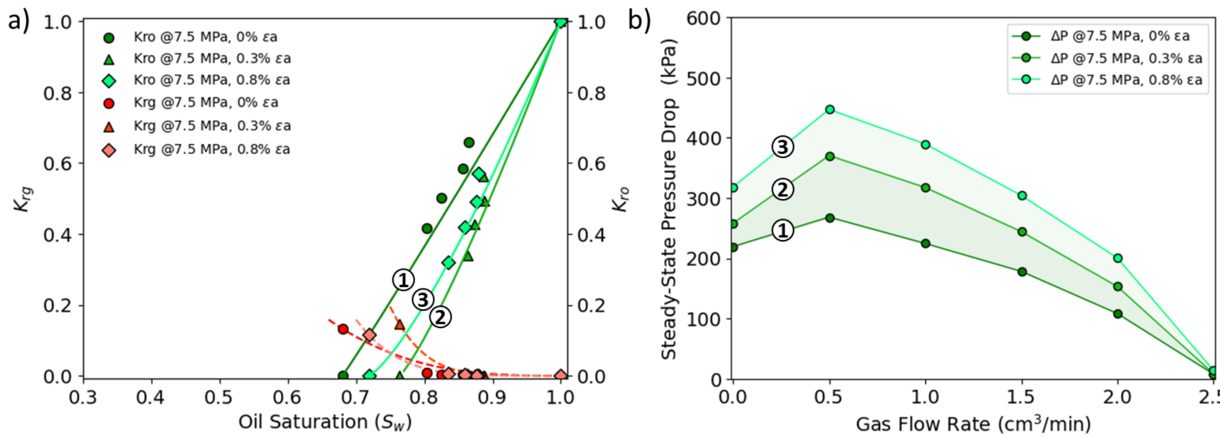


Figure 7.34. Changes in relative permeability under varying axial strain in intact rock samples. This figure demonstrates how relative permeability curves shift in response to increasing axial strain, highlighting the effects of pore space contraction and the potential opening and closure of fractures on residual wetting phase saturation.

The formation of a hypothetical fracture during the shearing process is illustrated in Figure 7.35. Initially, at Stage 1, the sample was intact. As the test progressed and axial stress was increased to 50% of the peak strength in Stage 2, a fracture was hypothesized to have been created. Subsequently, in Stage 3, which corresponds to 87% of the peak strength and involves higher axial strain, the fracture is believed to have closed. This hypothesis is well-supported by the evidence that the crack initiation threshold for the rock samples was determined to be approximately 39% of their peak strength, as detailed in Figure 7.28. Such a fracture behavior under varying axial stresses highlights the dynamic response of the rock matrix to mechanical stress, significantly influencing the overall permeability and fluid flow characteristics within the rock.

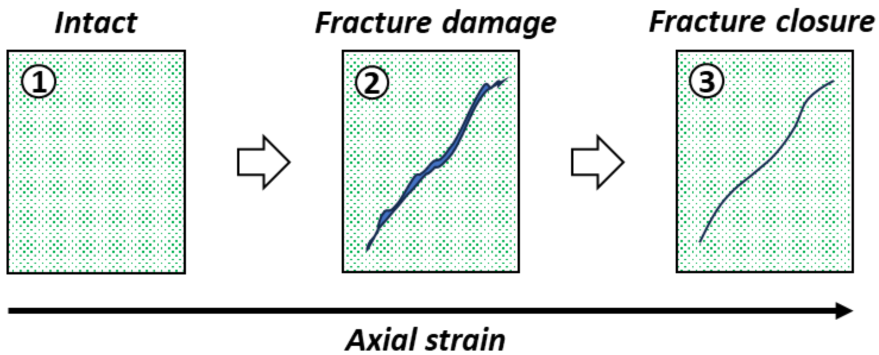


Figure 7.35. Schematic representation of fracture evolution under axial stress in rock samples. This figure depicts the initial intact state at Stage 1, the formation of a fracture at Stage 2 (50% of peak strength), and the subsequent closure of the fracture at Stage 3 (87% of peak strength).

The relative permeability of the 3D-printed fractured reservoir rock analogues was also examined under the influence of shear stress, following the stress-strain path outlined in Section 7.7.2. Notably, under nearly isotropic conditions, the relative permeability curves exhibited a characteristic rapid transition between wetting phase-dominated flow and non-wetting phase-dominated flow (Figure 7.36). In simpler terms, during the simultaneous flow of oil and gas, the oil phase dominated the flow in the fracture, with minimal gas flow. However, once a certain residual oil saturation threshold was crossed, the flow dynamics shifted abruptly from oil-dominated to gas-dominated. At this stage, the relative permeability to the oil phase dropped to zero, and the gas phase completely dominated the total flow. As the axial strain increased, the transition range between the relative permeabilities of oil and gas broadened, suggesting an evolution towards a flow behavior more characteristic of porous media. This finding is particularly significant in understanding flow behavior in naturally fractured reservoirs, where the fracture system largely governs the flow, and the rock matrix primarily serves as a storage unit.

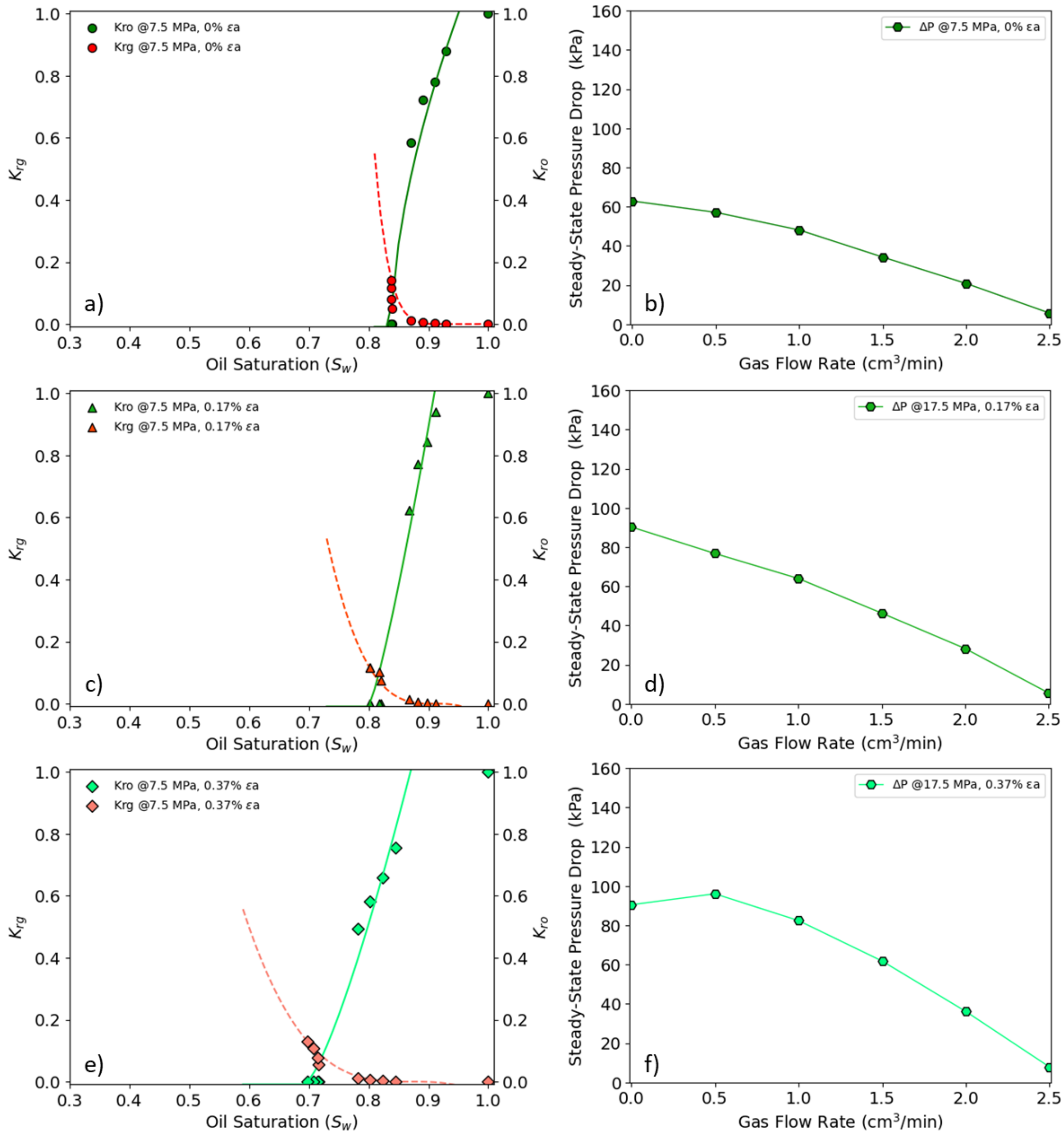


Figure 7.36. Evolution of relative permeability in fractured rock under triaxial stress. This graph illustrates how relative permeability changes at different stages of axial strain.

As the relative permeability curves were compared across different stages, it was observed that the relative permeability of oil showed minimal change from Stage 1 to Stage 2, as depicted in Figure 7.37. However, a notable shift occurred at Stage 3, where the relative permeability curve for oil moved to the left. This shift indicates a possible closure of the fracture, which would result in an increased interaction of the non-wetting phase with the matrix storage, corroborating previous descriptions. Such a change is consistent with the hypothesized behavior of fractures under varying stress conditions, suggesting that the closure of fractures at higher stress levels significantly influences the fluid flow dynamics within the rock matrix.

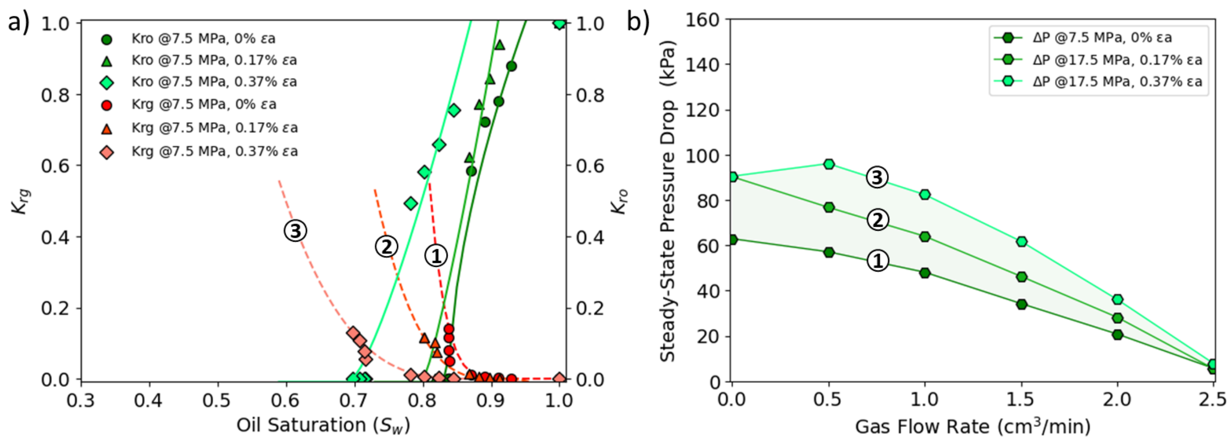


Figure 7.37. Changes in relative permeability under varying axial strain in fractured rock samples. This figure demonstrates how relative permeability curves shift in response to increasing axial strain, highlighting the effects of fracture closure on the residual wetting phase saturation.

Furthermore, Figure 7.38 illustrates the progression of oil recovery from the 3D-printed fractured reservoir rock analogues as a function of the nitrogen gas flow rate. The darker regions in the figure reflect the increase in oil recovery corresponding to the increasing axial strain. The selected stress and strain conditions aim to reflect the evolution of the fractured porous media's drainage recovery. This progression ranges from the onset of hydrocarbon production to the state observed in the reservoir after two decades or more. These conditions are particularly relevant in the context of reservoirs under normal faulting conditions, where the overburden stress exceeds the horizontal stresses.

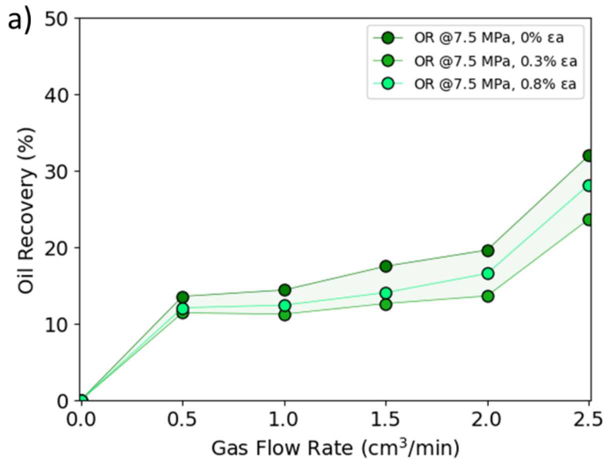


Figure 7.38. Progressive evolution of oil recovery from the fractured porous media as a function of nitrogen gas flow rate. The figure highlights the correlation between increased nitrogen gas injection and oil displacement.

### 7.7.4. Drainage Capillary Pressure

The drainage capillary pressure tests under triaxial stress conditions were conducted at the same stress and strain levels as those used for the relative permeability tests. As outlined in Section 7.4.4, these tests employed the Porous Plate Method. Following complete saturation of the samples with canola oil, nitrogen gas was injected at a constant flow rate. This process led to an increase in injection pressure as the gas permeated the porous spaces until a breakthrough occurred. After this point, the nitrogen pressure decreased and eventually stabilized, marking the ending of the wetting phase fluid flow and allowing for the measurement of the steady-state drainage capillary pressure. Figure 7.39 illustrates the transient behavior of the breakthrough pressure prior to its stabilization in the intact material. Initially, under nearly isotropic conditions, the gas pressure increased to 45 kPa before achieving a breakthrough in the core specimen. As the gas exited the downstream end, it displaced the oil within the rock's pore space (see Figure 7.39a). With an increase in axial strain to 0.3% at Stage 2, the breakthrough pressure rose to 50 kPa. This pressure further intensified to 80 kPa with an additional axial deformation of 0.8%. Notably, Figure 7.39 also depicts the breakthrough pressure in relation to oil recovery. The observed increase in capillary breakthrough pressure can be attributed to the reduction of pore throat size and pore collapse during axial deformation.

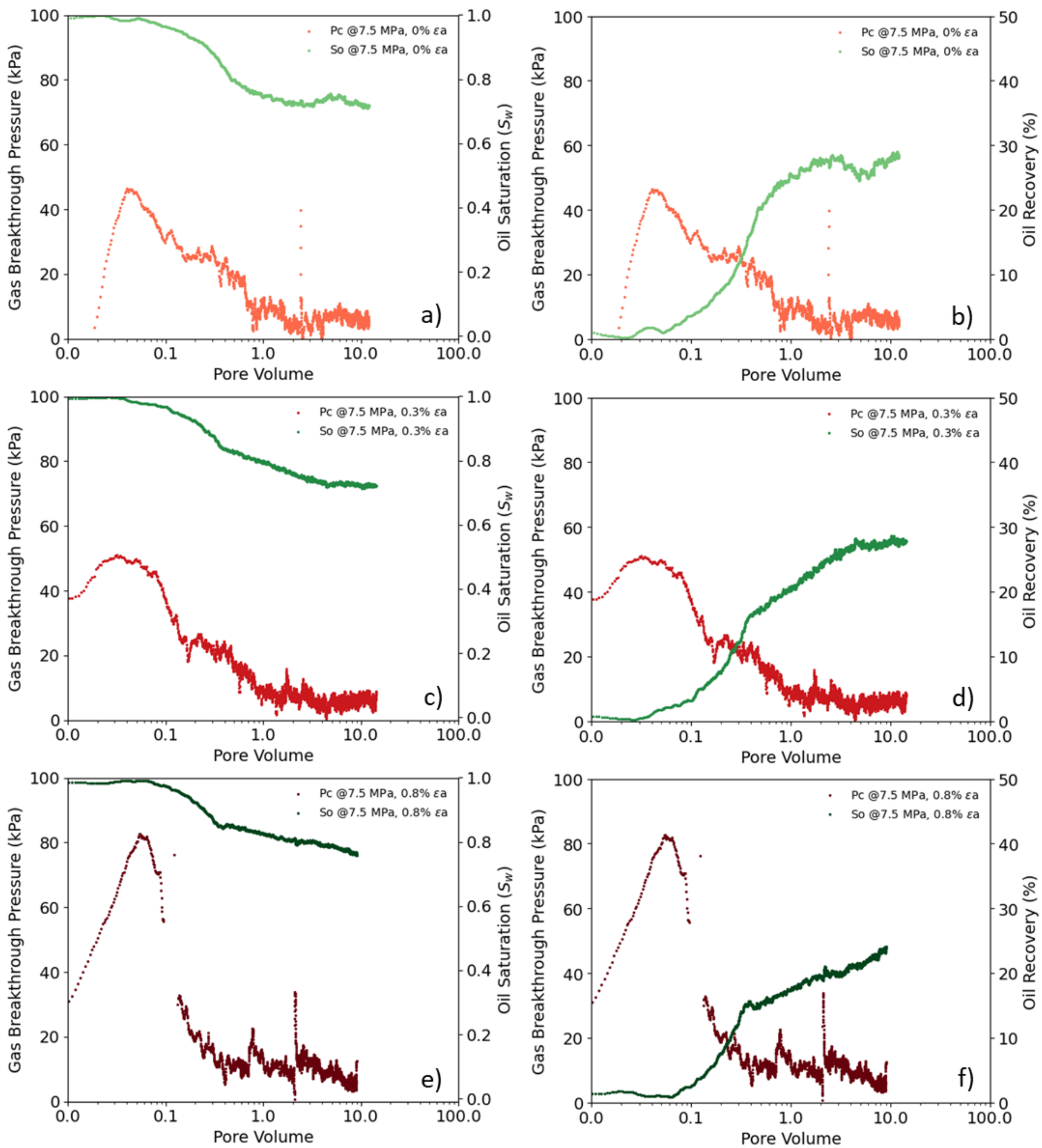


Figure 7.39. Sensitivity of breakthrough pressure and oil displacement in intact porous media. This figure illustrates the response of gas breakthrough pressure and consequent oil displacement under varying axial strain conditions, with red curves representing gas pressure evolution and green curves depicting the volume of oil displaced from the core specimen.

Figure 7.40 depicts the evolution of the breakthrough pressure across a range of axial deformations. A notable trend observed is the increase in breakthrough pressure as axial deformation progressed, although the magnitude of change was minimal when the non-wetting phase exited the core sample. An intriguing observation is the increase in residual wetting phase saturation with higher axial strain. This observation lends further credence to the hypothesis that a fracture was generated during shearing, which in turn facilitated the flow of nitrogen through high conductivity channels.

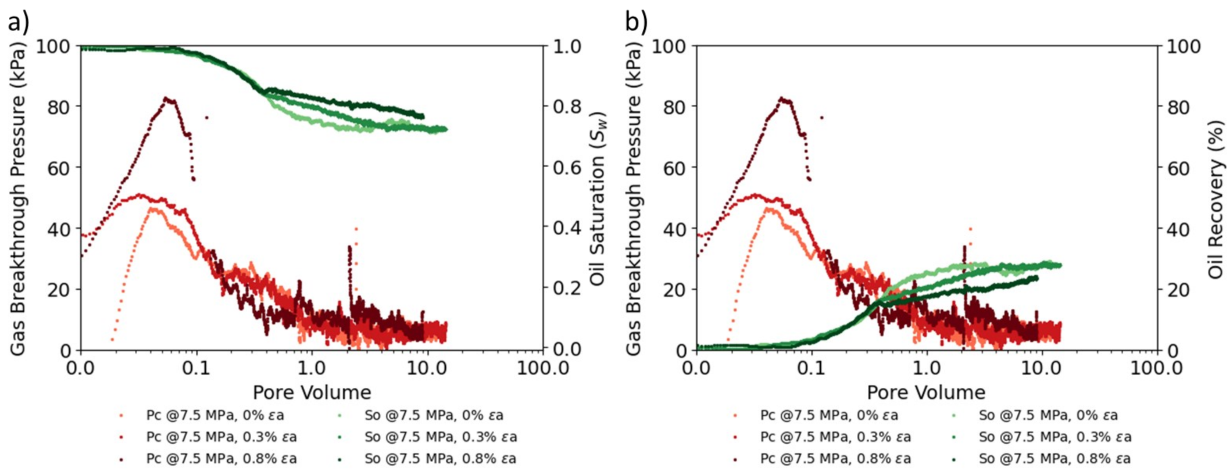


Figure 7.40. Evolution of breakthrough pressure with axial strain in 3D-printed reservoir rock analogues. This graph illustrates the changes in breakthrough pressure as axial strain increases, highlighting the dynamic response of the rock analogues to varying degrees of deformation.

Figure 7.41 depicts the steady-state drainage capillary pressure in the rock samples. After breakthrough, the nitrogen pressure diminished and eventually stabilized, signifying the attainment of steady-state conditions. The differential pressure across the samples reached a steady state after 8 to 12 pore volumes in the tests conducted at various axial deformations. Under these steady-state conditions, the wetting phase flow ceased, allowing for the measurement of drainage capillary pressure at the upstream face of the specimen.

In Stages 1 and 2, the steady-state capillary pressure showed only a marginal change. During the transient phase of these tests, approximately 20% of the oil phase saturation was displaced. Subsequently, as the nitrogen flow rate was incrementally increased, the residual wetting phase saturation decreased to around 0.71. However, at Stage 3, an increase in axial deformation led to a rise in the steady-state capillary pressure, as observed in Figure 7.41. Interestingly, even at this higher capillary pressure, the residual wetting phase saturation did not decrease further, reinforcing the evidence of shear-induced fracture.

Measuring capillary pressure in the fracture-designed 3D-printed reservoir rock analogues posed challenges due to the relatively low differential pressures present in the fractured media. As a result, the capillary pressure measurements for the fractured-designed 3D-printed samples were inferred from the relative permeability curves. The relevant data points correspond to conditions of 100% gas injection at irreducible wetting phase saturation, marked with a cross in Figure 7.41.

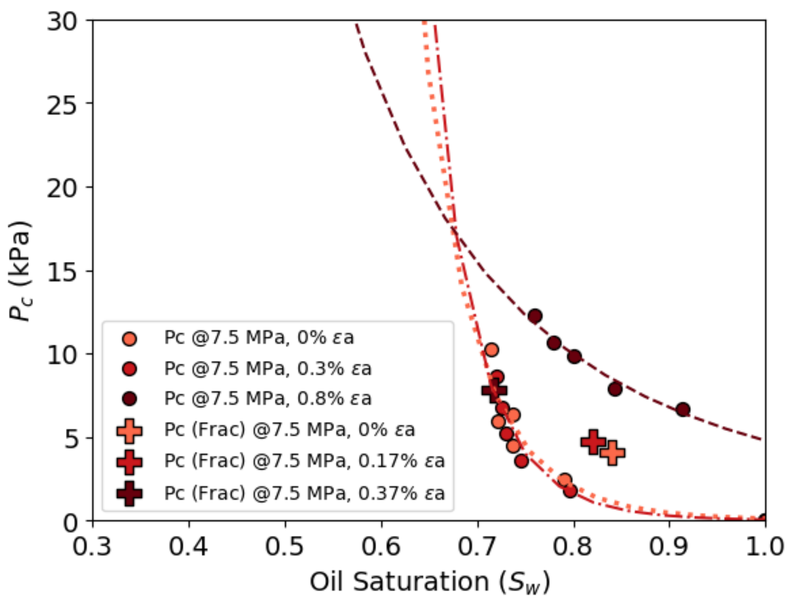


Figure 7.41. Drainage capillary pressure in 3D-printed reservoir rock analogues. This graph shows the evolution of capillary pressure at steady-state conditions across different stages of axial deformation.

Figure 7.42 illustrates the progression of oil recovery as a function of nitrogen gas flow rate during the drainage capillary pressure tests. The darker region in the figure indicates an increase in oil recovery, correlating with increasing axial deformations. In contrast to the relative permeability tests, which were performed under full steady-state conditions, the capillary pressure tests revealed an initial transient phase. This phase resulted in a more pronounced displacement of the wetting phase at the beginning of the nitrogen injection.

In Stages 1 and 2, there were minimal differences in oil recovery, suggesting consistent behavior under these conditions. However, Stage 3 exhibited a decrease in recovery, which can be attributed to the shear-induced fracture. This variation in oil recovery across different stages underlines the impact of shear stress and resultant fracture behavior on the efficiency of fluid displacement in the rock matrix.

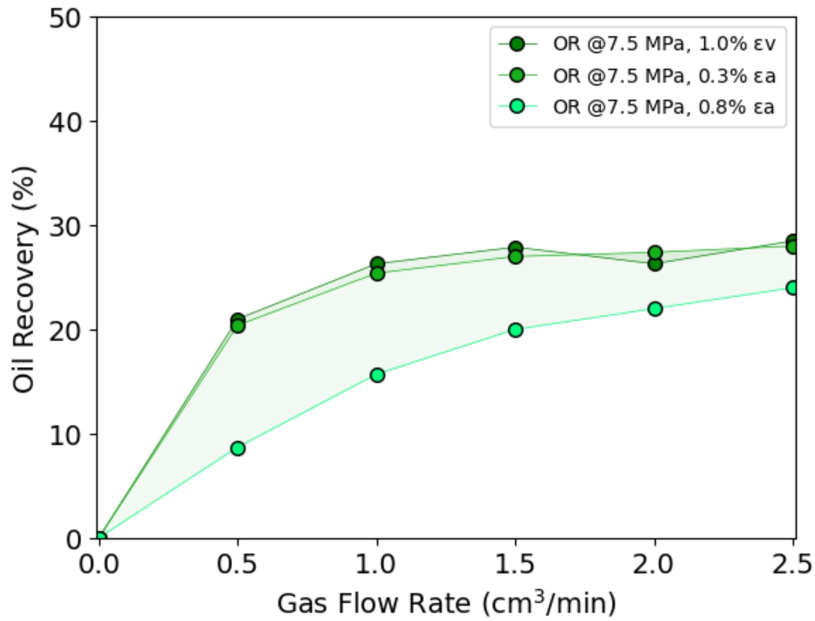


Figure 7.42. Oil recovery progression during drainage capillary pressure tests. The darker regions in the graph emphasize the enhanced recovery, which correlates with increasing axial strains.

## 7.8. Conclusion

This study provides a comprehensive examination of how various stress regimes, particularly isotropic and triaxial stresses, affect multiphase flow within fractured 3D-printed reservoir rock analogues. Key findings reveal that both shear and normal stresses significantly alter flow properties across intact and fractured samples, affecting porosity, absolute permeability, fracture aperture sensitivity, drainage relative permeability, and drainage capillary pressure.

The absolute permeability significantly decreased under stress for both intact and fractured rocks. This behavior closely aligns with the response of Berea sandstone, offering a tangible comparison between 3D-printed analogues and natural reservoir rocks. Notably, fractures dominated the flow in fractured samples, initially contributing 95.3% of the flow, which reduced to 84% under higher stress levels, while the hydraulic aperture decreased by 71%.

The analysis of drainage relative permeability under varying stress conditions highlighted changes in oil displacement and saturation levels within fractured porous media. The irreducible wetting phase saturation was reduced by 10% for intact samples. At a lower stress level, in the fractured samples, nitrogen gas injection resulted in a modest displacement of the saturating fluid (8.58% of its volume), predominantly affecting the matrix beyond the fractures. As stress and deformation increased, a notable decrease in wetting phase saturation was observed, leading to a more substantial displacement of oil (26.62%), with the vast majority being extracted from the matrix. The drainage capillary pressure also increased with these stress changes, suggesting a reduction in the fractured porous media.

The study highlights the critical influence of stress on flow behaviors, especially through the generation and alteration of fractures, which significantly impact relative permeability and capillary pressure. The sensitivity of fractures emerged as a key aspect in reservoir geomechanics, capable of drastically modifying the permeability of fractured porous media during hydrocarbon production, shifting flow dominance from the matrix to fractures.

# 8. Applications: Impact of Stress-Dependent Relative Permeability on Oil Recovery in the Akal KL Field

## 8.1. Introduction

The oil and gas industry is fundamental to the global energy economy, with an ever-increasing quest for new reserves to satisfy the growing demand. Reservoir modeling and simulation are crucial for the exploration and production of hydrocarbons. However, traditional models often neglect the complex interaction between fluid flow responses and *in-situ* stress changes, leading to inaccuracies in predicting reservoir behavior under diverse geomechanical conditions. To address this, advanced simulation methodologies integrate fluid flow with geomechanics, updating porosity and permeability in response to stress changes, thereby enhancing model accuracy. However, for these simulations to be effective, they must accurately reflect realistic geomechanical behaviors, requiring laboratory tests to validate the results and guarantee the quality of input data, such as the stress-dependent multiphase properties of reservoir rocks.

Traditionally, properties of reservoir rocks are derived from core samples, a process that can be costly, time-consuming, and sometimes impractical due to various constraints. An alternative approach, as detailed in previous chapters, employs binder-jet additive manufacturing (3D printing) to achieve high accuracy and precision in obtaining rock properties.

This chapter focuses on assessing the impact of stress-dependent multiphase flow properties on the recovery mechanisms within the naturally fractured Akal KL reservoir. Specifically, it examines how geomechanical processes, such as changes in relative permeability observed in 3D-printed fractured reservoir rock analogues under different stress and deformation conditions, affect oil recovery. These insights are applied in a flow simulation of a sector model of Akal KL, aiming to evaluate their influence on cumulative oil production over 15 years of exploitation. This analysis intends to clarify the effects of normal and shear stress on fractured porous media, analogous to reservoir rock, thereby enhancing our understanding of their impact on reservoir management and recovery strategies.

## 8.2. Geological Model

The Akal KL reservoir, highlighted in Chapter 3, is situated on the northwest side of the broader Akal field. The development of Akal has been segmented into several blocks for detailed analysis, with Akal KL being one of these areas. This specific sector is particularly useful for study due to its well-defined boundaries, identified by normal faults to the east and west, as illustrated in Figure 8.1. The reservoir is set at an approximate reference depth of 2500 meters, hosting its main productive formations in the Upper Cretaceous, as well as in the Medium and Lower Cretaceous intervals, as shown in Figure 8.2. The geological model of this reservoir was developed utilizing Petrel Exploration and Production® software (Schlumberger, Houston, TX, USA).

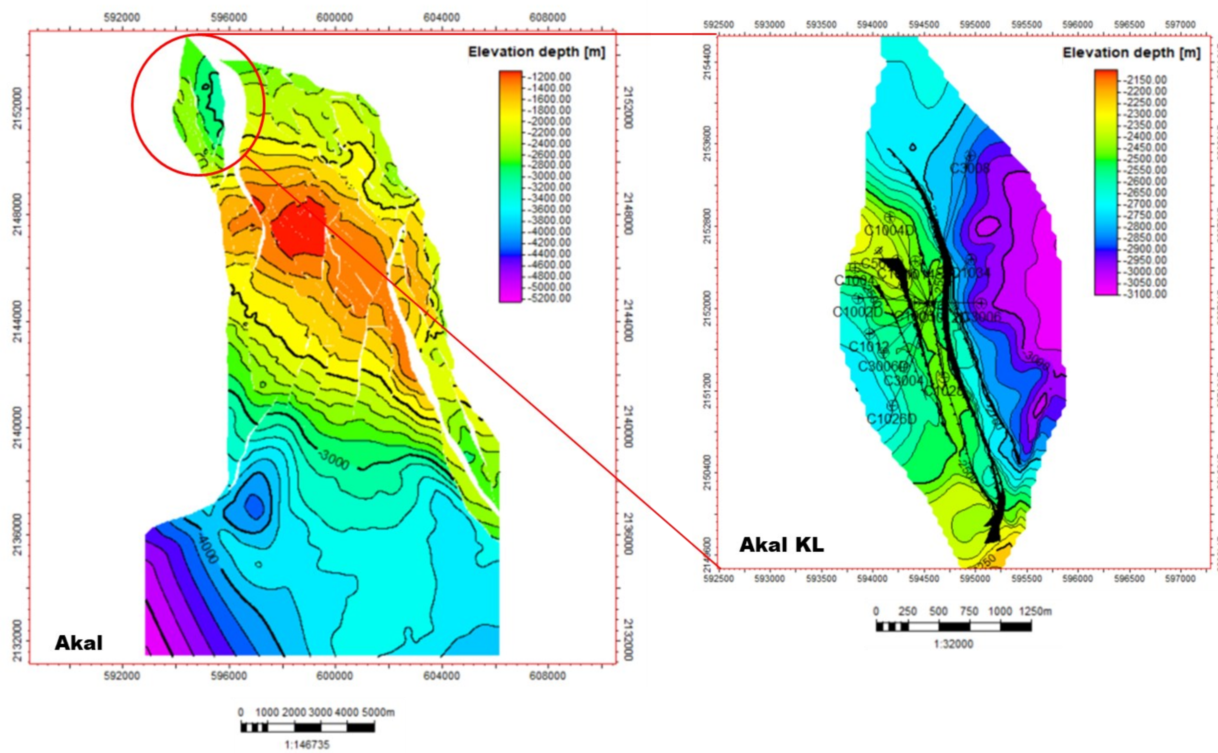


Figure 8.1. Location of the Akal KL block within the Akal field. This figure illustrates the elevation depths and the contours of the well-defined faults.

### 8.2.1. Stratigraphic and Structural Model

The stratigraphic model of the Akal KL reservoir is characterized by an upper interval from the Cretaceous Paleocene period, predominantly composed of breccia dolomite. This formation, marked in Figure 8.2 with a red arrow for emphasis, is the focus of this study. The breccia formation is closely tied to the region's dynamic geological history, including the impact event that formed the Chicxulub crater at the end of the Cretaceous period. This catastrophic event produced a widespread layer of breccia, a rock composed of angular fragments of various sizes. The breccia in this area is likely the result of this massive impact which pulverized existing rock formations and flung them together with high energy, creating a chaotic deposit (Grajales-Nishimura et al., 2000). The energy from the impact would have been sufficient to fragment the bedrock, producing a mixture of coarse and fine materials. The resulting breccia is a testament to the violent forces at play, including shock metamorphism and rapid deposition under extreme conditions. This breccia layer serves as a geological marker for the Cretaceous-Paleogene (K-Pg) boundary, containing evidence such as shocked quartz and other features indicative of a high-energy impact event.

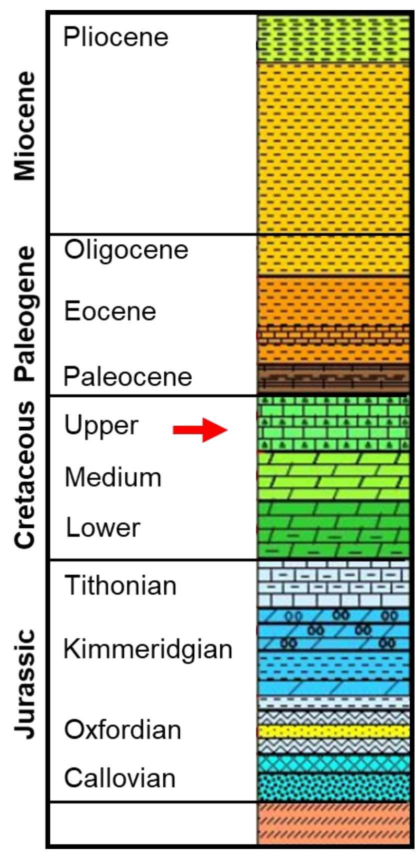


Figure 8.2. Stratigraphic section of Akal KL highlighting the breccia formation. The red arrow indicates the primary reservoir within the Upper Cretaceous Paleocene interval.

The structural model comprises five horizons that delineate the primary zones within the Upper Cretaceous interval, namely BKS, ULKS2, ULKS3, ULKS4, and KM, marking the boundary between the Upper and Medium Cretaceous. The thicknesses of these zones are 30, 70, 70, and 90 meters respectively, spanning from the BKS upper horizon at a depth of 2500 meters to the KM upper horizon at 2800 meters. To enhance resolution, the model specifies two layers for BKS and four layers for the remaining zones. The model encompasses 61992 grid cells, each averaging a volume of 41055 $m^3$.

Additionally, the model identifies nine faults, with two primary faults delineating the reservoir's boundaries, effectively isolating it as an independent structure, as illustrated in Figure 8.3. These faults extend slightly northwest, characterized by a dip angle of 83° and a dip direction of 250°. The dip angle, measured in degrees from the horizontal plane, indicates the fault's inclination, while the dip direction, measured in degrees from north, specifies the compass direction in which the angle inclines, ranging from 0° to 360°.

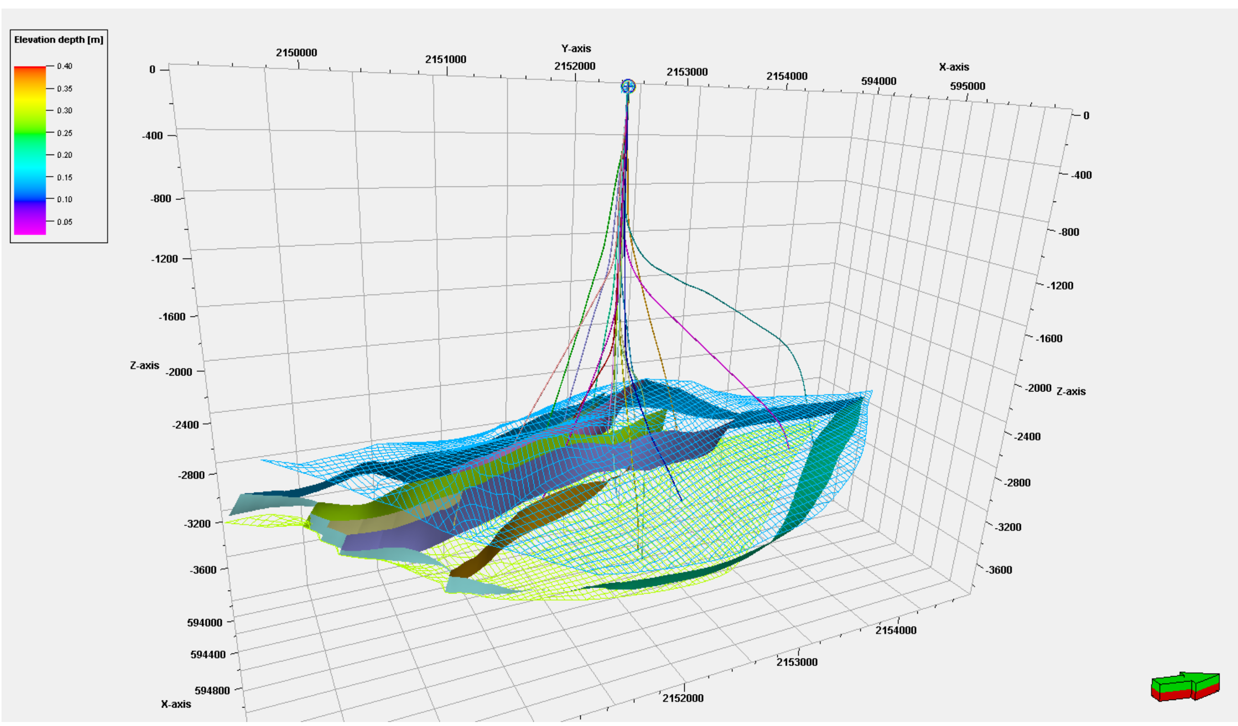


Figure 8.3 . Structural model of Akal KL showing main horizons and faults. This figure depicts the orientation and distribution of geological features, including the significant faults framing the reservoir.

### 8.2.2. Facies Model

The development of the facies model presented unique challenges due to the high-energy and chaotic nature of the depositional environment. In constructing the facies, or lithofacies, a combination of well logs was utilized. It's important to note that log signatures for lithofacies are not uniquely distinctive; while lithofacies may exhibit different property values, there is often an overlap, making it difficult for a single log type to accurately differentiate between various lithofacies. This overlap is attributed to the limited sensitivity of the logs, ambient noise, and measurement errors, which can sometimes be mitigated by employing a combination of two or more log types (Ma, 2019).

For this model, a correlation involving density, porosity, photoelectric (PEF) log, and spectral gamma-ray logs was employed to delineate the carbonate sequence. The combination of density and neutron logs is commonly used to identify limestone and dolostone within carbonate sequences (Lucia, 2007). Here, the density log serves as the fundamental lithology tool, enhanced by porosity data derived from the neutron log. The PEF log, which targets low-energy gamma rays, facilitates lithology identification through energy loss correlation. This log is particularly effective for distinguishing between calcite and dolomite, especially in scenarios where anhydrite and quartz are not predominant.

The facies classification was validated against Pemex Exploration and Production's interpreted well logs, demonstrating strong correlation as shown in Figure 8.4. This data was then upscaled, and the model was created using sequential indicator simulation from the facies module in Petrel. The model predominantly features dolomite (85%) and calcite (14%), with minimal shale presence. Figure 8.5 presents the detailed facies model of the reservoir.

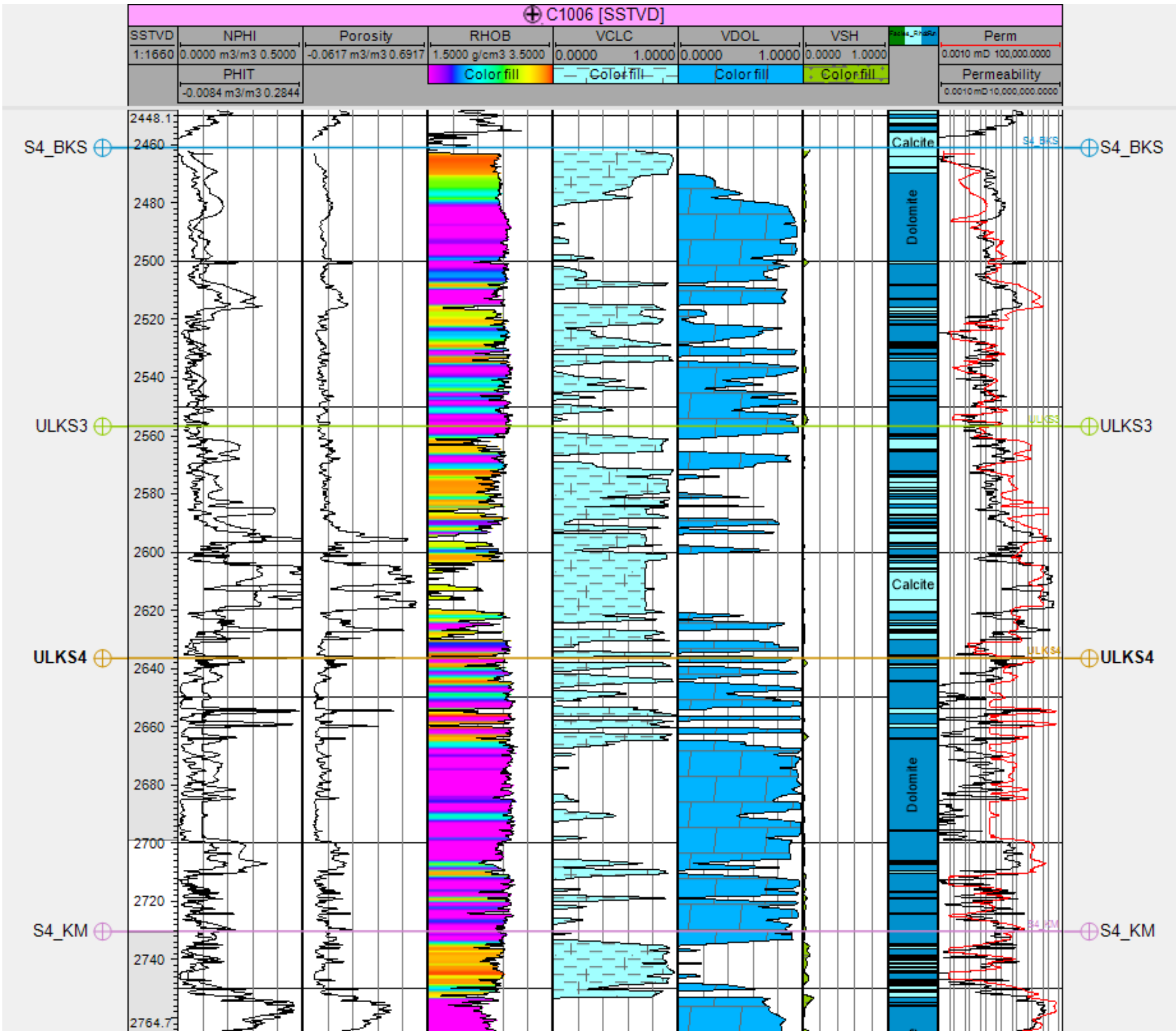


Figure 8.4. Comparison of lithofacies classification with interpreted well logs from Pemex Exploration and Production.

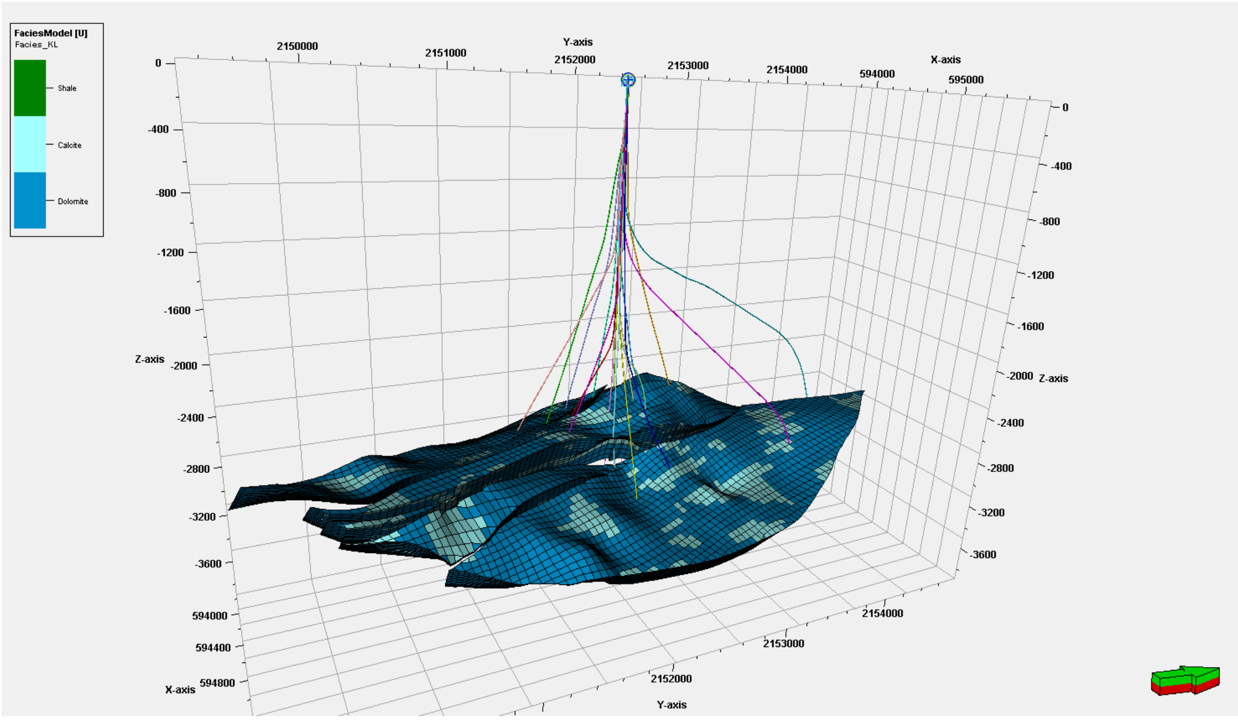


Figure 8.5. Facies model of the Akal KL reservoir highlighting dolomite and calcite distributions.

## 8.3. Flow Properties

This section examines the flow properties of the Akal KL reservoir, characterized by its dual-porosity configuration. The reservoir's architecture consists of matrix blocks combined with vugs and enclosed by fractures, reflecting its chaotic depositional history. Upcoming discussions will cover the porosity and absolute permeability models, as well as the relative permeability parameters, crucial for this study.

### 8.3.1. Porosity-Permeability Relationship

The evaluation of porosity within the Akal KL reservoir was primarily conducted through the analysis of well logs, supplemented and validated by core analysis. The region, characterized by 16 wells, provided extensive neutron and sonic porosity logs. These logs were meticulously analyzed to derive not just total and effective porosity, but also discrete measurements for the matrix, fractures, and vugs, offering a comprehensive view of the reservoir's porosity landscape.

Absolute permeability, a critical parameter for understanding fluid flow through the reservoir, was determined based on the porosity data. The correlation between porosity and permeability, crucial for reservoir characterization, was derived from Pemex Exploration and Production reports. This relationship was further corroborated against core analysis-derived permeability values, reinforcing the model's reliability. Figure 8.6 presents well logs from three important wells positioned in the upper structure of the reservoir. These logs include porosity and permeability measurements directly interpreted from the well data, providing valuable insights into the reservoir's geophysical properties.

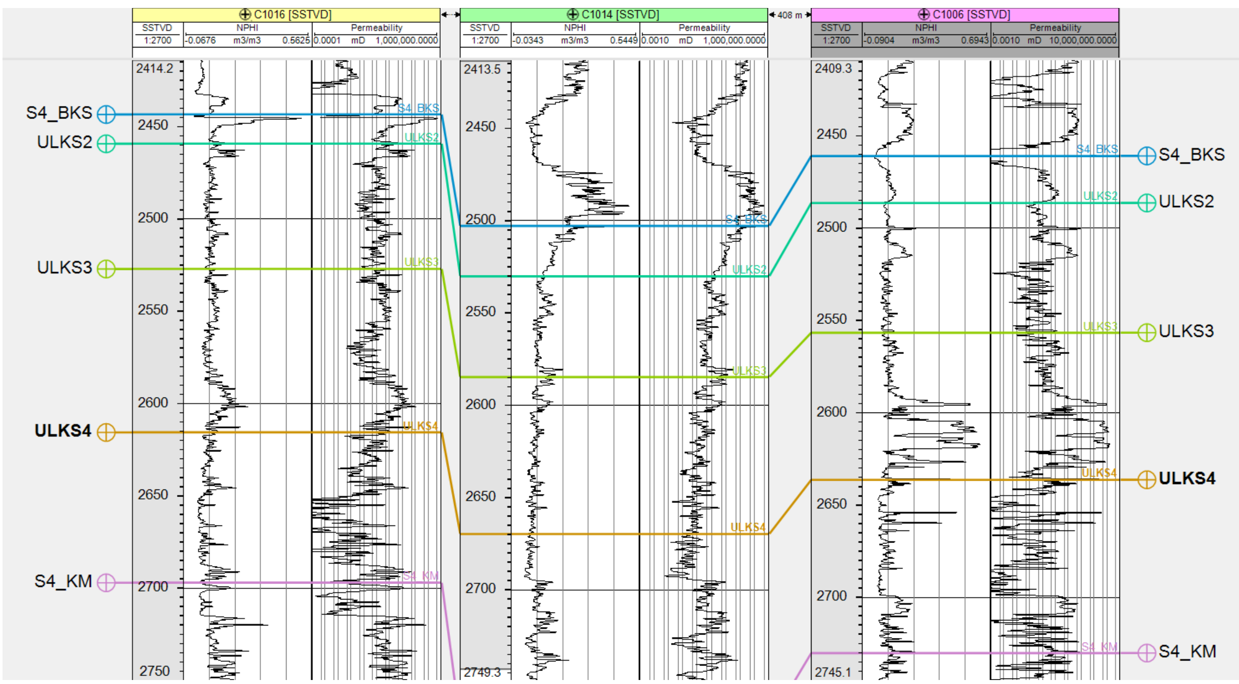


Figure 8.6. Porosity and permeability measurements from well logs of the Akal KL reservoir. This figure highlights interpreted well log data for three significant wells, showing the porosity and permeability within the reservoir's upper structure.

Figures 8.7 and 8.8 illustrate the application of upscale techniques to these well logs, employing Gaussian random function simulation in the petrophysical modeling module of Petrel software. This upscaling process is vital for integrating detailed log data into broader reservoir models, enabling more effective simulation and analysis of the reservoir's flow properties. Upscaling allows for the translation of fine-scale geological details into the model, though it requires careful consideration to ensure that critical features influencing flow dynamics are not overlooked.

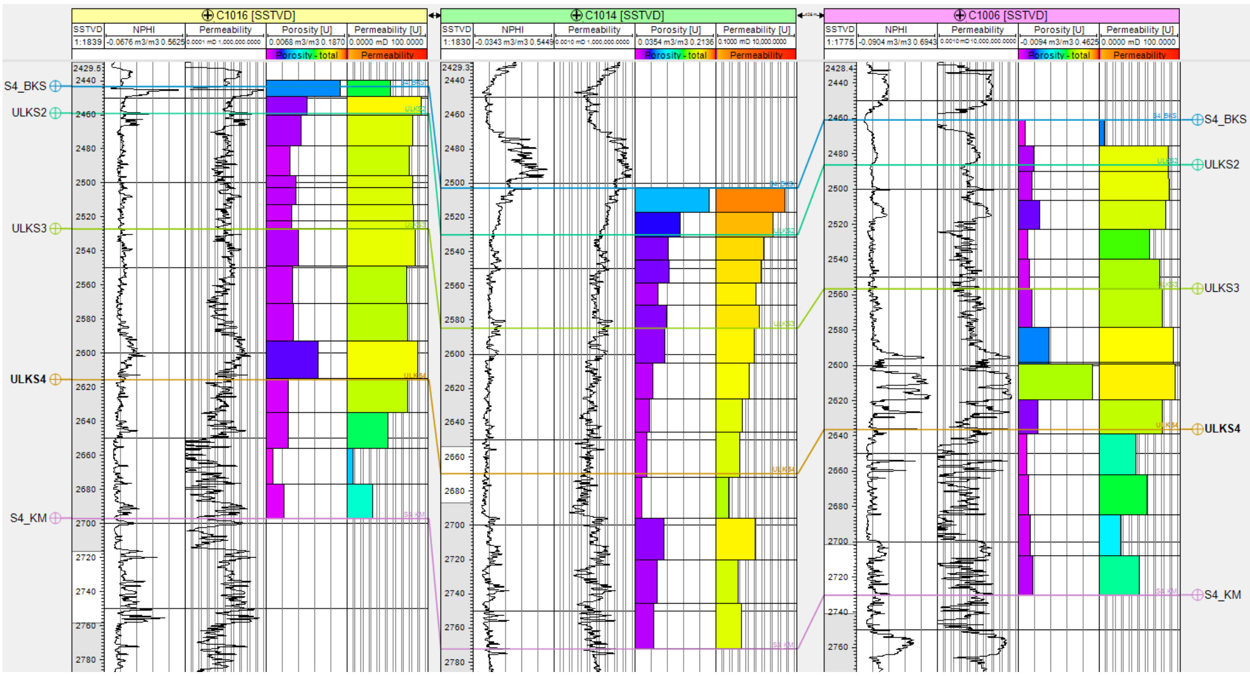


Figure 8.7. Upscaled well log data for Akal KL reservoir. This figure compares original log measurements with their upscaled counterparts, demonstrating the refinement process for inclusion in the reservoir model.

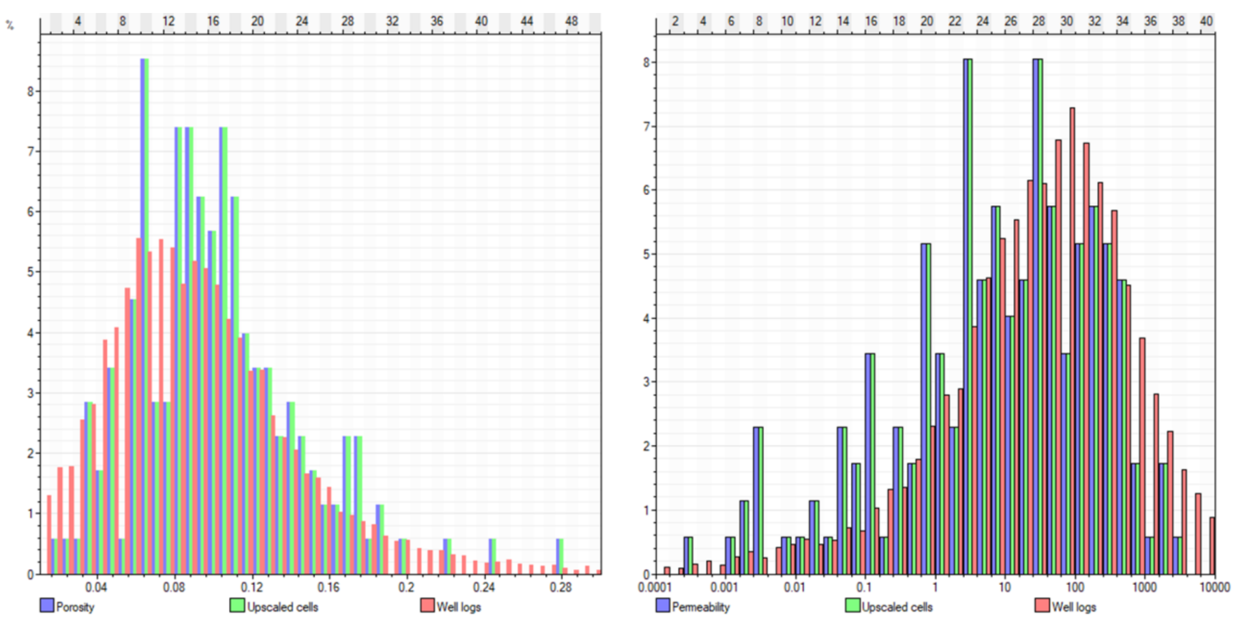


Figure 8.8. Histogram comparison of original and upscaled well log data.

Figure 8.9 illustrates the porosity-permeability relationship for the Akal KL reservoir, showing three distinct trends corresponding to the structural components of the rock: fractures, vugs, and matrix, as established by Pemex Exploration and Production. The graph includes data points in purple and orange representing porosity and permeability measurements taken from core samples extracted from wells C1006 and C1016. These core sample measurements align predominantly with the matrix and vug curves; however, caution is advised when considering these results as they stem from the more intact core samples that were available for testing. Green data points represent the porosity-permeability relationship as modeled in the Petrel geological software, which largely correlates with the physical measurements and established trends for matrix and vugs. Notably, the geological model appears to overstate the lower end of porosity and permeability values, potentially due to resolution loss in the upscaling process. The blue data points correspond to measurements from 3D-printed reservoir rock analogues. Although these values slightly overestimate the actual data, they generally fit well between the matrix and vug trend lines, effectively simulating the reservoir rock's dual-porosity structure. This comparison highlights the 3D-printed analogues' utility in replicating real rock properties and their potential in enhancing reservoir characterizations.

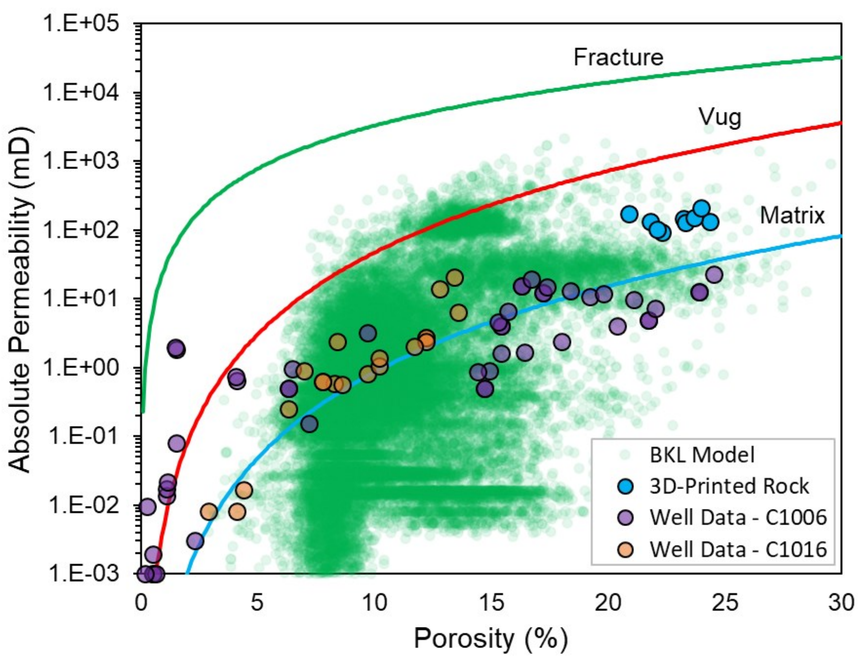


Figure 8.9. Porosity-permeability relationships in the Akal KL reservoir.

Figure 8.10 depicts the porosity model of the Akal KL reservoir. This model was generated using Gaussian random function simulations in Petrel software, across ten porosity realizations. An arithmetic mean of these realizations was then calculated to establish the final porosity model, which indicates an average porosity of 10.68% for the reservoir.

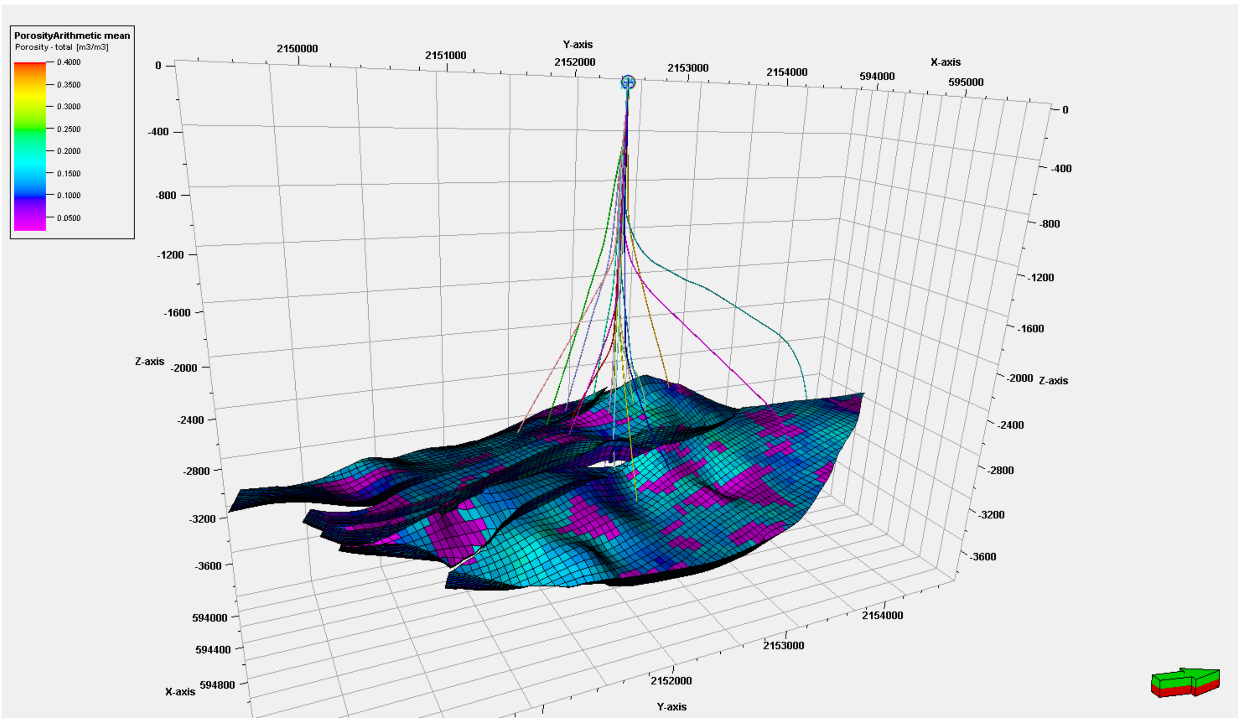


Figure 8.10. Spatial distribution of porosity in the Akal KL reservoir model.

Figure 8.11 presents the permeability model for the reservoir. Similar to the porosity model, it was constructed using Gaussian random function simulation based on ten permeability realizations. However, a harmonic mean was employed to consolidate the final model. The permeability distribution, as revealed by the histogram, shows two distinct peaks that correspond to the permeabilities of the matrix (1-5 mD) and the fractures and vugs (greater than 100 mD), illustrating the dual-permeability characteristics of the reservoir. The areas characterized predominantly by calcite rock type exhibited notably lower porosity and permeability. This observation is significant as it highlights the influence of lithology on the reservoir's storage and flow capacity.

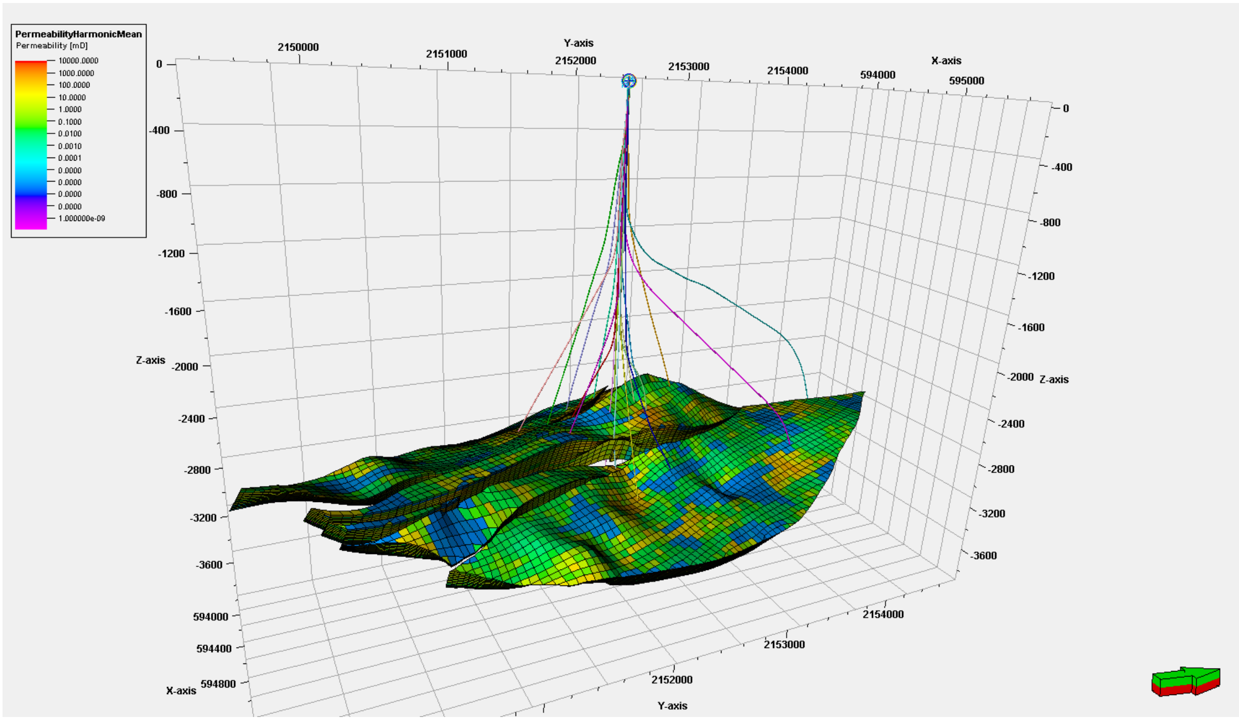

Figure 8.11. Permeability distribution and variation in the Akal KL reservoir model.

### 8.3.2. Relative Permeability

As detailed in Chapter 3, the relative permeability within the Akal KL reservoir was assessed using core samples from wellbore C1006, taken during the early stages of reservoir exploitation. The gas-oil relative permeability characteristics derived from these samples indicated that residual oil saturation ranged between 72% and 78%. The relative permeability to gas at this saturation level was found to be between 18% and 26% of the absolute permeability, suggesting significant residual oil remains post gas injection, a behavior consistent with the reservoir's dual-porosity nature (Figure 8.12). The rock allows the wetting phase to adhere to the smaller pores while the non-wetting gas phase flows through the larger apertures. Due to capillary forces, gas, predominantly occupying larger pores, is unable to displace oil from the smaller pores completely, leading to underutilization of the reservoir's absolute permeability by the gas phase. Additionally, Figure 8.12 presents the relative permeability data obtained from the 3D-printed reservoir rock analogues, as elaborated in Chapter 7. These analogues, analyzed using the modified Brooks-Corey model, exhibit relative permeability curves that mirror those observed in the actual reservoir. This correlation emphasizes the effectiveness of 3D-printed analogues in simulating and understanding multiphase flow dynamics within reservoirs.

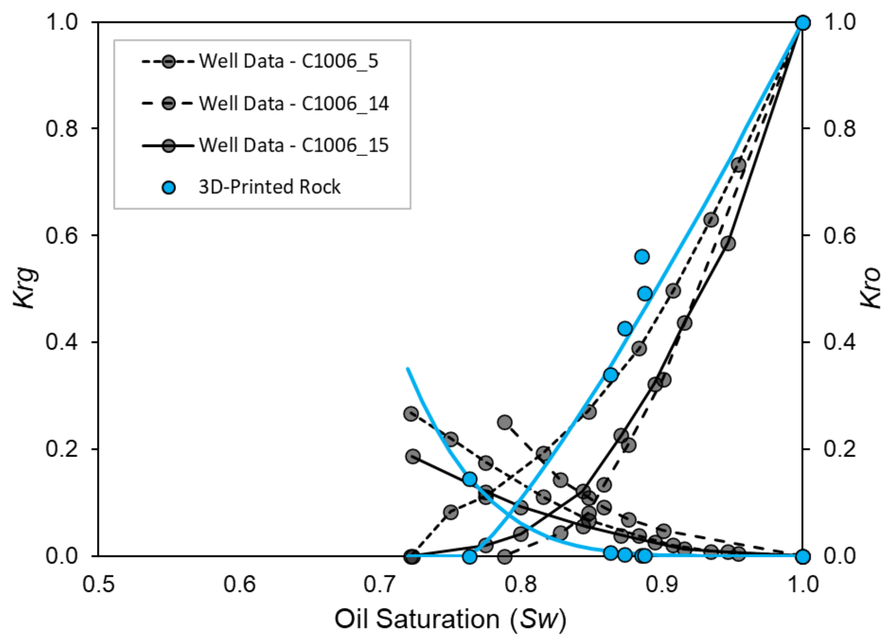


Figure 8.12. Comparative relative permeability curves for Akal KL reservoir and 3D-printed analogues. This graph presents the gas-oil relative permeability measurements from natural core samples and their corresponding values in 3D-printed rock analogues.

## 8.4. Development Strategy

The exploitation of the Akal KL field started in 2000 with the drilling of multiple wells for hydrocarbon extraction. From 2000 to 2005, additional wellbores were drilled to facilitate the recovery of hydrocarbons. The sector model simulation outlined in this study incorporates a select number of these wellbores, specifically those with accessible production and injection data vital for the history matching phase. The dataset, provided by the National Hydrocarbons Commission of Mexico and the Mexican Petroleum Institute, included comprehensive information on 16 wellbores. Although data from the majority were instrumental in constructing the static model, the dynamic simulation was limited to just eight wellbores.

The implementation timeline for these wellbores within the simulation adheres closely to their real production and injection schedules. Production commenced in 2002 with wellbores C1014 and C3006D, followed by C1012 and C1034 in 2004, and subsequently, C1006, C1028, and C3006 in 2005. That year also marked the start of injector well C568I, beginning its nitrogen injection at a rate of 80 MMSCFD. These wells remained operational over a span of approximately 20 years. The dynamic simulation spanned from 2002 to 2014, constrained by the period for which field data were available. The limited timeframe is attributed to the proprietary nature of the most recent data at the time of receipt. Figure 8.13 illustrates the operational timeline of the producer and injector wells as modeled in the dynamic simulation.

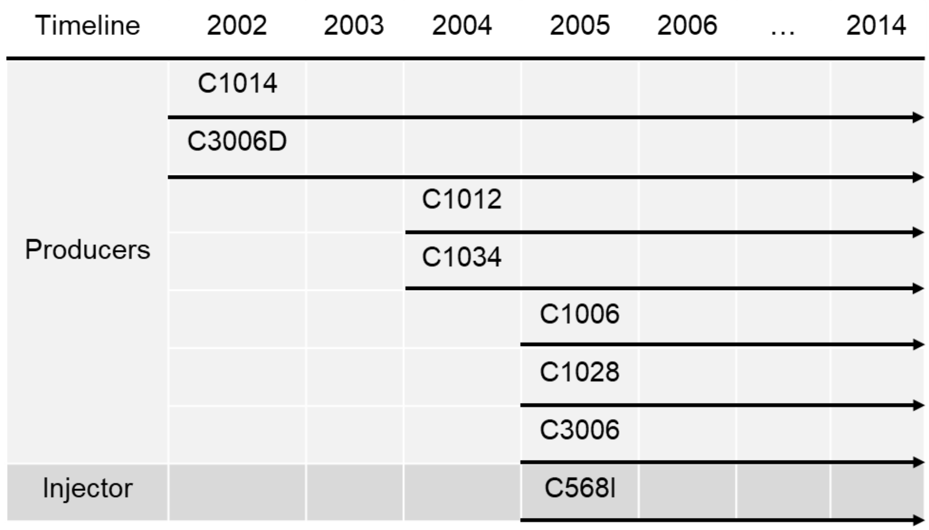


Figure 8.13. Timeline of well implementation in the Akal KL field simulation. This figure outlines the start dates of producing and injecting wells from 2000 to 2014, reflecting the sequence used in the dynamic reservoir model.

## 8.5. Influence of Stress-Dependent Relative Permeability on Oil Recovery Using 3D-Printed Reservoir Rock Analogues

This section explores the influence of stress-dependent multiphase flow properties on oil recovery for a sector model of the naturally fractured Akal KL reservoir. The analysis centers on the uncertainty range in which cumulative oil production might vary due to changes in relative permeability caused by stress or deformation of the rock. Initially, the relative permeability of the reservoir rock is matched with that derived from 3D-printed reservoir rock analogues. These analogues then undergo stress and deformation to evaluate their permeability changes, as outlined in Chapter 7. The extent of fracturing within the rock significantly affects this analysis; rocks that are more extensively fractured tend to exhibit a larger impact from stress or deformation, leading to notable changes in their relative permeability. This investigation is motivated by the reservoir's composition as a highly fractured dolomite breccia, where the degree of fracturing may significantly influence permeability changes. The use of 3D-printed rock analogues is primarily due to the limited availability of actual reservoir rock samples.

The dynamic simulation was carried out using Eclipse® 100 (Schlumberger, Houston, TX, USA) for black oil modeling, integrated with Petrel for seamless geological and petrophysical model handling. This simulation utilized the geological, porosity, and permeability models detailed in preceding sections as the basis for the simulation grid. A single porosity flow modeling technique was employed, adopting the black oil model parameters including oil density at 0.8 $g/cm^3$ and viscosity at 2.2 cP, as delineated in Chapter 3. The bubble point pressure was established at 14 MPa, with the initial reservoir pressure set at 10.3 MPa.

The baseline simulation, serving as the reference case, incorporated the relative permeability and capillary pressure data for both oil-water and oil-gas phases from the actual reservoir rock. Following the establishment of this base case, the relative permeability derived from the 3D-printed analogue rocks was integrated, specifically for the oil-gas phase. This focused approach on the oil-gas case stems from the objective to examine the stress-dependent drainage relative permeability's impact, particularly considering the prevalent nitrogen injection strategies used within this field. The development strategy outlined in the prior section was executed over a period spanning from 2002 to 2014, underscoring the strategic well placements and operational timelines that closely mimic real field operations, thereby providing a comprehensive framework to assess the impact of stress-dependent relative permeability on recovery processes.

Figure 8.14 illustrates the drainage relative permeability curves utilized in the simulations. The black curves represent relative permeability data from the actual reservoir rock, forming the basis for the base case scenario, whereas the blue curves represent data from the 3D-printed reservoir rock analogues. It is important to note that, during the dynamic simulation, only the

Brooks-Corey model curves, fitted to the experimental data, were employed. This approach ensures the experimental findings are effectively translated into the simulation.

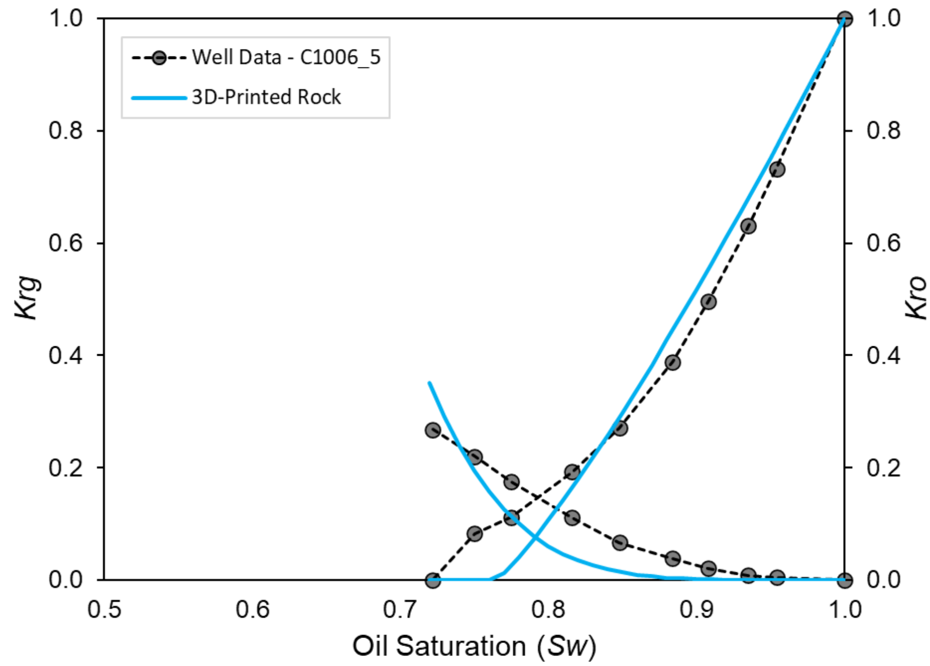


Figure 8.14. Oil-gas drainage relative permeability curves used in the dynamic simulation. Original reservoir rock (black curves) vs. 3D-printed analogues (blue curves).

The dynamic simulation focused on replicating the oil production from specific wellbores within Akal KL over a 12-year period, based on available field data, rather than modeling the entire reservoir. The history matching process involved manual adjustments to porosity, permeability models, and fluid properties to align with actual production data. This approach was essential, not with the goal of precisely replicating the field data, but to assess the impact of stress changes on oil recovery effectively. Figure 8.15a presents the oil production from Akal KL. The solid black line represents the total oil production reported by the National Hydrocarbons Commission of Mexico. The dashed black line indicates oil production from the sector model, correlating to individual wellbores for which detailed data was accessible. The red line depicts simulated oil production using actual reservoir data, showing a reasonable approximation of field behavior. The blue line illustrates the oil production scenario utilizing the drainage relative permeability data from 3D-printed rock analogues. This comparison validates the applicability of 3D-printed analogues in simulating reservoir dynamics and provides a baseline for further exploration of stress impacts on reservoir performance.

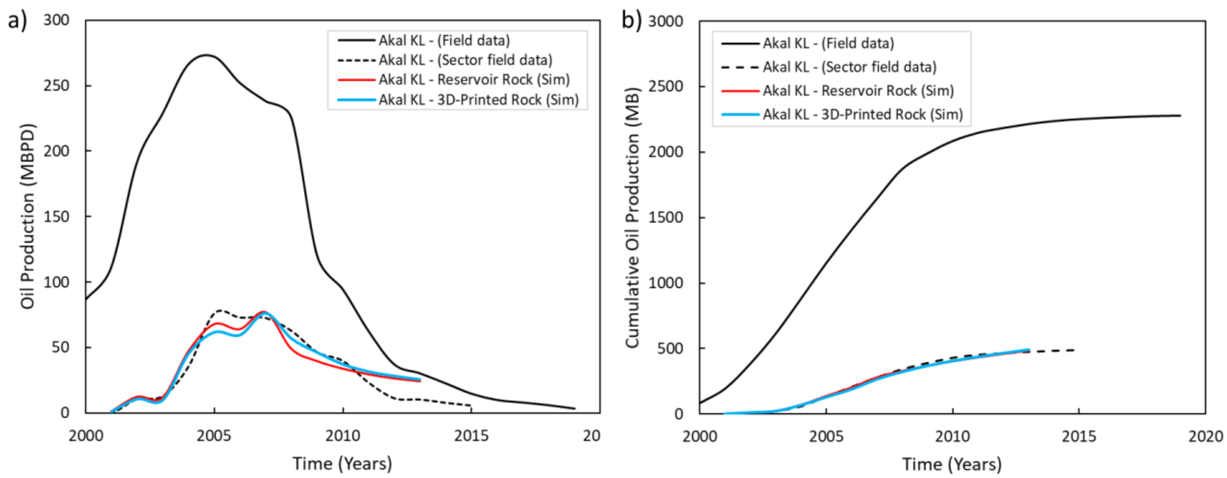


Figure 8.15. Comparative oil production in Akal KL. This figure displays the overall oil production from the field (continuous black line), sector model production (dashed black line), simulation with original rock properties (red line), and the results from simulations incorporating 3D-printed analogues (blue line).

Figure 8.15b displays the cumulative oil production. The simulation results using both actual reservoir rock data and 3D-printed rock analogues closely align with the observed cumulative oil production trend. Over a period of 15 years, reservoir pressure dropped by 53% from its initial value, as shown in Figure 8.16, and nitrogen injection failed to sustain reservoir pressure. This scenario likely elevated the effective stress, impacting the rock's structure and consequently its multiphase flow characteristics. As discussed in Chapter 7, geomechanical effects on the flow properties are contingent on the rock's physical state; stress or deformation tends to have a more pronounced impact on highly fractured rocks compared to intact formations.

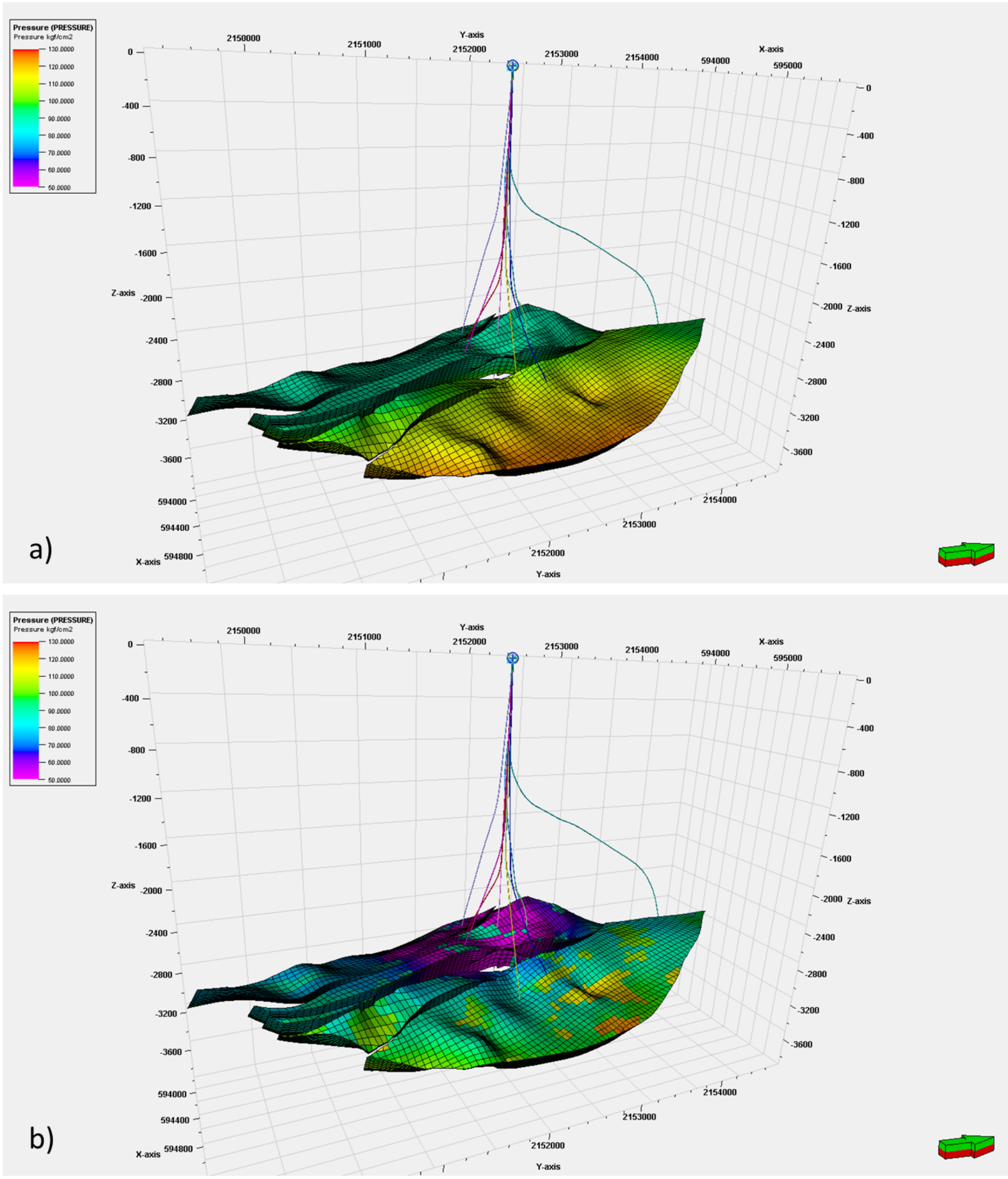


Figure 8.16. Reservoir pressure distribution in Akal KL: (a) Initial pressure distribution at the start of exploitation; (b) pressure distribution after 15 years of production, illustrating the decline in reservoir pressure and the spatial extent of pressure depletion.

### 8.5.1. Case Study 1: Slightly Fractured Rock

This segment of the analysis assesses the impact of stress-dependent drainage relative permeability on the simulated oil recovery in rock formations showing slight fracturing. A 3D-printed rock analogue, characterized by minimal fracturing, was subjected to triaxial stress conditions. The application of shear stress resulted in an axial strain increase to 0.5%, prompting a noticeable shift in the relative permeability curves towards lower saturation levels, as described in Section 7.7.3 of Chapter 7. This shift indicates a constriction in fracture apertures, consistent with the notion that a decrease in fracture aperture during shear stress leads to a reduction in residual wetting phase saturation within the rock. This case represents a scenario where pore pressure depletion could lead to increased effective stress following triaxial compression, similar to the conditions observed in Akal KL where the overburden stress is greater than the average horizontal stresses, as explored in Chapter 3. While the precise deformation of the reservoir rock during exploitation is not known, these case scenarios are essential for consideration during the design phase of related projects.

In the simulation phase, two distinct scenarios were constructed: SFR1, representing the initial drainage relative permeability condition, and SFR2, accounting for permeability adjustments following shear stress-induced deformation. The analysis revealed an 8.41% increase in total oil recovery for SFR2 compared to SFR1, as shown in Figure 8.17. This difference highlights a significant range of uncertainty in oil recovery for reservoir rocks that are not extensively fractured.

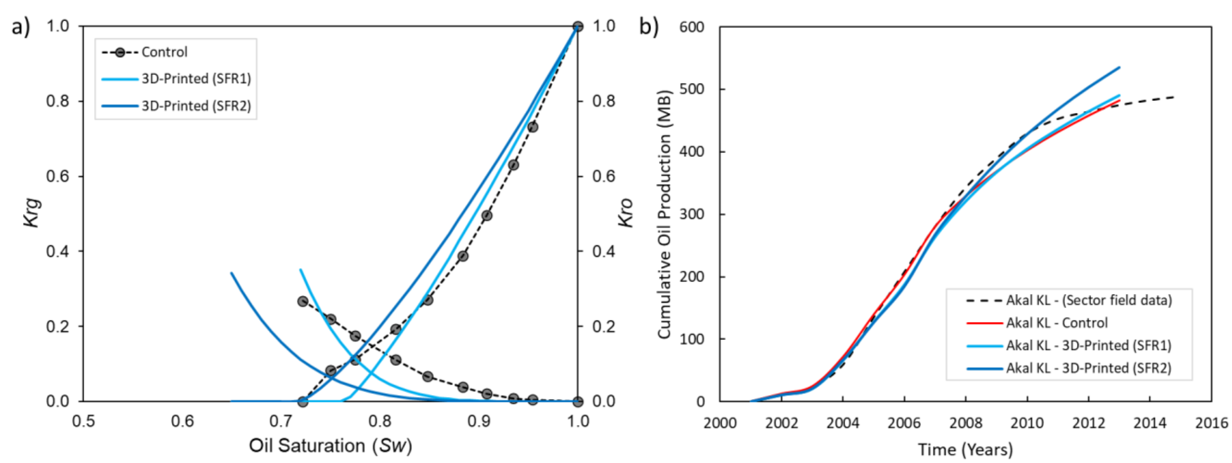


Figure 8.17. Comparison of the cumulative oil recovery between initial and shear stress-deformed relative permeability scenarios in slightly fractured rock.

## 8.5.2. Case Study 2: Highly Fractured Rock

The second case study investigates a highly fractured rock, building upon the findings presented in Section 7.6.4 of Chapter 7. This scenario explores the impact of isotropic stress on the rock's deformation and the subsequent effects on fracture closure. The rock experienced a 0.7% volumetric strain due to the increase in isotropic stress. The observed changes in the relative permeability endpoints indicate a significant decrease in the wetting phase's irreducible saturation within the fractured rock. Specifically, the irreducible wetting phase saturation decreased by 18.04%, dropping to a saturation level of 0.73 when compared to the initial state labeled HFR1.

In the dynamic simulation phase, two distinct states were considered: the initial state HFR1 and the state after isotropic stress deformation, referred to as HFR2 (Figure 8.18). The simulations revealed a notable 42% increase in the cumulative oil production when transitioning from HFR1 to HFR2. This marked increase suggests that even slight alterations in stress conditions can lead to substantial changes in oil recovery in highly fractured reservoir rocks. This underscores the significance of understanding the geomechanical behavior of the reservoir during the depletion phase and integrating such effects into reservoir management strategies.

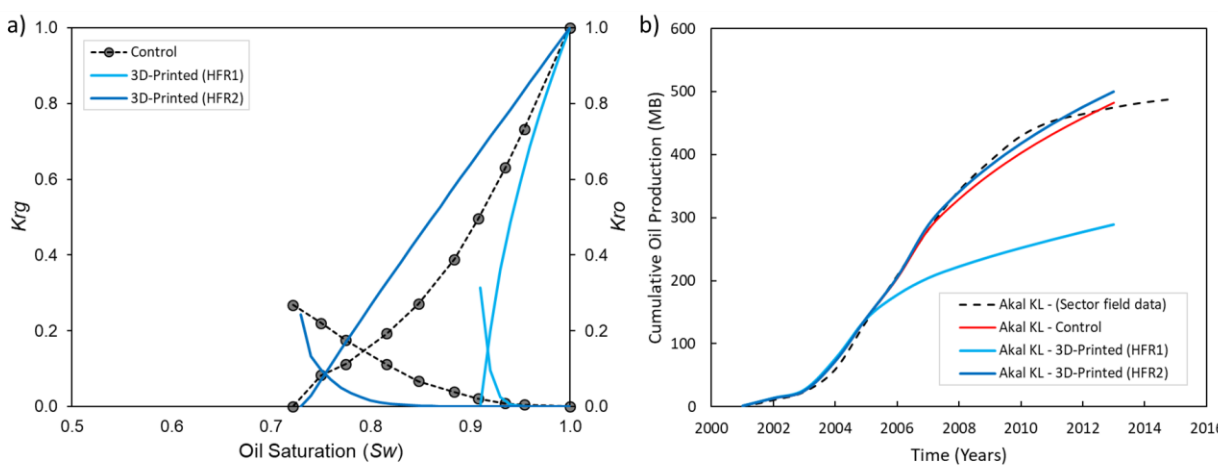


Figure 8.18. Comparison of the cumulative oil recovery between initial and isotropically stress-deformed relative permeability scenarios in highly fractured rock.

### 8.6. Conclusions

This chapter explored the effects of stress-dependent multiphase flow properties on oil recovery mechanisms within the naturally fractured Akal KL reservoir, focusing on the impact of geomechanical processes. It particularly analyzed how changes in relative permeability, seen in 3D-printed fractured reservoir rock analogues under different stress and deformation conditions, influence oil recovery efforts. The use of 3D-printed rock analogues to study stress changes in fractured rock highlights the crucial role of geomechanical factors in enhancing oil recovery. The study showed that variations in stress, especially in fractured reservoirs, can significantly increase oil production rates and total recovery. This chapter has established 3D-printed analogues as an effective method for simulating reservoir conditions, closely replicating actual reservoir behavior, and emphasizing the need for reservoir management strategies that include geomechanical changes alongside traditional fluid dynamics. Additionally, the analysis in this chapter highlighted the significance of the characteristics of the fractured media within the reservoir—such as the degree and nature of fracturing—in how stress alterations affect permeability and, consequently, oil recovery. This insight suggests that reservoir management should take into account the reservoir's geomechanical properties when devising recovery strategies, especially in settings like Akal KL where nitrogen injection and other enhanced recovery methods are applied.

# 9. Conclusions and Recommendations

## 9.1. Summary

This thesis has developed a detailed approach to investigate the influence of geomechanical processes on fluid flow within naturally fractured reservoirs, with a particular focus on the Akal KL field. Akal KL is a critical subsection of the larger Akal reservoir, which initially contained an estimated 32 billion stock tank barrels of oil. This significant volume positions the reservoir as one of Mexico's most crucial oil resources in its history. The study examines how shear and normal stresses impact multiphase flow properties, such as drainage relative permeability, drainage capillary pressure, and the dynamics of fluid transfer between the matrix and fractures. This research highlights the importance of stress-dependent flow properties on oil recovery in fractured porous media through a combination of theoretical analysis, comprehensive reservoir characterization, experimental studies, and dynamic simulations.

The investigation systematically assessed the Akal KL reservoir, analyzing its geological attributes and stress-strain behavior throughout its exploitation cycle. A significant innovation of this study is the use of binder-jet additive manufacturing (3D printing technology) to create physical sandstone models. These models closely replicate the reservoir rock's porosity, permeability, relative permeability, and other petrophysical and geomechanical properties. The 3D-printed reservoir rock analogues offer a novel approach to study the complex behavior of reservoir rocks under various stress scenarios, addressing the challenges of natural sample heterogeneity and scarcity.

A specially designed multiphase triaxial experimental setup was crucial in assessing the stress-dependent flow properties of these analogues, providing critical insights into the geomechanical behaviors influencing multiphase flow in fractured porous media. The experimental results, such as stress-dependent drainage relative permeability observed in 3D-printed fractured reservoir rock analogues, were used in a dynamic flow simulation of Akal KL to assess the uncertainty range in oil recovery due to changes in relative permeability. The findings from this study emphasize the profound effect of stress modifications on reservoir flow and recovery processes, offering valuable strategies for optimizing hydrocarbon extraction in fractured reservoirs.

## 9.2. Conclusions

The findings from this thesis highlight the significant impact of geomechanical factors on multiphase flow properties and their influence on oil recovery within naturally fractured reservoirs. The conclusions follow the structure developed in the chapters:

Following the introductory chapter, the thesis systematically presented the fundamental theoretical principles governing fluid flow within fractured porous media. These principles were restructured into a practical framework, facilitating the interpretation of experimental results via steady-state approaches. Critical equations transition from numerical to analytical solutions, ensuring their applicability to specific research problems.

Chapter 3 presented a thorough characterization of the Akal KL reservoir, integrating data from various sources, including well tests for pore pressure, well logs, flow and geomechanics laboratory tests, and geological databases. This integrated approach offered a comprehensive understanding of the reservoir's characteristics, laying the groundwork for the detailed experimental and simulation studies that followed.

As explained in Chapter 4, an integrated laboratory testing facility was developed to investigate the effects of triaxial stress on the governing mechanisms of multiphase fluid flow. The study presented the main components of the system and its performance. The individual components were tested on sandpack and Berea sandstone specimens to study the effect of geomechanics on fluid flow properties. These initial tests showed the theoretical and experimental procedures to calibrate and successfully measure the multiphase triaxial tests. Findings demonstrated how effective stress alterations impact bulk compressibility, bulk modulus, porosity, and permeability. Additionally, we investigated relative permeability across different porous media, from loose sandpacks to dense Berea sandstones, demonstrating how these properties vary according to the medium.

The 3D-printed sandstones, as discussed in Chapter 5, played a key role during the experimental testing. These analogues were subject to a thorough analysis, revealing the inherent variability in the mechanical properties of 3D-printed sandstones and assessing the effectiveness of densification techniques applied during the printing process. This analysis uncovered that, despite the isotropy and homogeneity within individual sandstone samples, significant variability exists among specimens from the same batch. This variability was addressed by categorizing the samples based on their specific locations within the build platform and the powder bed. It was observed that the strength and stiffness properties varied with the sample's position, with those printed at lower elevations and near the center of the powder bed exhibiting enhanced mechanical characteristics.

Further investigations into the 3D-printed sandstones explored the effects of different sand grain size distributions and compacting roller sizes on the sandstones' physical properties. Introducing a bimodal distribution with a higher proportion of fine grains led to reduced strength and increased porosity, deviating from prior studies' outcomes. This phenomenon was accentuated when utilizing smaller rollers, highlighting the significance of roller size in achieving optimal compaction and density. Conversely, larger rollers were found to be more effective in improving the density and strength of the sandstones by exerting greater pressure during the printing process. These findings highlight the complexities inherent in 3D printing for geomechanical applications and the crucial influence of material composition, print placement, and post-processing techniques.

After the 3D printing analysis, it was determined that the default flow properties, such as porosity and permeability, of the printed samples significantly differed from those of natural reservoir rocks—by two to three orders of magnitude—making them non-representative of actual reservoir conditions. Consequently, Chapter 6 introduced a methodology to modify the geomechanical and petrophysical properties of standard 3D-printed rocks to more closely resemble those of natural reservoir rock, followed by a comprehensive characterization of these modified properties. The adjustment process involved saturating the 3D-printed rocks with sodium silicate and then treating them with carbon dioxide for a specific period. This treatment reduced the porosity by 50%, leading to an 86% decrease in permeability. The outcomes of this process suggested that the porosity-permeability relationship in the modified 3D-printed rock analogues aligned with that of moderate-permeability reservoir rocks.

However, geomechanical testing showed that the 3D-printed analogues exhibited three to six times the volumetric deformation under stress compared to Berea sandstone and intact dolomite rocks, respectively. With increasing confining stress, the shear strength of these rocks also increased, indicating a transition from brittle behavior to ductility and strain hardening.

The 3D-printed reservoir rock analogues were tested under triaxial conditions. Key findings revealed that both shear and normal stresses significantly altered the flow properties of intact and fractured samples, affecting porosity, absolute permeability, fracture aperture sensitivity, drainage relative permeability, and drainage capillary pressure. The absolute permeability decreased under stress for both intact and fractured rocks. Notably, when a fracture was created, fractures dominated the flow by 95%, which slightly reduced to 84% of the flow under higher stress levels, while the hydraulic aperture decreased by 71%.

The analysis of drainage relative permeability under varying stress conditions highlighted changes in oil displacement and saturation levels within fractured porous media. The irreducible wetting phase saturation was reduced by 10% for intact samples. At a lower stress level, in the fractured samples, the nitrogen gas injection resulted in a modest displacement of the saturating fluid (8.58%). As stress and deformation increased, a significant decrease in wetting phase saturation was observed, leading to a more substantial displacement of oil (26.62%), with the vast majority being extracted from the matrix. The drainage capillary pressure also increased with these stress changes, suggesting a reduction in the fractured porous media.

The stress-dependent drainage relative permeability curves were used to assess the impact of geomechanical processes on the recovery mechanisms of Akal KL, finding a good match with the base case results that used the reservoir rock properties. The study showed that variations in stress, especially in fractured reservoirs, can significantly increase oil production rates and total recovery.

## 9.3. Contributions

This thesis contributes significantly to the field of reservoir geomechanics and fluid dynamics, offering insights and methodologies that bridge theoretical models with practical applications. Key contributions include:

1. Akal KL Reservoir Characterization: A comprehensive integration of existing and new data provided an in-depth analysis of the Akal KL reservoir. This included a detailed examination

of the *in-situ* stress state, encompassing overburden stress, principal horizontal stresses, and the orientation of maximum horizontal compression. Flow properties such as porosity, permeability, relative permeability, and capillary pressure were thoroughly examined, alongside static and dynamic geomechanical properties derived from both laboratory measurements and well log data. This extensive characterization supports effective reservoir management strategies, informed by accurate PVT analysis of reservoir fluids.

2. Multiphase Triaxial Testing Facility: The design, construction, and calibration of a multiphase triaxial testing facility represented a significant advancement, enabling the detailed study of stress-dependent multiphase flow properties under controlled laboratory conditions.

3. 3D Printing for Geomechanics: The innovative use of binder-jet additive manufacturing to create accurate physical models of sandstone that statistically mirror the reservoir rock. This approach allows for a direct examination of geomechanical behaviors under various stress conditions, overcoming limitations posed by natural rock sample variability.

4. Experimental Validation: The application of 3D-printed rock analogues in validating theoretical models highlighted the tangible impact of stress and deformation on reservoir fluid flow properties, thus enhancing the precision of geomechanical simulations.

5. Advanced Multiphase Triaxial Testing: The development and application of an advanced multiphase triaxial testing methodology provided a detailed understanding of the interactions between geomechanical stresses and multiphase fluid flow, facilitating a more accurate prediction of reservoir behavior under different stress conditions.

6. Alterations of Relative Permeability and Capillary Pressure: Investigating how reservoir rock deformation during pore pressure depletion impacts relative permeability and capillary pressure, providing insights into fluid flow dynamics as reservoir conditions change.

7. Optimizing Multiphase Flow Displacements: Identifying the optimal conditions for multiphase flow drainage displacements (Pc and krog) that facilitate gas driving from fracture to matrix, thereby displacing additional oil, enhances understanding of efficient hydrocarbon extraction methods.

8. Dynamic Simulation Insights: The integration of experimental data into dynamic simulation models offered novel insights into the effects of geomechanical alterations on oil recovery. This was particularly evident in the study of the Akal KL field, where simulations incorporating stress-dependent properties revealed potential pathways to optimize hydrocarbon extraction strategies.

### 9.4. Recommendations and Future Work

Based on the outcomes of this research, several avenues for future work and recommendations can be proposed to extend the scope and applicability of the findings:

1. Further Development of 3D-Printed Analogues: Future efforts should focus on exploring advanced materials and printing techniques to improve the realism and applicability of 3D-printed analogues for simulating complex reservoir conditions. Investigating different materials to infill pore spaces could effectively reduce porosity and permeability, offering more accurate representations of natural rocks.
2. Application of Fitting Functions: Utilizing fitting functions to describe the overall behavior of two-phase flow is recommended. Comparisons between models such as Brooks and Corey (1964) and van Genuchten (1980) can provide insights into their effectiveness in capturing the dynamics of fluid flow in fractured porous media. Other models, including Corey (1954), Burdine (1953), and Stone's models, should also be considered.
3. Numerical Validation at Core Scale: It's recommended to pursue numerical validation efforts that complement the experimental tests, focusing on core-scale simulations. This approach would bridge the gap between laboratory findings and real-world reservoir conditions, ensuring that experimental insights translate effectively into practical applications.
4. Exploration of Additional Testing Conditions: Expanding the testing conditions to include gases such as carbon dioxide and hydrogen can provide insights into their behavior in reservoirs, particularly for applications in carbon capture and storage (CCS) and subsurface energy storage. This exploration could uncover new methods for enhancing oil recovery and mitigating environmental impacts.

5. Interdisciplinary Studies: There is a significant opportunity for interdisciplinary research that merges geomechanics, fluid dynamics, and material science. Such collaborative efforts can lead to the development of integrated models that more accurately predict reservoir behavior under varied stress conditions, ultimately improving recovery techniques and reservoir management practices.

## References

Adler, P.M., & Thovert, J.-F. (2013). *Fractures and Fracture Networks*. Springer Science & Business Media.

Agar, J. G. (1984). Geotechnical behaviour of oil sands at elevated temperatures and pressures [Doctoral dissertation, University of Alberta]. https://doi.org/10.7939/R3RV0DC1P

Agheshlui, H., Sedaghat, M. H., & Matthai, S. (2018). Stress Influence on Fracture Aperture and Permeability of Fragmented Rocks. *Journal of Geophysical Research: Solid Earth*, *123*(5), 3578–3592. https://doi.org/10.1029/2017JB015365

Anderson, W. G. (1987). Wettability literature survey - Part 5: The effects of wettability on relative permeability. *Journal of Petroleum Technology*, 39 (11), 1453–1468. https://doi.org/10.2118/16323-PA

Andreola, F., Leonelli, C., Romagnoli, M., & Miselli, P. (2000). Techniques used to determine porosity. *American Ceramic Society Bulletin*, *79* (7), 49–52.

Ardila, N. (2018). *Hydraulic Properties Characterization of 3D Printed Sandstone Analogues* [Master's thesis, University of Alberta]. https://doi.org/10.7939/R3X34N686.

Ardila, N., Zambrano-Narvaez, G., & Chalaturnyk, R. J. (2018). Wettability Measurements on 3D Printed Sandstone Analogues and Its Implications for Fluid Transport Phenomena. *Transport in Porous Media*. https://doi.org/10.1007/s11242-018-1176-1

Arevalo, J. A., Samaniego, F., & Lopez, F. F. (1996). On the Exploitation Injection Conditions of the Akal Reservoir Considering Gas Cap Nitrogen. *Spe 35319*, 1–11.

Arias-Buitrago, J. A., Alzate-Espinosa, G. A., Arbelaez-Londoño, A., Zambrano-Narvaez, G., & Chalaturnyk, R. (2021). Experimental study on the effect of temperature on the mechanical properties of unconsolidated silty sandstones. *Energies*, 14(21). https://doi.org/10.3390/en14217007

ASTM Standard D7012-14; Standard Test Methods for Compressive Strength and Elastic Moduli of Intact Rock Core Specimens under Varying States of Stress and Temperatures. ISO: West Conshohocken, PA, USA, 2014.

ASTM Standard ISO/ASTM 52900:2015(E); Standard Terminology for Additive Manufacturing—General Principles—Terminology. ISO: West Conshohocken, PA, USA, 2015

Asar, H., & Handy, L. L. (1989). Influence of interfacial tension on gas/oil relative permeability in a gas-condensate system. *Spe Reservoir Engng.*, *3*(1, Feb. 1989), 257–264. https://doi.org/10.2118/11740-pa

Bareither, C. A., Benson, C. H., & Edil, T. B. (2008). Comparison of shear strength of sand backfills measured in small-scale and large-scale direct shear tests. *Canadian Geotechnical Journal*, 14 August 2008. https://doi.org/10.1139/T08-058

Barenblatt, G. I., Zheltov, I., & Kochina, I. N. (1960). Basic concepts in the theory of seepage of homogeneous liquids in fissured rocks [strata]. *Journal of Applied Mathematics and Mechanics*, *24*(5), 1286–1303. https://doi.org/https://doi.org/10.1016/0021-8928(60)90107-6

Barton, C. A., Zoback, M. D., & Moos, D. (1995). Fluid flow along potentially active faults in crystalline rock. *Geology*, 23(8), 683–686. https://doi.org/10.1130/0091-7613(1995)023<0683:FFAPAF>2.3.CO;2

Batchelor, G. K. (1967). An Introduction to Fluid Dynamics. Philippines: *Cambridge University Press*.

Bell, F. G. (1978). The physical and mechanical properties of the fell sandstones, Northumberland, England. *Engineering Geology*, *12*(C), 1–29. https://doi.org/10.1016/0013-7952(78)90002-9

Bertei, A., & Nicolella, C. (2011). A comparative study and an extended theory of percolation for random packings of rigid spheres. *Powder Technology*, 213, 100–108. https://doi.org/10.1016/j.powtec.2011.07.011

Bertei, A., Choi, H.-W., Pharoah, J. G., & Nicolella, C. (2012). Percolating behavior of sintered random packings of spheres. *Powder Technology*, *231*, 44–53. https://doi.org/https://doi.org/10.1016/j.powtec.2012.07.041

Bewick, R. P., Amann, F., Kaiser, P. K., & Martin, C. D. (2015). Interpretation of UCS test results for engineering design. *13th ISRM International Congress of Rock Mechanics*, *2015-MAY*(May), 1–14.

Biot, M. A. (1941). General theory of three-dimensional consolidation. *Journal of Applied Physics*, 12(2), 155–164. https://doi.org/10.1063/1.1712886

Brooks, R. H., & Corey, A. T. (1966). Properties of porous media affecting fluid flow. *Journal of the Irrigation and Drainage Division*, 92(2), 61–90.

Buchsteiner, H., Warpinski, N. R., & Economides, M. J. (1993). Stress-induced permeability reduction in fissured reservoirs. *Proceedings - SPE Annual Technical Conference and Exhibition*, *Pi*, 65–74.

Carmichael, R.S. (Ed.). (1982). *Handbook of Physical Properties of Rocks*, Vol. I. CRC Press.

Castañeda-Herrera, C. A., Black, J. R., Llanos, E. M., Stevens, G. W., & Haese, R. R. (2018). Formation of an amorphous silica gel barrier under CO2 storage conditions. *International Journal of Greenhouse Gas Control*, 78(July), 27–36. https://doi.org/10.1016/j.ijggc.2018.07.013

Celis, E., Garcia-Hernandez, J., Morales-Ramirez, J. M., Cabrera-Toledo, C., Sheridan, J., Ward, C., & Wiprut, D. (2006). Fault leakage potential analysis in the Cantarell field, Mexico, using geomechanics. *Proceedings - SPE Annual Technical Conference and Exhibition*, 2, 955–964.

Chou, P.C., & Pagano, N.J. (1992). *Elasticity—Tensor Dyadic, and Engineering Approaches*. Dover Publications.

Cone, J. A., Martin, T. M., Marcellin-Little, D. J., Harrysson, O. L. A., & Griffith, E. H. (2017). Accuracy and repeatability of long-bone replicas of small animals fabricated by use of low-end and high-end commercial three-dimensional printers. *American Journal of Veterinary Research*, *78*(8), 900–905. https://doi.org/10.2460/ajvr.78.8.900

Coussy, O. (2004). Poromechanics. Germany:*Wiley*.

Craig, F. F. (1971). *The Reservoir Engineering Aspects of Waterflooding*. Monograph Volume 3 of the Henry L. Doherty Series. Society of Petroleum Engineers.

Cruz, L., Sheridan, J., Aguirre, E., Celis, E., & García-Hemandez, J. (2009). Relative contribution to fluid flow from natural fractures in the Cantarell field, Mexico. *SPE Latin American and Caribbean Petroleum Engineering Conference Proceedings*, *2*, 871–881. https://doi.org/10.2118/122182-ms

Das, B. M., & Sobhan, K. (2014). *Principles of geotechnical engineering* (8th ed.). Cengage Learning.

Deisman, N., Chalaturnyk, R. J., & Lang, P. (2011). A hydromechanical testing facility for tight reservoirs. *45th US Rock Mechanics / Geomechanics Symposium*.

Duncan, J. M., & Bursey, A. (2013). Soil Modulus Correlations. *Foundation Engineering in the Face of Uncertainty*, 321–336. https://doi.org/10.1061/9780784412763.026

Rangel German, E. R. (2002). *Water infiltration in fractured porous media: In-situ imaging, analytical model, and numerical simulation* [Doctoral dissertation, Stanford University].

Fairhurst, C. (2003). Stress estimation in rock: A brief history and review. *International Journal of Rock Mechanics and Mining Sciences*, 40(7–8), 957–973. https://doi.org/10.1016/j.ijrmms.2003.07.002

Fernø, M. A. (2016). (2016). Enhanced Oil Recovery in Fractured Reservoirs. Introduction to Enhanced Oil Recovery (EOR). *Processes and Bioremediation of Oil-Contaminated Sites*. ISBN, 978–95313.

Friedman, G. M. (1962). On sorting sorting coefficients and log normality of the grain size distribution of sandstone. *Journal of Geology*, 70, 737-756. https://doi.org/10.1086/jg.70.6.30066373

Gomez, J. S., Chalaturnyk, R. J., & Zambrano-Narvaez, G. (2018). Experimental Investigation of the Mechanical Behavior and Permeability of 3D Printed Sandstone Analogues Under Triaxial Conditions. *Transport in Porous Media*. https://doi.org/10.1007/s11242-018-1177-0

Grajales-Nishimura, J. M., Cedillo-Pardo, E., Rosales-Dominguez, C., Moran-Zenteno, D. J., Alvarez, W., Claeys, P., Ruiz-Morales, J., Garcia-Hernandez, J., Pedilla-Avila, P., & Sanchez-Rios, A. (2000). Chicxulub impact: The origin of reservoir and seal facies in the southeastern Mexico oil fields. *Geology*, 28(12), 1152. https://doi.org/10.1130/0091-7613(2000)28<307:CITOOR>2.0.CO;2

Gregorski, S. (1996). *High green density metal parts by vibrational compaction of dry powder in the three-dimensional printing process* [Doctoral dissertation, Massachusetts Institute of Technology].

Kazemi, H. (1969). Pressure transient analysis of naturally fractured reservoirs with uniform fracture distribution. *Old SPE Journal*, 9(4), 451-462.

Hadley, G. F., & Handy, L. L. (1956). *A Theoretical and of The Steady State Experimental Study Capillary End Effect*. http://onepetro.org/SPEATCE/proceedings-pdf/56FM/All-56FM/SPE-707-G/2086408/spe-707-g.pdf/1

Haghi, A. H., Talman, S., & Chalaturnyk, R. (2020). Consecutive experimental determination of stress-dependent fluid flow properties of Berea sandstone and implications for two-phase flow modeling. *Water Resources Research*, 56(1), e2018WR024245. https://doi.org/10.1029/2018WR024245

Hale, P. A., & Shakoor, A. (2003). A laboratory investigation of the effects of cyclic heating and cooling, wetting and drying, and freezing and thawing on the compressive strength of selected sandstones. *Environmental and Engineering Geoscience*, *9*(2), 117–130. https://doi.org/10.2113/9.2.117

Hamoud, M., Chalaturnyk, R., & Leung, J. (2020). Experimental studies of shear-induced changes in two-phase relative permeability. *Arabian Journal of Geosciences*, *13*(14). https://doi.org/10.1007/s12517-020-05495-4

Hassler, G. L., & Brunner, E. (1945). Measurement of Capillary Pressures in Small Core Samples. *Transactions of the AIME, 160*(01), 114–123. https://doi.org/10.2118/945114-g

Hendraningrat, L., Li, S., & Torstæer, O. (2013). A coreflood investigation of nanofluid enhanced oil recovery in low-medium permeability Berea sandstone. *Proceedings - SPE International Symposium on Oilfield Chemistry*, 2, 728–741. https://doi.org/10.2118/164106-ms

Hodder, K. J., & Chalaturnyk, R. J. (2019). Bridging additive manufacturing and sand casting: Utilizing foundry sand. *Additive Manufacturing*, *28*(April), 649–660. https://doi.org/10.1016/j.addma.2019.06.008

Hodder, K. J., Nychka, J. A., & Chalaturnyk, R. J. (2018). Process limitations of 3D printing model rock. *Progress in Additive Manufacturing*, *3*, 173–182. https://doi.org/10.1007/s40964-018-0042-6

Hodder, K. J., Sanchez-Barra, A. J., Ishutov, S., Zambrano-Narvaez, G., & Chalaturnyk, R. J. (2022). Increasing Density of 3D-Printed Sandstone through Compaction. *Energies*. https://doi.org/10.3390/en15051813

Hodder, K., Ishutov, S., Sanchez, A., Zambrano, G., & Chalaturnyk, R. (2020). 3D printing of rock analogues in sand: A tool for design and repeatable testing of geomechanical and transport properties. *E3S Web of Conferences*, *205*. https://doi.org/10.1051/e3sconf/202020504014

Hoek, E. (1965). *Rock fracture under static stress conditions*. Council for Scientific and Industrial Research Report MEG383. Pretoria, South Africa: Council for Scientific and Industrial Research.

Hoek, E., & Brown, E. T. (1980). Empirical strength criterion for rock masses. *Journal of the Geotechnical Engineering Division, ASCE, 106(9)*, 1013-1035.

Hoek, E., & Brown, E. T. (1997). Practical estimates of rock mass strength. *International Journal of Rock Mechanics and Mining Sciences, 34(8)*, 1165-1186. https://doi.org/10.1016/S1365-1609(97)80069-X

Hoek, E., & Brown, E. T. (2019). The Hoek–Brown failure criterion and GSI – 2018 edition. *Journal of Rock Mechanics and Geotechnical Engineering, 11(3)*, 445-463. https://doi.org/10.1016/j.jrmge.2018.08.001

Hoek, E., & Martin, C. D. (2014). Fracture initiation and propagation in intact rock - A review. *Journal of Rock Mechanics and Geotechnical Engineering*, 6(4), 287–300. https://doi.org/10.1016/j.jrmge.2014.06.001

Hoek, E., Carranza-Torres, C., & Corkum, B. (2002). Hoek-Brown failure criterion – 2002 edition. Journal of The South African Institute of Mining and Metallurgy, 74(8), 312–320. https://doi.org/10.1016/0148-9062(74)91782-3

Huo, D., & Benson, S. M. (2015). An Experimental Investigation of Stress-Dependent Permeability and Permeability Hysteresis Behavior in Rock Fractures. *Fluid Dynamics in Complex Fractured-Porous Systems*, 99–114. https://doi.org/10.1002/9781118877517.ch7

Huo, D., & Benson, S. M. (2016). Experimental Investigation of Stress-Dependency of Relative Permeability in Rock Fractures. *Transport in Porous Media*, *113*(3), 567–590. https://doi.org/10.1007/s11242-016-0713-z

Iscan, A. G., & Kok, M. v. (2009). Porosity and permeability determinations in sandstone and limestone rocks using thin section analysis approach. *Energy Sources, Part A: Recovery, Utilization and Environmental Effects*, 31(7), 568–575. https://doi.org/10.1080/15567030802463984

Jaeger, J. C., Cook, N. G. W., & Zimmerman, R. (2007). *Fundamentals of Rock Mechanics* (4th ed.). Blackwell Publishing.

Jahanbakhsh, A., Shahverdi, H., & Sohrabi, M. (2016). *Gas / Oil Relative Permeability Normalization : Effects of Permeability , Wettability , and Interfacial Tension*. *October 2014*, 27–29.

Jones, F. O. (1975). Laboratory Study of the Effects of Confining Pressure on Fracture Flow and Storage Capacity in Carbonate Rocks. *JPT, Journal of Petroleum Technology*, *27*, 21–27. https://doi.org/10.2118/4569-PA

Gomez, J. S. (2018). Mechanical properties characterization of 3D printed reservoir sandstone analogues [Master's thesis]. Retrieved from https://doi.org/10.7939/R31V5BV4Z.

Kazemi, H., Gilman, J. R., & Elsharkawy, A. M. (1992). Analytical and numerical solution of oil recovery from fractured reservoirs with empirical transfer functions. *SPE reservoir engineering*, 7(02), 219-227.

Khanal, A., & Weijermars, R. (2019). Visualization of drained rock volume (DRV) in hydraulically fractured reservoirs with and without natural fractures using complex analysis methods (CAMs). *Petroleum Science*, *16*(3), 550–577. https://doi.org/10.1007/s12182-019-0315-9

Leon-G, A., Sanchez, L., Jose, B., Ascencio, C. F., Ladron, G. J. E., Galindo, A., Samaniego-V, F., Ley, H. C., & Rodriguez, F. (2005). A Study of the Initial and Exploitation Conditions of the Super Giant Akal Offshore Naturally Fractured Reservoir. *18th World Petroleum Congress*.

Lian, P. Q., Cheng, L. S., & Ma, C. Y. (2012). The characteristics of relative permeability curves In naturally fractured carbonate reservoirs. *Journal of Canadian Petroleum Technology*, *51*(2), 137–142. https://doi.org/10.2118/154814-PA

Limón-Hernández, T., De-la-Fuente, G., Garza-Ponce, G., & Monroy-Hernandez, M. (1999). Overview of the Cantarell Field Development Program. *Offshore Technology Conference*, 1–9. https://doi.org/10.4043/10860-MS

Longeron, D. G., Kalaydjian, F., Bardon, C., & Desremaux, L. M. (1994). Gas/oil capillary pressure: measurements at reservoir conditions and effect on gas-gravity drainage. *Proceedings - SPE Annual Technical Conference and Exhibition*, *Sigma* (pt 2), 23–28. https://doi.org/10.2523/28612-ms

Lucia, F. J., Kerans, C., & Jennings, J. W. (2007). Carbonate Reservoir Characterization. In *Journal of Petroleum Technology* (Vol. 55, Issue 06). https://doi.org/10.2118/82071-jpt

Ma, Y. Z. (2019). Quantitative Geosciences: *Data Analytics, Geostatistics, Reservoir Characterization and Modeling*. https://doi.org/10.1007/978-3-030-17860-4

McDonald, A. E., Beckner, B. L., Chan, H. M., Jones, T. A., & Wooten, S. O. (1991). Some Important Considerations in the Simulation of Naturally Fractured Reservoirs. *SPE*, 117–124. https://doi.org/10.2118/21814-ms

Moghadam, A. A., & Chalaturnyk, R. (2016). Analytical and experimental investigations of gas-flow regimes in shales considering the influence of mean effective stress. *SPE Journal*, *21*(2), 557–572. https://doi.org/10.2118/178429-PA

Morales, J., Caycedo, F., & Forero, G. (2006). Porosity Partition in Akal Field: From Thin Section Petrography to the Simulation Grid. *SPWLA 41st Annual Logging Symposium*, 1–10.

National Hydrocarbons Commission of Mexico. (2018). Retrieved [July, 2018], from https://www.gob.mx/cnh

Nelson, P. H. (1994). Permeability-porosity relationships in sedimentary rock. *The Log Analyst*, May-June, 38-62.

Nelson, R. A. (1985). *Geologic analysis of naturally fractured reservoirs* (Vol. 1). Gulf Professional Publishing.

Nelson, R. A. (2001). Evaluating fractured reservoirs. *Geologic analysis of naturally fractured reservoirs*, 1-100.

Nur, A., & Byerlee, J. D. (1971). An exact effective stress law for elastic deformation of rock with fluids. *Journal of Geophysical Research (1896-1977)*, *76*(26), 6414–6419. https://doi.org/https://doi.org/10.1029/JB076i026p06414

Olsson, R., & Barton, N. (2001). An improved model for hydro-mechanical coupling during shearing of rock joints. *International Journal of Rock Mechanics & Mining Sciences*, 38, 317-329. http://dx.doi.org/10.1016/S1365-1609(00)00079-4

Osinga, S., Zambrano-Narvaez, G., & Chalaturnyk, R. (2015). Study of geomechanical properties of 3D printed sandstone analogue. *Proceedings from American Rock Mechanics Association*, 15–547.

Pedro, J., & Salazar, M. (2018). Pore Pressure Prediction in Carbonates Using Pore and Matrix Compressibilities. *Ingeniería Petrolera*, *58*(2), 100–113.

Perras, M. A., & Vogler, D. (2019). Compressive and Tensile Behavior of 3D-Printed and Natural Sandstones. *Transport in Porous Media*, *129*(2), 559–581. https://doi.org/10.1007/s11242-018-1153-8

Phillips, T., Bultreys, T., Bisdom, K., Kampman, N., Van Offenwert, S., Mascini, A., Cnudde, V., & Busch, A. (2021). A Systematic Investigation into the Control of Roughness on the Flow Properties of 3D-Printed Fractures. *Water Resources Research*, *57*(4), 1–23. https://doi.org/10.1029/2020WR028671

Pini, R., & Benson, S. M. (2013). Simultaneous determination of capillary pressure and relative permeability curves from core-flooding experiments with various fluid pairs. *Water Resources Research*, 49(6), 3516–3530. https://doi.org/10.1002/wrcr.20274

Pini, R., Krevor, S., Krause, M., & Benson, S. (2013). Capillary heterogeneity in sandstone rocks during CO2/water core-flooding experiments. *Energy Procedia*, 37, 5473–5479. https://doi.org/10.1016/j.egypro.2013.06.467

Primkulov, B., Chalaturnyk, J., Chalaturnyk, R., & Zambrano Narvaez, G. (2017). 3D Printed Sandstone Strength: Curing of Furfuryl Alcohol Resin-Based Sandstones. *3D Printing and Additive Manufacturing*, *4*(3), 149–156. https://doi.org/10.1089/3dp.2017.0032

Pruess, K., & Narasimhan, T. N. (1985). A practical method for modeling fluid and heat flow in fractured porous media. *Society of Petroleum Engineers Journal*, 25(01), 14-26.

Pyrak-Nolte, L.J., Cook, N.G., Myer, L. (1991). Fluid flow through single fractures. In *International Journal of Rock Mechanics and Mining Sciences & Geomechanics Abstracts* (Vol. 28, Issues 2–3, p. A149). https://doi.org/10.1016/0148-9062(91)92849-t

Rangel-German, E. R., & Kovscek, A. R. (2005). Matrix-fracture shape factors and multiphase-flow properties of fractured porous media. *SPE Latin American and Caribbean Petroleum Engineering Conference Proceedings*, *2005-June*.

Rangel-german, E., Akin, S., & Castanier, L. (2006). *Multiphase-flow properties of fractured porous media*. *51*, 197–213. https://doi.org/10.1016/j.petrol.2005.12.010

Rojas, A. G., & Torres, A. R. (1994). Akal Field (Cantarell Complex) Conditions of Exploration, Analysis, and Prediction. *Society of Petroleum Engineers*, 445–455. https://doi.org/10.2118/28714-MS

Rostami, P., Sharifi, M., Aminshahidy, B., & Fahimpour, J. (2020). Enhanced oil recovery using silica nanoparticles in the presence of salts for wettability alteration. *Journal of Dispersion Science and Technology*, 41(3), 402–413. https://doi.org/10.1080/01932691.2019.1583575

Sahoo, P. K., Soltani, S., & Wong, A. K. C. (1988). A survey of thresholding techniques. *Computer Vision, Graphics, and Image Processing*, 41(2), 233-260. https://doi.org/10.1016/0734-189X(88)90022-9

Sanchez Bujanos, J. L., Astudillo Abundes, A. V., Rodriguez-De La Garza, F., Morales, J., & Rodriguez Torres, A. (2005). Nitrogen Injection in the Cantarell Complex: Results After Four Years of Operation. *SPE Latin American and Caribbean Petroleum Engineering Conference*. https://doi.org/10.2118/97385-MS

Sanchez-Barra, A., Deisman, N., Guerrero, F., Brandl, J., & Chalaturnyk, R. (2022). Experimental Facility for Testing Unconventional Reservoirs: Effect of Geomechanics on Multiphase Flow Properties. *American Rock Mechanics Association*. https://doi.org/https://doi.org/10.56952/ARMA-2022-0543

Sanchez-Barra, A., Zambrano-narvaez, G., & Chalaturnyk, R. (2023). An In-Depth Analysis of Strength and Stiffness Variability in 3D-Printed Sandstones : Implications for Geomechanics. *Energies*, 16(14). https://doi.org/10.3390/en16145406

Smart, B. G. D., Somerville, J. M., Edlman, K., & Jones, C. (2001). Stress sensitivity of fractured reservoirs. *Journal of Petroleum Science and Engineering*, *29*(1), 29–37. https://doi.org/10.1016/S0920-4105(00)00088-7

Song, R., Wang, Y., Ishutov, S., Zambrano-Narvaez, G., Hodder, K. J., Chalaturnyk, R. J., Sun, S., Liu, J., & Gamage, R. P. (2020). A Comprehensive Experimental Study on Mechanical Behavior, Microstructure and Transport Properties of 3D-printed Rock Analogs. *Rock Mechanics and Rock Engineering*, *53*(12), 5745–5765. https://doi.org/10.1007/s00603-020-02239-4

Song, R., Wu, M., Wang, Y., Liu, J., & Yang, C. (2023). In-situ X-CT scanning and numerical modeling on the mechanical behavior of the 3D printing rock. *Powder Technology*, *416*(January), 118240. https://doi.org/10.1016/j.powtec.2023.118240

Sui, W., Quan, Z., Hou, Y., & Cheng, H. (2020). Estimating pore volume compressibility by spheroidal pore modeling of digital rocks. *Petroleum Exploration and Development*, *47*(3), 603–612. https://doi.org/10.1016/S1876-3804(20)60077-5

Sun, S., & Pollitt, D. A. (2020). Optimising development and production of naturally fractured reservoirs using a large empirical dataset. *Petroleum Geoscience*, *27*(2). https://doi.org/10.1144/petgeo2020-079

Terzaghi, K. (1943). *Theoretical Soil Mechanics*. Wiley. http://dx.doi.org/10.1002/9780470172766

Touhidi-Baghini, A. (1998). *Absolute permeability of McMurray Formation oil sands at low confining stresses* [Doctoral dissertation, University of Alberta]. https://doi.org/10.7939/R3Z31P07M

Vanessa Santiago, Francy Guerrero Zabala, Angel J. Sanchez-Barra, Nathan Deisman, Richard J. Chalaturnyk, Ruizhi Zhong, S. H. (2022). Experimental Investigation of the Flow Properties of Layered Coal-Rock Analogues Vanessa. *Chemical Engineering Research and Design*. https://doi.org/10.1016/j.cherd.2022.08.046

Vogler, D., Settgast, R. R., Annavarapu, C., Madonna, C., Bayer, P., & Amann, F. (2018). Experiments and Simulations of Fully Hydro-Mechanically Coupled Response of Rough Fractures Exposed to High-Pressure Fluid Injection. *Journal of Geophysical Research: Solid Earth*, *123*(2), 1186–1200. https://doi.org/10.1002/2017JB015057

Vogler, D., Walsh, S. D. C., Dombrovski, E., & Perras, M. A. (2017). A comparison of tensile failure in 3D-printed and natural sandstone. *Engineering Geology*, *226*(June), 221–235. https://doi.org/10.1016/j.enggeo.2017.06.011

Warren, J. E., & Root, P. J. (1963). The Behavior of Naturally Fractured Reservoirs. *Society of Petroleum Engineers Journal*, *3*(03), 245–255. https://doi.org/10.2118/426-pa

Witherspoon, P. A., Wang, J. S. Y., Iwai, K., & Gale, J. E. (1980). Validity of Cubic Law for Fluid Flow in a Deformable Rock Fracture. *Water Resources Research*, 16, 1016-1024. http://dx.doi.org/10.1029/WR016i006p01016

Wu, Y. S., & Pruess, K. (1988). A multiple-porosity method for simulation of naturally fractured petroleum reservoirs. *SPE Reservoir Engineering*, 3(01), 327-336.

Wu, Y.-S. (2016). Multiphase Fluid Flow in Porous and Fractured Reservoirs. *Elsevier*. ISBN 978-0-12-803848-2.

Yang, Y., Liu, Z., Sun, Z., An, S., Zhang, W., Liu, P., Yao, J., & Ma, J. (2017). Research on stress sensitivity of fractured carbonate reservoirs based on CT technology. *Energies*, *10*(11). https://doi.org/10.3390/en10111833

Yin, Q., Ma, G., Jing, H., Wang, H., Su, H., Wang, Y., & Liu, R. (2017). Hydraulic properties of 3D rough-walled fractures during shearing: An experimental study. *Journal of Hydrology*, *555*, 169–184. https://doi.org/10.1016/j.jhydrol.2017.10.019

Yu, C., Tian, W., Zhang, C., Chai, S., Cheng, X., & Wang, X. (2021). Temperature-dependent mechanical properties and crack propagation modes of 3D printed sandstones. *International Journal of Rock Mechanics and Mining Sciences*, *146*(May), 104868. https://doi.org/10.1016/j.ijrmms.2021.104868

Zhang, B. (2019). Integrated Reservoir-Geomechanics Upscaling Workflow [Doctoral dissertation, University of Alberta]. https://doi.org/10.7939/r3-gzas-n027

Zhu, W., & Wong, T. (1997). The transition from brittle faulting to cataclastic flow: Permeability evolution. *Journal of Geophysical Research: Solid Earth*, 102(B2), 3027–3041. https://doi.org/10.1029/96jb03282

Ziaee, M., & Crane, N. B. (2019). Binder jetting: A review of process, materials, and methods. *Additive Manufacturing*, *28* (December 2018), 781–801. https://doi.org/10.1016/j.addma.2019.05.031

Zimmerman, R. W. (2018). Imperial College Lectures In Petroleum Engineering, The - Volume 5: Fluid Flow In Porous Media. Singapore: *World Scientific Publishing Company*.

Zimmerman, R. W., & Bodvarsson, G. S. (1996). Hydraulic conductivity of rock fractures. *Transport in Porous Media*, *23*(1), 1–30. https://doi.org/10.1007/BF00145263

Zimmerman, R. W., Somerton, W. H., & King, M. S. (1986). Compressibility of porous rocks. *Journal of Geophysical Research: Solid Earth*, *91*(B12), 12765–12777. https://doi.org/10.1029/jb091ib12p12765

Zoback, M. D. (2007). Reservoir Geomechanics. In *Reservoir Geomechanics*. Cambridge University Press https://doi.org/10.1017/CBO9780511586477

# Appendix A - 3D-Printed Reservoir Rock Analogues

## CT-Scan Images of 3D-Printed Fractured Reservoir Rock Analogues

This section presents the CT-scanning data and analysis of 3D-printed fractured reservoir rock analogues, focusing on capturing and understanding the internal structures critical for studying multiphase flow behaviors. Through detailed CT imagery, we explore the porosity, fractures, and material consistency of the analogues, comparing them with natural reservoir properties.

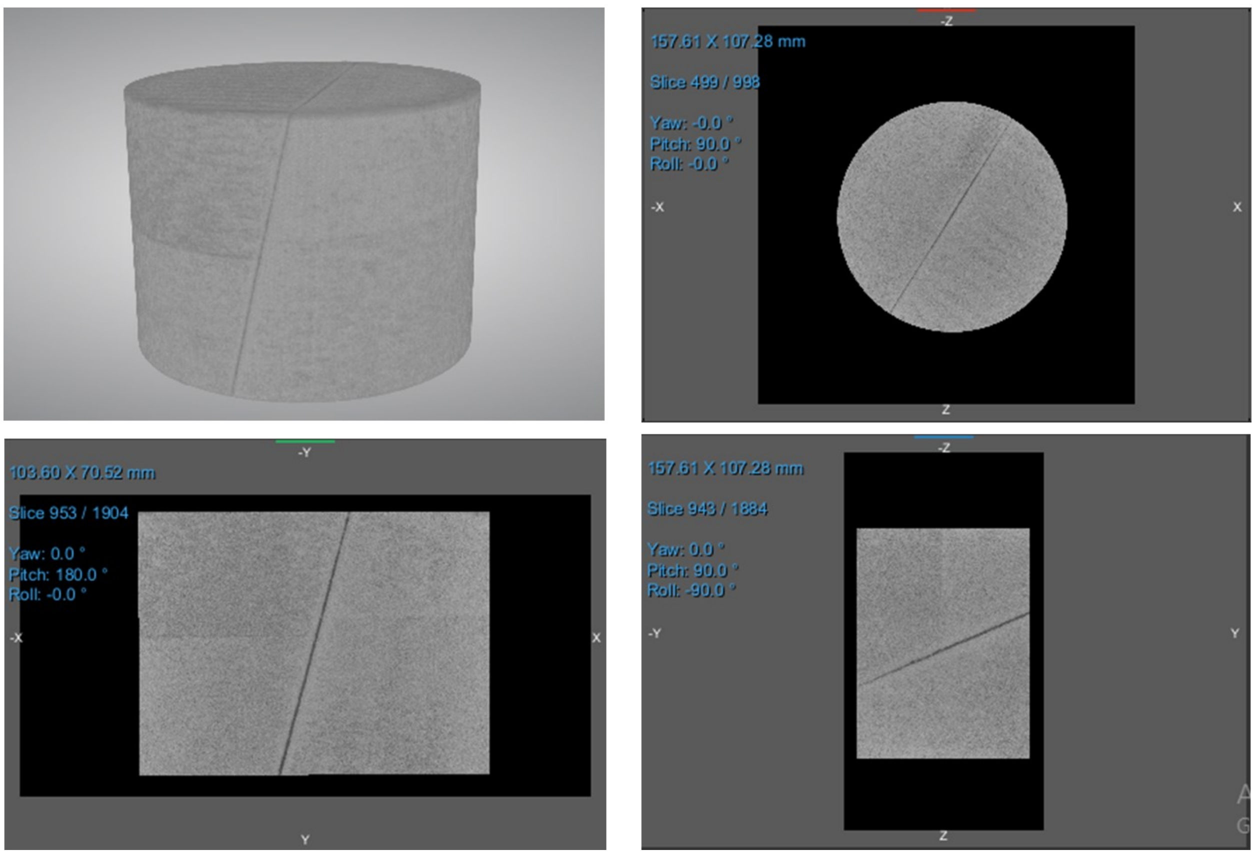


Figure A.1. Collage of CT-scan images of a 3D-printed reservoir rock analogue at different angles.

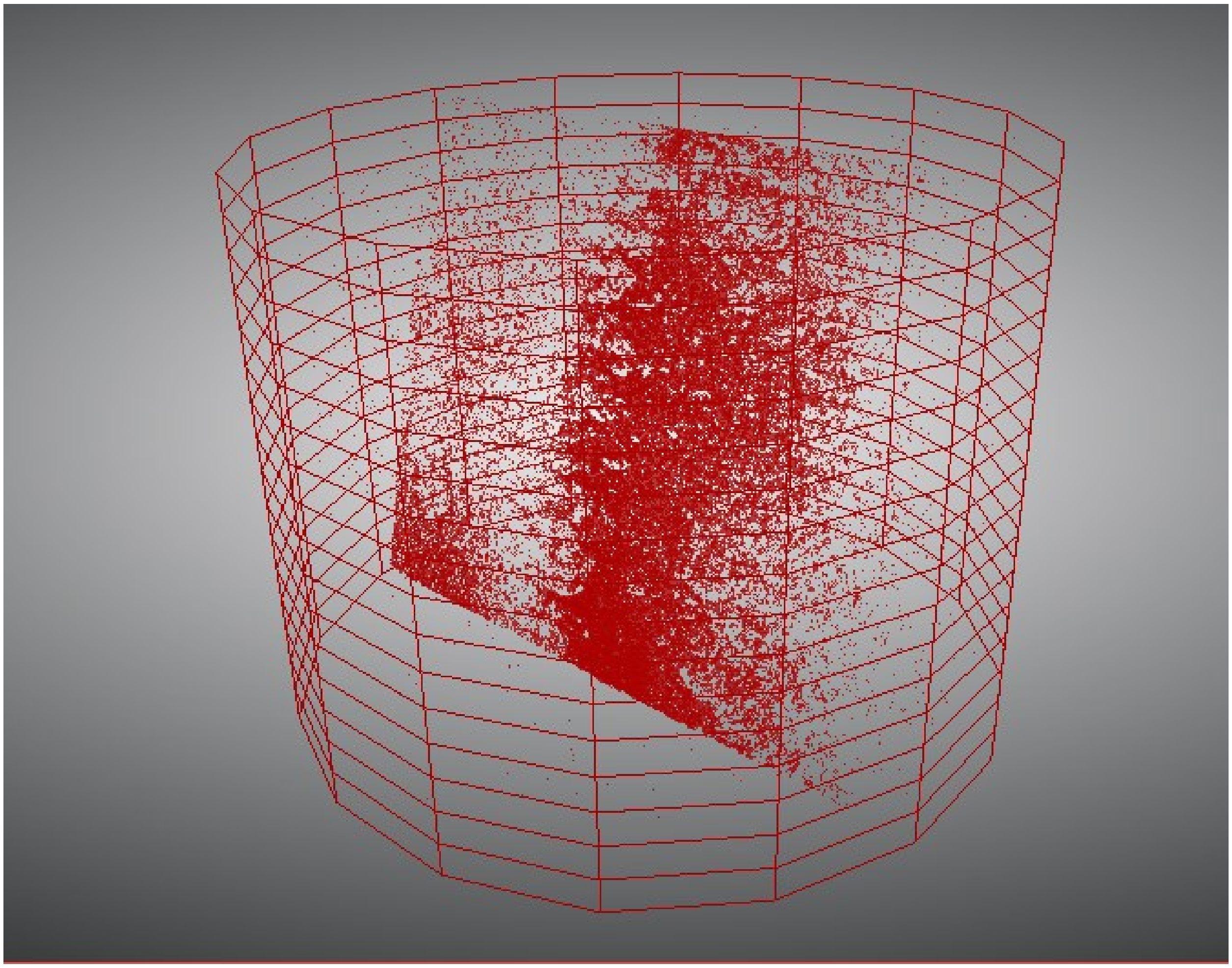

Figure A.2. Reconstructed CT-scan image of a 3D-printed fracture post-multiphase testing.

# Appendix B - Multiphase Triaxial Testing Data

## Nitrogen-Oil Relative Permeability for 3D-Printed Reservoir Rock Analogues

Figure B.1 displays the transient data from a relative permeability test conducted on a 3D-printed fractured reservoir analogue. Initially, the section details the procedure for measuring absolute permeability. Following this, it describes a process where the oil flow rate is gradually decreased, while the nitrogen flow rate is simultaneously increased. This alteration leads to a variation in pressure drop across the sample, first increasing then decreasing. The data illustrate how changes in fractional flow can trigger a transitional phase before reaching a state of equilibrium.

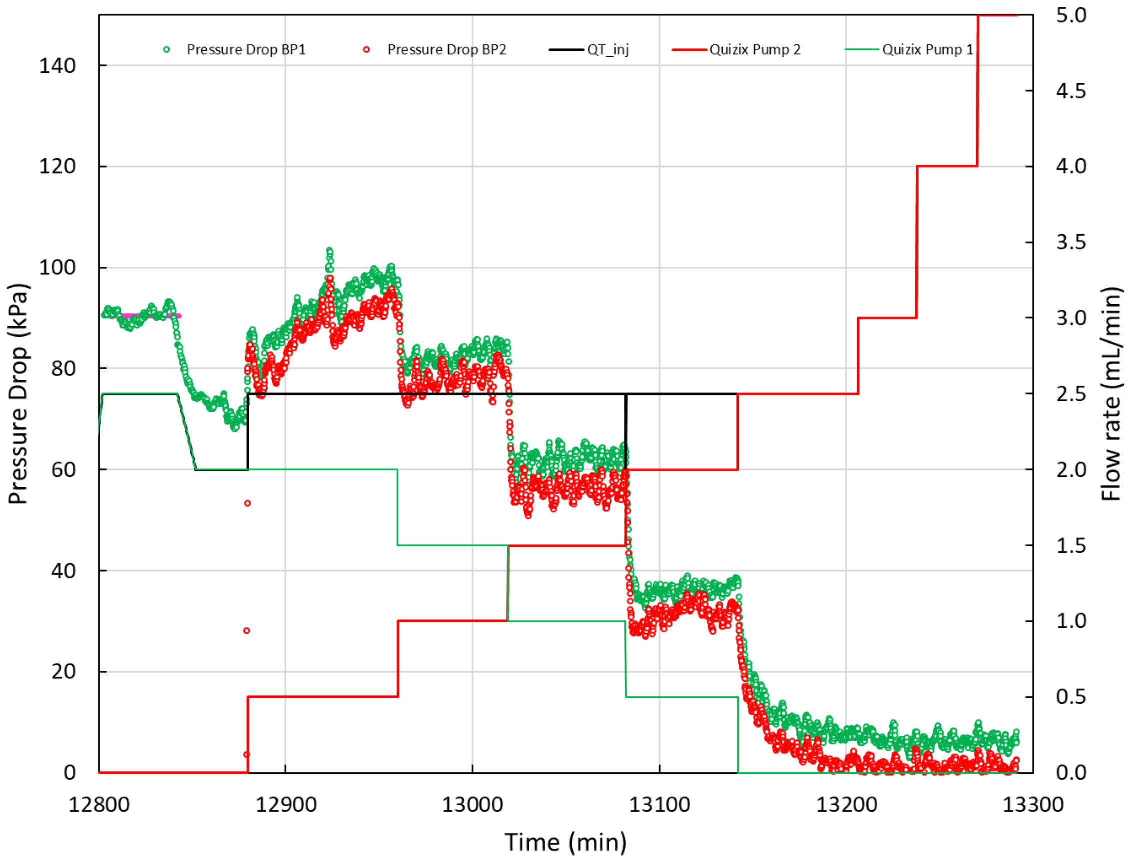


Figure B.1. Transient behavior in relative permeability testing for a 3D-printed fractured reservoir analogue.

## Nitrogen-Water Relative Permeability for Berea Sandstone

This section presents the results of nitrogen-water relative permeability and capillary pressure tests conducted on Berea sandstones. It includes detailed analyses of effective permeability for both water and gas, accompanied by observations on pressure drop behaviors. Additionally, this part showcases the derived relative permeability and capillary pressure curves, offering insights into the fluid dynamics within the Berea sandstone under varying conditions.

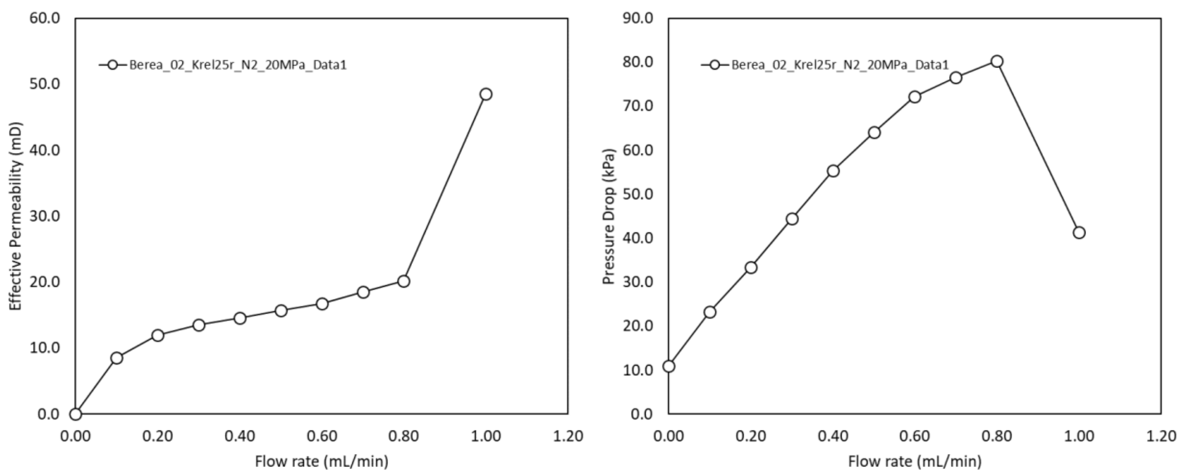


Figure B.2. Effective water permeability in a partially saturated medium within a nitrogen-water system.

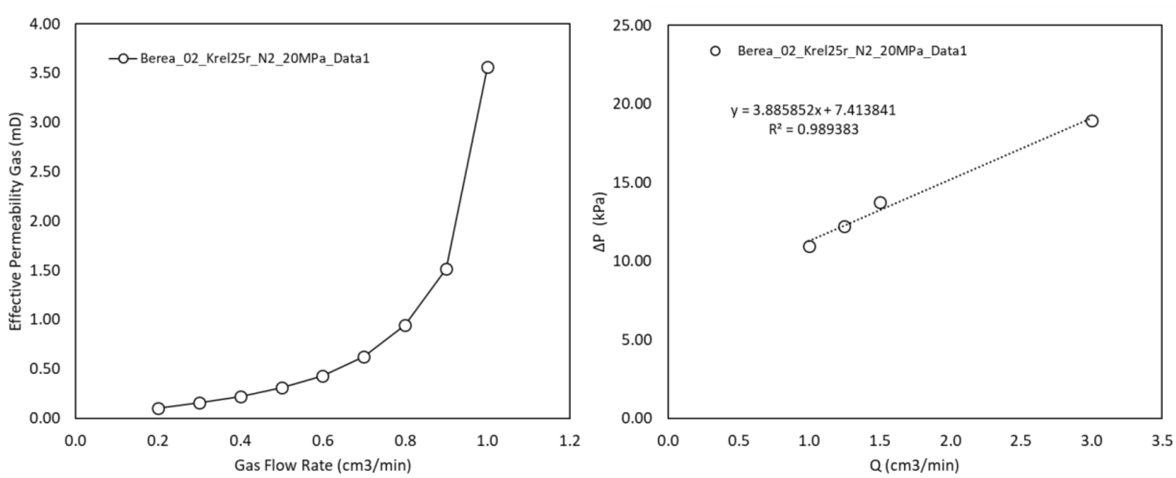


Figure B.3. Effective gas permeability in a partially saturated medium within a nitrogen-water system.

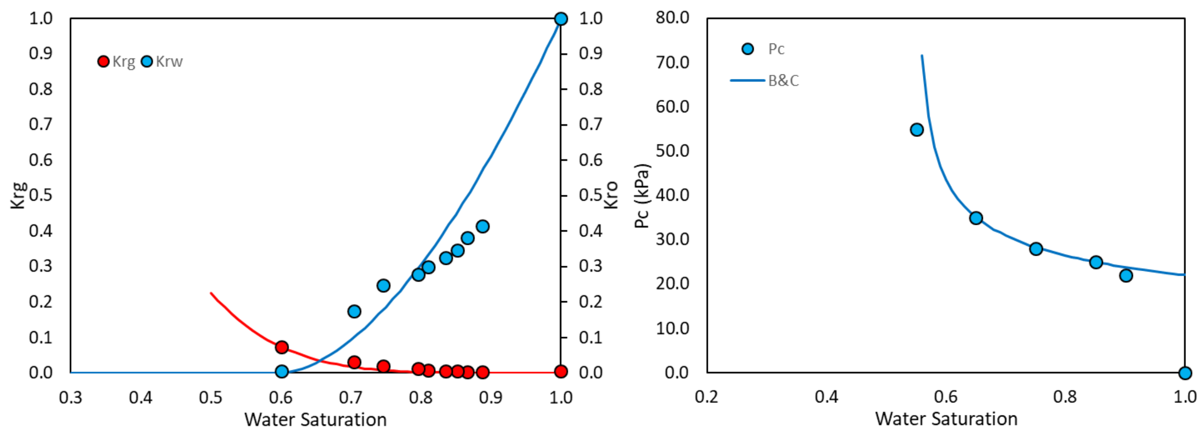


Figure B.4. Drainage relative permeability and capillary pressure in nitrogen-water system.